Strain Engineering, Quantum Transport and Synthesis of Atomically-thin Two-dimensional Materials

Abdollah (Ali) Motmaen Dadgar

Submitted in partial fulfillment of the
requirements for the degree of
Doctor of Philosophy
in the Graduate School of Arts and Sciences

COLUMBIA UNIVERSITY
2017

Abstract:

Strain Engineering, Quantum Transport and Synthesis of Atomically-thin Two-dimensional Materials

Abdollah (Ali) Motmaen Dadgar

Two-Dimensional (2D) materials such as graphene, Transition Metal Dichalcogenides (TMDs) and Metal Monochalcogenides (MMs) are the next generation of smart devices because of their outstanding novel properties. Monolayer (one molecule thick.) of famous TMDs such as MoS_2, $MoSe_2$, WS_2 and WSe_2 exhibit phenomenal physical properties including but not limited to low-energy direct bandgap and large piezoelectric responses. These have made them potential candidates for cutting-edge electronic and mechanical devices such as novel transistors and PN-junctions, on-chip energy storage and piezoelectric devices which could be applied in smart sensors and actuators technologies. Additionally, reversible structural phase transition in these materials from semiconducting phase ($1H$) to metallic phase ($1T'$) as a function of strain, provide compelling physics which facilitates new era of sophisticated flexoelectric devices, novel switches and a giant leap in new regime of transistors.

One iconic characteristics of monolayer 2D materials is their incredible stretchability which allows them to be subjected to several percent strains before yielding. In this thesis I provide facile techniques based on polymer encapsulation to apply several percent (6.5%) controllable, non-destructive and reproducible strains. This is the highest reproducible strain reported so far. Then I show our experimental techniques and object detection algorithm to verify the amount of strain. These followed up by device fabrication techniques as well as in-depth polarized and unpolarized Raman spectroscopy. Then, I show interesting physics of monolayer and bilayer TMDs under

strain and how their photoluminescence behaviors change under tensile and compressive strains. Monolayers of TMDs and MMs exhibit 1-10 larger piezoelectric coefficients comparing to bulk piezo materials. These surprising characteristics together with being able to apply large range strains, opens a new avenue of piezoelectricity with enormous magnitudes higher than those commercially available. Further on 2D materials, I show our transport experiments on doped and pristine graphene micro devices and unveil the discoveries of magneto conductance behaviors. To complete, we present our computerized techniques and experimental platforms to make these 2D materials.

Table of Contents

CHAPTER **Page**

Preface ……. vi

PART A – PHYSICS OF TWO-DIMENSIONAL MICROSYSTEMS

1 An Introduction to Two Dimensional Materials ……..….. 2

1.1 Physics in Two Dimensional Limits ……... 3

1.2 Transition Metal Dichalcogenides (TMDs) ……... 10

2 Phonon Structure and Raman Spectroscopy of TMDs ……..... 22

2.1 Introduction to the Physics of Raman ……..... 23

2.2 Polarized and Unpolarized Raman Spectroscopy …….. 26

2.3 Phonon Specifications …… 32

2.4 Strengths of Raman Signals ……... 35

3 Band structure, Excitons and Photoluminescence Spectroscopy ……..….. 39

PART B - STRAIN ENGINEERING

4 Strain Engineering of Two Dimensional Materials ……..…… 45

4.1 Introduction ……... 46

4.2 1D or Uniaxial Stress (thin membranes) ……...… 49

4.3 1D or Uniaxial Strain (thick parts) ……..…….. 49

4.4 2D or Plane Stress (thin membranes) ……...……. 50

4.5 2D or Plane Strain (thick parts) ……..…….. 52

4.6 Methods of Applying Uniaxial Stress ……..……. 53

4.7 Groundbreaking Reproducible Strain© ……...….. 60

5 Device Micro / Nano Fabrication Techniques …….. 72

5.1 Introduction ……... 73

5.2 Introduction to polymers and polymers based devices ……. 73

5.3 Flexible devices …… 77

5.4 Field-effect transistors and transport devices ……..….. 82

5.5 Micro transfer techniques ……..… 84

6 Experimental Results ……..… 86

6.1 Raman Signals Processing ……... 87

6.2 Photoluminescence Signals Processing ……... 107

PART C – TRANSPORT PROPERTIES OF PRISTINE AND CHEMICALLY DOPED GRAPHENE

7 Quantum Transport of Pristine Graphene …….. 138

8 Quantum Transport of N-doped Graphene ……. 153

PART D – MANUFACTURING OF TWO-DIMENSIONAL MATERIALS

9 Production of Pristine and N-doped Graphene …… 207

10 Production of Transition Metal Dichalcogenides ……. 212

References ……...……. 219

Acknowledgements

After long career life time, I decided to come back to graduate school to pursue higher academic degrees as well as satisfy my scientific curiosity. This long-lasting dream sounded weird and unusual to many people who claimed it might not be a good decision at older ages with long working experiences. I appreciate Columbia University that paved this way for me. During graduate school, I found myself even more enthusiastic and energetic than I was ever before. Instead of those tough times, I enjoyed my decision, learned many thing and diversified my knowledge. As a rule-breaker, I shined in course works and worked very hard on research projects to produce many publishable and novel results. I realized that the only limit for human is the cliché type of thinking, negative mindsets and limited imaginations.

I am feeling grateful and honored to have Professor Abhay Pasupathy in Physics Department as my sponsor, advisor and manager during PhD. My academic life and success would not be possible without his generous supports, thoughtfulness and scientific leadership and advice. He never stopped his gracious helps and provided whatever I needed to advance in science and technology.

I warmly thank professor James Hone – my departmental advisor in Mechanical Engineering Department for his leadership and constructive guidelines who lead me to the research position in Physics Department. My PhD would not be possible without his advice.

I also cordially thank Professors Jeffrey Kysar and Sinisa Vukelic for discussions and for being in my committee. I sincerely thank Prof. Daniel Esposito for being generous on using his lab especially his laser microscope.

I would like to thank and appreciate Prof. Liuyan Zhao, Dr. Alexander (Sasha) Gondarenko, Prof. Arend Van der Zande, Prof. Adam Wei Tsen, Prof. Youngduck Kim, Prof. E.H Yang, Prof.

Gwan-Hyoung Lee, Prof. Elton Santos, Prof. Jonathan Owen, Prof. Michael Steigerwald, Prof. Colin Nuckolls, Dr. Kyungnam Kang, Prof. Irving Herman, Dr. Christopher Gutiérrez, Dr. Daniel Chenet and Prof. Chee Wei Wong for their helps and discussions.

Many ups and downs but still lots of pleasant memories during graduate school. I made many nice and helpful friends. Thanks for Drew Edelberg for his generous helps on making stuffs and for the discussions. Erick Andrade – many nice memories with hot sauce barrels and the electric kettle; he drew my attention and interests to Linux operating system a few years ago. I always enjoyed talking to him about Machine Learning, coding, Data Science, etc. Ayelet Notis for great discussions and for her generous helps when I needed. Dennis Wang for his helps on device fabrication – I always stunned with his exfoliation and fabrication talents. Ghidewon Arefe for his gracious helps especially when I had to make something urgently. Further, many thanks for Alex Kerelsky, Da Wang, Nathan Finney, Christopher DiMarco, Jaeeun Yu, Dottore Augusto Ghiotto for their helps.

I would like to thank Columbia's administration in mechanical engineering and physics departments; Sandra Morris for her genuine care of students, Emily-Anne McCormack for her generous helps as an excellent career placement officer, Randy Torres, Melbourne Francis, Michael Adan for their supports.

To:

My parents, Davood and Masoomeh for their eternal love and prayers.

And especially dedicated to my wife, Delband for her love, support and understanding, together with my sweetheart daughter, Nikki for being such a blessing.

And everyone who shined in my life and taught me lessons.

Preface

This thesis is divided into four parts. Part A which covers chapters 1-3 provides basic science to understand 2D microsystems. Part B, chapters 4-6 is the main body of this thesis which gives experimental and theoretical studies of mechanical deformation and strain in microsystems. Part C - chapter 7 and 8, elaborates quantum transport of 2D devices focused on pristine and n-doped graphene. Part D covers the experimental methods of manufacturing these materials; graphene and TMDs presented in chapter 9 and 10 respectively.

In Part A – chapters 1, 2 and 3, I provide some brief physics of 2D systems which is crucial to understand the rest of the thesis. Starting with principles of quantum mechanics, we present the foundations of 2D devices with their exceptional physical properties. We then introduce famous materials such as graphene and TMDs focusing on their structural characteristics such as polymorphism, electronic and phonon structures, Van der Waals interactions, etc.

Part B consisting chapters 4, 5, 6, convey the main message of this thesis: strain engineering of two-dimensional microsystems. In chapter 4, we first discuss different types of strains applicable to 2D microsystems: uniaxial stress, uniaxial strain, plane stress – all for thin membranes and plane strain for thicker devices. Then we introduce all possible methods for applying strain. At the end of this chapter, we introduce our novel technique to apply groundbreaking and controllable strain. Moreover, chapter 5 is dedicated some state-of-the-art fabrication techniques which are crucial to understand device requirements for this dissertation. Finally, chapter 6 are main experimental results which is divided into chapter 6.1 – Raman Signals Processing and 6.2 – Photoluminescence Signals Processing.

Part C comprises chapters 7 and 8. It presents interesting results of transport measurements of pristine and n-doped graphene. In these measurements we explain how magneto resistance is different in two different types of graphene micro devices. We use advanced data analysis

techniques to discover the giant temperature dependence and inherent oscillation of conductivity of n-doped graphene in different carrier densities with various magnetic fields, which do not exist in pristine graphene devices.

Part D at the end of this thesis, provides detailed technology of growing graphene and how to dope it with nitrogen. Then, we explain the Chemical Vapor Deposition (CVD) techniques to grow single layer TMDs in the fully computerized furnace setup we made for this purpose. We represent our results on $MoSe_2$ which we successfully made it for the first time – since there was no report at that time (2013).

PART A

PHYSICS OF TWO DIMENSIONAL MICRISYSTEMS

CHAPTER 1

An Introduction to Two Dimensional Materials

1.1 Physics in Two Dimensional Limits

Two dimensional (2D) or layered materials which exhibit strong in-plane covalent bounds and weak van der Waals out-of-plane forces have attracted incredible attention because of their unusual astonishing phenomena. These properties are attributed to modulation of band structure and quantum limitations of density of states while moving from bulk to thin and single layers.

Graphene

Graphene is the most famous 2D material and it is well known for its novel optical, electronical and mechanical properties. In 2004 Novoselov and Geim demonstrated novel technique of single layer exfoliation of graphene revealing its interesting physical properties. These properties are the reasons of linear energy dispersion of single layer graphene at K-point. Those properties directed researches to new field of Fermi-Dirac physics. Figure 1.1-1 shows a single layer graphene and it allotropes in Carbon Nano Tubes (CNTs) and C_{60} carbon balls [1] [2]

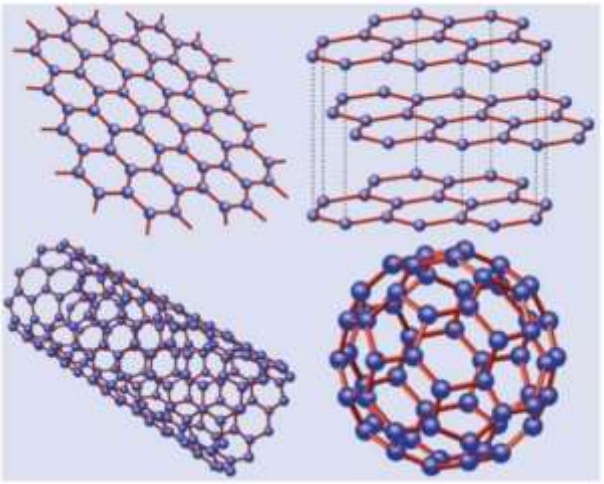

Figure 1.1-1- Various allotropes of graphene formed in honeycomb lattice. Top left: single layer graphene, top right: how stacks of monolayers are formed; bottom left: carbon nano tube (CNT) which is considered as rolled monolayer graphehe; bottom right: C60, a monolayer graphene in spherical form [2]

Graphene unit cell and lattice vectors:

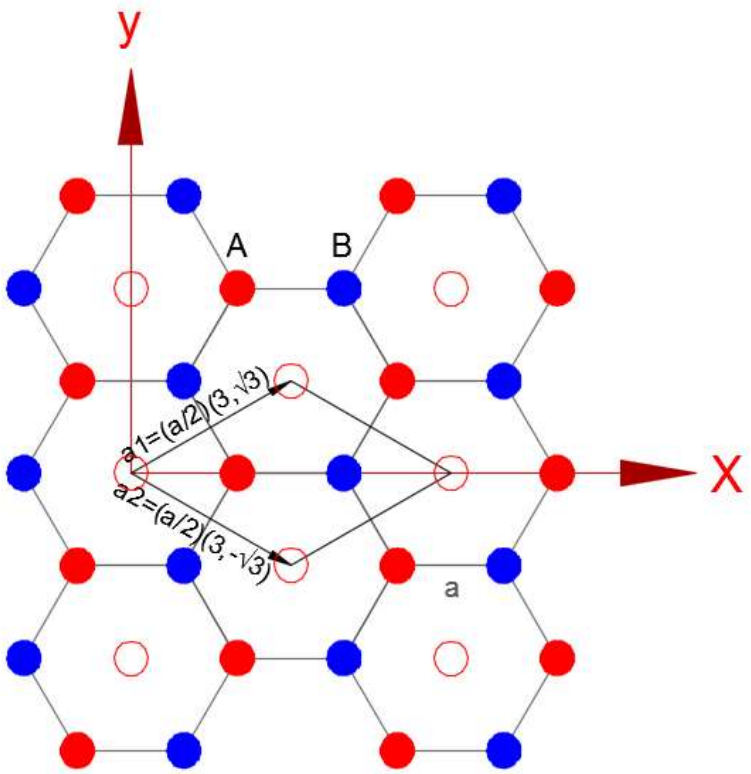

Figure 1.1-2- Wigner-Seitz unit cell and lattice vectors of graphene in real space. A and B show different sublattices in honeycomb structure of graphene

In order to understand the physics of solids we need to understand the atomic structure and the unit cell which presents the repeating structure of solids. The unit cell simplifies the structure. Wigner-Seitz cell is the locus of points in the crystal that are the closet to the lattice points. These points represent the lattice vectors as shown in Fig. 1.1-2 for graphene structure:

$$\vec{a}_1 = \frac{a}{2}\left(3, \sqrt{3}\right)$$

$$\vec{a}_2 = \frac{a}{2}\left(3, -\sqrt{3}\right)$$

Once we have the lattice vectors in Wigner-Seitz unit cell in real space, we can produce the reciprocal lattice (RL) which presents the momentum space. The primitive cell for momentum

space is called Brillouin Zone (BZ) which is a Wigner-Seitz cell of reciprocal lattice. According to the quantum mechanics and the free electron model, for periodic lattice, the potential is also periodic. According to Bloch's theorem, the wave function solution of Shrodinger's Equation (SE), when the potential is periodic is, for two dimensional lattice:

$$\psi(x,y) = e^{i\vec{k}.\vec{r}}u(x,y)$$

Where $\psi(x,y)$ is the steady state solution of Shrodinger's Equation which could be written as:

$$-\frac{\hbar^2}{2m}\frac{d^2\psi}{dx^2} + V\psi = E\psi$$

This equation is called time independent Schrodinger's equation (TISE). In these relations, $\vec{r}$ is lattice vector, $\vec{k}$ is wave or momentum vector, $\hbar$ is Dirac constant, m is the mass, V is potential and E is constant.

In order the wave equation to be periodic, the $e^{i\vec{k}.\vec{r}}$ part of the Bloch's theorem should be periodic then we simply have:

$$e^{i\vec{k}.\vec{r}} = 1 \rightarrow \vec{k}.\vec{r} = 2\pi$$

Now we will use this relation to produce the momentum space or BZ in graphene. In three dimensional space, we can write reciprocal vectors as following:

$$\vec{b}_1 = 2\pi\frac{\vec{a}_2 \times \vec{a}_3}{\vec{a}_1 \cdot \vec{a}_2 \times \vec{a}_3}$$

$$\vec{b}_2 = 2\pi\frac{\vec{a}_3 \times \vec{a}_1}{\vec{a}_2 \cdot \vec{a}_3 \times \vec{a}_1}$$

$$\vec{b}_3 = 2\pi\frac{\vec{a}_1 \times \vec{a}_2}{\vec{a}_3 \cdot \vec{a}_1 \times \vec{a}_2}$$

Then for graphene which is in two dimensional space, we will have:

$$\vec{b}_1 = \frac{2\pi}{3a}\left(1, \sqrt{3}\right)$$

$$\vec{b}_2 = \frac{2\pi}{3a}(1, -\sqrt{3})$$

As shown below, these two vectors represent the first BZ in the momentum space:

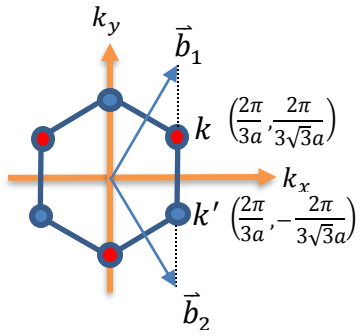

Figure 1.1-3- Wigner-Seitz unit cell of Reciprocal Lattice of graphene which is the first Brillouin Zone

Which provides two different energy dispersions corresponding to two different sublattices A and B, shown in Fig. 1.2-1. In order to compute energy dispersion in graphene, we first focus on tight binding model.

In tight binding (TB) model, a solid is assumed to have periodic potential. Any electron is bounded to the neighbor electrons. Then the wave function of any electron is simplified to be considered of being affected by neighboring electrons. We write SE for steady state situation

$$E\psi = H\psi$$

$$E\psi_n = t\psi_{n-1} + \varepsilon\psi_n + t\psi_{n+1}$$

Since Hamiltonian matrix H, is Hermitian, then all its diagonal elements are ε and elements on top of diagonal and under should be t. These will lead us the wave equation as following:

$$\psi_n = \psi_0 e^{i\vec{k}.\vec{r}_n}$$

$$E\psi_n = \sum_m H_{nm}\psi_m$$

Then, we will have the relation for periodic energy state E – the energy dispersion relation:

$$E(\vec{k}) = \sum_m H_{nm} e^{i\vec{k}.(\vec{r}_m - \vec{r}_n)}$$

$$E(k_x + k_y) = \varepsilon + 2tcos(k_x a) + 2tcos(k_y a)$$

Fig. 1.1-4 shows the lattice vectors of graphene in real space. The Hamiltonian for the center lattice pair which is the *nth* element in the lattice – without considering the TB model, will be:

$$h = \begin{bmatrix} \varepsilon & t \\ t & \varepsilon \end{bmatrix}$$

With considering the TB model to the neighboring sublattices, we will have:

$$h(\vec{k}) = \begin{bmatrix} \varepsilon & h_0^* \\ h_0 & \varepsilon \end{bmatrix}$$

$$h_0 = t\left(1 + e^{i\vec{k}.\vec{a}_1} + e^{i\vec{k}.\vec{a}_2}\right)$$

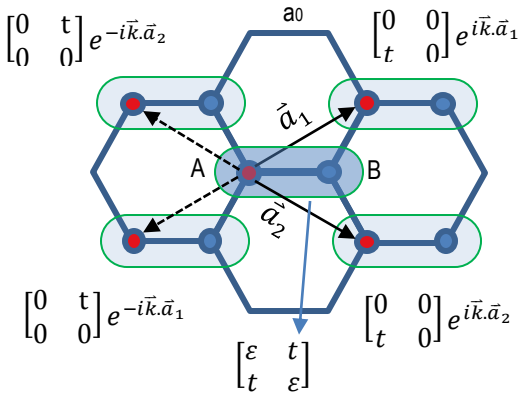

Figure 1.1-4- The lattice vectors of graphene in real space in a tight binding model

The dispersion relation will the eigenvalues of Hamiltonian which will be:

$$eigenvalues = \varepsilon \pm |h_0|$$

Now we would like to calculate $|h_0|$ in order to derive dispersion relation for graphene. Before that, lets simplify lattice vectors as following:

$$\vec{a}_1 = \frac{3a_0}{2}\hat{x} + \frac{\sqrt{3}}{2}a_0\hat{y} \equiv a\hat{x} + b\hat{y}$$

$$\vec{a}_2 = \frac{3a_0}{2}\hat{x} - \frac{\sqrt{3}}{2}a_0\hat{y} \equiv a\hat{x} - b\hat{y}$$

$$h_0 = t\left(1 + e^{i\vec{k}.\vec{a}_1} + e^{i\vec{k}.\vec{a}_2}\right) = t\left(1 + e^{ik_x a + ik_y b} + e^{ik_x a - ik_y b}\right) = t(1 + 2e^{ik_x a}\cos(k_y b))$$

$$|h_0|^2 = h_0 h_0^*$$

$$\frac{|h_0|^2}{t^2} = 1 + 4\cos(k_x a)\cos(k_y b) + 4cos^2(k_y b)$$

$$E = \varepsilon \pm t\sqrt{1 + 4\cos(k_x a)\cos(k_y b) + 4cos^2(k_y b)}$$

Considering the Taylor's expansion for cosine function for small x values:

$$cos^2 x \simeq 1 - x^2$$

$$cosx \simeq 1 - x^2/2$$

and after doing algebra and simplifications:

$$E = \varepsilon \pm t\sqrt{k_x^2 + k_y^2} = \varepsilon \pm t|k| = \varepsilon \pm \hbar v|k|$$

This gives a cone shape dispersion relation with a famous Dirac point in the origin:

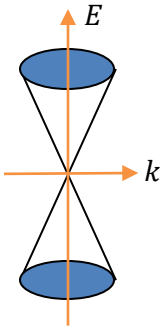

Figure 1.1-5- The energy dispersion relation of graphene showing the Dirac point in the origin.

Doping effects

Graphene doping – which is the substitution of some of carbon atoms with another atom is used to control and engineer the physical properties of pristine graphene. This technique and related transport measurements will be discussed in part C of this dissertation. Depending on the type of doping – n or p, we can increase or decrease Fermi level. One famous method of n-doping is replacing some of carbon atoms with nitrogen atoms that introduce 1 excess electron per replaced nitrogen atom because of the atomic number discrepancy between carbon and nitrogen. Instead, in order to p-dope graphene lattice, we can – for example use boron atoms replacing some of carbon atoms. This will cause lack of one electron per boron atom replaced with carbon atoms. Since n-doping introduce more electrons to the lattice, it shifts Fermi level while p-doping plays opposite role.

1.2 Transition Metal Dichalcogenides

1.2.1 Basics

Transition Metal Dichalcogenides (TMDs) are one category of 2D materials with chemical formula MX_2 where M is a transition metal and X is a chalcogen atom. These materials demonstrate unique optical and electronical properties [3, 4]. In single layers of these materials, a hexagonally-ordered M atoms are sandwiched between two another hexagonally-ordered X atmos. Figure 1.2-1 and 1.2-2 show atomic arrangement of these materials in 2H and 1T phases [5]. About 40 compounds of these materials are assumed to be layered materials [6]. Different stacking orders of monolayers causes different bulk types [7]; while monolayers could exist in metallic, semiconductor or semi metallic phases.

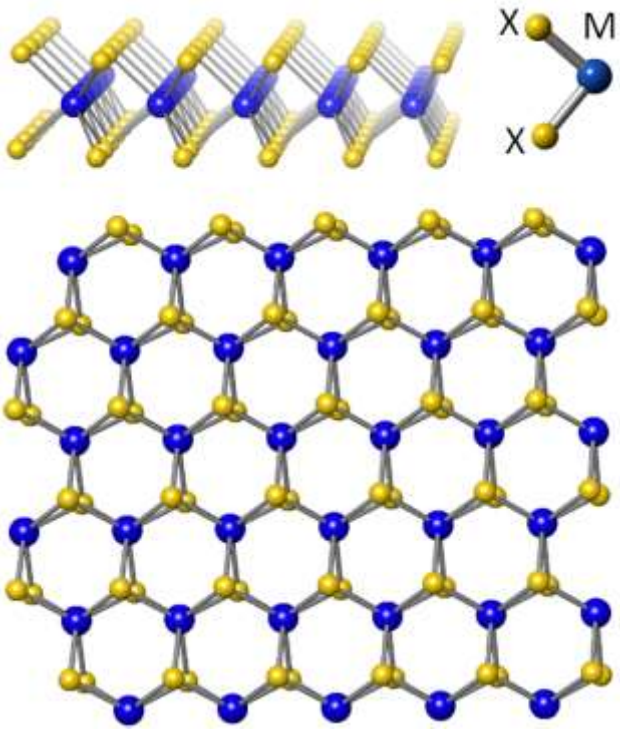

Figure 1.2-1- Transition metal dichalcogenides (TMDs) in the form of MX2 semiconductor (2H) phase. Upper right: single molecule; upper left: side view of chain of molecules; bottom: outline view in which metallic plane sandwiched between two chalcogen planes.

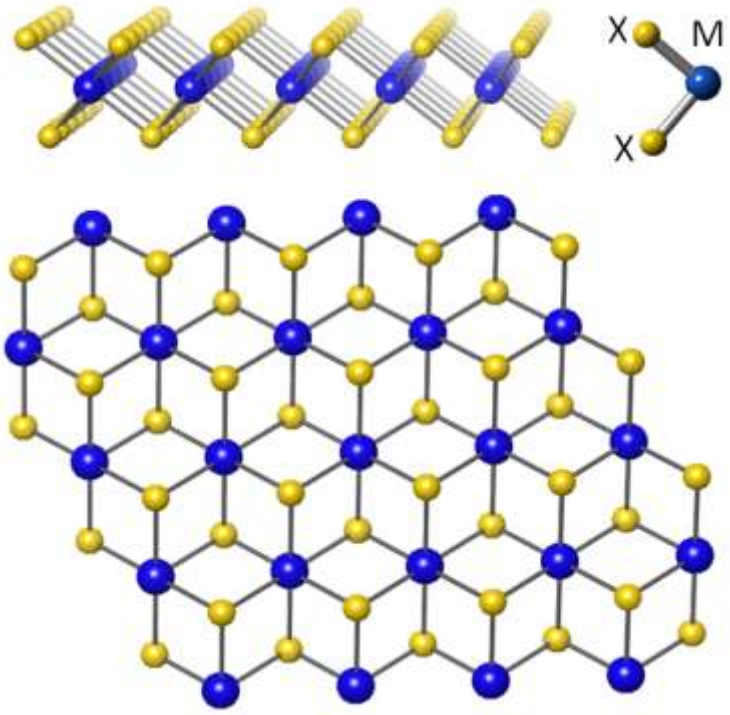

Figure 1.2-2 - Transition metal dichalcogenides (TMDs) in the form of MX2 in 1T phase. Upper right: single molecule; upper left: side view of chain of molecules; bottom: outline view in which metallic plane sandwiched between two chalcogen planes. This phase could be assumed as X-planes glided with respect to M-plane and each other.

MoS_2, $MoSe_2$, WS_2, WSe_2 are the most common TMDs. $MoTe_2$, WTe_2 are another examples. All of these materials are semiconductor at 2H atomic arrangements and metallic at 1T outline [8]. Some TMDs such as $PtSe_2$ demonstrate metallic characteristics in 2H phase instead – and are semiconductor at 1T atomic arrangements [9] [10]. More information about phases is indicated in the next section.

One interesting aspect of monolayer TMDs is their direct bandgap because of different bandstructure comparing to bulk form. Figure 1.2-3 shows how an indirect bandgap changes to a direct bandgap with eliminating phonon effects. In monolayer TMDs, electrons and holes have the

same momentum in conduction and valence bands. These causes an electron directly emit a photon. In multilayer or bulk TMDs, the momentum of electrons and holes are different in conduction and valence bands, then an electron should pass through an intermediate state and transfer its momentum to the crystal lattice. This causes an indirect photon radiation which is called indirect bandgap.

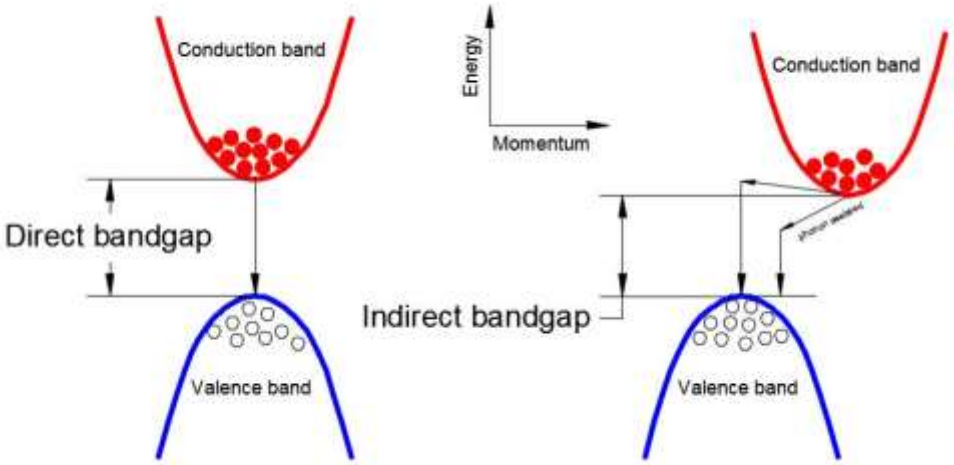

Figure 1.2-3- direct and indirect bandgap of semiconductor (2H) phase TMDs. Unlike to monolayer TMDs, in bulk or multilayer forms, the photon emission is phonon assisted.

1.2.2 Polymorphism

Unlike graphene in which the electronic properties is the cause of hybridization of 's' and 'p' orbitals, in TMDs, electronic structure depends on 'd' orbitals of metallic atoms because 'p' orbitals are located much lower than Fermi level. Single layer TMDs are found in three polytypes: 1H(2H), 1T and 1T' phases. The unit cell of 2H and 1H phases is trigonal prismatic which is D_{3h} point group - honeycomb motif. On the other hand, 1T phases have octahedral unit cell – D_{3d} point group – centered honeycomb motif. The international structural symbol, space group number and Schönflies symbols for 2H phases are $\bar{6}m2$, 187 and D_{3h}^{1} respectively. The same nomenclature for 1T phase is $R\bar{3}m$, 166 and D_{3d}^{5} respectively. Since 1T phase is not stable, the newly formed 1T phase distorts to 1T' phase which is a stable metallic phase [11]. Figure 1.5 and 1.6 illustrate these definitions. In general, group 6 transition metals Cr, Mo, W, demonstrate semiconducting behavior (1H phase) because of their half-filled 'd' orbitals. Their bandgap increases with the atomic number of correlated chalcogens. For instance, the bandgap of monolayer WSe2 (1.65 eV) is smaller than the bandgap of monolayer WS2 (2.05 eV) since the atomic number of sulfur (16) is much smaller than the atomic number of selenium (34) [1].

[1] These bandgaps are measured on polymer stack – not on SiO2 substrates. Detail will be discussed in the Results section.

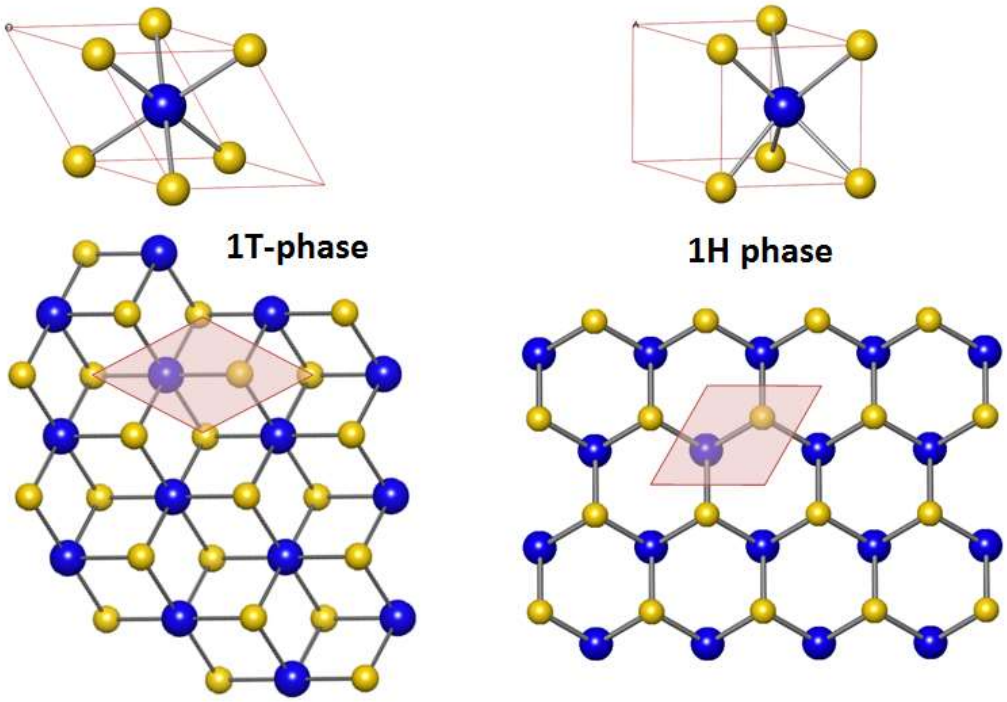

Figure 1.2-4- Two main polytypes of single layer TMDs. Right: 1H phase with trigonal prism in which the top and bottom chalcogen atoms are aligned and form an equilateral triangle. Left: 1T phase which is trigonal antiprism – top and bottom triangularly-formed chalcogen are now rotated by 60°. This phase is not stable and eventually distorts to 1T' phase. Diamonds on the bottom images show the primitive cells for each phase.

In 1H phase, 'd' orbitals split into 3 degenerate states: d_{z2}, $d_{x2-y2,xy}$ and $d_{xy,yz}$,while in 1T phase, 'd' orbitals split into 2 different degenerate states: $d_{xy,yz,zx}$ and $d_{x2-y2,xy}$. Theoretically, these phases are reversibly alterable to each other by structural deformation [5]. They eventually deform to a distorted version 1T' phase which is an intrinsic band inversion between 'p' orbitals of chalcogen atoms and 'd' orbitals of metal atoms. While these structural deformation occur, there are possible boundary structures revealing that the crystal structures on the edges and boundaries are complex [12]. For any different glide in metallic or chalcogen planes we might have different phase transitions as table 1.2.1 shows this.

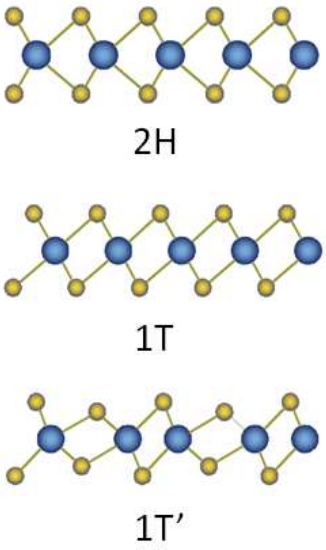

Figure 1.2-5- Three main polytypes of single layer TMDs. 2H or 1H phase is semiconductor phase, while 1T and 1T' are metallic phases. 1T phase is not stable then upon formation, changes to 1T' phase which is a stable and distorted version of 1T phase. Blue spheres represent metal atoms and yellow spheres represent chalcogen atoms.

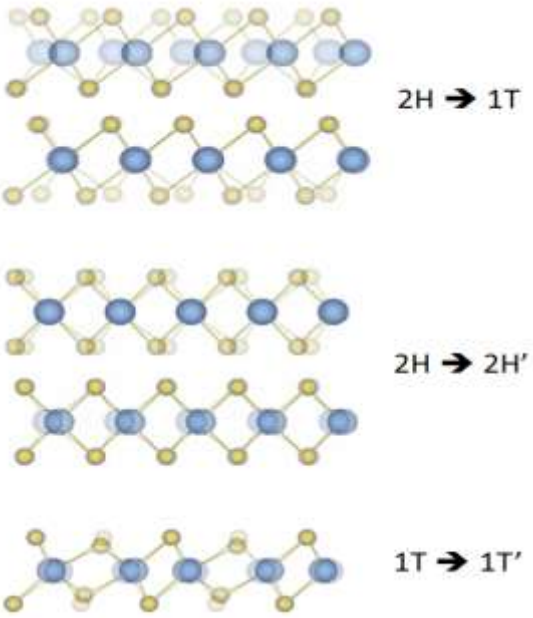

Figure 1.2-6- Three different possible glides of atomic planes that might generate various polytypes

Phase Transition	Gliding Plane	Possible Boundary Structures
2H ➔ 1T	M + X (or X') X (or X')	α+β+γ α+γ or γ
2H ➔ 2H'	M X + X'	α+β+γ γ
1T ➔ 2H	M + X (or X') X (or X')	α+β+γ α+γ
1T ➔ 1T'	M + X (or X')	α+β+γ

Table 1.2-1- possible boundary structures for various glides. Boundaries and edges undergo complex structural changes under any atomic glides. These complex atomic structures are known as α, β and ϒ [12]. This literally means that phase change is not a uniform process – edges do not undergo the same structural change as it is expected in the middle regions.

Following table shows space group symmetry and metal coordination of TMDs in 1T and 2H phases:

Phase	Space group symmetry	Metal coordination
1T, 1T'	P3m1	Octahedral
2H	P6m2	Trigonal prismatic
3R	R_3m	Trigonal prismatic

Table 1.2-2- space group symmetry of different phases on TMDs

1.2.3 Principal Structural Directions

2H phase TMDs have honeycomb lattice structure as illustrated in previous figures. Figure 1.8 shows two main lattice directions named zigzag and armchair. Later we will see that these principal directions are very important in characterizing the physical properties.

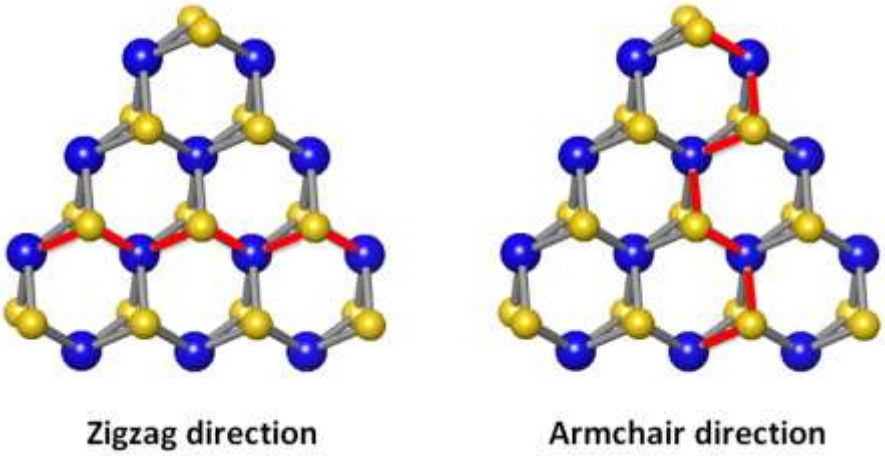

Figure 1.2-7-Two principal directions – zigzag and armchair are shown in perspective view of 2H phase TMDs

Determination of zigzag and armchair directions in graphene

In graphene, both G and 2D peaks undergo redshift by strain. G peak splits into two different peaks called as G^+ and G^-. These peaks are not only linearly polarized, but they have also orthogonal polarization [13]. Polarization dependence of scattering intensity is $I_s \propto |e_i \, Re_s \,|^2$ where e_i and e_s are the unit vectors of the polarizations of incident and emitted lights [14]. The intensity of the scattered Raman spectrum of G^+ and G^- modes will be as follows: [13]

$$\begin{cases} I_{G+} \propto d^2 cos^2(\emptyset + \varphi + 3\theta) \\ I_{G-} \propto d^2 sin^2(\emptyset + \varphi + 3\theta) \end{cases}$$

Where d is the amplitude of vibration in Raman tensors and θ is the angle between arbitrary (unknown) axis of strain and x-axis of zigzag direction as shown in the following figure[13] :

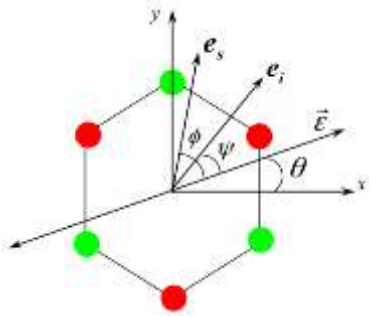

Fig 1.2.9 - Schematic diagram of unknown direction of applied strain with the unit vectors of incident and emitted lights for graphene

In order to realize the direction of crystal in the sample, there is a need to apply about 2% uniaxial strain in any arbitrary direction to make sure splitting in G peak occurs. The above set of equation reveal that I_{G+} is maximized when $(\emptyset + \varphi + 3\theta)$ is minimized. In Renishaw Raman setup, the incident light is always linearly polarized in x-axis when x is left-to-right direction while looking into the microscope. The polarization could be rotated by applying a half-wave plate in the path of incident light (a rotation of $\varphi/2$ will rotate the polarization by φ in which the scattered light intensity is proportional to $sin^2\varphi$). Meanwhile, the emitted light is always set to be in horizontal (x) direction in order to be able to acquire maximum possible intensity by the grating. As a conclusion, once we rotate the polarization of incident light, when its direction overlaps the strain direction $(\varphi = 0)$, then the intensity becomes maximum. On the other hand, the intensity of I_{G-} will be minimized because of the orthogonality of these split peaks.

Determination of zigzag and armchair directions in TMDs – CVD grown single layers

For CVD grown samples with triangular shapes, the direction of structures are shown in Figure 1.2.10. Nucleation happens in equilateral triangles by nature in which the size is controllable by process parameters. Proofs are indicated in the next sections.

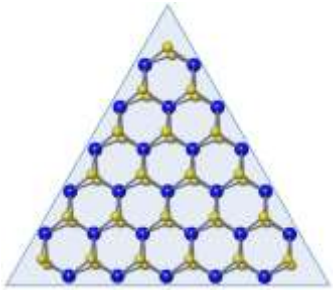

Fig 1.2.10. Atomic arrangement of molecular CVD grown triangular shape flakes. Orthogonal to one edge is armchair direction – while parallel is zigzag direction

Determination of zigzag and armchair directions in TMDs – straining method

In the cases that there are Raman peaks split into two orthogonal polarizations such as the G peak in graphene, the polarization dependent Raman spectroscopy could also be applied to realize the crystal orientation. For instance, E_{2g}^{1} peak in MoS_2 splits into two orthogonal peaks (E_{2g}^{1+} and E_{2g}^{1-}) under strain[15] [16]. Similar to graphene, when the intensity of E_{2g}^{1+} mode is maximized then the related angle of polarization on the substrate reveals the direction of the crystal (θ). Then the sample could be rotated to align the desired crystal direction in the direction of the strain.

Determination of zigzag and armchair directions in TMDs – SHG method

In addition, the direction of crystal in triangular CVD grown structures may be determined by second harmonic generation (SHG) analysis. These results were verified by atomic resolution scanning Transmission Electron Microscopy (TEM) [17]. SHG is a nonlinear optical process in which photons interact with a crystal and generate secondary photon with twice frequency.

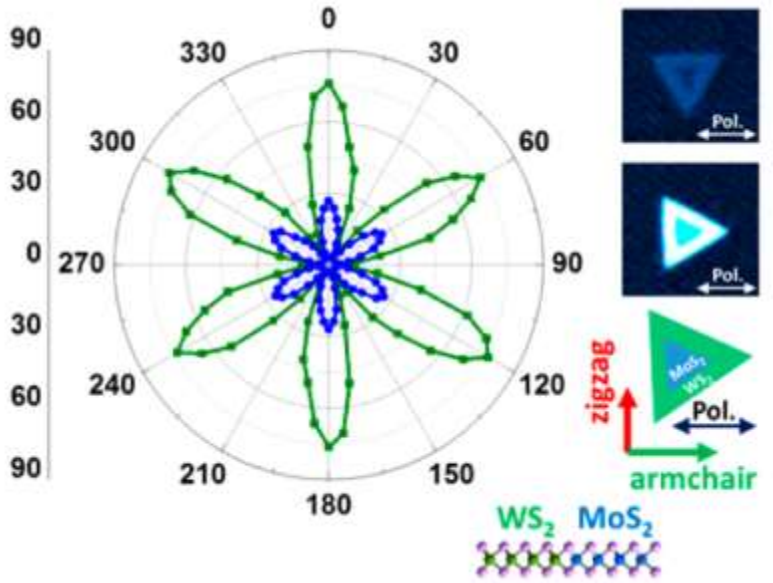

Fig 1.2.11- Second Harmonic Generation analysis used to identify crystal orientation. As the polar plot reveals, the intensity of second harmonic is maximized when the polarization direction of the incident laser is aligned with armchair direction [17]

Determination of zigzag and armchair directions in TMDs – TEM and STM assisted

As the structure of TMDs exhibit strong anisotropy response for Raman scattering, Raman intensity polar plot also could be compared with the real atomic resolution image out of TEM or STM to observe the effect of polarization direction on the intensity of each Raman mode. Then the acquired polar plot could be referred as the base of arbitration of the crystal orientation [18]

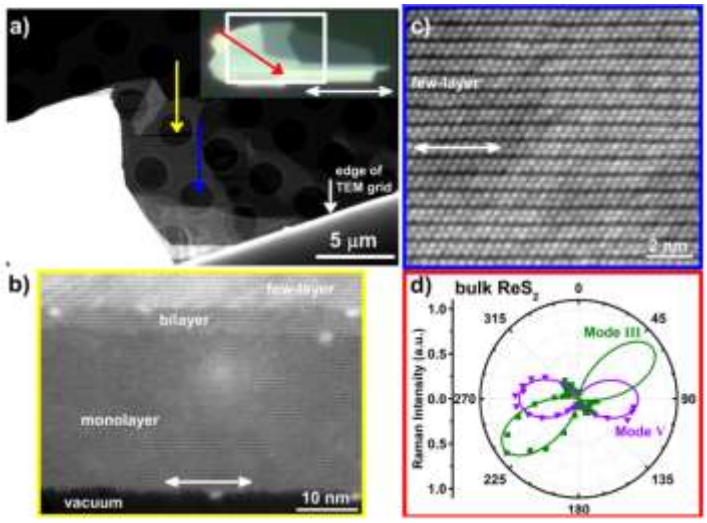

Fig 1.2.12- Anisotropic response of ReS2 together with TEM atomic resolution images used to generate polar plot and compare the intensity of the modes with the polarization angle of the incident laser light

1.2.4 Electronic Characteristics

The physical properties of TMDs are strongly dependent on the coordination of metal and chalcogen atoms and degeneracy of 'd' orbitals of metal atoms. This gives variety of possible electronic behaviors to TMDs. These properties are summarized in table 1.2.3 [19]

Group	**M**	**X**	**Properties**
4	Ti, Hf, Zr	S, Se, Te	Semiconductor: Eg=0.2-2.0 eV Diamagnetic
5	V, Na, Ta	S, Se, Te	Narrow band metals ($\rho \sim 10^{-4}\ \Omega cm$) or Semimetals. Superconducting. Charge density wave (CDW). Paramagnetic, antiferromagnetic, or diamagnetic
6	Mo, W	S, Se, Te	Sulfides and selenides are semiconducting (Eg~1.5-1.8 eV). Tellurides are semimetallic ($\rho \sim 10^{-3}\ \Omega cm$). Diamagnetic
7	Tc	S, Se, Te	Small gap semiconductors. Diamagnetic
10	Pd, Pt	S, Se, Te	Sulfides and selenides are semiconducting (Eg~0.4eV) and diamagnetic. Tellurides are metallic and paramagnetic. PdTe2 is superconducting. PtSe2 is semiconductor (Eg~1.2 eV)

Table 1.2-3- General physical properties of TMDs [19]

CHAPTER 2

Phonon Structure and Raman Spectroscopy

2.1 Introduction to the Physics of Raman

Raman spectroscopy is a light scattering technique to probe vibrational modes of materials which was discovered by *Sir C.V.Raman*. In 1928, he observed frequency-shifted lines in the spectrum of scattered laser light. He used laser light to shoot monochromatic photons to a sample and discovered the relative shift of primary photons corresponded to the vibrational and rotational frequencies of the scattering molecules. At the time, this process had been theoretically predicted by *Smekal* in 1925. *Raman* called it Raman effect and became the fundamental of Raman Spectroscopy.

The interaction of photons and the material (phonons) could be elastic or inelastic. Fig. 2.1-1 illustrates different scattering techniques when laser light interacts with a material. Elastic or Rayleigh scattering causes no shift in neither photons' frequencies nor wavelengths. Instead, inelastic scattering of monochromatic light involves with some frequency or wavelength shifts. The quality and quantity of these corresponding shifts represent the vibrational physics of molecules or atoms [14] [20].

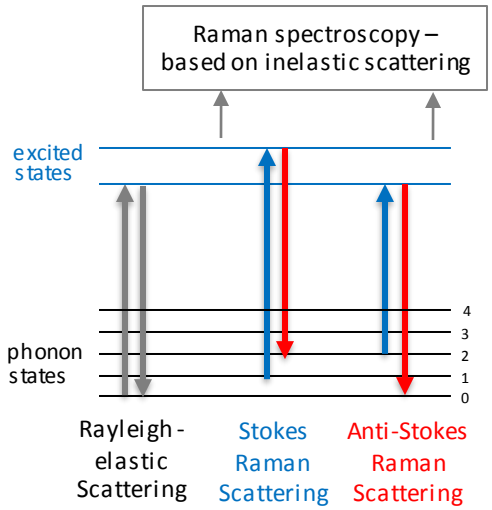

Figure 2.1-1- Different types of scattering. Basics of Raman Scattering is based on inelastic Stokes and Anti-Stokes scattering.

Stokes inelastic scattering happens when the energy of the scattered photons is decreased. On the other hand, anti-Stokes inelastic scattering happens when the energy of photons increases (redshifts). The amount of frequency shift is independent of the initial frequency of incident light and therefore, is a unique property of atom.

In order to observe Raman spectrum, we need high spectral resolution – less than 1 cm^{-1}. When light interacts with matter, an electric dipole moment[2] is generated which emits radiation. The induced diploe moment $\vec{P}$ which is a measure of the systems polarity, is the product of polarizability or Raman tensor $\tilde{R}$ and incident laser light's electric field $\vec{E}$:

$$\vec{P} = \tilde{R}\,\vec{E}$$

Raman or polarizability tensor, $\tilde{R}$ which is a second rank tensor, exhibits the effect of incident light's electric field on the generated dipole moments. I other words, it shows how easy a molecule can distort the electric field of the incident light. In general, we may write the following equation in the matrix format:

$$\begin{bmatrix} P_x \\ P_y \\ P_z \end{bmatrix} = \begin{bmatrix} R_{xx} & R_{xy} & R_{xz} \\ R_{yx} & R_{yy} & R_{yz} \\ R_{zx} & R_{zy} & R_{zz} \end{bmatrix} \begin{bmatrix} E_x \\ E_y \\ E_z \end{bmatrix}$$

Recall that electric field of incoming light has sinusoidal oscillation: $E = E_o \cos(2\pi v_0 t)$ where E_o is the amplitude and v_0 is the frequency of the incident light and t is time. This results dipole moment to be $P = RE_o \cos(2\pi v_0 t)$. As a conclusion, an oscillating monochromatic light E with coherent frequency v_0, generates an oscillating dipole moment P with the frequency that might be affected with the corresponding Raman or polarizability tensor $\tilde{R}$. Polarizability of a molecule

[2] Electric dipole moment $\vec{P} = q\vec{d}$, where q is coulomb charges with d as displacement vector, is the result of polarizability of polar molecules as a function of nuclear coordinates.

changes a function of distance r of vibrating atoms. Therefore, Raman tensor could be expanded by Taylor's expansion in powers of internuclear distance r:

$$R = R_o + \frac{\partial R}{\partial r} r + higher\ orders$$

where R_o is static polarizability and $\partial R/\partial r$ is the contribution of vibrational modulations. Since, molecular vibrations are time-dependent, assuming that the frequency of the molecule's vibration is v_m then, the vibrational coordinates could be written as:

$$r = r_o \cos(2\pi v_m t)$$

Concretely, the applied dipole moment could be expressed as:

$$P = R_o E_o \cos(2\pi v_0 t) + \frac{1}{2}\frac{\partial R}{\partial r} r_o E_o \{\cos[2\pi(v_0 - v_m)] + \cos[2\pi(v_0 + v_m)]\}$$

The first term $R_o E_o \cos(2\pi v_0 t)$ is Rayleigh or elastic scattering term that the frequency of light is reserved. Meanwhile, second term redshifts the frequency which is called Stokes Raman scattering. On the other hand, third term blueshifts (increases) the frequency of incoming light which is called Anti-Stokes Raman scattering.

Considering that the Raman tensor is symmetric, it could be diagonalized by transferring to a new coordinate system $\acute{x}\acute{y}\acute{z}$ such that:

$$R = \begin{bmatrix} R_{\acute{x}} & 0 & 0 \\ 0 & R_{\acute{y}} & 0 \\ 0 & 0 & R_{\acute{z}} \end{bmatrix}$$

The Raman Polarizability Ellipsoid is then defined as:

$$(R_{\acute{x}})\acute{x}^2 + \left(R_{\acute{y}}\right)\acute{y}^2 + (R_z)\acute{z}^2 = 1$$

$$\left(\frac{\acute{x}}{\frac{1}{\sqrt{R_{\acute{x}}}}}\right)^2+\left(\frac{\acute{y}}{\frac{1}{\sqrt{R_{\acute{y}}}}}\right)^2+\left(\frac{\acute{z}}{\frac{1}{\sqrt{R_{\acute{z}}}}}\right)^2=1$$

that crosses $\acute{x}$-axis at $1/\sqrt{R_{\acute{x}}}$, $\acute{y}$-axis at $1/\sqrt{R_{\acute{y}}}$ and $\acute{z}$-axis at $1/\sqrt{R_{\acute{z}}}$. When the shape of this Raman Ellipsoid changes after scattering the light, then there would be at least one vibrational mode in the related material which is Raman active – that is, changes the frequency of the incident light.

2.2 Polarized and Unpolarized Raman Spectroscopy

In normal Raman spectroscopy, the incident light is normally monochromatic linearly polarized light. The direction of polarization – that is the direction of incident light's electric field could be rotated by half-wave plate and in addition, its polarization could be altered to circularly polarized light by the means of a quarter-wave plate [21].

Here we focus to use half-wave plate to be able to rotate the direction of incoming linearly-polarized light since we won't use circularly-polarized light. If the plate's axis is located in the direction of light, then the outgoing light will remain at the same direction. However, if we rotate the half-wave plate by θ, then the direction of electric field will be rotated by 2θ.

Once the laser light – with the electric field in the controlled direction is shined into the sample, the scattered light could contain all polarization directions. The Raman Spectroscopy Setup, should contain an analyzer which acts as a polarizer and transmits photons to CCD detector as shown in the Fig. 2.2-1. This figure shows the Renishaw © Raman setup that we used for this dissertation.

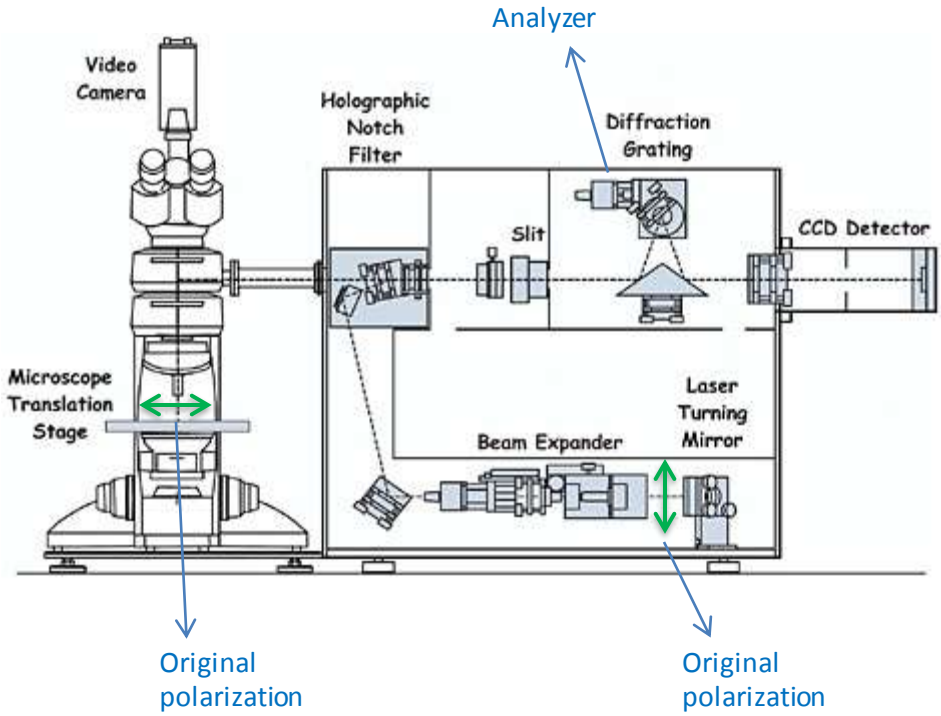

Figure 2.2-1- Renishaw Raman Microscope setup for unpolarized Raman Spectroscopy. The linearly-polarized light is always from left to right but the scattered light could comprise all directions.

As I will describe later in this chapter for 2D materials, we need to probe polarized Raman spectroscopy. For this purpose, after controlling the incident light's direction, we need to send the scattered light to the analyzer in parallel or orthogonal to the direction of incident light. As described, analyzer acts as a polarizer. Then it is sensitive to its transmission axis. Understanding this axis is crucial for polarized Raman spectroscopy. Once the axis is defined, we can investigate the scattered light in desired/polarized directions.

First of all, we have to add optical elements to our unpolarized Raman setup as shown in Fig. 2.2-2. We use half-wave plate to rotate the direction of incident light into the desired axis and a linear polarizer on a rotatable mount before analyzer to rotate the scattered light in a desired direction. The first goal is to realize the direction of analyzer so we would be able to send scattered light parallel or perpendicular to the axis of analyzer. For this purpose we need a material that does

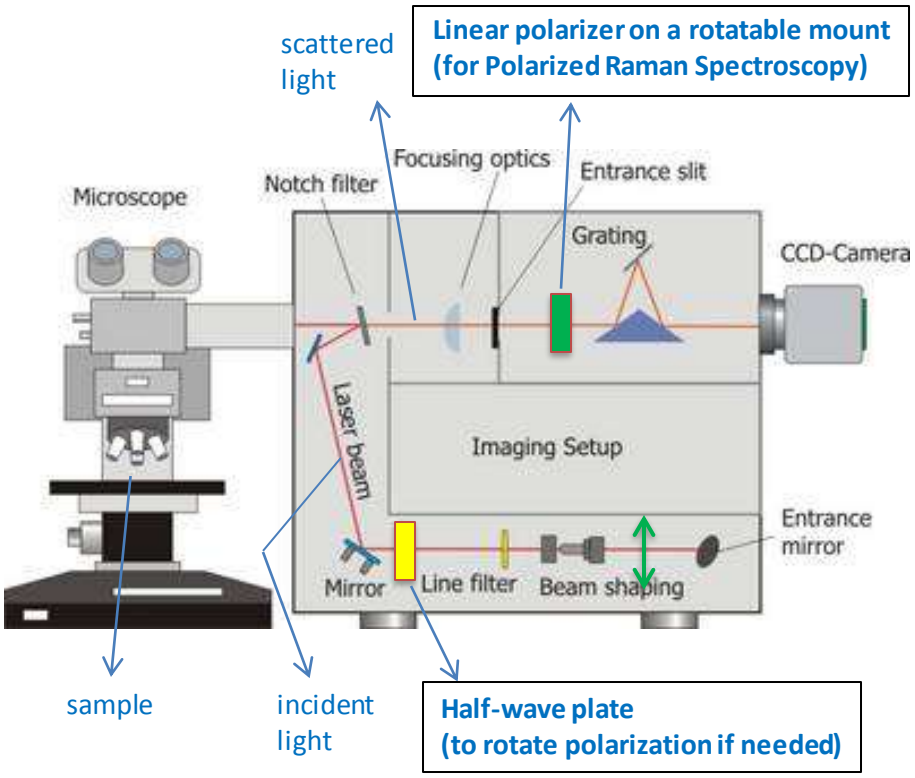

Figure 2.2-2- Renishaw Raman Microscope setup for unpolarized Raman Spectroscopy, modified for polarized Raman spectroscopy by adding two optical elements: half-wave plate and a linear polarizer on a rotatable mount.

not change the direction of scattered light. CCl_4 molecule is a famous material for this purpose which has a symmetric phonon mode at 460 cm^{-1} famous as $A1$ mode. Then the direction of polarization remains unchanged for this mode. See Fig. 2.2-3 for illustration of the molecule and modes. By inserting a rotatable linear polarizer before analyzer while keeping the incident polarization direction fixed, we could play with different polarization direction of scattered light to realize which direction is parallel to the incident light which is orthogonal. The intensity of $A1$ mode for parallel polarization is maximum while it is diminished almost to zero for cross-polarization. When incident light and probed scattered light are parallel it is called *parallel-polarized* spectroscopy. Meanwhile, when the probed scattered light is orthogonal to the incident light's direction it is called *cross-polarized* spectroscopy. We use *Porto's Notation* to show these terminologies. In the case of parallel-polarization we use $Z(XX)\bar{Z}$ or $Z(YY)\bar{Z}$. Z indicates the direction of the incident light and $\bar{Z}$ shows the direction of scattered light which in this case, is

along the Z direction. (XX) or (YY) reveals that the direction of polarization of incident and scattered light are parallel. Furthermore, in the case of cross-polarization we use $Z(XY)\bar{Z}$ or $Z(YX)\bar{Z}$ that indicates the direction of incoming light and scattered light are perpendicular.

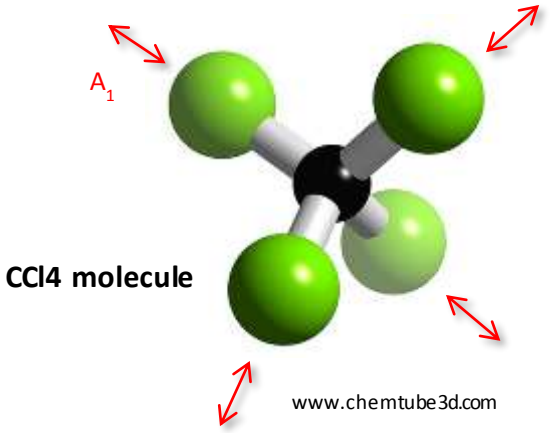

Figure 2.2-3- Symmetric molecule of CCl4 with symmetric vibration modes $A1$

By now, we know the direction of the analyzer. By rotating the direction of linear polarizer before analyzer, we can measure cross- and parallel-polarized Raman. The ratio between the perpendicular component and the parallel component is called *depolarization ratio* ρ:

$$\rho = \frac{I_c}{I_p}$$

Where I_c and I_p are the intensities of modes in cross- and parallel-polarization setup. For a symmetric vibrational mode, depolarization ratio is very small. For higher values of $\rho > 0.75$, the mode is called *highly depolarized band*. Meanwhile, for $\rho < 0.75$, the phonon mode is considered polarized and symmetric such as $A1$ mode in CCl_4. Higher the depolarization ratio is – the more asymmetric the vibration mode will be.

Fig 2.2-4 shows the unpolarized Raman spectrum of CCl4 with 532nm of excitation laser energy at different incident angles. As you notice, with unpolarized setup – even by rotation of incident light's polarization direction, we were not able to observe the depolarization effect.

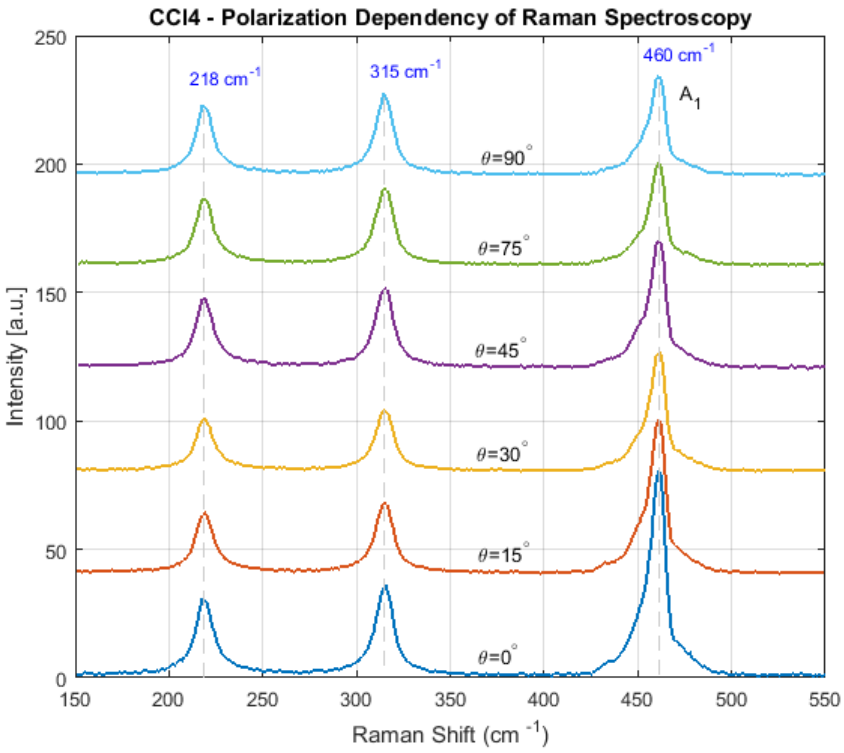

Figure 2.2-4- Unpolarized Raman spectroscopy of CCl4. With unpolarized Raman, it is not possible to observe the symmetric effect of $A1$ mode.

Then, we have to switch to polarized Raman spectroscopy to use the characteristics of $A1$ mode to determine the analyzer's direction. Fig 2.2-5 shows the polarized Raman scattering of this molecule. Dividing the intensities of modes in cross- and parallel-polarization setups, computes the depolarization ratio. The calculated ratio $\rho = 0.03$ shows a totally-polarized and symmetric phonon mode at 460 cm^{-1} as we expected. For measuring cross-polarized Raman scattering of a

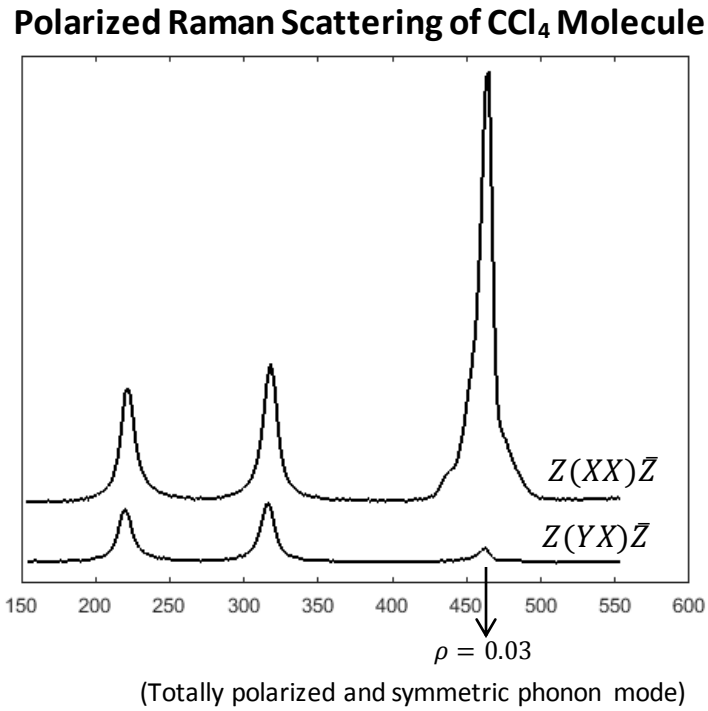

Figure 2.2-5- Symmetric molecule of CCl4 with symmetric vibration modes $A1$. With the help of polarized Raman spectroscopy, the angle corresponding to the lowest intensity recorded which is the angle of analyzer.

material, we change the setup to the cross-polarization or orthogonal state in which the incident light and probed scattered light are perpendicular to each other. This is opposite for parallel setup in which the incident and probed scattered lights are parallel.

Fig. 2.2-6 is schematic diagram of polarized Raman setup for measuring Raman spectrum of TMDs. More descriptive analysis is provided in Experimental Results section. The incident light

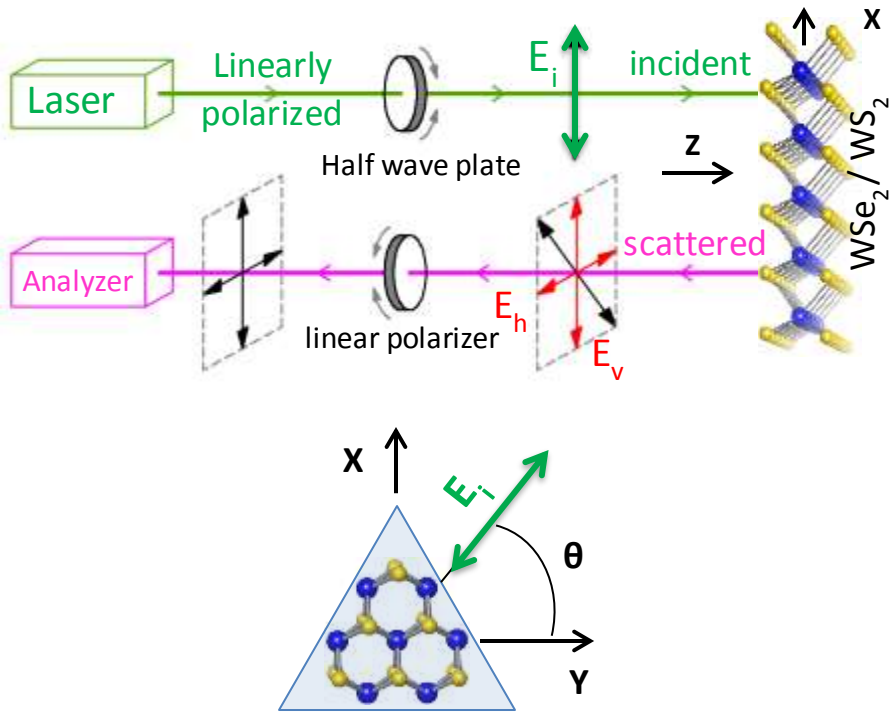

Figure 2.2-6- Schematic diagram of polarized Raman setup for measuring parallel- and cross- polarized Raman spectra of TMDs

could be rotated for a desired crystal direction. In this case, for any crystal direction – subject of experiment, we should change the linear polarizer's direction to match with the incident light's direction – perpendicular for cross-polarized Raman and vice versa.

2.3 Phonon Specifications

Raman active modes for odd number of layers (ONL) and even number of layers (ENL) of TMDS are as follow, which shows the phonon modes at Γ point.;

$$\Gamma_{ONL} = 0.5(3N-1)(A_1' + E'') + 0.5(3N+1)(A_2'' + E')$$

$$\Gamma_{ENL} = 1.5N(A_{1g} + E_g + A_{2u} + E_u)$$

Where N is number of layers. Therefore, for single layer TMDs:

$$\Gamma_{1L} = 2A_2'' + A_1' + 2E' + E''$$

in which only A_1', E' and E'' are Raman active modes. Meanwhile, A_2'' is acoustic and infrared active mode, and E' mode – other than Raman active, is also acoustic, and infrared active mode. Fig. 2.3-1 shows phonon modes of two layer (2L) and monolayer (1L) TMDs. For 2L TMDs, phonon modes at Γ will be:

$$\Gamma_{2L} = 3A_{1g} + 3A_{2u} + 3E_g + 3E_u$$

In general, for bulk TMDs:

$$\Gamma_{bulk} = A_{1g} + 2A_{2u} + 2B_{2g} + B_{1u} + E_{1g} + 2E_{1u} + 2E_{2g} + E_{2u}$$

In the bulk form, only A_{1g}, E_{1g} and E_{2g} are Raman active modes.

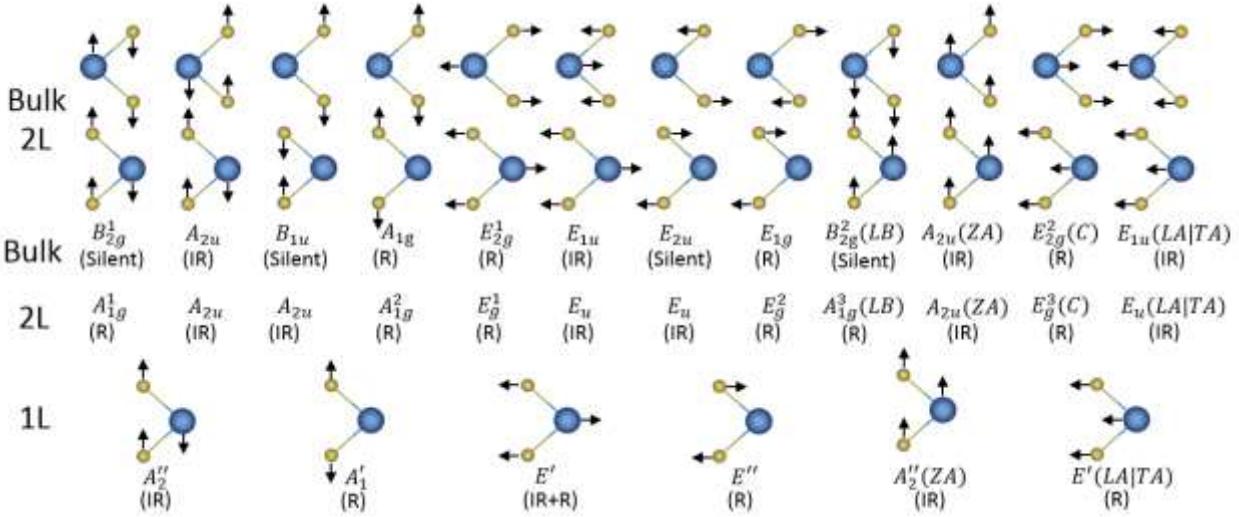

Figure 2.3-1- Phonon modes of bulk, 2L and 1L TMDs.

Fig. 2.3-2 [20] shows phonon dispersion graph of monolayer MoS2. Optical active modes could be out-of-plane mode (ZO), longitudinal optical mode (LO) or transverse optical modes (TO). There are also three acoustic mods in longitudinal, transverse and out-of-plane modes (LA, TA and ZA respectively).

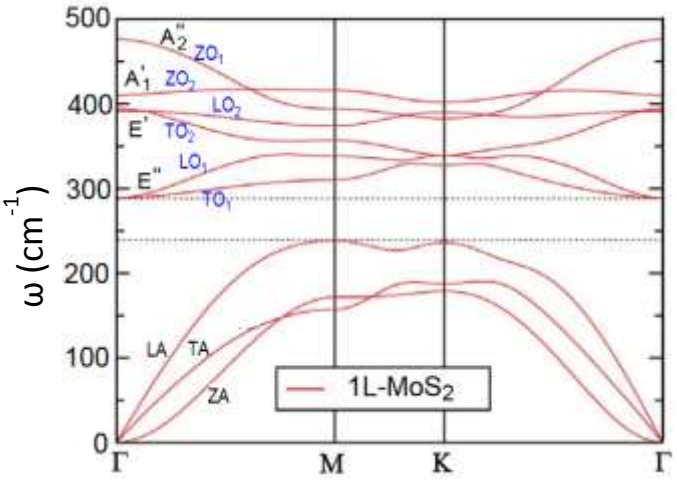

Figure 2.3-2- Phonon modes of monolayer MoS2 [20].

For different modes in samples we might have different Raman or polarizability tensors. For example, for bulk TMDs with orthorhombic crystal systems, the Raman active modes have the following Raman tensors [14] [20]:

$$A_{1g}: \begin{pmatrix} a & 0 & 0 \\ 0 & b & 0 \\ 0 & 0 & c \end{pmatrix}$$

$$E_{1g}: \begin{pmatrix} 0 & 0 & 0 \\ 0 & 0 & d \\ 0 & d & 0 \end{pmatrix}, \begin{pmatrix} 0 & 0 & -d \\ 0 & 0 & 0 \\ -d & 0 & 0 \end{pmatrix}$$

$$E_{2g}: \begin{pmatrix} 0 & e & 0 \\ e & 0 & 0 \\ 0 & 0 & 0 \end{pmatrix}, \begin{pmatrix} e & 0 & 0 \\ 0 & -e & 0 \\ 0 & 0 & 0 \end{pmatrix}$$

For even number of layers of TMDs – ENL, the Raman tensor for Raman active modes are:

$$A_{1g}: \begin{pmatrix} a & 0 & 0 \\ 0 & b & 0 \\ 0 & 0 & c \end{pmatrix},$$

$$E_g: \begin{pmatrix} c & 0 & 0 \\ 0 & -d & e \\ 0 & e & 0 \end{pmatrix}, \begin{pmatrix} 0 & -d & -e \\ -d & 0 & 0 \\ -e & 0 & 0 \end{pmatrix}$$

For odd number of layers of TMDs – ONL, the Raman tensor for Raman active modes are:

$$A_1': \begin{pmatrix} a & 0 & 0 \\ 0 & b & 0 \\ 0 & 0 & c \end{pmatrix},$$

$$E': \begin{pmatrix} 0 & d & 0 \\ d & 0 & 0 \\ 0 & 0 & 0 \end{pmatrix}, \begin{pmatrix} d & 0 & 0 \\ 0 & -d & 0 \\ 0 & 0 & 0 \end{pmatrix}$$

$$E'': \begin{pmatrix} 0 & 0 & 0 \\ 0 & 0 & e \\ 0 & e & 0 \end{pmatrix}, \begin{pmatrix} 0 & 0 & -e \\ 0 & 0 & 0 \\ -e & 0 & 0 \end{pmatrix}$$

The Raman tensor for monolayer TMDs is discussed in the next section.

2.4 Strength of Raman Signals

The magnitude of the Raman tensor $\tilde{R}$ represents the intensity or strength of Raman signal. Depending on the direction of scattered signal, we can calculate the corresponding signal via:

$$cross\ polarization: I \propto \left|\hat{e}_s^T . \tilde{R} . \hat{e}_i\right|^2$$

$$parallel\ polarization: I \propto \left|\hat{e}_i^T . \tilde{R} . \hat{e}_i\right|^2$$

where $\hat{e}_i$ is the unit vector in the direction of incident light's electric field, and $\hat{e}_s$ unit vector along the scattered light's direction - perpendicular to the incident light. Intensity of Raman signal along these directions could be probed by choosing parallel or cross polarization setups. Figure 2.4-1 shows these directions for two dimensional 2H-phase Transition Metal Dichalcogenides.

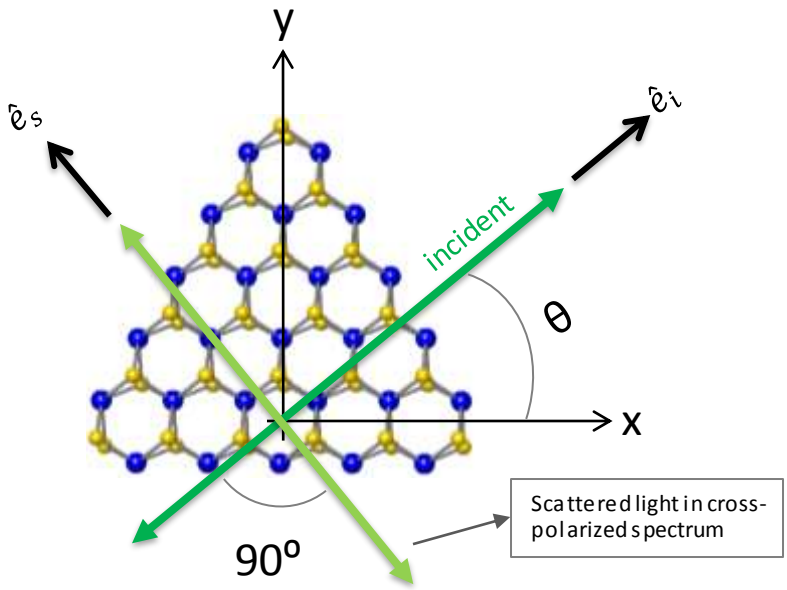

Figure 2.4-1 – Directions of incident and scattered light with respect to crystal's Cartesian coordinate systems. x- and y-directions represent zigzag and armchair directions respectively. The scattered light is set to the cross-polarization geometry with a unit vector perpendicular to the incident light's direction.

Corresponding unit vectors of incident and scattered lights could be represented as follows:

$$\hat{e}_i = (\cos\theta)\hat{x} + (sin\theta)\hat{y}$$

$$\hat{e}_s = -(sin\theta)\hat{x} + (cos\theta)\hat{y}$$

or in matrix format:

$$\hat{e}_i = \begin{bmatrix} cos\theta \\ sin\theta \\ 0 \end{bmatrix}$$

$$\hat{e}_s = \begin{bmatrix} -sin\theta \\ cos\theta \\ 0 \end{bmatrix}$$

Now, let's calculate the Raman signal for A' mode in cross spectroscopy setup. First we right the equation of intensity in cross-polarization setup:

$$I_{XY}^{A'} = \left| (-sin\theta \quad cos\theta \quad 0) \begin{pmatrix} a & 0 & 0 \\ 0 & b & 0 \\ 0 & 0 & c \end{pmatrix} \begin{pmatrix} cos\theta \\ sin\theta \\ 0 \end{pmatrix} \right|^2$$

$$I_{XY}^{A'} = \frac{1}{4}(b-a)^2 sin^2(2\theta)$$

This means that for orthorhombic crystal systems, if we shine the laser light in the direction of crystal lattice, that is $\theta = 0$ or $\theta = 90$, the intensity of cross-polarized Raman signal for A' mode will be zero. This interesting physics can be used to determine the crystallographic direction of single layer orthorhombic TMDs in cross-polarized setup. I will explain this in detail in Experimental Results section.

The intensity of A' mode in parallel-polarized setup could also be written as follows:

$$I_{XX}^{A'} = \left| (cos\theta \quad sin\theta \quad 0) \begin{pmatrix} a & 0 & 0 \\ 0 & b & 0 \\ 0 & 0 & c \end{pmatrix} \begin{pmatrix} cos\theta \\ sin\theta \\ 0 \end{pmatrix} \right|^2$$

$$I_{XX}^{A'} = (acos^2\theta + bsin^2\theta)^2$$

Which is always nonzero. Then we expect to observe A' mode in parallel polarization all the time. Furthermore, we would like to calculate the intensity of E' mode in both cross- and parallel-spectrums. Considering the Raman tensor for orthorhombic crystal systems, we can write:

$$I_{XY}^{E'} = \left| (-sin\theta \quad cos\theta \quad 0) \begin{pmatrix} 0 & d & 0 \\ d & 0 & 0 \\ 0 & 0 & c \end{pmatrix} \begin{pmatrix} cos\theta \\ sin\theta \\ 0 \end{pmatrix} \right|^2 + \left| (-sin\theta \quad cos\theta \quad 0) \begin{pmatrix} d & 0 & 0 \\ 0 & -d & 0 \\ 0 & 0 & c \end{pmatrix} \begin{pmatrix} cos\theta \\ sin\theta \\ 0 \end{pmatrix} \right|^2$$

$$I_{XY}^{E'} = d^2(1 - 2sin^2\theta)^2 + d^2sin^2(2\theta)$$

And, in parallel-polarized Raman spectrum for this mode, we should have:

$$I_{XX}^{E'} = \left| (cos\theta \quad sin\theta \quad 0) \begin{pmatrix} 0 & d & 0 \\ d & 0 & 0 \\ 0 & 0 & c \end{pmatrix} \begin{pmatrix} cos\theta \\ sin\theta \\ 0 \end{pmatrix} \right|^2 + \left| (cos\theta \quad sin\theta \quad 0) \begin{pmatrix} d & 0 & 0 \\ 0 & -d & 0 \\ 0 & 0 & c \end{pmatrix} \begin{pmatrix} cos\theta \\ sin\theta \\ 0 \end{pmatrix} \right|^2$$

$$I_{XX}^{E'} = d^2(1 - 2sin^2\theta)^2 + d^2sin^2(2\theta)$$

As a conclusion, the intensity of Raman spectrum for E' mode is the same for cross- and parallel-polarized Raman spectroscopy:

$$I_{XX}^{E'} = I_{XY}^{E'}$$

We will use this important physics in extracting Raman data for single layer TMDs.

Meanwhile, larger strains could change the lattice orientation to a triclinic system in which the corresponding Raman tensor is a non-diagonal and non-scalar matrix:

$$A_1': \begin{pmatrix} a & c & 0 \\ -c & b & 0 \\ 0 & 0 & d \end{pmatrix}$$

Then the Raman intensity of $\acute{A}$ mode is always nonzero independent of incident light's angle :

$$I_{XY}^{A'} = \left| (-sin\theta \quad cos\theta \quad 0) \begin{pmatrix} a & c & 0 \\ -c & b & 0 \\ 0 & 0 & d \end{pmatrix} \begin{pmatrix} cos\theta \\ sin\theta \\ 0 \end{pmatrix} \right|^2$$

$$I_{XY}^{A'} = |(b-a)cos\theta sin\theta + c|^2 \neq 0$$

Concretely, intensity of $\acute{A}$ mode at cross-polarization setup could be used to investigate the crystallographic orientation of TMDs at rest or zero strain. When the strain is applied it is not guaranteed that the mode's intensity remains zero because of transformation of Raman tensor. This is the reason that we observe $\acute{A}$ mode at highly-strained WS_2 samples only. Subsequently, for WSe_2, there might be possible contributions of $\acute{A}$ mode at higher strains but we could not observe because $\acute{A}$ and $\acute{E}$ modes are accidentally degenerate in this material.

CHAPTER 3

Bandstructure, Excitons and Photoluminescence Spectroscopy

Basics

Spin-valley Coupling

As indicated in the previous chapter, metal and chalcogen planes of TMDs make honeycomb lattice similar to graphene – leading to generate two valleys: K and K' in momentum space. These points are the touch points of conduction and valence bands in semimetal graphene while there is clear distance between these points in 2H phase TMDs. Ab initio study of the band structure of 2D MoS2 reveals a direct bandgap at K-point [22]. The broken symmetry of TMDs because of lack of inversion symmetry in parallel with spin-orbit coupling leads to interesting spin-valley physics which facilitates spin and valley control in these materials [23]. Fig. 3.1 shows first Brillouin zone which contains two valleys in momentum space [24].

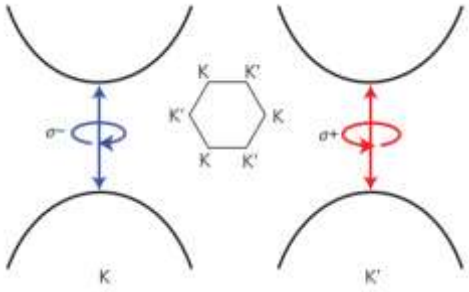

Fig 3.1- First Brilluoin zone and K, K' valleys which have orthogonal spins [24]

As indicated in chapter 1, the degeneracy level of 'd' orbital of the metal atom reveals the physical properties of TMDs. 'd' orbitals of the valence band (VB) of 2H phase monolayers, has strong spin orbit (SO) coupling. This together with the lack of symmetry causes strong spin-splitting at VB which is as strong as 148-456 meV for group VI TMDs [25]. Fig. 3.2 shows the selection rules for valley polarization.. Then any excitation frequency larger than ω_u but smaller than ω_d will excite the upper valence band. Lack of inversion symmetry causes non-zero Berry phases and curvatures in K and K' valleys. Any electron in these valleys possess orthogonal

magnetic field with different signs in K and K'. Then any circularly-polarized excitation laser, creates excitons in only one valley (K for instance); while the opposite polarization creates excitations on the adjacent valley (K' for instance).

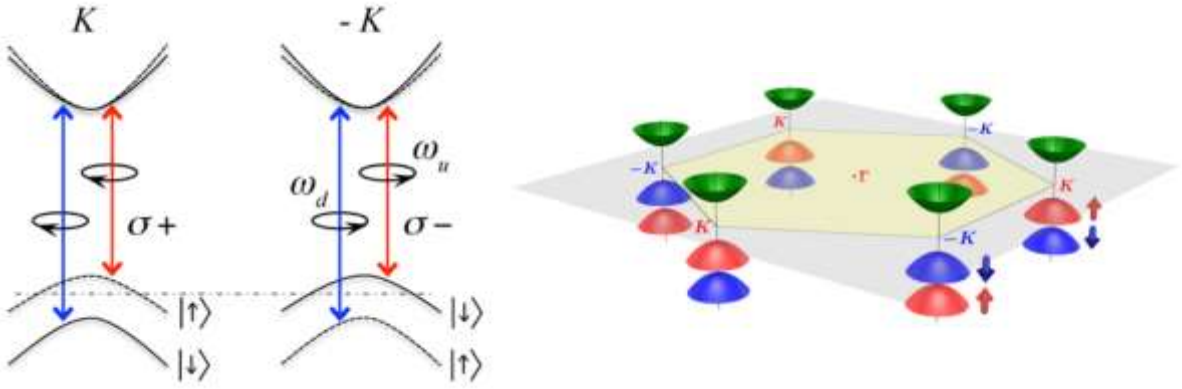

Fig 3.2- Spin-valley coupling and selection rules for group VI TMDs. There is giant spin splitting in valence band, while it is ignorable in conduction band [23]

Electronic Band Structure

As indicated in the previous chapter, one of the most significance of TMDs is their direct bandgap of monolayers at K-point. Fig. 3.3 shows the change of bandstructure of MoS2 moving from bulk to monolayer. As you can see, at one layer MoS2, conduction band and valence band get closed at K-point causing a direct optical transition at this point [26]

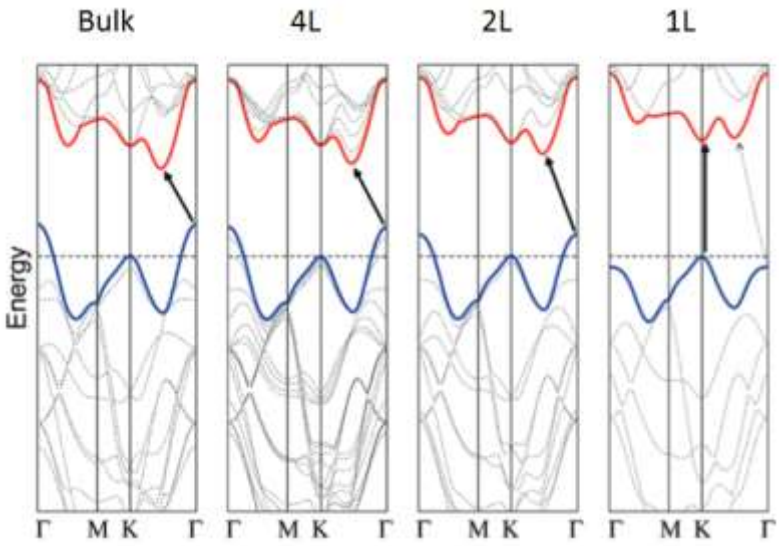

Fig. 3.3- Calculated bandstructure of MoS2 – difference from bulk to monolayer [26]

Electronic band structure of famous monolayer TMDs – MoS2, MoSe2, WS2 and WSe2 are shown in figure 3.4 Fully relativistic first-principle calculations based on density functional theory are used to calculate these energy bands [25]

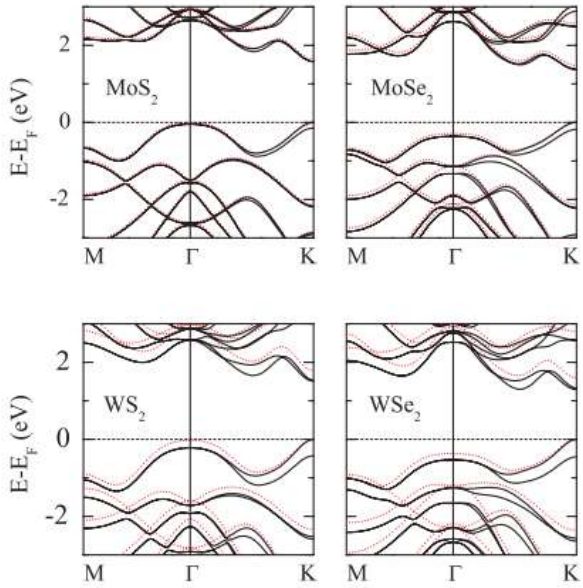

Fig 3.4- Electronic bandstructure of group VI TMDs calculated using first-principles based on density functional theory. Dotted lines show the inclusion of spin-orbit interaction and its effects on bandstructure. [25]

The main player of the electronic properties of TMDs is the degeneracy of 'd' orbitals of metal atoms. Fig. 3.5 shows the contribution of different orbital degeneracies to the bandstructure. This reveals that for monolayer TMDs which have direct bandgap at K-point, p_x, p_y, d_{xy} and d_{yz} are the main contributors for this bandgap. Instead, at thicker layers or bulk, p_z of valence band also takes action for the optical transition [27].

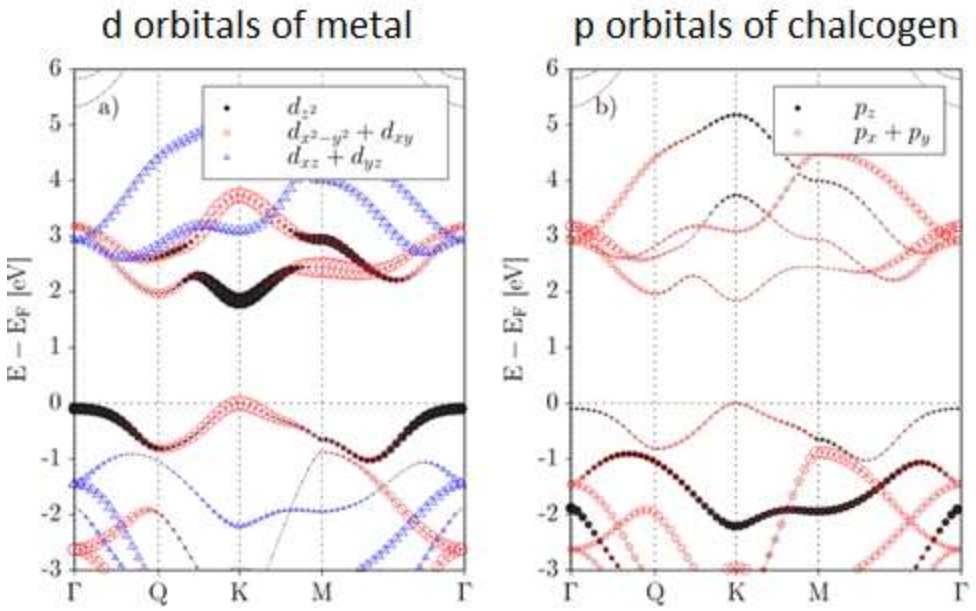

Fig. 3.5- contribution of d (p) orbitals of metal (chalcogen) atoms in the evolution of bandstructure [27]

Excitons

Any bound state between an electron and a hole is called an exciton. Electron-hole pair is a quasiparticle with a coulomb interaction which has neutral charge in total. Any photon with energy more than the bandgap of a semiconductor can move an electron from valence band to conduction. This process generates a hole in the valence band. The strength of the coulomb interaction of this electron-hole pair is called 'exciton binding energy' that could be as much as hundreds of meV.

PART B

STRAIN ENGINEERING

CHAPTER 4

Strain Engineering of Two Dimensional Materials

4.1 Introduction

2D materials are capable of undergoing large range strains up to their yield limits [28]. Reports reveal huge alteration of their mechanical, electrical, optoelectonical and magnetic properties under strain [29, 30]. It is also predicted and experimentally observed that tensile strain at room temperature may induce direct-to-indirect bandgap transition [8] [31] [32]. In addition, tensile strain enhances the mobility because of scattering of intrinsic phono modes; while compressive strain reduces mobility [33, 34]. Other effect of strain is reversible semiconductor-to-metal phase change in which those materials undertake structural phase transition from semiconductor to metal and vice versa [5, 31, 35, 36].

Dynamical control of optical and electrical properties by modifying atomic structure is technologically important for information storage and tailoring the physical properties of smart materials [37]. This empowers electrical and optoelectronical flexible nanodevices with potential stretchability [38]. Furthermore, large mechanical stretchability of odd-layer TMDs and absence of inversion symmetry in parallel to their high piezoelectric coefficients, made them novel materials for pirezoelectric devices [39].

The main effect of the strain on 2D materials is the modulation of electronic band structure and also affecting the phonon modes and lattice vibrations as well as magnetic properties. The detailed effect of strain on various 2D materials depends on how the applied strain changes anharmonicity of atomic potentials, effective masses and phonon frequencies. These phonon modes could be measured by Raman spectroscopy [13].

Hooke's Law for Isotropic, linear and elastic material

Considering an isotropic, linear and elastic material, Hooke's law in Compliance Format can be described in the following set of equations:

$$\varepsilon_x = \frac{1}{E}\left[\sigma_x - v(\sigma_y + \sigma_z)\right]$$

$$\varepsilon_y = \frac{1}{E}\left[\sigma_y - v(\sigma_x + \sigma_z)\right]$$

$$\varepsilon_z = \frac{1}{E}\left[\sigma_z - v(\sigma_y + \sigma_x)\right]$$

$$\gamma_{xy} = \frac{\tau_{xy}}{G}$$

$$\gamma_{yz} = \frac{\tau_{yz}}{G}$$

$$\gamma_{xz} = \frac{\tau_{xz}}{G}$$

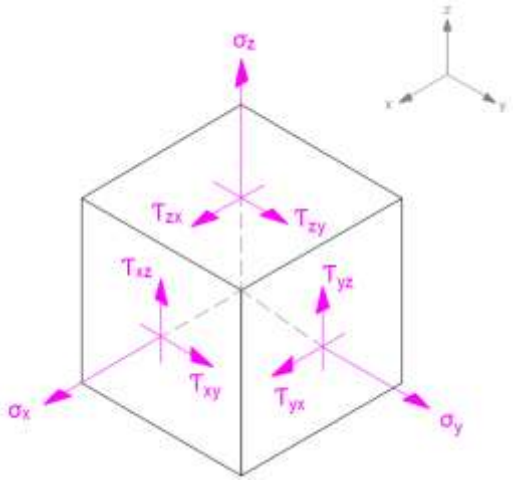

In Stiffness Format, the Hooke's law will be in the following form:

$$\sigma_x = \frac{E}{(1+v)(1-2v)}\left[(1-v)\varepsilon_x + v(\varepsilon_y + \varepsilon_z)\right]$$

$$\sigma_y = \frac{E}{(1+v)(1-2v)}\left[(1-v)\varepsilon_y + v(\varepsilon_z + \varepsilon_x)\right]$$

$$\sigma_z = \frac{E}{(1+v)(1-2v)}\left[(1-v)\varepsilon_z + v(\varepsilon_x + \varepsilon_y)\right]$$

$$\tau_{xy} = G\gamma_{xy}$$

$$\tau_{yz} = G\gamma_{yz}$$

$$\tau_{xz} = G\gamma_{xz}$$

For a uniaxial loading in which the strain and stress are applied in one direction – as shown in Figure 4.1, the Hooke's law simplifies to the following set of equations

$$\varepsilon = \frac{1}{E}[\sigma - 2v\sigma_L]$$

$$\varepsilon_L = \frac{1}{E}[(1-v)\sigma_L - v\sigma] \qquad \text{(L:Lateral)}$$

$$(\varepsilon_x = \varepsilon, \sigma_x = \sigma, \sigma_y = \sigma_z = \sigma_L, \tau_{xy} = \tau_{xz} = \tau_{yz} = 0)$$

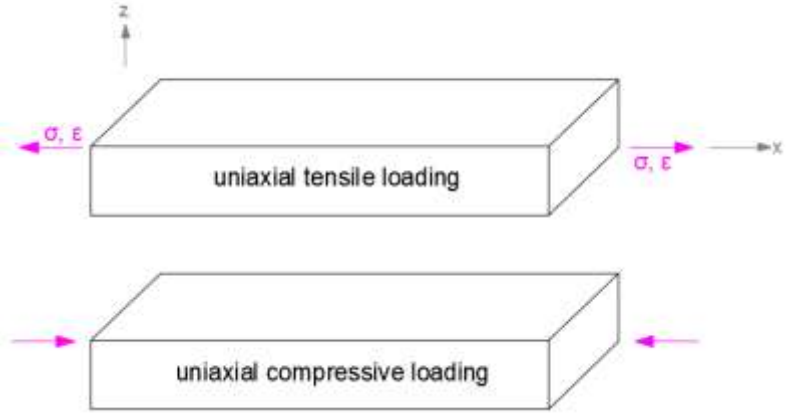

Figure 4.1- illustration of uniaxial tensile and compressive loading

4.2 1D or Uniaxial Stress (thin membranes)

For thin membranes where the thickness is much smaller than the other dimensions, the uniaxial loading simplifies as following set of equations. In the case of uniaxial stress, the out plane stress is zero ($\sigma_z = 0$), then for an isotropic material, constitutive relations or Hooke's laws will be reduced to:

$$\sigma_z = 0 \qquad \text{(Condition of plane stress)}$$

$$\sigma = E\varepsilon$$

$$\varepsilon_y = \varepsilon_z = -v\varepsilon$$

$$\sigma_y = -v\sigma$$

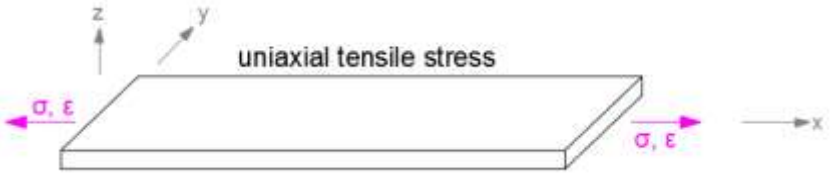

4.3 1D or Uniaxial Strain (thick parts)

If the thickness of the part – or the dimension orthogonal to the axis of loading is comparable to the dimensions in other directions, Hooke's law reduces to a very different form:

$$\varepsilon_z = 0 \qquad \text{(Condition of plane strain)}$$

$$\sigma = \frac{E(1-v)}{(1+v)(1-2v)}\varepsilon$$

$$\sigma_y = \sigma_z = \frac{-v}{1-v}\sigma$$

$$\varepsilon_y = 0$$

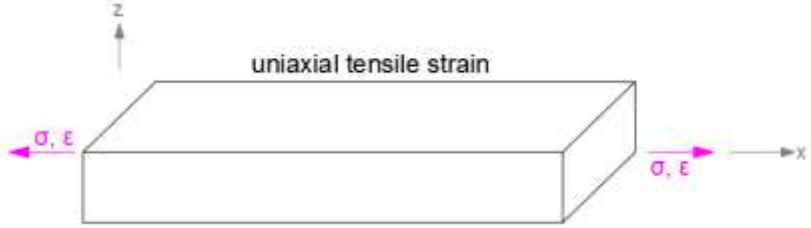

4.4 2D or Plane Stress (thin membranes)

2D stress is defined to be a state of stress in which the normal stress σ_z and the shear stresses τ_{xz} and τ_{yz} in the direction perpendicular to the x-y plane are assumed to be zero. This is the case of thin plates in which the stress is ignorable in the direction of the plate thickness.

For isotropic materials:

$$\sigma_z = \tau_{xz} = \tau_{yz} = 0 \quad \text{(normal and shear stresses)}$$

$$\gamma_{xz} = \gamma_{yz} = 0 \quad \text{(shear strains in normal directions)}$$

$$\sigma_x, \sigma_y, \varepsilon_x, \varepsilon_y, \varepsilon_z, \tau_{xy}, \gamma_{xy} \neq 0$$

The constitutive relations are:

$$\varepsilon_x = \frac{1}{E}(\sigma_x - v\sigma_x)$$

$$\varepsilon_y = \frac{1}{E}(\sigma_y - v\sigma_x)$$

$$\gamma_{xy} = \frac{1}{G}\tau_{xy} \qquad G = \frac{E}{2(1+v)}$$

$$\varepsilon_z = \frac{1}{E}(-v)(\sigma_x + \sigma_y)$$

or

$$\sigma_x = \frac{E}{1-v^2}(\varepsilon_x + v\varepsilon_y)$$

$$\sigma_y = \frac{E}{1-v^2}(\varepsilon_y + v\varepsilon_x)$$

$$\tau_{xy} = G\gamma_{xy}$$

where ν is Poisson's ratio and E is Young's modulus of elasticity and G is shear modulus.

Special case: biaxial plane stress

When the two in-plane stresses are equal in the case of plane stress, then biaxial plane stress occurs.

$$\sigma_x = \sigma_y = \sigma$$

$$\varepsilon_x = \varepsilon_y = \varepsilon$$

$$\sigma = \left(\frac{E}{1-v}\right)\varepsilon \qquad \left(\frac{E}{1-v}\right): biaxial\ modulus$$

In this case, if we apply a uniform strain in direction normal to the plate thickness ε_z, then the relation between in plane strain $\varepsilon_x = \varepsilon_y = \varepsilon$ and ε_z will be:

$$\varepsilon = \frac{1-v}{2v}\varepsilon_z$$

4.5 2D or Plane Strain (thick parts)

2D strain is defined to be states of strain in which the normal strain ϵ_z and the shear strains Υ_{xz} and Υ_{yz} in the direction perpendicular to the x-y plane are assumed to be zero. This is the case of thick plates where the dimension in z-direction is comparable to the other directions and loads are applied in x- and y-directions only.

For isotropic materials:

$$\varepsilon_z = \gamma_{xz} = \gamma_{yz} = 0 \quad \text{(normal and shear strains)}$$

$$\tau_{xz} = \tau_{yz} = 0 \quad \text{(shear stresses in normal directions)}$$

$$\sigma_x, \sigma_y, \varepsilon_x, \varepsilon_y, \sigma_z, \tau_{xy}, \gamma_{xy} \neq 0$$

The constitutive relations are:

$$\varepsilon_x = \frac{1}{E^*}(\sigma_x - v^* \sigma_y)$$

$$\varepsilon_y = \frac{1}{E^*}(\sigma_y - v^* \sigma_x)$$

$$\gamma_{xy} = \frac{1}{G}\tau_{xy} \qquad G = \frac{E}{2(1+v)}$$

or

$$\sigma_x = \frac{E^*}{1-v^{*2}}(\varepsilon_x + v^* \varepsilon_y)$$

$$\sigma_y = \frac{E^*}{1-v^{*2}}(\varepsilon_y + v^* \varepsilon_x)$$

$$\tau_{xy} = G\gamma_{xy}$$

Where

$$E^* = \frac{E}{1-v^2} \qquad \text{and} \qquad v^* = \frac{v}{1-v}$$

For large deformations but small strains, Green's stress-stress relations are applicable. Instead for large deformations together with large strains, Hencky or logarithmic stress-strain formulas could be applied.

4.6 Methods of applying uniaxial stress

The main purpose of uniaxial stress is to investigate the physical properties of materials in specific directions. Then it is crucial to develop an accurate platform to apply adjustable incremental strains on 2D materials. There are potentially 5 uniaxial methods, each having its pros and cons.

- Horizontal clamped stretching
- Cantilever bending
- AFM tip bending
- Extra-neutral axis bending – horizontal pushing method
- Extra-neutral axis bending – vertical pushing

Here I am going to introduce all. I will expand and explain in detail the last method – '*Extra-neutral axis bending – vertical pushing'* in which our platform is developed on.

Horizontal clamped stretching method

The following picture shows this method. Perhaps it is the simplest method that comes to mind when thinking of applying strain – just pulling:

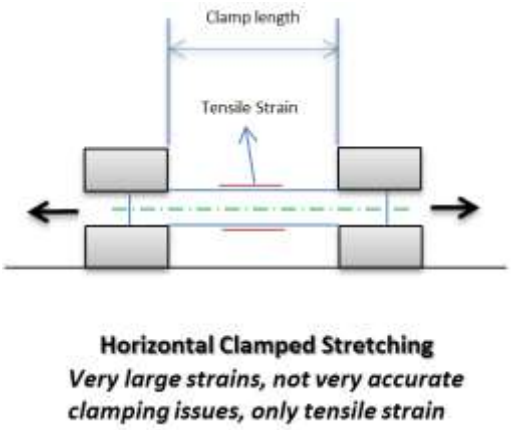

Figure 4.2-Illustration of horizontal clamped stretching method

In this setup, the thin membrane is fixed to clamps by means of some vertical loading screws. Strain could be applied as much as the material breaks. Accuracy depends on how accurate the motion is designed to move the jaws apart. One downside of this mechanism is the requirement of high clamping force that smashes the substrates on the clamp areas. Another downside is the clamp length is not

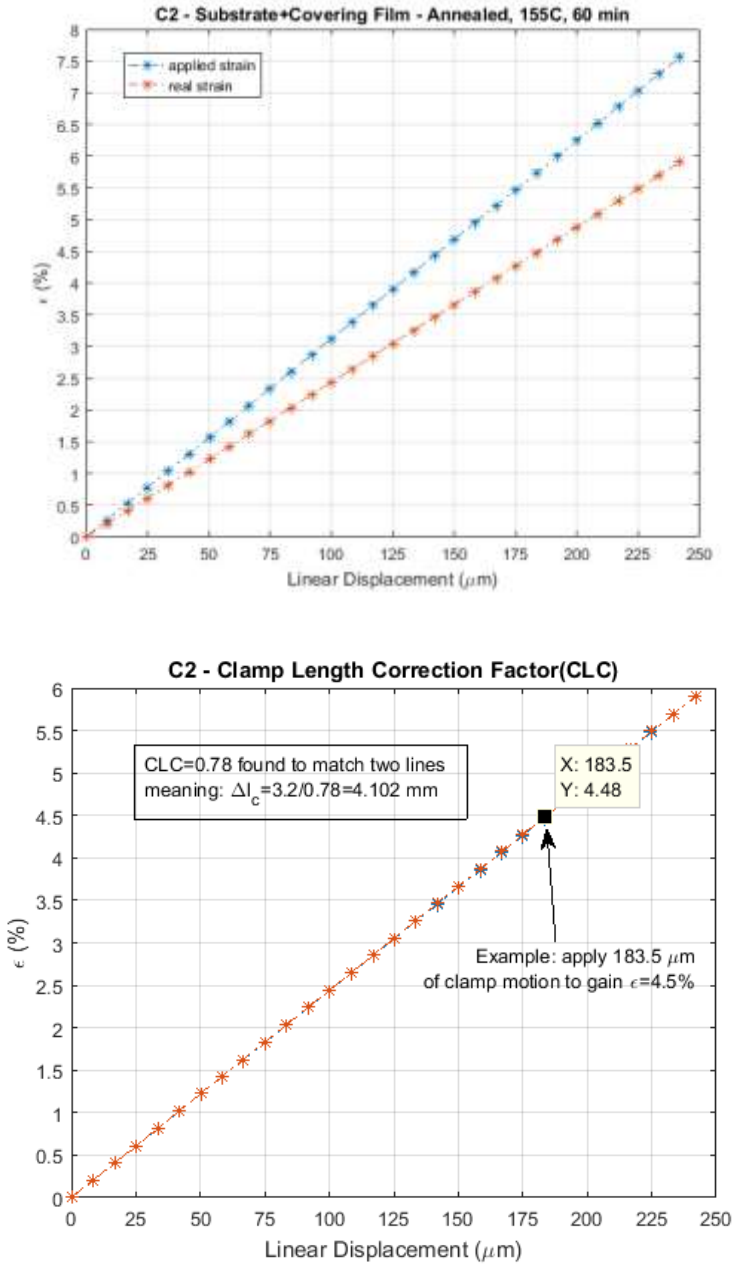

Figure 4.3-Clamp length correction (CLC) factor calculation in horizontal clamp stretching method

always exactly as it is measured before applying strain. Figure 4.3 shows the difference of applied strain and the real strain measured by optical microscope. As you notice on the top picture, there is a discrepancy between real strain and measured strain. The measured strain is $\Delta l_c / l_c$ where l_c is the clamp's primary length and Δl_c is the applied displacement. At each step, the real strain is also calculated. The difference reveals that the real l_c is different than we measured before applying strain. The bottom image on this figure is mathematical correction of the real strain in order to find a coefficient for difference. We call this, clamp length correction (CLC) factor which in this case is 0.78. This tells us that the real clamping length was 3.2/0.78=4.102mm instead of 3.2mm. Realizing CLC is important prior to any experiment.

Cantilever bending method

In this method, a thin plate is cantilevered in one end. Vertical displacement of another end causes stretching or tensile strain on top of this plate as depicted in Figure 4.4.

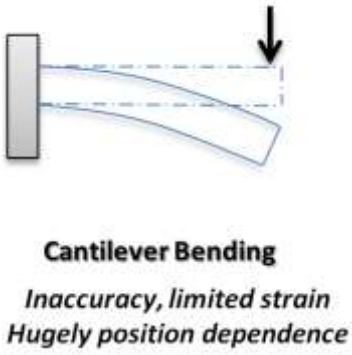

Figure 4.4-Illustration of cantilever bending method for applying strain

Since the bending moment is a function of the distance from the vertical load, then closed to the wall, the strain is highest and any slight change of location, changes the strain value drastically. This is the most prominent downside of this method. The amount of strain could be calculated in

two ways. One can consider the beam a circle to calculate the deformation of the beam at the top approximately. Instead, Euler-Bernoulli's method could be applied. I will develop this in full detail for '*Extra-neutral axis bending – vertical pushing'* method. Since this method has the fundamental problem of position-dependency, this accurate calculation is not explained here.

AFM tip bending

The tip of atomic force microscope (AFM) could be used to apply high amount of strain [13]. In this method, the sample is usually suspended over a cavity. AMF tip approaches the cavity to apply force and deflection under controlled condition. Figure 4.5 is schematic picture of this method.

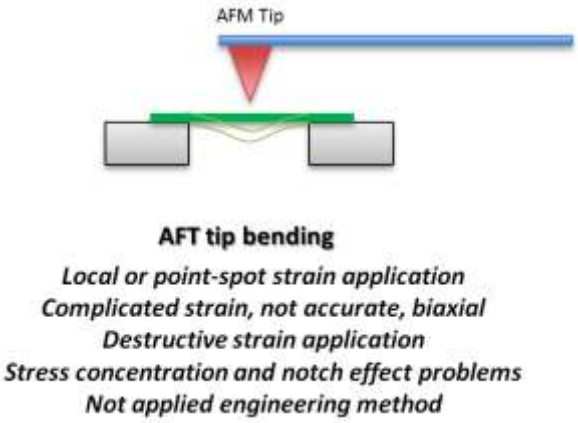

Figure 4.5-Illustration of AFM tip bending method for applying strain

The main advantage of this method is being able to apply strain locally on a desired spot. The spot should be suspended on a cavity as it is shown. For exfoliated samples, this method seems the most functional [36]. The reason will be discussed in chapter 5 – 'Strain device fabrication'. The method enables of applying large strains up to the yield limit. Because of the nature of cavity and suspension, strain is complicated on the edges closed to the cavities' sidewalls. The most accurate strain value is on the center only. The strain is biaxial. Another advantage of using tip is being capable of calculating amount of force at each strain values. This gives opportunities to investigate the mechanical properties of 2D materials [13].

Extra-neutral axis bending – horizontal pushing method

This is one of the most common methods of applying uniaxial strains. In this method, a thin plate is pushed from both sides towards the middle as shown in Figure 4.6. Deformation of the beam generates tensile strain on the top and compressive strain on the bottom.

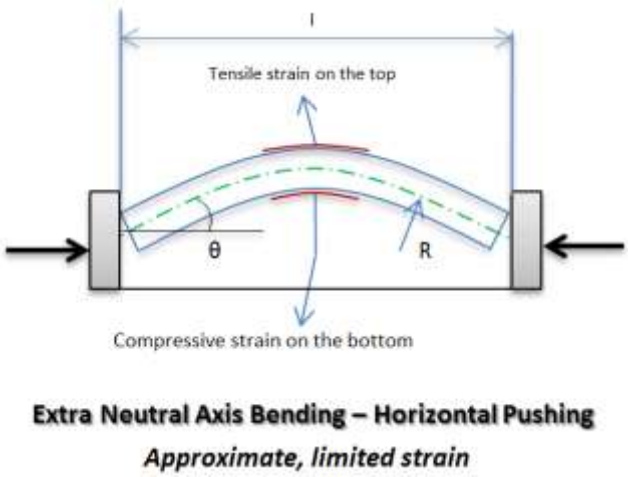

Figure 4.6-Illustration of extra neutral axis bending – horizontal pushing method for applying strain

For simplicity, it is assumed that the arc is circular and θ is very small. Then triangular symmetry, the governing equations will be written as following:

$$R = \frac{l/2}{sin\theta}$$

$$\varepsilon = \frac{t}{2R}$$

$$\varepsilon = \frac{t\,sin\theta}{l}$$

Where t is the thickness of the thin plate, R is the radius of curvature. At each step, θ should be measured. Strain is limited in this method. In parallel, increasing strain kills the strain accuracy because of its fundamental assumptions.

Electrostatic Pull-in Mechanism

Using voltage-driven parallel-plate electrostatic actuator, we can exploit important behavior called pull-in mechanism [40]. According to Figure-4.7, any applied voltage to the parallel plates with a dielectric material between, can cause pulling force between opposite poles. The net force is the equilibrium between electrostatic and the spring force.

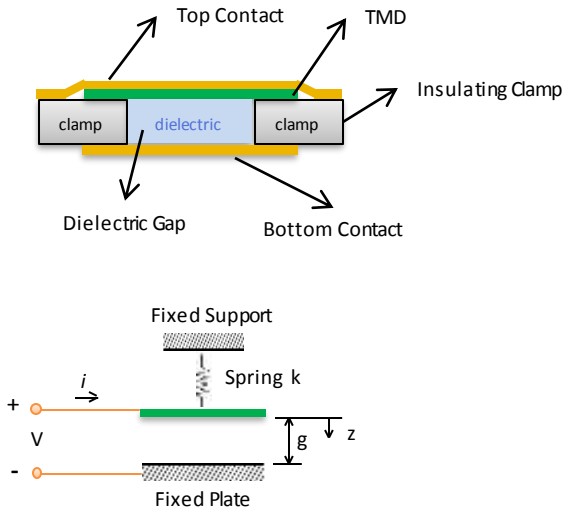

Figure 4.7- Electrostatic pull-in mechanism. Proposed architecture for 2D materials (top) and the modeling diagram of the same architecture (bottom)

The net force applied to 2D material once a DC voltage applied is:

$$F_{net} = -\frac{\epsilon A V^2}{2g^2} + k(g_0 - g)$$

where g_0 is the initial gap with no voltage and no spring force and A is the cross sectional area of the material. This net force varies with small perturbation of gap:

$$\delta F_{net} = \frac{\partial F_{net}}{\partial g}\bigg|_V \delta g$$

$$\delta F_{net} = \left(\frac{\epsilon A V^2}{g^3} - k\right)\delta g$$

For a static equilibrium condition, the clamp spring constant should be strong enough to overcome the electrostatic force:

$$k > \frac{\epsilon A V^2}{g^3}$$

The gap is a function of applied voltage V, spring constant, k and initial gap g_0 which could be analytically achieved from the following equation:

$$2kg^3 - 2kg_0g^2 + \epsilon AV^2 = 0$$

Each gap represents a center deformation which is directly dependent to the applied stress. However, with increasing applied voltage between two poles, the gap decreases until the equilibrium is lost. This is called the pull-in voltage, V_{PI}. At this condition, the net force is zero and the gap will be reduced to g_{PI} which is called pull-in gap:

$$k = \frac{\epsilon A V_{PI}^2}{g_{PI}^3}$$

Plugging this equation to F_{net} relation, we will have:

$$g_{PI} = \frac{2}{3} g_0$$

$$V_{PI} = \sqrt{\frac{8kg_0}{27\epsilon A}}$$

Pressurized Thin Membranes (biaxial)

For suspended devices as shown in Fig. 4.8, any internal pressure would apply biaxial strain on thin film membranes. The strain is a function of applied pressure.

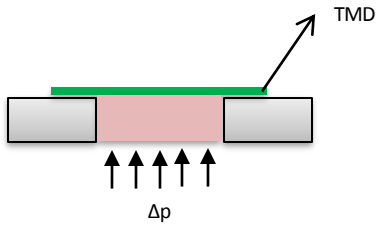

Figure 4.8- Pressurized thin membrane method to apply biaxial strain.

4.7 Groundbreaking Reproducible Strain

Extra-neutral axis bending – vertical pushing method

The last but not the least, is the same straining phenomenon of extra-neutral axis bending but not with the circular or limited angle assumptions. In this method I aim to bend a flexible substrate that applies tensile strain on the top and compressive strain on the bottom of neutral axis. Figure 4.7 is the schematic diagram of this method.

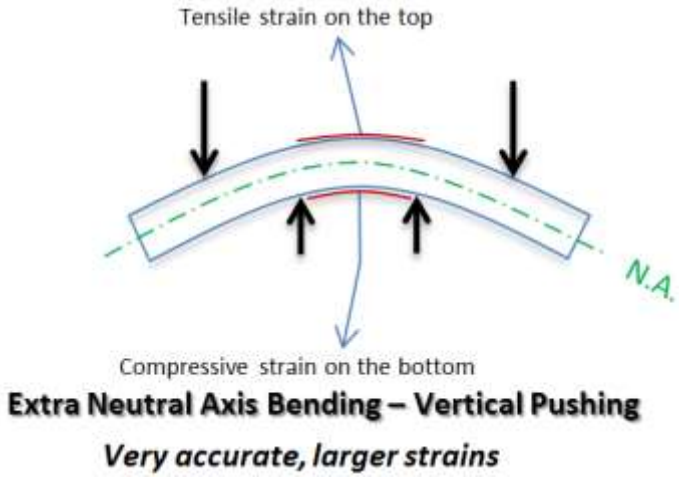

Figure 4.7-Illustration of extra neutral axis bending – vertical pushing method for applying strain

Statics of the beam

What we need is to develop a mathematical function demonstrating the relationship between the vertical motion of the ends and the applied strain on the middle region - $\varepsilon = f(\delta)$. We assume uniaxial strain case in which we have axial load on a thin plate. The simple mechanical and loading notation for this method is illustrated in Figure 4.8. In this figure the center supports (points B and C) are assumed to be fixed and two vertical loads are applied to the ends (points A and D) in order to deform the beam. Points A and D also could be considered fixed with applying force on points B and C.

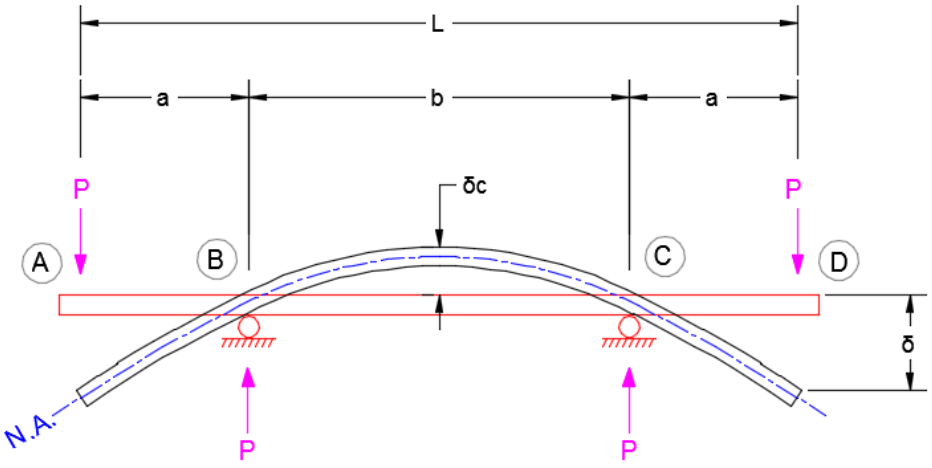

Figure 4.8-Statics of extra-neutral axis bending – vertical pushing method. It is assumed that the ends move downward buckling the beam up in the center. P introduces the load applied to the system

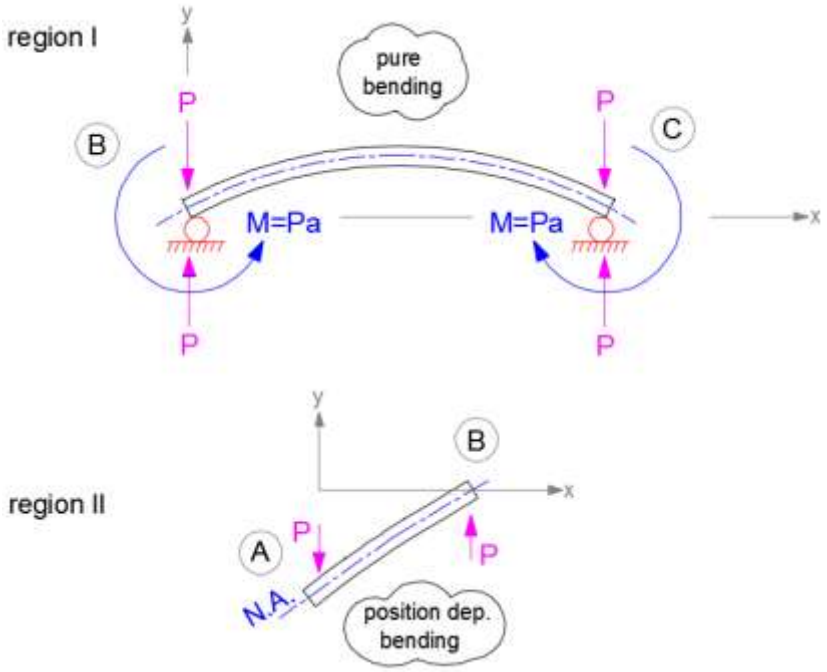

Figure 4.9-Bending moment and force analysis in different regions of the beam under vertical loading. The center region is under 'pure bending' while it is position dependent in Region II.

Statics of the beam with force and bending moment analysis is shown in Figure 4.9. As it is shown in this figure, the center region – 'region I' between points B and C is under pure bending. This

means that all points in the center undergo the same moment independent of position, causing a uniformly distributed strain in top and bottom of the center region. This is promising since any flake could be positioned on the center – between points B and C – and it will go under the same calculated strain. Then the important remaining itme is to determine strain ϵ, as a function of vertical deflection, δ. In order to do this, we need to understand beam deflection first.

Geometrical considerations of strain in deflected beam

Figure 4.10 shows an infinitesimal arc on a point in the center region. As it is clear in the figure, $\overline{bd}$

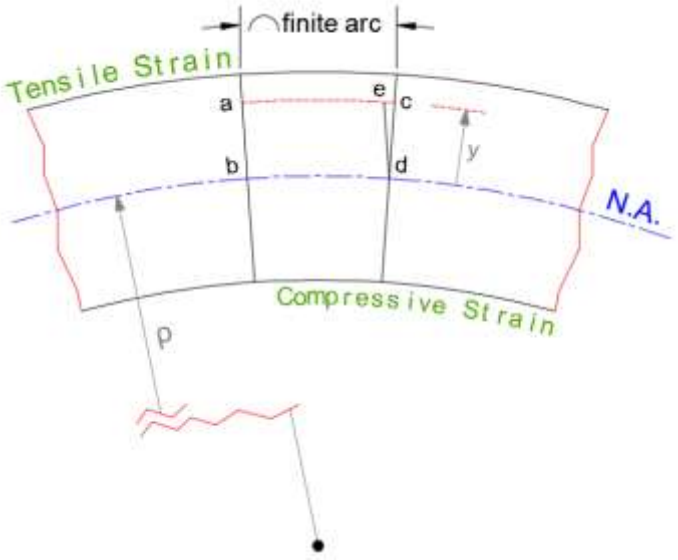

Figure 4.10- a slice of the beam in the center region. Neutral axis (N.A.) doesn't go under deformation while $\overline{bd}$ enlarges to $\overline{ac}$ at an arbitrary distance y from neutral axis.

located on the neutral axis (N.A.) doesn't go to any deformation; while moving out to the top surface by 'y' reveals that the length $\overline{bd}$ changes to $\overline{ac}$. The amount of length expansion is $\overline{ec}$. Top surface is under tensile strain while the bottom surface undergoes compressive strain with the same absolute value – if N.A is located on the geometrical center of cross section. We define strain by:

$$\varepsilon = \frac{\overline{ec}}{\overline{bd}}$$

Using similarity of triangles:

$$\frac{\overline{ec}}{y} = \frac{\overline{bd}}{\rho} \rightarrow \frac{\overline{ec}}{\overline{bd}} = \frac{y}{\rho}$$

Then, strain simply will be:

$$\varepsilon = \frac{y}{\rho} \qquad (1)$$

Using Hooke's law for uniaxial stress– thin plate's case, we will have the stress relation:

$$\sigma = E\varepsilon \rightarrow \sigma = \frac{1}{\rho} Ey \qquad (2)$$

$$\frac{1}{\rho} = \frac{\sigma}{Ey}$$

Force, bending moment and stress calculation

Now we should find a relation independent of ρ since it is not the parameter we can easily calculate. Let's take a piece of the bending cross section of the center region – region I, as shown in Figure 4.9. This cross section is illustrated in Figure 4.11.

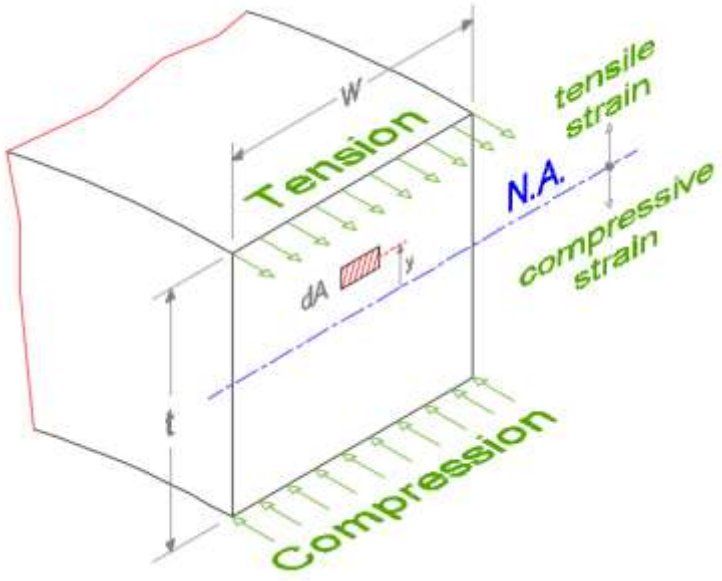

Figure 4.11- cross section of bending beam in the center region – region I, under pure bending

Regions above the N.A. are under tensile strain while the bottom section is under compressive strain. If we take an infinitesimal piece of cross section dA with a distance y from N.A., then the force acting on this segment will be as following:

$$dF = \sigma . dA$$

Then using equation (2),

$$F = \int \sigma . dA = \int \frac{Ey}{\rho} dA = \frac{E}{\rho} \int y \, dA$$

The term $\int ydA$ is first moment of the area of the cross section with respect to neutral axis – N.A. The total resultant force acting on the cross section must be zero since there is no external force acting on the cross section. This yield:

$$\int ydA = \bar{y}A = 0 \ \rightarrow \bar{y} = 0 \qquad (3)$$

This claims that the neutral axis lies on the centroid of the cross section area.

Now lets us calculate amount of the bending moment applies to the segment dA in Figure 4.11.

$$dM = ydF = \frac{E}{\rho} y^2 dA \ \rightarrow M = \frac{E}{\rho} \int y^2 \, dA$$

$$I = \int y^2 \, dA \qquad (4)$$

$$M = \frac{1}{\rho} EI \qquad (5)$$

Where I is the cross-sectional moment of inertia. Doing integration for a rectangular cross section, with width w and height h as shown in Figure 4.11, we will have:

$$I = w \, t^3/12 \qquad (6)$$

Considering that $1/\rho = \sigma/Ey$, then the famous formula for beam stress will be:

$$\sigma = My/I \qquad (7)$$

Differential equation of elastic curve and Euler-Bernoulli's equation

From differential calculus, the curvature of a deflected elastic beam at any point is:

$$\frac{1}{\rho} = \frac{d^2y/dx^2}{[1+(dy/dx)^2]^{3/2}} \approx d^2y/dx^2 \qquad (8)$$

This approximation is accurate for small curvatures. Then having in consideration that $1/\rho = M/EI$ from equation (5), we will have:

$$EI\frac{d^2y}{dx^2} = M \quad \textit{'Euler-Bernoulli's equation'} \quad (9)$$

This is *Euler-Bernoulli's* equation. In any problem it is necessary to integrate this equation to obtain an algebraic relationship between deflection y and x. Different loadings with various geometries will provide different boundary conditions which generate different solutions of this equation.

Solution of Euler-Bernoulli's equation for our geometry

In region I – the center region which is depicted in Figure 4.9, the bending moment is fixed, $= Pa$; and there is no other loadings which we called 'pure bending' region. Considering this figure, if we take the origin located on B then at any x from the origin, we can solve Euler-Bernoulli's equation as following:

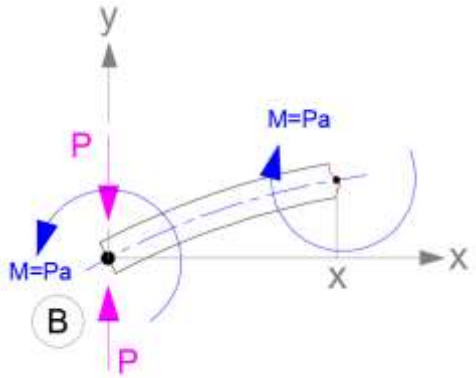

$$EI\frac{d^2y}{dx^2} = M = Pa \qquad (10)$$

$$EI\frac{dy}{dx} = Pax + c_1 \qquad (c_1 \text{ is constant}) \qquad (11)$$

Now, let us apply boundary conditions to our case. In this region, since we deform the beam symmetrically, then at the center, the slope of the curve will be zero:

$$x = b/2 \rightarrow dy/dx = 0$$

$$pa\,(b/2) + c_1 = 0 \rightarrow c_1 = -\frac{1}{2}Pab$$

Now we plug in (11) and integrate again:

$$EI\frac{dy}{dx} = Pax - \frac{1}{2}Pab \qquad (12)$$

$$EIy = \frac{1}{2}Pax^2 - \frac{1}{2}Pabx + c_2 \qquad (13)$$

Applying boundary conditions:

$$x = 0 \rightarrow y = 0$$

$$c_2 = 0$$

Then the deflection curve for the center region will be:

$$EIy = \frac{1}{2}Pax^2 - \frac{1}{2}Pabx \qquad (14)$$

This equation reveals that the deformation is a parabola – not a circle.

In region II – the end sides as shown in Figure 4.9, the bending moment is a function of position – not independent of x. Then we should re-solve Euler-Bernoulli's equation:

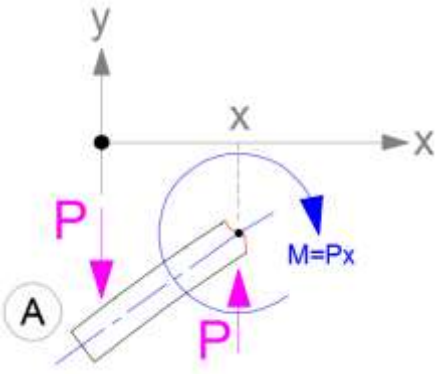

$$EI\frac{d^2y}{dx^2} = M = Px \qquad (15)$$

$$EI\frac{dy}{dx} = \frac{1}{2}Px^2 + c'_1 \qquad (16)$$

Boundary condition for the slope equation of this region is not straightforward. The only existing relation is that the slope of the curve at $x = a$, should be the same slope of the region I at $x = 0$. Then comparing equation (12) which is slope of the region I, with equation (16) which is the slope of region II, we will have:

$$\frac{dy}{dx}(eq.12)\Big|_{x=0} \equiv \frac{dy}{dx}(eq.16)\Big|_{x=a} \qquad (17)$$

$$-\frac{1}{2}\frac{Pab}{EI} = \frac{1}{EI}\left(\frac{1}{2}Pa^2 + c'_1\right) \rightarrow c'_1 = -\frac{1}{2}Pab - \frac{1}{2}Pa^2$$

Plugging in (7) and integrating again:

$$EIy = \frac{1}{6}Px^3 - \frac{1}{2}Pa(a+b)x + c'_2 \qquad (18)$$

Now we can apply boundary condition for this equation:

$$x = a \rightarrow y = 0$$

$$c'_2 = -\frac{1}{6}Pa^3 + \frac{1}{2}Pa^2(a+b)$$

The deflection curve for the end regions will be:

$$EIy = \frac{1}{6}P(x^3 - a^3) - \frac{1}{2}Pa(x-a)(a+b) \qquad (19)$$

This equation reveals that the deformation is a cubic function – not a circle.

Since our main intention is to relate δ – the end deflection to the center strain, with equation (19) we can easily calculate δ as a function of geometry and beam mechanical data:

$$x = 0 \rightarrow y = \delta$$

$$\delta = \frac{1}{6}\frac{Pa^2}{EI}(2a + 3b) \qquad (20)$$

Equation (20) is important as we should find relating parameters with the center region's strain. What we need is to calculate the strain at the top surface. Considering that our case is uniaxial stress, then we can apply Hooke's law in the simplest form that we found. Paying attention to Figure 4.11, the strain on the top and in region II will be:

$$\sigma = \frac{My}{I}, y = \frac{t}{2}, M = Pa \qquad (21)$$

Then we will have:

$$\sigma = \frac{Pat}{2I} \qquad (22)$$

Rewriting Hooke's law for uniaxial stress and plugging into (22)

$$\sigma = E\varepsilon \rightarrow \varepsilon = \sigma/E$$

$$\varepsilon = \frac{Pat}{2EI} \qquad (23)$$

$$\frac{Pa}{2EI} = \frac{\varepsilon}{t} \qquad (24)$$

Plugging equation (24) into (20), we will have our desired formula, δ as a function of beam geometry, independent of mechanical data:

$$\varepsilon = \frac{3t\delta}{a(3b+2a)} \qquad (25)$$

This means that the strain is linearly dependent to the plate thickness and also applied δ. Then by exerting linear vertical motion to the end points, we can apply linear strain increase.

Example:

If t=0.5mm, a=b=2mm, then: $\varepsilon(\%) = 7.5\delta$ *with* δ *in millimeters. For* δ*=20* μm, $\varepsilon = 0.15\%$.

If t=0.5mm, a=b=1mm, then: $\varepsilon(\%) = 30\delta$ *with* δ *in millimeter. For* δ*=20* μm, $\varepsilon = 0.6\%$.

This example reveals that we need to design very accurate mechanism to be able to apply stepwise vertical motions. From mechanisms point of views and the standard shelf items available, we can choose δ=20 μm as a reference minimum motion. Then a=b=2mm which is in the applicable device range dimensions, sounds reasonable target parameters for the mechanism. I call this mechanism 'Strain Jig'. Figure 4.12 is a version of this mechanism with the possibility of adding wire bounds for electrical connections to the sample.

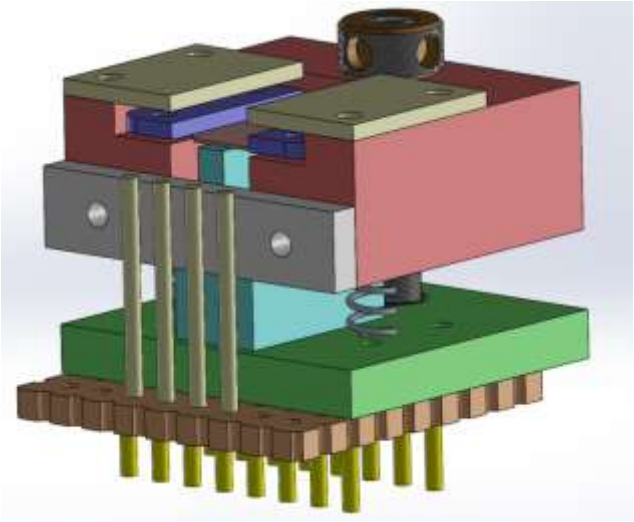

Figure 4.12- Strain Jig – miniature version for wire bonding – designed for cryostats.

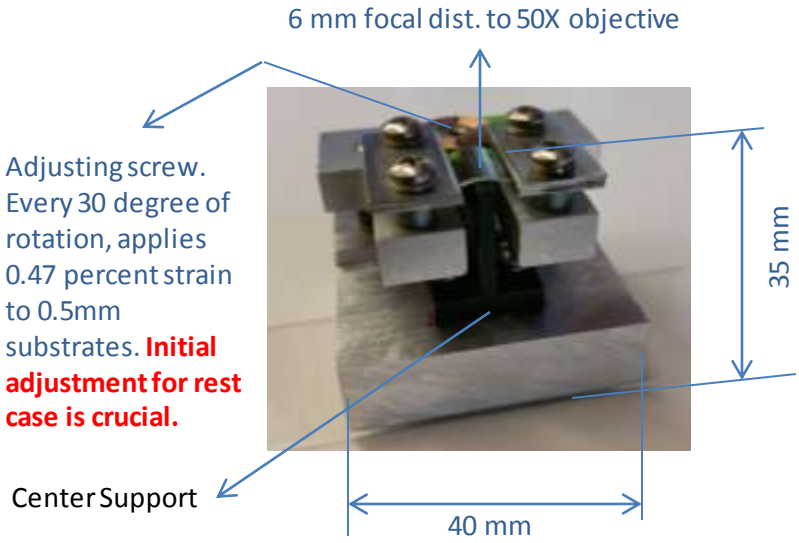

Figure 4.13- Strain Jig – main version used in our strain experiments.

CHAPTER 5

Device Micro / Nano Fabrication Techniques

5.1 Introduction

Device fabrication is crucial for an experimentalist. For the main purpose of this dissertation which are flexible devices, we provide here the basics and fundamentals of device fabrication for high strain devices. Sections 5.2 is introduction to polymers and polymers based devices, followed up by section and 5.3 which is flexible devices. Section 5.4 presents the techniques we used for making transport devices that we used for the experiments explained in part C of this dissertation. In section 5.5, I provide information to how to make heterostructures and stacked devices with the use of polymers.

5.2 Introduction to polymers and polymers based devices

A polymer is a large molecule made of many subunits which usually appear in chain-like structure. These chains are normally amorphous which give nonlinear mechanical properties to the polymer. In addition to nonlinearity, the long chains cause them to be flexible with higher elastic range. These polymer chains are cross-linked with another smaller molecule or atom which makes even longer and bigger chains.

Curing

Curing of polymers means hardening the molecular structure by cross-linking the chains. Since cross-linking needs energy, this process can be done by either heating or applying chemicals. In the case of chemicals, ultra violet (UV) light is needed to activate the chemical agent. We use heating to cure polymers. Following parameters are important factors which should be decided before going to the process of heating.

- $T_c = curing\ temperature$
- $t_c = curing\ time$

- $r_c = ramping\ rate\ to\ T_c from\ room\ temperature$
- $P_c = curing\ pressure$

For each device and polymer stack these parameters should be investigated experimentally. In addition, if the polymer is used for lifting off a sensitive device such as a TMD, following parameters should be carefully studied before finalizing those parameters:

- The polymer doping effect on the device
- Temperature sensitivity of the device
- Chemical sensitivity of the device to the main solvent of the polymer

Polymers are normally solved in their related solvents which are covered later in this chapter. One of the curing purposes is to evaporate the solvent until only the chains are remained which will be in a solid form. In order to bond (stick) two polymers together or to use a polymer for lifting off a device, we need to understand glass transition temperature first.

Glass Transition Temperature

Glass transition temperature, T_g is a temperature region in which the polymer starts being soft and rubbery from a hard material. This is normally a range of temperature in which we select the middle point as the reference. Fig. 5.1 shows the location of a glass transition temperature and how the heating flow rate occurs with respect to this region.

Glass transition temperature is strongly dependent on the curing schedule. Low curing temperature T_c, such as room temperature: $T_c = RT$, will result in lower T_g. Then if we want to use a polymer in conjunction with a temperature sensitive material, we have to cure it at room temperature (RT). Another parameter which has huge impact on T_g is humidity. Moisture absorbs in polymer structures and results in lowering T_g.

Since mechanical properties are very important to our experiments, in the next section, we will be discussing the effects of T_g in mechanical characteristics of polymers.

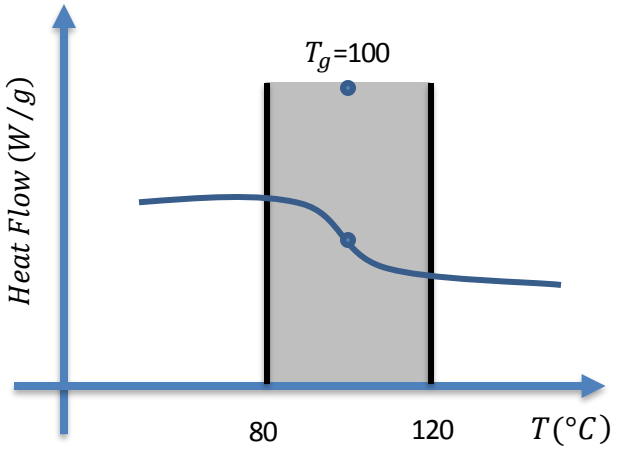

Fig. 5.1- Glass transition temperature of polymers. In the example the transition region is 80-120. The average is taken as glass transition temperature $T_g = 100$

Effects of glass transition temperature on mechanical properties

We realized that we can lower glass transition temperature by controlling the processes of polymer fabrication. I hereby indicate four important properties that may affect a polymer:

Young's Modulus:

Higher the T_g, the higher the cross-linked density and then the Young's modulus will have higher values. This results in low energy dissipation and less flexible polymer. Then, as a conclusion, if we need more flexible polymer, we have to cure it at room temperature. Fig.5.2 shows the Young's modulus of Cellulose Acetate Butyrate (CAB) polymer on a stress-strain diagram. We measured the yield point of this polymer 7% in which starts flowing and strain hardening.

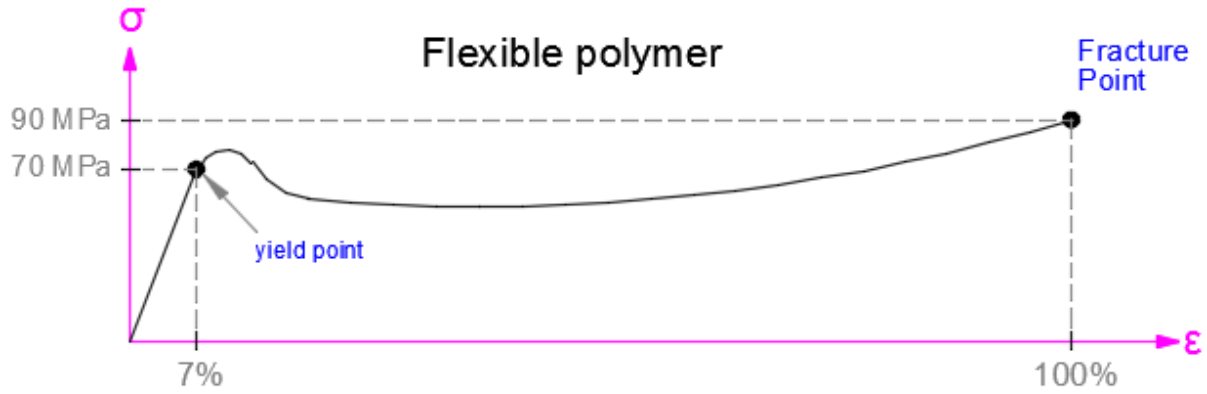

Fig. 5.2 – stress strain curve of a flexible polymer. The numeric value in this graph represent data for CAB

Lap Shear:

Fig. 5.3 is schematics of lap shear. It presents shear strength of adhesives for bonding materials when tested on a single-lap-join specimen. Then test procedure is according ASTM D3163. As T_g increases, lap shear decreases.

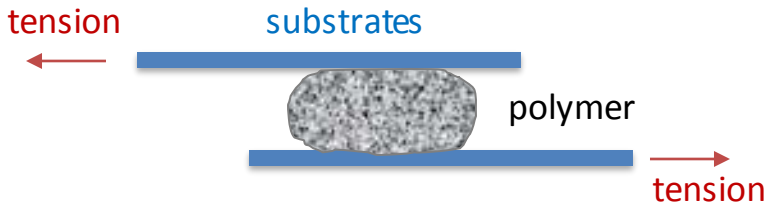

Fig. 5.3– Lap shear experiment according to ASTM D3163

Die Shear:

Fig. 5.4 shows the definition and mechanism of die shear. With increased T_g, die shear decreases. Then if we need flexible devices that endure higher die shear and lap shear, we have to decrease glass transition temperature, T_g.

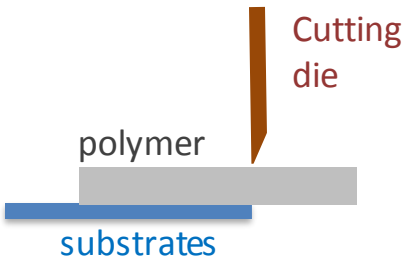

Fig. 5.4– Die shear experiment. Glass transition temperature directly affects the shear strength of a polymer.

Coefficient of Thermal Expansion (CTE):

The thermal expansion coefficient is directly related to glass transition temperature T_g. Any increase in T_g, will rise the CTE.

5.3 Flexible devices

As mentioned, polymers are the basics of flexible devices. Here I explain the device fabrication protocols we developed for strain-based devices. Some detailed explanations are discussed in chapter 6 – Raman signals processing section though, here we explain more in detail the fabrication processes.

Making Cellulose Acetate Butyrate (CAB)

We use CAB to lift off CVD grown TMDs. Then the first step is making the CAB solution. The concentration we use for this purpose is 300 grams of CAB powder, solved in 1-liter of anisole. We use a magnetic stirring bar in a glass bottle – both cleaned and rinsed with anisole first, for this purpose. After mixing power with anisole, we use a hot plate with magnet to heat on 80C with 120 rpm of spinning for overnight.

Spin coating CAB

The CAB is then spin coated to the silicon substrates that have TMDs. The spin coating is data is 3000 rpm, 10,000 rev/sec of acceleration for a minute. Then we cure CAB on hot plate with 80C temperature for 10 minutes. TMDs or any layered material can be used with this technique since CAB plays a glue-like role to lift off thin materials very efficiently. This produces 3 μm thickness CAB films.

Lift off

When the substrate is ready with the CAB film on the top, it is the time to lift off. We use DI water for this purpose. But since polymer absorbs humidity, the technique should be done very fast. We first clean the edges of the substrates to open the interface to be permeable to DI water. Then we put in DI water and play with sharp tweezer to lift off the CAB film. This should not take more than 10 seconds. Then we eventually place the film in desiccator for at least 4 hours to dry.

Bonding, Annealing

We use polycarbonate (PC) plates as a standard substrate. We selected this material after hundreds of experiments to find a good match with the top covering film. It turned out that PC is a good match with CAB. This means that they can bond very well in the temperature regime that are safe for TMDs and graphene.

One of our chief innovations is the development of a novel polymer-based encapsulation method to enable the application of large strain to 2D materials. In our technique, these two polymers are bonded to produce encapsulated monolayers and multilayers. The key to achieving good bonding is perfect control over the temperature, time and pressure during the bonding process. Additionally, polymer layers that are in the amorphous phase cause nonlinear strain-deflection behavior which is not desirable in our experiments. To resolve this issue, we crystallize

the polymer stacks by annealing near the glass transition temperature followed by slow cooling. First, we measured the glass transition temperature, T_g of each polymer blend we use, by continuously heating it on an accurate PID-controlled hotplate (± 0.1℃ accuracy) while checking its ductility. After determining T_g, we assemble the polymer stack and perform the bonding process at $T_B = 0.97T_g$. We use a compressive pressure of 3.0 psi for 60 min to complete the bonding, followed by slow cooling at a rate of 2 K/min to room temperature. We find that this process of encapsulation does not modify the peaks or intensity ratios in the Raman spectra, indicating that the structural qualities of the films are maintained during the encapsulation process. To additionally check the electronic properties of the bonded film, we perform photoluminescence (PL) spectroscopy of the monolayers before and after encapsulation. We find that the major electronic features observed in the PL spectra are maintained during the bonding process. The crystallized polymers are fully flexible, elastic and springy substrates. After all of our processing steps, we find that the polymer stacks enter into the plastic regime at 7% strain. We find that strains up to this value are perfectly transferred to the encapsulated 2D material as described below. The final bonded device is shown in Fig. 5.5. We can bond the device either in open-phase or closed-phase (encapsulated) geometries as shown in Fig. 5.6.

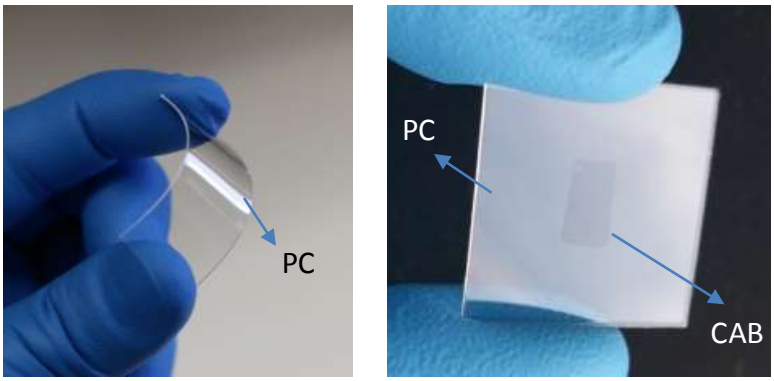

Fig. 5.5 – Flexible device used to encapsulate 2D materials. The technique can be used for making fully encapsulated devices or face up devices as shown in Fig. 5.6.

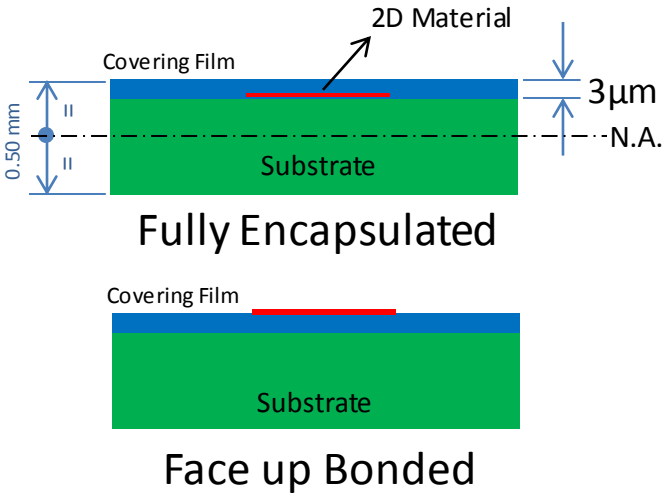

Fig. 5.6 – Fully encapsulated devices and face up devices. The difference is the direction of bonding.

Face up bonded devices would be subjected to air and then might not be suitable for air sensitive devices. Fig. 5.7 is the schematic diagram of these fabrication steps.

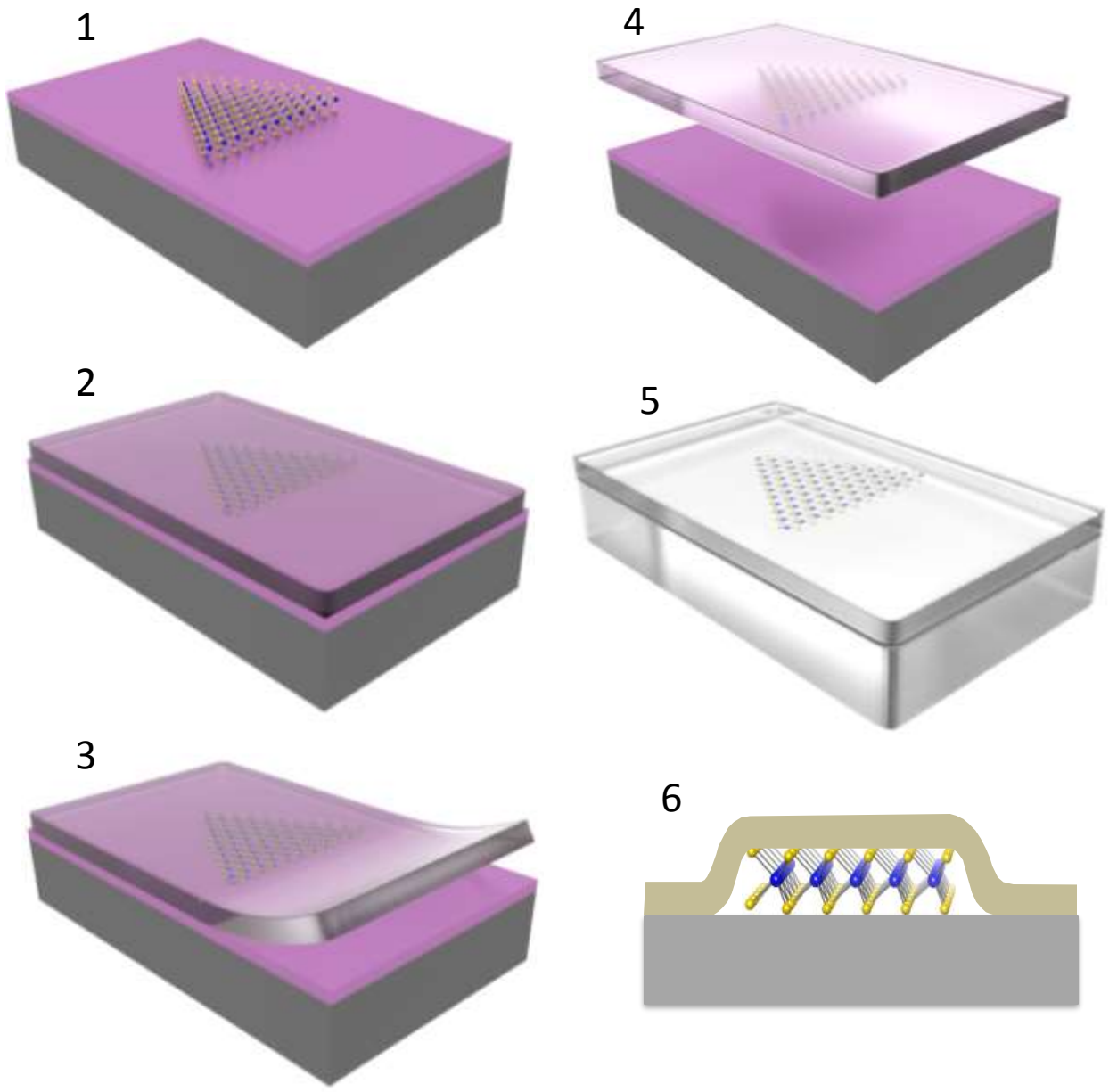

Fig. 5.7 – Device fabrication procedure for encapsulated devices. Step 1: growing/preparing TMD on oxide substrates. Step 2: spin coating CAB. Step 3, 4: lift off. Step 5: bonding and annealing. (6): cross section of encapsulated device.

5.4 Field-effect transistors and transport devices

Part C of this dissertation is dedicated to transport measurements of pristine and nitrogen doped graphene. The growing techniques of both types of graphene are explained in part D. Here, we briefly explain the device fabrication steps for these type of devices.

As explained in chapter 9 and 10, graphene is grown on copper foils which have to transferred on to the silicon substrates. There are many techniques to transfer. We first cut copper foils in small pieces of 3x3 mm and then transfer to PDMS – graphene faced down to the PDMS. Then we use oxygen plasma for 30 seconds to etch and clean the backside. We put the whole stack in ammonium persulfate (APS) on hot plate at 40C. Once the copper is resolved, we wash PDMS substrate six times in fresh DI water and nitrogen dry. PDMS now has graphene on the top and could be used to transfer.

Having in consideration that PDMS loses adhesion at about 65C, we put a clean silicon dioxide substrate on a hot plate at this temperature. Then we approach PDMS to the silicon dioxide with graphene side. This leaves graphene to the substrate with very clean and the gentlest way. We observed that this technique gives the cleanest and largest continuous graphene on silicon substrates. These steps are summarized in Fig. 5.8.

Once the graphene is transferred to the desired silicon substrate, we use electron beam lithography to pattern the desired region which is cleanest single crystal. We pattern Hall bar for transport measurements which is explained in part D of this dissertation. Fig.5.9 shows the Hall bar and the real device which is wire bonded for cryogenic transport studies.

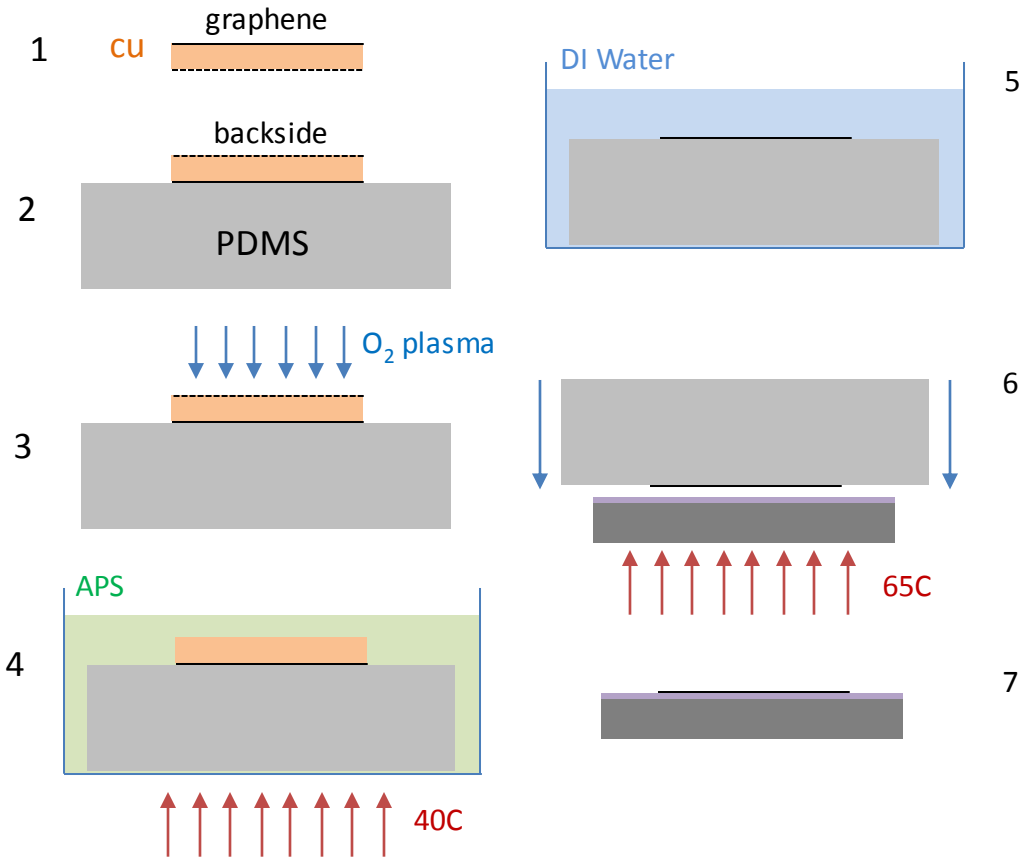

Fig. 5.8 – Transfer technique of CVD graphene to silicon dioxide substrates. This technique provides cleanest devices for transport experimetns.

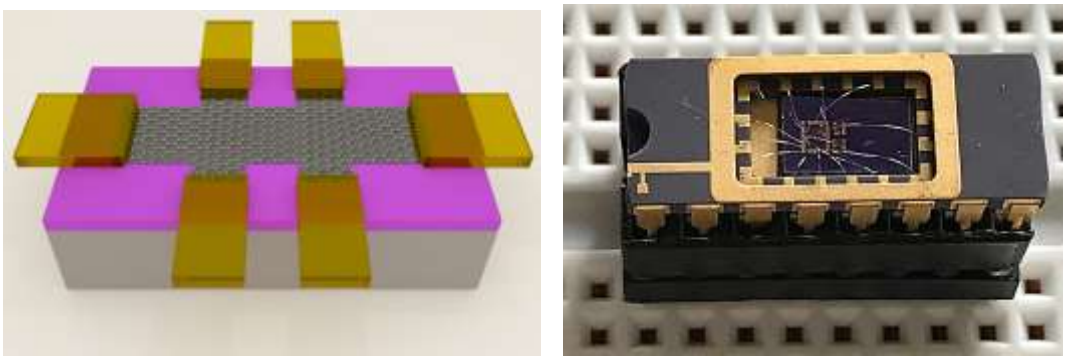

Fig. 5.9 – Hall bar designed with graphene transport technique and electron beam lithography (left) and the final device wire bonded ready for experiment (right)

5.5 Micro transfer techniques

In this part I will explain state-of-the-art technique to produce stacked hetero structures of single layer TMDs. The target device is aligned single crystal MoS2 on top of MoSe2 both monolayer with very accurate and controlled angle and also very clean interface. We first grow each of these TMDs on separate substrates.

We tune our processes to grow MoSe2 very big single crystals and in contrary, MoS2 very small monolayers. Then we spin coat PMMA on top of small crystals and cure the polymer at lowest possible temperature – 130C. This minimizes the doping effect to MoS2 and gives the cleanest interface. Then we use KOH solution to etch silicon oxide and with careful washing with DI water, we transfer to the MoSe2 substrate under microscope station. The final device is shown in Fig. 5.10. As you notice from the picture, we have many aligned MoS2 on top of MoSe2 which allows us to choose the desired angle for experiment. The target experiment is investigation of interlayer excitons in aligned hetero structure which is beyond this dissertation. In order to demonstrate the validity of the fabrication technique I explained, Fig. 5.11 is provided with some results that we observe the interlayer excitons are generated only in perfectly aligned flakes.

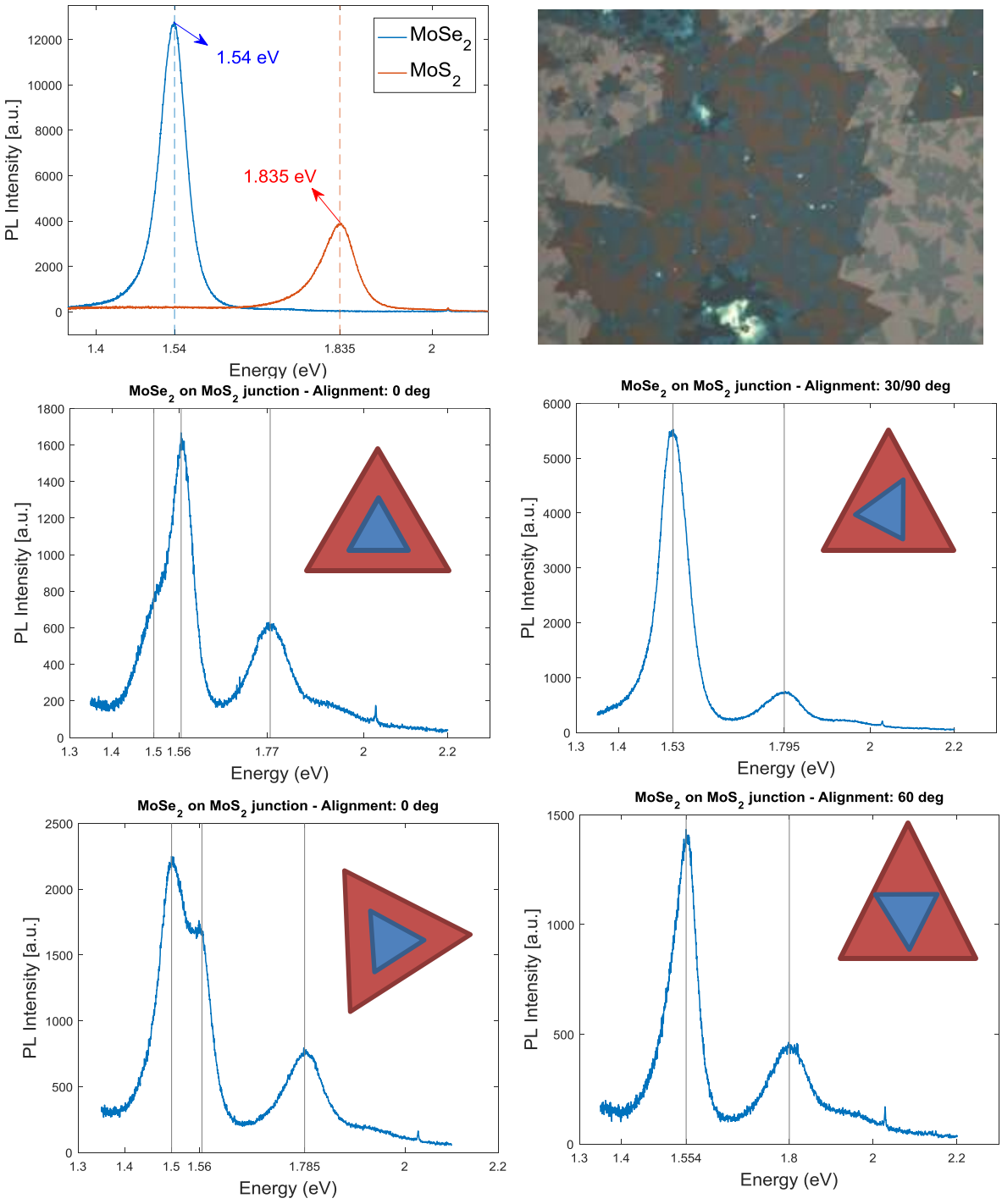

Fig. 5.10 – The hetero structure of MoS2 (blue) on MoSe2 (brown) monolayer TMDs (top) made with accurate stacking techniques. (Graphs): show that the interlayer excitons generated in in just perfectly aligned substrates.

CHAPTER 6

Experimental Results

6.1 Raman Signal Processing

Here we describe our findings corresponding Raman spectroscopy under strain. The detailed physics of Raman is discussed in chapter 2. Here we explain the techniques we used to investigate the behavior of monolayer WSe_2 and WS_2 under strain as well as our discoveries.

We use polymer encapsulation method which is discussed in chapter 5, to study the lattice response to strain via polarized Raman spectroscopy. The application of strain causes mode-dependent redshifts, with larger shift rates observed for in-plane modes. We observe a splitting of the degeneracy of the in-plane E' modes in both materials and measure the Grüneisen parameters. At large strain, we observe that the reduction of crystal symmetry can lead to a change in the polarization response of the A' mode in WS2. While both WSe2 and WS2 exhibit similar qualitative changes in the phonon structure with strain, we observe much larger changes in mode positions and intensities with strain in WS2. These differences can be explained simply by the degree of iconicity of the metal-chalcogen bond.

One of the iconic characteristics of monolayer 2D materials is their incredible stretchability which allows them to be subjected to several percent strain before yielding [28]. The application of moderate (~1%) strains is expected to change the anharmonicity of interatomic potentials [13, 41], phonon frequencies [42, 43] and effective masses [33, 44]. At larger strains, topological electronic[11, 45] and semiconductor-metal structural phase changes have been predicted [5, 31, 35, 36]. Important technological applications such as piezoelectricity can be explored by the application of systematic strain [39, 46]. One of the chief problems in achieving reproducible strain is the intrinsic nature of 2D materials as single layer sheets - they need to be held to a flexible substrate which is then stretched or compressed. Previous experiments [15, 32, 47, 48] have used flexible polymers as substrates and metal or polymer caps in order to constrain the 2D material.

Using these techniques, approximate strains up to 4% have been reported so far in the literature, but independent verification of the applied strain has been lacking. Achieving large reproducible strains in engineered geometries will allow us to probe these exciting properties of individual 2D materials and their heterostructures [29, 34, 42, 47, 49-53].

We use our technique to apply strain as explained in chapter 4. This technique allows to apply reproducible and controllable step-wise and accurate strains on our samples to investigate Raman spectra.

As explained in chapter 4, our strain method adopts the extra-neutral axis bending technique – Fig.

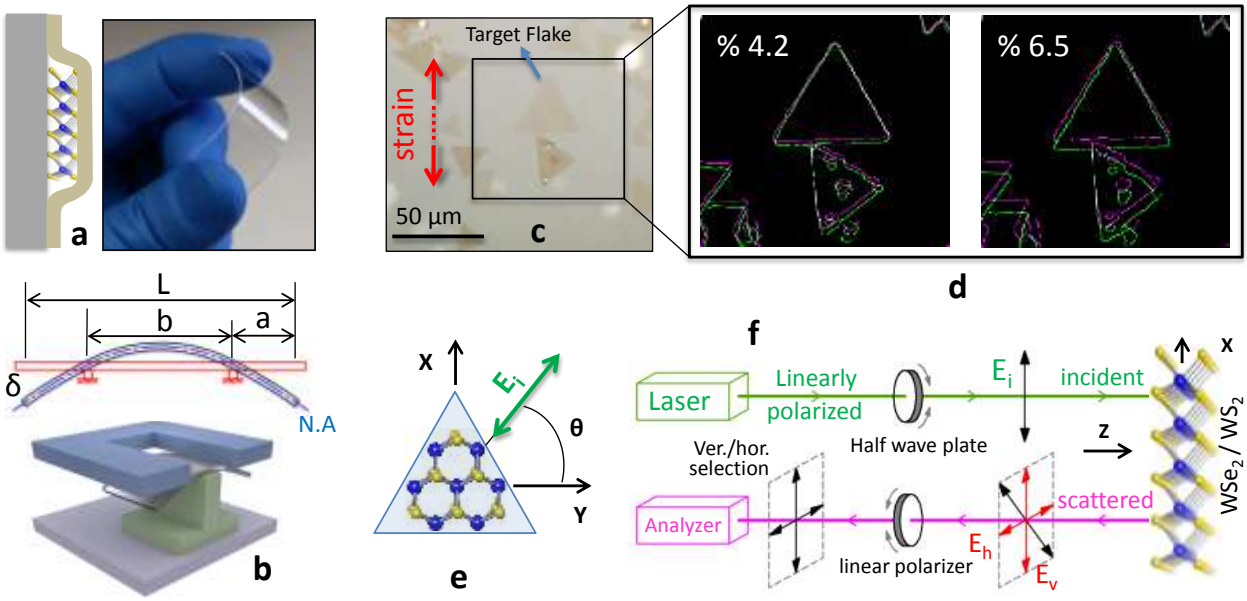

Figure 6.1-1. (a) Polymer encapsulated monolayer TMDs. (b) Strain apparatus. (c) Encapsulated WSe2 monolayers. (d) Overlaid edge-detected images of strained(green) and unstrained(purple) monolayer edges for 4.2% and 6.5% calculated strains. (e) Incident light (Y, θ=0) and strain (X) directions with respect to crystal lattice. (f) Raman spectrometer setup.

6.1-1(b) in which areas above the neutral axis undergo tensile strain while those below the axis experience compressive strain. In our method, we use a screw-driven vertical translation stage to apply strain to the polymer stacks. We solve the Euler-Bernoulli equation for our geometry in order

to achieve an accurate relation between the vertical displacement δ of the translation stage and the strain ε of the 2D material. For a fully isotropic, linear and elastic material, the strain-displacement relation is derived as: $\varepsilon = 3t\delta/a(3b + 2a)$ where t is the substrate thickness, b and a are center support and cantilever lengths respectively. In our experiments, the use of a fine adjustment screw gives us a resolution of 0.05% strain for 0.5 mm substrates, with essentially no limit to the maximum strain that can be applied. More details are provided in the Supplemental Material.

Shown in Fig. 6.1-1(c) is an optical image of triangular flakes of WSe2 encapsulated by this process. We adjust the CVD process to produce triangular flakes in order to easily identify the crystallographic directions of the grown monolayers. Since the strains achievable in our experiments are large, we can directly verify from optical measurements that the strain being applied to 2D layer is the calculated value. This is illustrated in Fig. 6.1-1(d). Each of these images is obtained by overlaying two images, one at zero strain and one at a fixed value of strain (4.2% and 6.5% respectively). Only the edges of the triangles are shown in the images, which are lined up to be at the same vertical height at the top vertex of the triangle. We can directly see by inspection that the length of the triangle along the strain direction is larger when strained as one expects. A pixel-height measurement of the edge-detected images gives us a direct experimental measure of the applied strain, which can be compared to the calculated strain based on the screw displacement. It is found that the two measurements match within 0.1% absolute strain. Thus, our technique allows for the application of uniform, highly repeatable and independently measurable strain on TMD monolayers and heterostructures.

In order to probe the effects of strain on our samples, we choose to characterize with Raman spectroscopy - a simple yet powerful way to measure lattice properties and their coupling to the electronic degrees of freedom. Strains were applied in both zigzag and armchair directions (Y and X axes in Fig. 6.1-1(e)) in our experiments. Our Raman setup with 532 nm excitation wavelength

is shown in Fig. 1 (f). The measurements were performed while controlling for the incident light's polarization (E_i) direction (θ in Fig. 6.1-1(e)). For each experiment, Raman spectra were collected in both the parallel- ($E_s \,||\, E_i$) and cross-polarized ($E_s \perp E_i$) detector geometries, shown with standard notations $Z(YY)\overline{Z}$ and $Z(YX)\overline{Z}$ respectively. In our experiments, we found no dependence of the Raman spectra on the angle of incidence relative to the crystallographic axis at zero strain. We therefore fix our incidence angle of E_i to the Y direction, and measure the unpolarized, parallel-polarized and cross-polarized Raman spectra at each value of strain which is applied in the X direction.

We first discuss the properties of monolayer WSe2. Shown in Fig. 6.1-2(a) are a sequence of spectra taken at different values of strain in the unpolarized, parallel and cross polarization geometries. Previous Raman spectroscopy measurements performed on monolayer WSe2 have identified three vibrational modes [54-56] termed A', E' and $2LA$. A' is an out-of-plane phonon mode in which the top and bottom chalcogen atoms vibrate in opposing directions; while E' is in-plane mode where the metal atoms vibrate out-of-phase with the chalcogen atoms [57]. The $2LA$ mode results from a double resonance process involving two phonons from the LA branch. Second order processes can in general give rise to a complex lineshape in the Raman spectrum; yet, in the case of WSe2 we find that a single Lorentzian can be used to model well the $2LA$ mode lineshape. Although $A'$and E' modes are nearly degenerate, they can be distinguished from each other by polarization dependency of their intensities. The out of plane, symmetric A' mode disappears due to its symmetry in the cross polarization geometry, leaving behind only the E' mode. Our spectra in the cross-polarization geometry can thus be modeled well as the sum of two Lorentzian peaks corresponding to E' and $2LA$ modes. Information of the E' mode position can then be used to fit

the spectra seen in the parallel polarization geometry in order to extract the nearly-overlapping A' mode position.

Having understood the polarization-dependent Raman spectra of unstrained monolayer WSe2, we apply uniaxial strains and measure the Raman response. The effects of uniaxial strain up to 1% on monolayer WSe2 has previously been experimentally investigated via unpolarized Raman [47] and absorption spectroscopy [58]. Raman spectra under increasing uniaxial strain up to 3% are shown in Fig. 6.1-2(a). A close examination of spectral lineshapes in the cross polarization geometry shows that the E' mode becomes broader with increasing strain. In general, we expect that the initially doubly degenerate E' mode splits on the application of strain into E'^{+} and E'^{-}. The displacement eigenvector of the E'^{+} mode is orthogonal to the direction of strain, while it is parallel for the E'^{-}mode, as has previously been observed for MoS2 and graphene [13, 15, 50]. While we cannot observe a complete separation of the E'^{+} and E'^{-} modes in our data, it is nevertheless straightforward to fit the lineshape to two Lorentzian functions and extract the splitting as a function of strain, as shown in Fig. 6.1-2(e). The splitting of the E' mode under tensile strain due to the anharmonictiy of molecular potentials can be described by Grüneisen parameter γ and shear deformation potential β:

$$\gamma = \frac{|\Delta\omega_{E'+}| + |\Delta\omega_{E'-}|}{2\omega_{E'}(1-\nu)}$$

$$\beta = \frac{\big||\Delta\omega_{E'+}| - |\Delta\omega_{E'-}|\big|}{2\omega_{E'}(1+\nu)}$$

where $\omega_{E'}$ is the frequency of E' mode, $\Delta\omega_{E'+}$ and $\Delta\omega_{E'-}$ are the frequency shifts of split modes per unit percent strain and ν is Poisson's ratio which is 0.27 for our substrates. We obtain values of $= 0.38$, $\beta = 0.10$ for WSe2 which are smaller than those reported for graphene [13, 41]. Using the fits for E' mode from the cross-polarization geometry, we then extract the behavior

of the A' mode as a function of strain. We find that this mode expectedly does not shift significantly with strain due to its nature as an out-of-plane excitation. Finally, the $2LA$ mode can be easily fit in both parallel and cross polarization spectra. Small redshifts are observed in its position with increasing strain. We also observe an increase in the width of the A' and $2LA$ modes with increasing strain, as well as a decrease in the intensities of all observed modes at higher strains. These observations are summarized in Fig. 6.1-2(d).

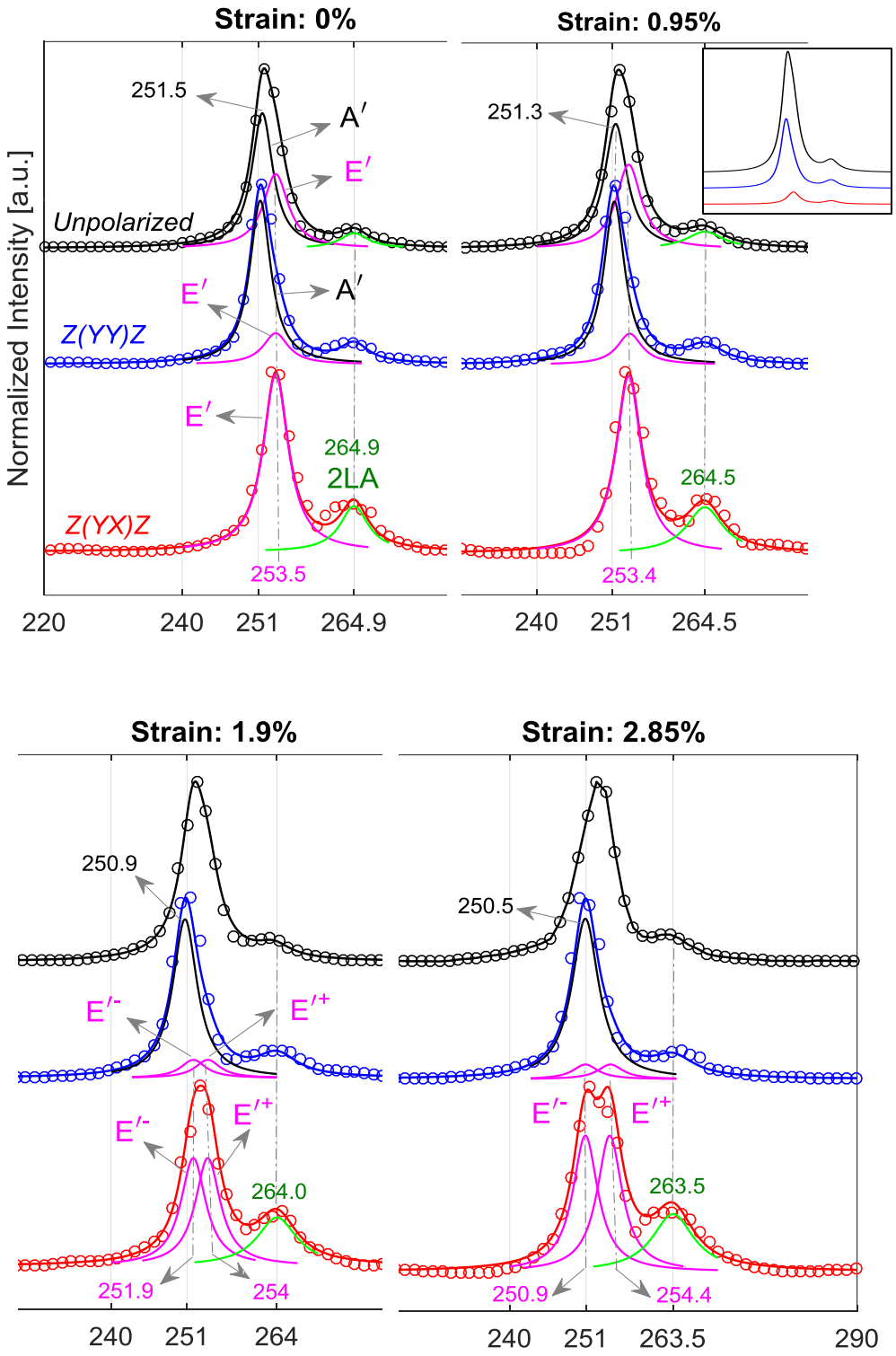

Figure 6.1-2 (a) Unpolarized (black), parallel-polarized (blue) and crosss-polarized (red) Raman spectro of monolayer WSe2 under various tensile strains. Inset: real Raman intensities without normalization.

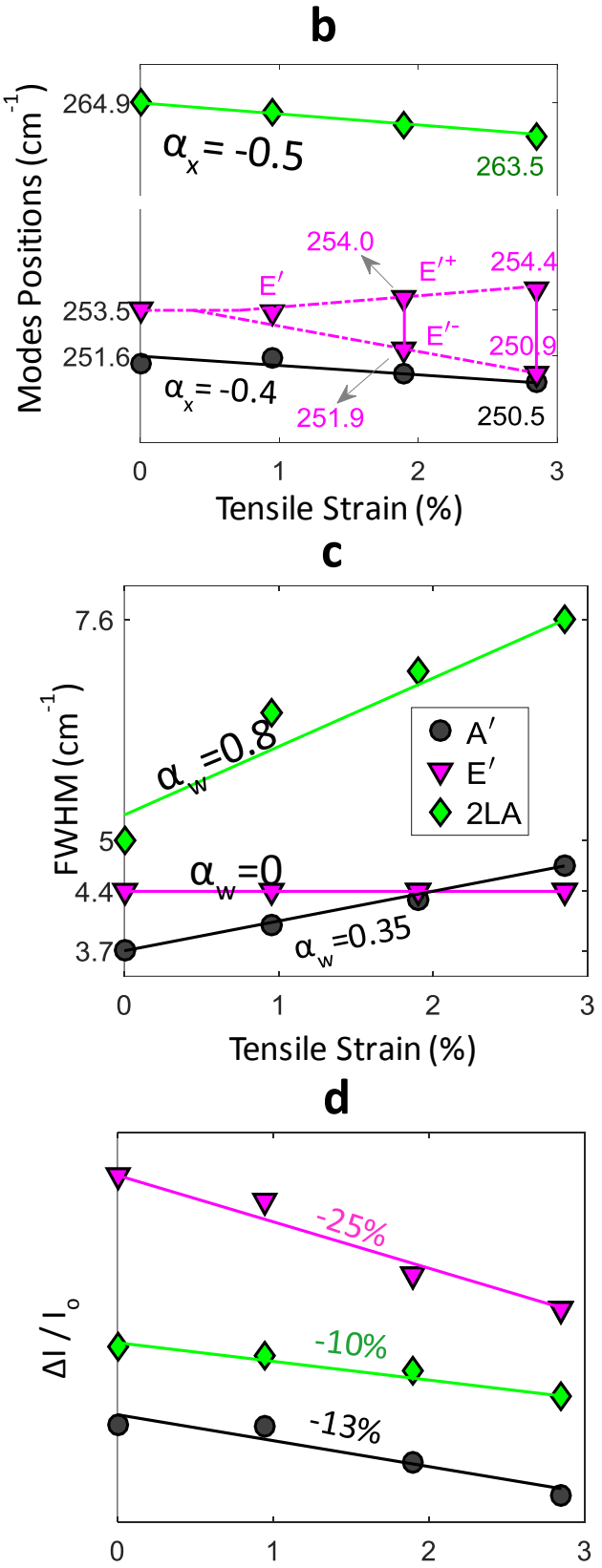

Figure 6.1-2 (a), (c), (d). Position of phonon modes, Full Width at Half Maximum (FWHM) and relative intensity changes vs tensile strain. ±α denotes the amount of change per percent tensile strain.

The spectra of WS2 show additional structure [59], as can be seen in Fig. 6.1-3(a). Firstly, two additional lines that we term P_1 and P_2 are observed in the spectra at 303 and 332 cm-1 respectively. We clarify the mode assignment of these peaks based on theory as described below. The A' mode is well separated from the other modes and is located at 423 cm-1. Secondly, the region between 345 cm-1 and 365 cm-1 shows a complex lineshape. Previous measurements have shown that the $2LA$ and E' modes are nearly degenerate in WS2. However, we find that even two Lorentzians are not sufficient to accurately model the lineshape at zero strain, and we need a minimum of three Lorentzians to reasonably fit the lineshape. One of these three peaks is related to E'mode while we associate the other two with the LA branch and label them by $2LA_1$ and $2LA_2$. The description of the LA branch as the sum of two Lorentzians has been made before in the case of MoS2 [60]. Such complex lineshapes are in general expected in double-resonance processes where one has to properly account for the phonon density of states as well as the electron-phonon couplings at different points in the Brillouin Zone. Our strain-dependent measurements help make the distinction between the E' and $2LA$ bands as described below.

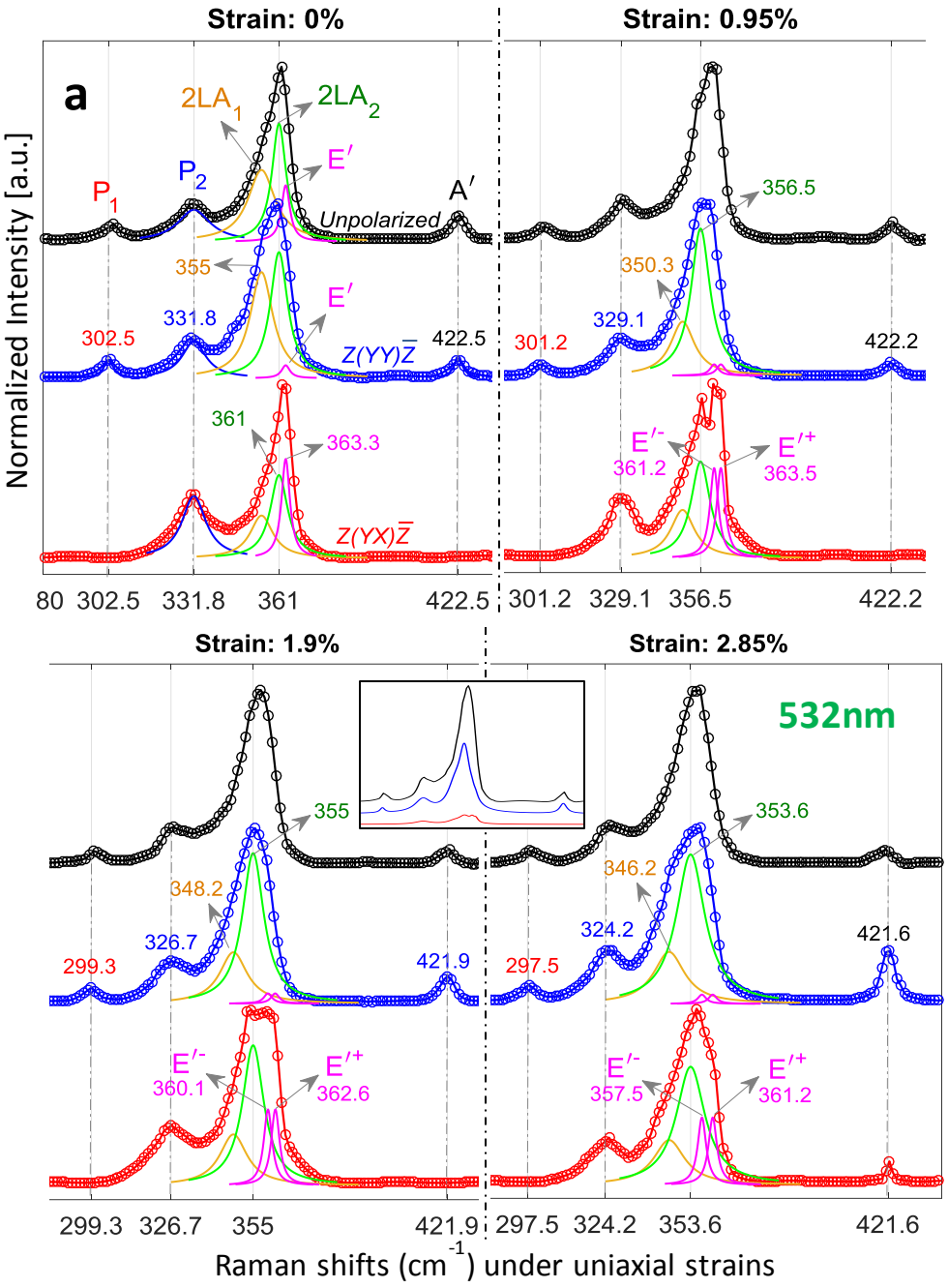

Figure 6.1-3 (a) Unpolarized (black), parallel-polarized (blue) and crosss-polarized (red) Raman spectro of monolayer WS2 under various tensile strains. Inset: real Raman intensities without normalization.

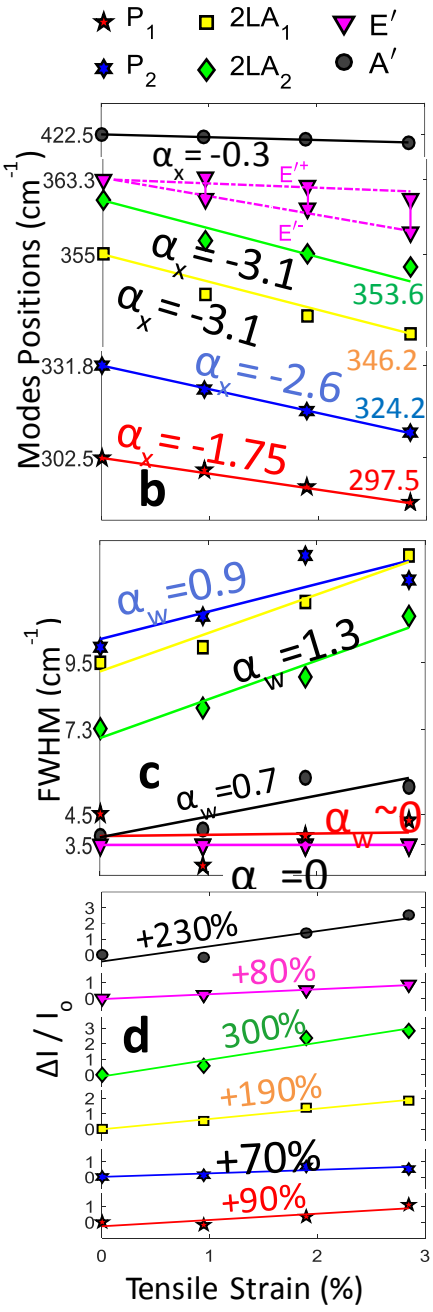

Figure 6.1-3 (a), (c), (d). Position of phonon modes, Full Width at Half Maximum (FWHM) and relative intensity changes vs tensile strain. ±α denotes the amount of change per percent tensile strain.

Shown in Fig. 6.1-3(a) are a sequence of Raman spectra of WS2 obtained at different values of strains. At each strain, we fit both the parallel and cross-polarization spectra to obtain a consistent set of peaks. Similar to WSe2, we find a splitting of the $\boldsymbol{E'}$ mode with applied strain. The measured Grüneisen parameter and shear deformation potential are $= \mathbf{0.54}$, $\boldsymbol{\beta} = \mathbf{0.14}$ respectively. All extracted peaks positions, intensities and widths as a function of strain are shown in Fig. 3(b,c,d). Similar to WSe2, the $\boldsymbol{A'}$ mode shows a minimal response to strain due to its out of plane nature. Different from WSe2, the intensity of all the modes increases as a function of strain. Very interestingly, we find that at high strain (>2.5%), the $\boldsymbol{A'}$ mode appears in cross polarization geometry while the P1 mode continues to be fully suppressed. We discuss these observations below.

To better understand the vibrational properties of monolayer WS2 and WSe2, we perform first-principles functional theory (DFT) calculations. In order to apply uniaxial strain, we use orthorhombic unit cell of different sizes, where a specific direction of the lattice, either armchair or zigzag is strained. Similar results were obtained at both directions, using a hexagonal cell (see figure S3 in Supplemental Material). Fig. 6.1-4(a and b) show the phonon dispersion curves for WS2 and WSe2 respectively at zero and finite strains. Vibrational modes are labelled accordingly to their symmetry at the Γ-point. It can be seen that there are six optical modes ($\boldsymbol{2E''}$, $\boldsymbol{2E'}$, $\boldsymbol{A_1'}$, $\boldsymbol{A_2'}$) which are consistent with the 2H phase D3h space group symmetry. The observed phonon dispersion is consistent with previous theoretical studies [31, 43, 61-67]. With the application of uniaxial strain we observe a splitting of the doubly degenerate $\boldsymbol{E'}$ and $\boldsymbol{E''}$ modes in both materials, due to reduction of the crystal symmetry. The variation in the frequency of the Raman active modes with applied strain is plotted in Fig. 6.1-4(c,d). All modes red shift with uniaxial strain with the exception of the $\boldsymbol{A'}$ mode in WSe2 which shows a variation of 0.03 cm-1 per percent strain (see

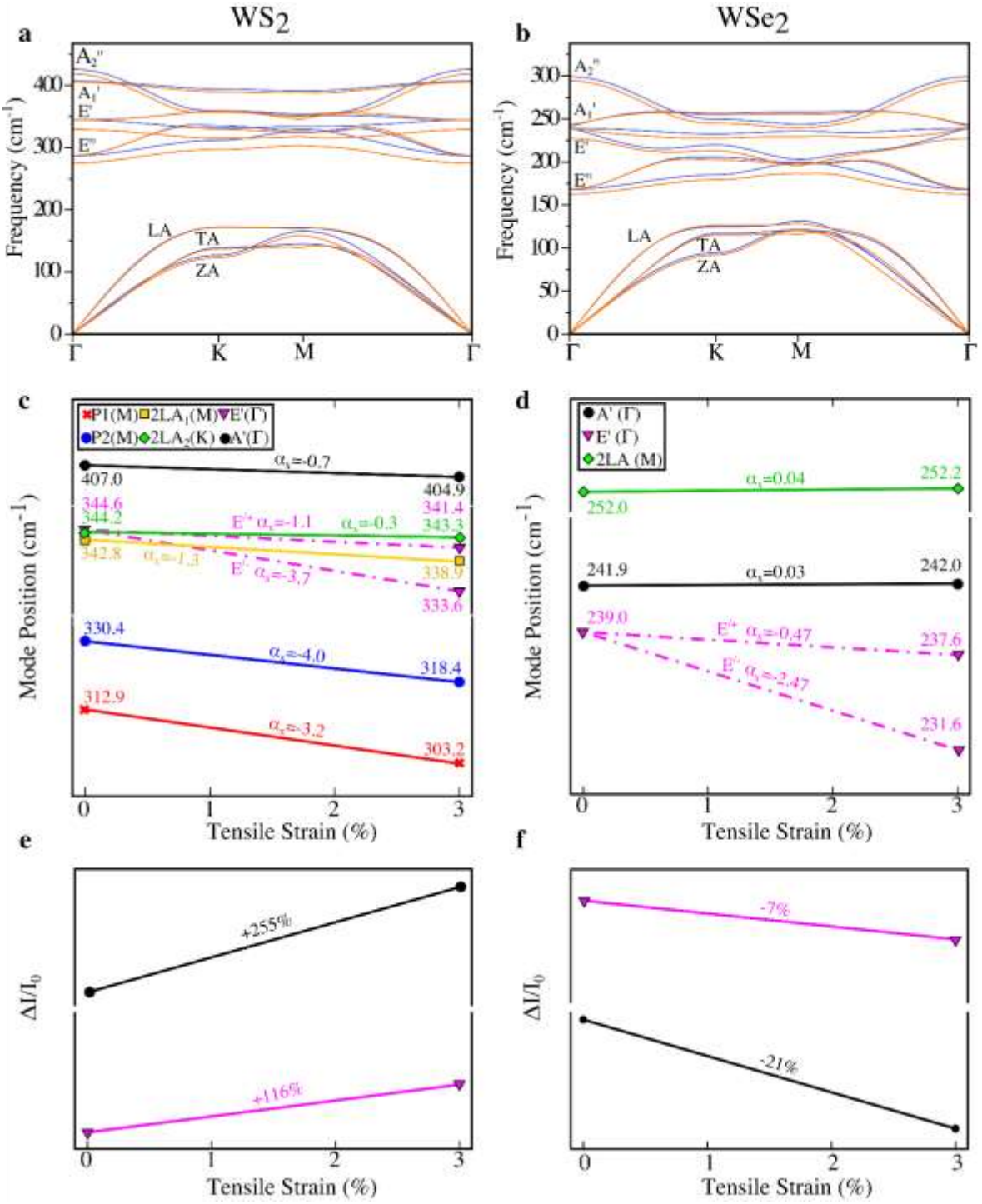

Figure 6.1-4 . Theoretical results on the vibrational properties of WS2 and WSe2 under strain. (a,b) Phonon dispersion curves. The blue and orange curves indicate unstrained (0%) and strained (3%) systems, respectively with the strain applied along armchair direction. Similar results have been obtained for zigzag directions (not shown). (c, d) Variation in mode frequencies with applied strain. In (c) P1 and P2 are defined at the M-point; and 2LA1 and 2LA2 are the M-point and K-point respectively, apart from E' and A' at Γ-point. In (d) 2LA is defined as M-point, and A' and E' at Γ-point. α shows curve slopes. Polarizations for WS2 and WSe2 are set on A' at parallel; and E' at cross-polarized. (e, f) Relative intensity change of the Raman active modes at Γ-point

figures S4 and S5 in Supplemental Material). The variations in mode frequency for WS2 are consistent with the experimental results shown in Fig. 6.1-3(b). We also calculated the Grüneisen parameters from the phonon dispersion relations at different k-points using $\boldsymbol{\gamma} = -(\boldsymbol{V}/\boldsymbol{\omega}(\boldsymbol{qv}))(\boldsymbol{\partial\omega}(\boldsymbol{qv})/\boldsymbol{\partial V})$ (see figure S6 in the Supplemental Material). The results obtained for the $\boldsymbol{E'}$ modes are 0.45 and 0.54 for WSe2 and WS2, respectively, which are in remarkable agreement with the experimental results. Interestingly, these $\boldsymbol{\gamma}$ values are well reproduced using a simple GGA approximation within the DFT functional. This is to be contrasted with other 2D materials such as hBN, where the exchange-correlation potential has to be fine-tuned to achieve a quantitative agreement with experiment [68].

To study the second order Raman active modes, we examine phonon dispersions at the edges of Brillouin Zone. The frequencies of peaks $\boldsymbol{P_1}$ and $\boldsymbol{P_2}$ are found to be consistent with the transverse optical (TO) $\boldsymbol{E''}$ and $\boldsymbol{E'}$ modes respectively [43]. To approximate the frequency of the $\boldsymbol{2LA}$ mode we multiply the frequency of the $\boldsymbol{LA}$ mode at the M-point of the Brillouin Zone by a factor of two, as this is a two-phonon process. An overall good agreement is seen between experimental and theoretical results with the exception of the $\boldsymbol{2LA(M)}$ mode of WSe2, which is increasing in wavenumber whereas experimental results show it to be decreasing. The smaller variation of this mode in the calculations is probably due to limitation in calculation of the second-order process.

In general, the intensity of a phonon mode in Raman spectrum depends both on the optical response of the material via the polarizability as well as the details of the electronic structure and electron-phonon coupling. All of these quantities evolve with applied strain. In our theoretical calculations, we examine the contribution of polarizability change with strain to the Raman intensity. In Fig. 6.1-4(e and f), the intensities of $\boldsymbol{A'}$ and $\boldsymbol{E'}$ modes show large increase in WS2,

and small reduction in WSe2 instead. Both of these are consistent with the experimental observations. Our results for mode frequencies, anharmonicities and polarizabilities give us insight into the nature of the chemical bond between the metal and chalcogen atoms. WS2 has larger phonon frequency by about factor of two with higher anharmonicities, that would be simply expected for lighter chalcogen atom. However, we also see from experiment that its polarizability is several times larger than that of WSe2. This can be explained by comparing the ionic character of the W-S bond with that of the W-Se bond. A Bader analysis performed for both systems with various strains shows that the charge transfer towards the chalcogenide atoms in the W-S and W-Se bonds is -0.80 electrons/unit cell, and -0.18 electrons/unit cell, respectively, at 0% strain. These magnitudes increase by 3.5% and 16.07% as 3% strain applied into WS2 and WSe2, respectively. This difference in the ionic character of the two bonds and their response to strain provides a simple picture for the evolution of Raman spectra in these compounds with strain.

An intriguing finding in our Raman spectra is the presence of the $\boldsymbol{A'}$ mode in the cross-polarization geometry at high strain shown in Fig. 6.1-3(a). From the symmetry perspective, the $\boldsymbol{A'}$ mode is not cross-polarized Raman active at zero strain when the unit cell is hexagonal. However, upon the application of strain the symmetry is lowered from hexagonal to monoclinic (for a generic strain direction), making the $\boldsymbol{A'}$ mode observable in the Raman spectrum (see Supplemental Material). In general, we expect the intensity of this mode to increase with the size of the monoclinic distortion which is proportional to applied strain. We investigate this in our theoretical calculations applied to the cross polarization geometry with the monoclinic unit cell. At zero strain we indeed find a complete suppression of the $\boldsymbol{A'}$ mode. At a strain of 3%, we observe a non-zero intensity for the $\boldsymbol{A'}$ mode, though its intensity is 99% lower in cross polarization when compared to the parallel polarization case. These results point to the role of large strains in actually modifying the symmetry of the lattice and thus changing selection rules. Such “strain engineering”

is a promising avenue to tune the opto-electronic properties of both the semiconducting and metallic monolayer transition metal dichalcogenides.

General Theoretical Methods:

Theoretical calculations were performed using the DFT formalism as implemented in the Vienna ab initio simulation package (VASP)[69, 70]. For the calculations of phonon modes, PHONON [71, 72] was used. A $2x2x1$ supercell was used for these calculations. This was increased to $3x3x1$ and there was no appreciable difference found in the Γ-point phonon frequencies. For the calculations of Raman band frequency, PHONON was used implementing the PEAD method. The PBE functional [73] was used along with the plane-wave cutoff of 800 eV combined with the projector-augmented wave (PAW) method [74, 75]. Atoms were allowed to relax under the conjugate-gradient algorithm until the forces acting on the atoms were less than $10^{-8}\ eV/A$. The self-consistent field (SCF) convergence was also set to $10^{-8}\ eV$. We employ an orthorhombic cell to apply uniaxial strain. Relaxed lattice constants were found to be $a = 3.187A$, $b = 5.52A$ for monolayer WS2 and $a = 3.319A$, $b = 5.750A$ for WSe2. A $20A$ vacuum space was used to restrict interactions between images. A $182x12x1$ gamma-centered k-grid was used to sample the Brillouin Zone for both systems. Our calculations neglect the effect of the substrate which can influence the electron-phonon coupling via screening.

First-Principle Ab Initio Calculations

Theoretical calculations were carried out on the n×n (n=1,2,3) orthorhombic cells for both WS2 and WSe2 (see Figure S3). The lattice constants were found to be a=3.187Å, b=5.520Å for

WS2 and a=3.319Å, b=5.750Å for WSe2. A 25Å vacuum space was used in all calculations. Strain was applied along of the armchair direction. There was no observed geometric transition from an orthorhombic unit cell to a monoclinic unit cell after the strain was applied. Even though, the high magnitudes of strain (>3.0%) can incidentally change the local symmetry of the atoms from D3h to a lower-symmetry group.

At zero strain, under cross polarization, both the P1 and A' mode are suppressed. When strain is applied to the system (~3.0%), we see an increment of the intensity from zero to 5x10-6 a.u. for the A' mode and 1x10-8 a.u. for the P_1 mode. The large difference in intensities between both modes (500 times) indicates that the P_1 mode is incredibly weak relative to A', which is almost at the numerical accuracy of the calculation. As a matter of fact, just the A' mode is experimentally observed at the high-strain regime (figure 3a in the main text), which fully corroborates the vibrational analysis performed. This suggests that large strain can indeed change the selection rules for the modes, even though their weak intensities may not be measured within the limit of resolution of the analyzer.

In general, major features of the strain dependence of the peak positions and intensities are in good agreement with our theoretical calculations. A comparison of the broad trends in the mode frequencies in WS2 and WSe2 can be explained on the basis of the difference between the chalcogen masses and the difference in the ionicity of the metal-chalcogen bond. We note that the detailed features of the spectra such as the splitting of the E' mode with strain depend on the details of the anharmonicity in the interatomic potentials.

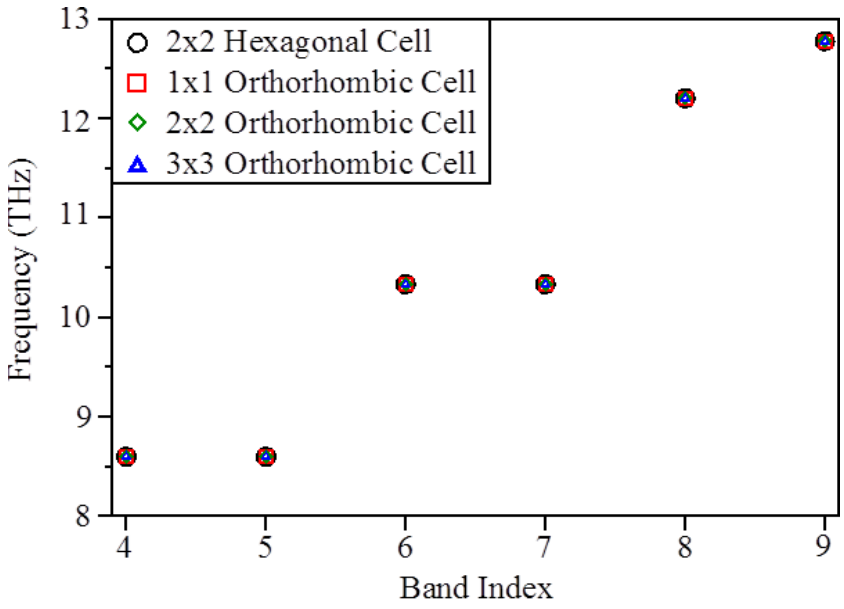

Figure 6.1-5 – Convergence of phonon frequencies with respect to the size of the supercell. As it can be seen, there is no change in the phonon frequency while changing the supercell size.

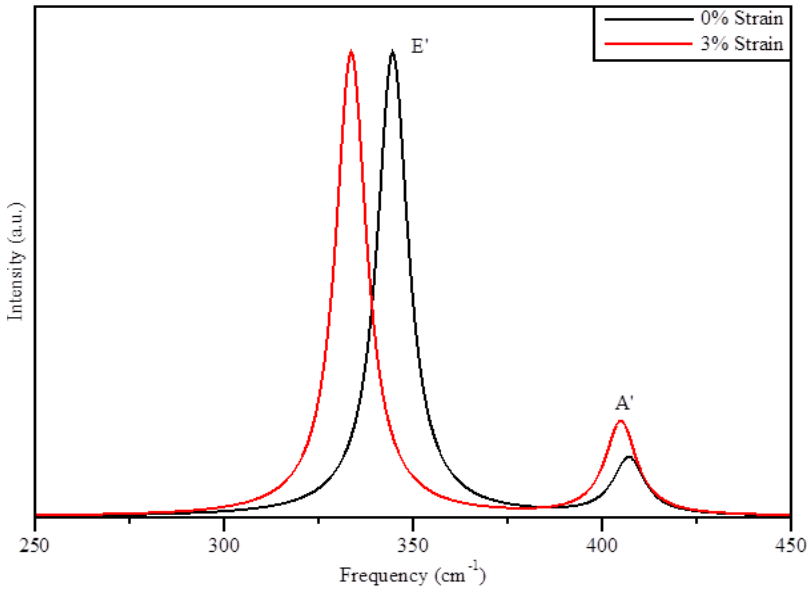

Figure 6.1-6 – Raman peaks for WS2 generated using a Gaussian smearing with the A' and E' modes labelled. As it can be seen both modes decrease in frequency with applied strain whilst the intensity increases.

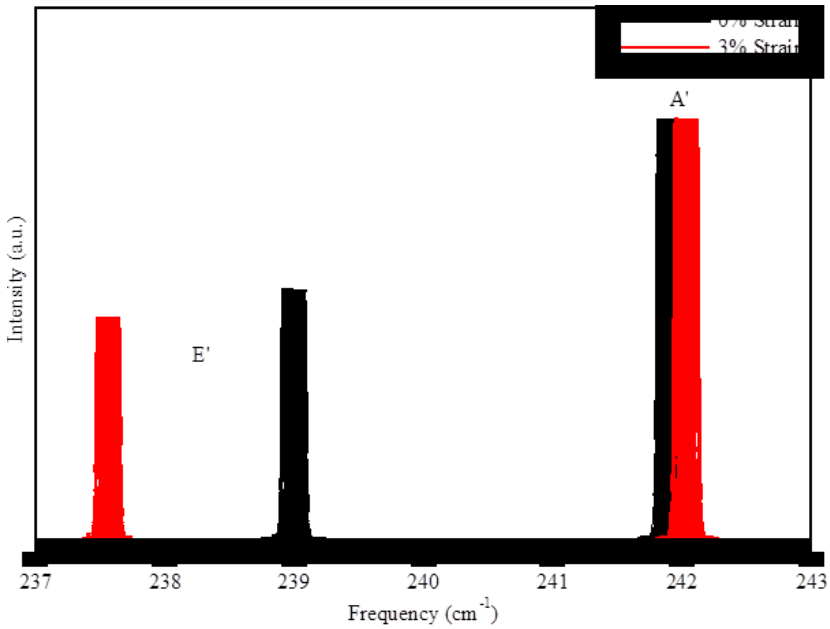

Figure 6.1-7 – Raman peaks for WSe2 generated using a Gaussian smearing with the ***A′*** and ***E′*** modes labelled. It can be seen that the e' mode decreases in frequency with applied strain whereas the A' mode increases in frequency. Both modes decrease in intensity with applied strain.

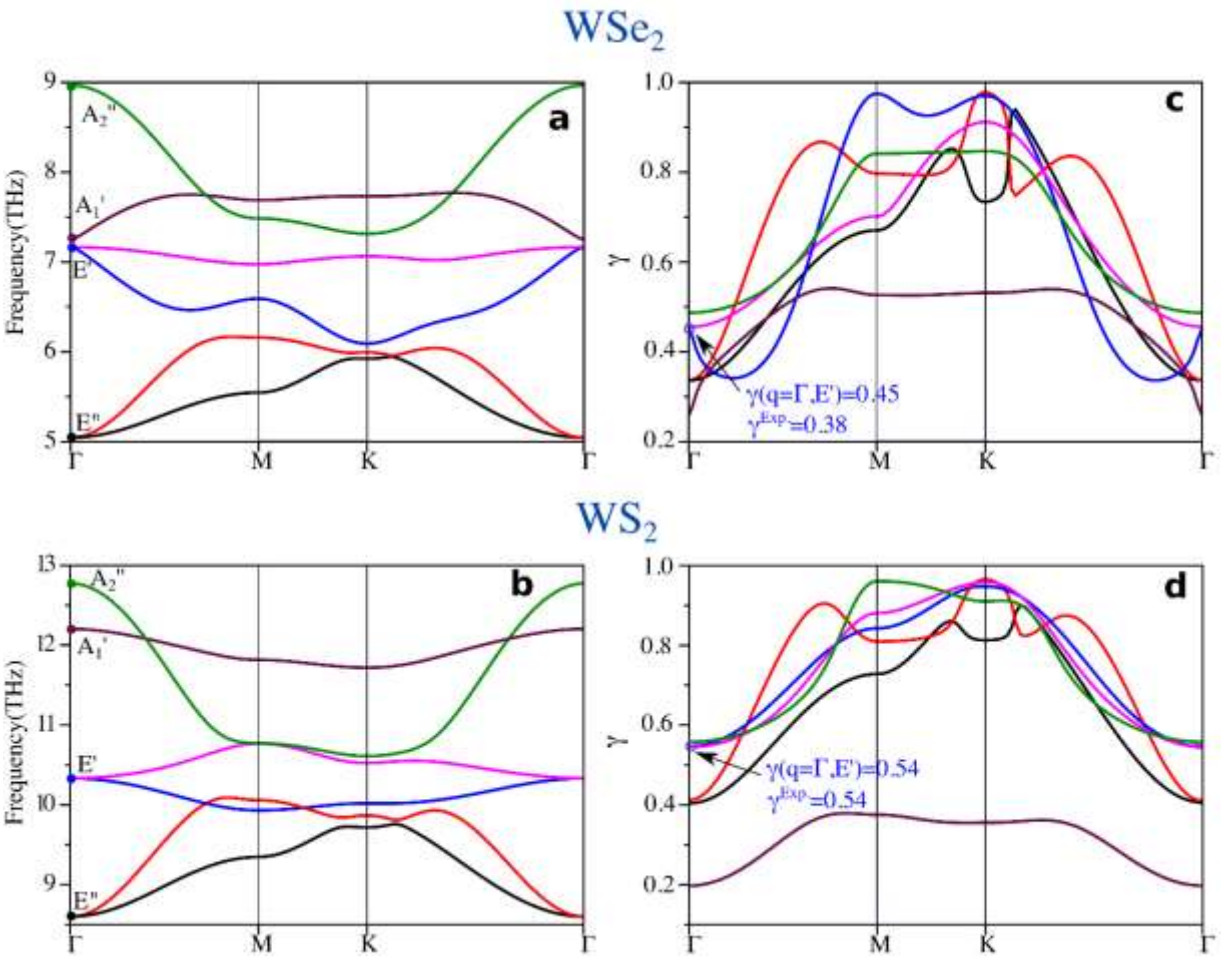

Figure 6.1-8 – (a,b) Phonon dispersion branches for optical modes (A_2'', A_1', E', E'') and their respective (c,d) Grüneisen parameters γ calculated along of Γ–M–K–Γ path for monolayer WSe2 and WS2. Modes are labeled according to their symmetries at Γ–point (filled dots) in a and b. The different colors correspond to different phonon branches, which follow the same labeling for γ. At Γ–point, the calculated values of the Grüneisen parameters are γ=0.45 and γ=0.54 for WSe2 and WS2, respectively. This is in remarkable agreement with the experimental results γExp.=0.38 (WSe2) and γ Exp.=0.54 (WS2).

6.2 Photoluminescence

In this part, I will present our data regarding photo luminescence (PL) studies. There are few sub chapters as following:

- Part 6.2.1 …. Monolayer WSe2 under tensile strain
- Part 6.2.2 …. Monolayer WS2 under tensile strain
- Part 6.2.3 …. Monolayer MoSe2 under tensile strain
- Part 6.2.4 …. Monolayer WSe2 under compressive strain
- Part 6.2.5 …. Bilayer WSe2 under tensile strain

We use our strain platform to apply tensile and compressive strains to the encapsulated TMDs to study their characteristics under strain.

6.2.1 – Monolayer WSe2 Under Tensile Strain

Fig. 6.2-1 shows PL studies of monolayer WSe2 under tensile strain in armchair direction. Intensity of PL signals increase by strain as it is shown in the inset. PL peaks are normalized to better illustrate their shapes and locations. All peaks monotonically redshift by strain as it is shown in Fig. 6.2-2. Interestingly, intensity also continuously and monotonically increase by applied strain. Meanwhile, Full Width at Half Maximum (FWHM) of the PL signals drastically decrease by strain up to about 2.5% then, start to increase.

Interestingly, by applying strain in zigzag direction, we observe splitting of peaks after 2.85% strain that is shown in Fig. 6.2-3 and 6.2-4. As it is shown in the figures, splitting happens by showing up a second peak which is higher in energy. These two peaks monotonically and linearly redshift by strain with the same slope. The intensity of PL signals grows until the splitting occur in which the intensity of low energy peak starts decreasing while, the intensity of high energy peaks grows by strain after splitting. Total photo luminescence area – considering both peaks keeps linearly increase by strain which reveal that the intensity of low energy peak decrease by increasing intensity of high energy peak. Fig. 6.2-5 shows the real PL under strain which are un-normalized data to demonstrate how the second peak starts showing up.

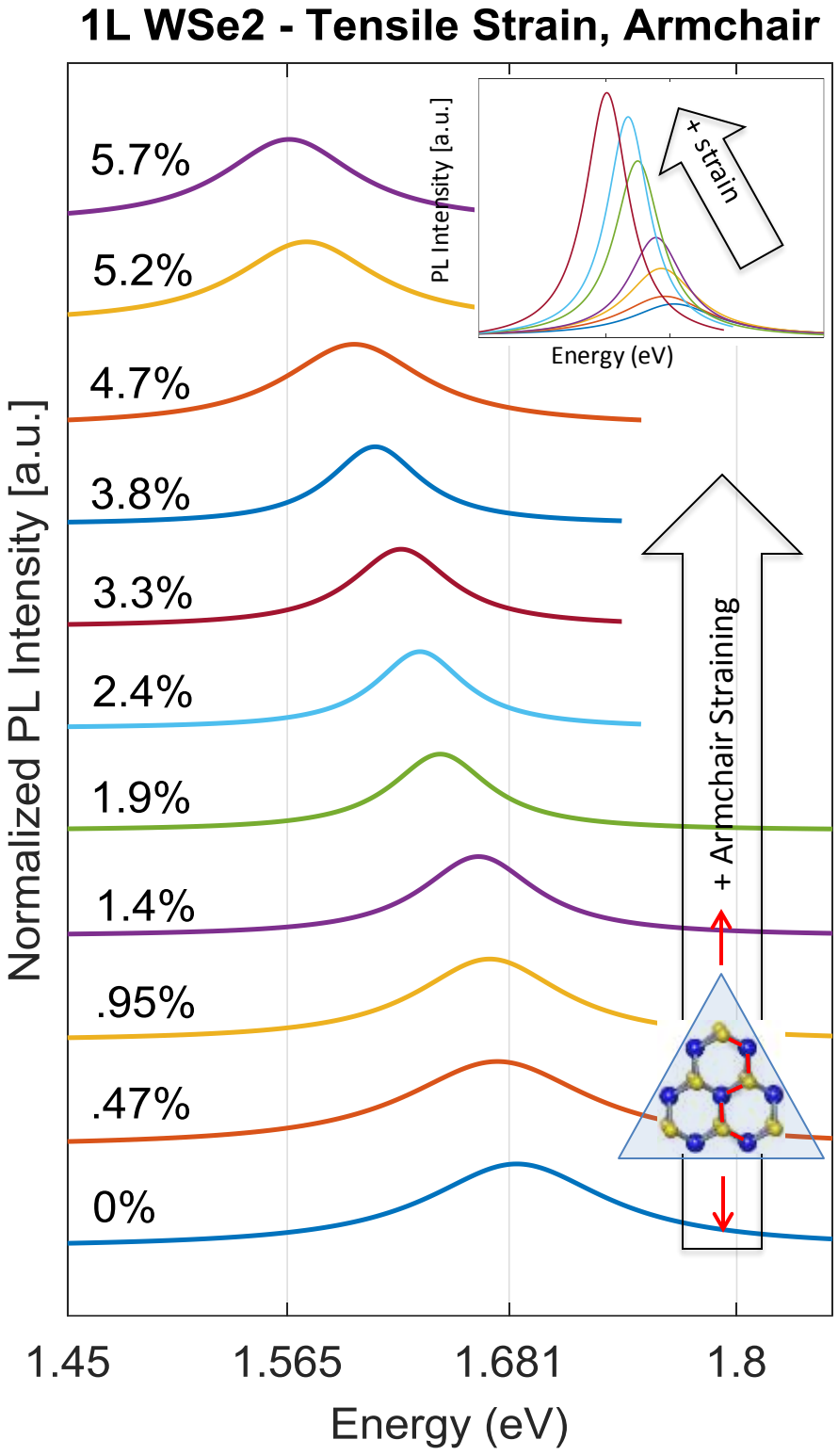

Figure 6.2-1 – PL studies of WSe2 monolayer under tensile strain in armchair direction. PL signals are normalized to their maximum intensities and shifter in y-direction for better illustration. Inset: normal PL – not normalized to demonstrate the intensity change.

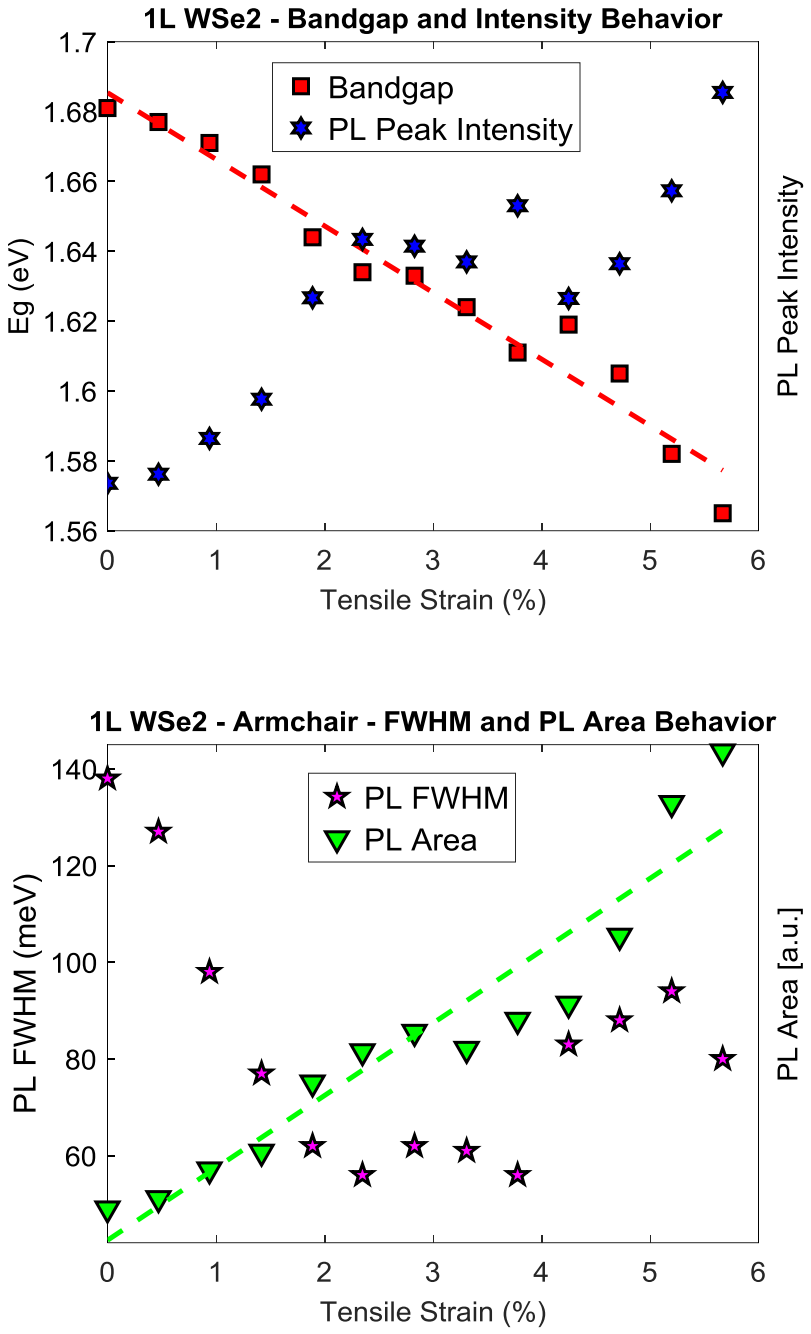

Figure 6.2-2 – PL signals processing of WSe2 monolayer under tensile strain in armchair direction. Continuous and linear bandgap redshift and continuous monotonic intensity increase by tensile strain (top). Drastic decrease of FWHM until 2.5% then slow increase after under tensile strain.

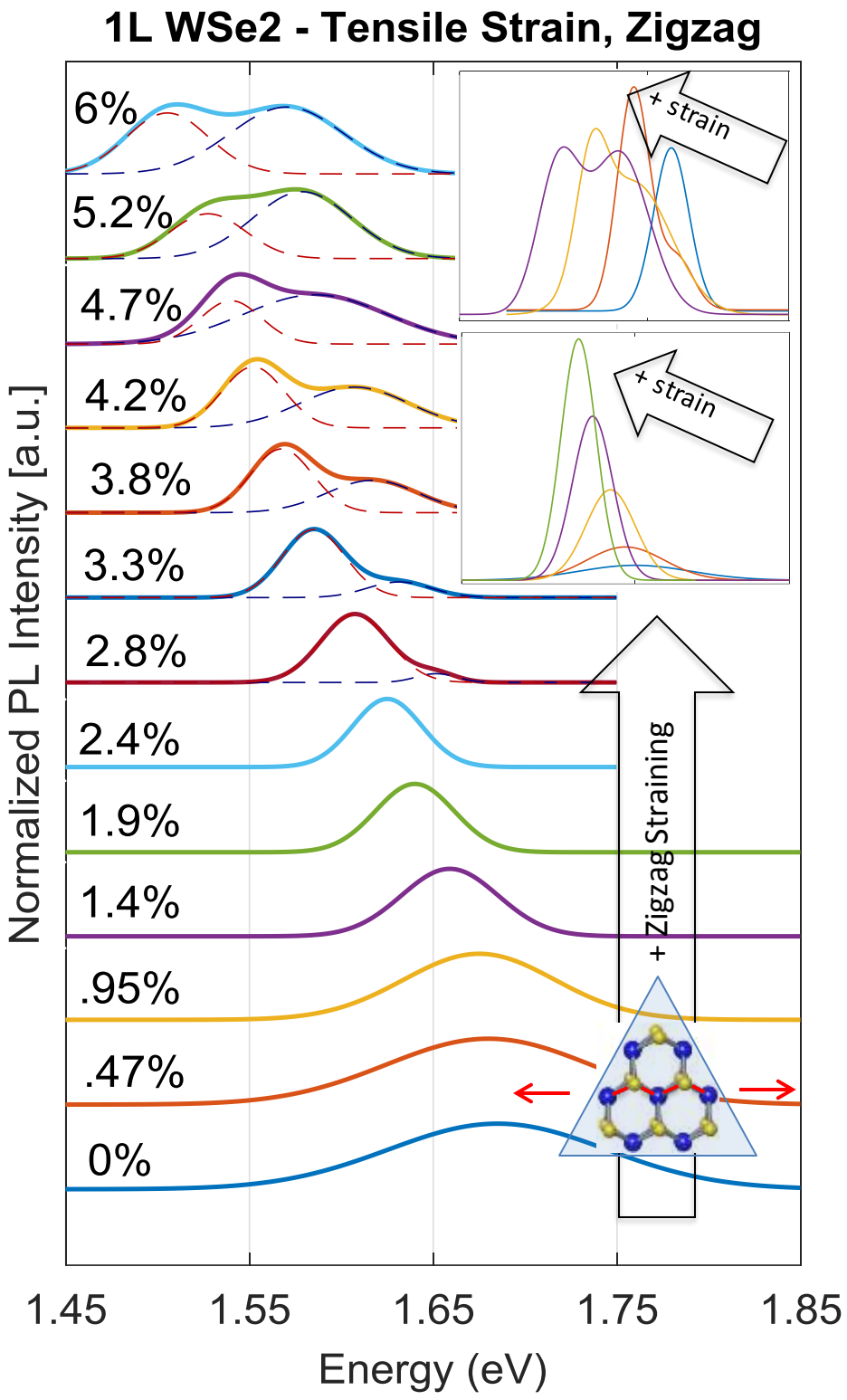

Figure 6.2-3 – PL studies of WSe2 monolayer under tensile strain in zigzag direction. PL signals are normalized to their maximum intensities and shifter in y-direction for better illustration. We observe PL signals splitting at 2.85% strain when a second peak starts showing up. Bottom inset: normal PL – not normalized before splitting, and top inset: after splitting - to demonstrate the intensity change.

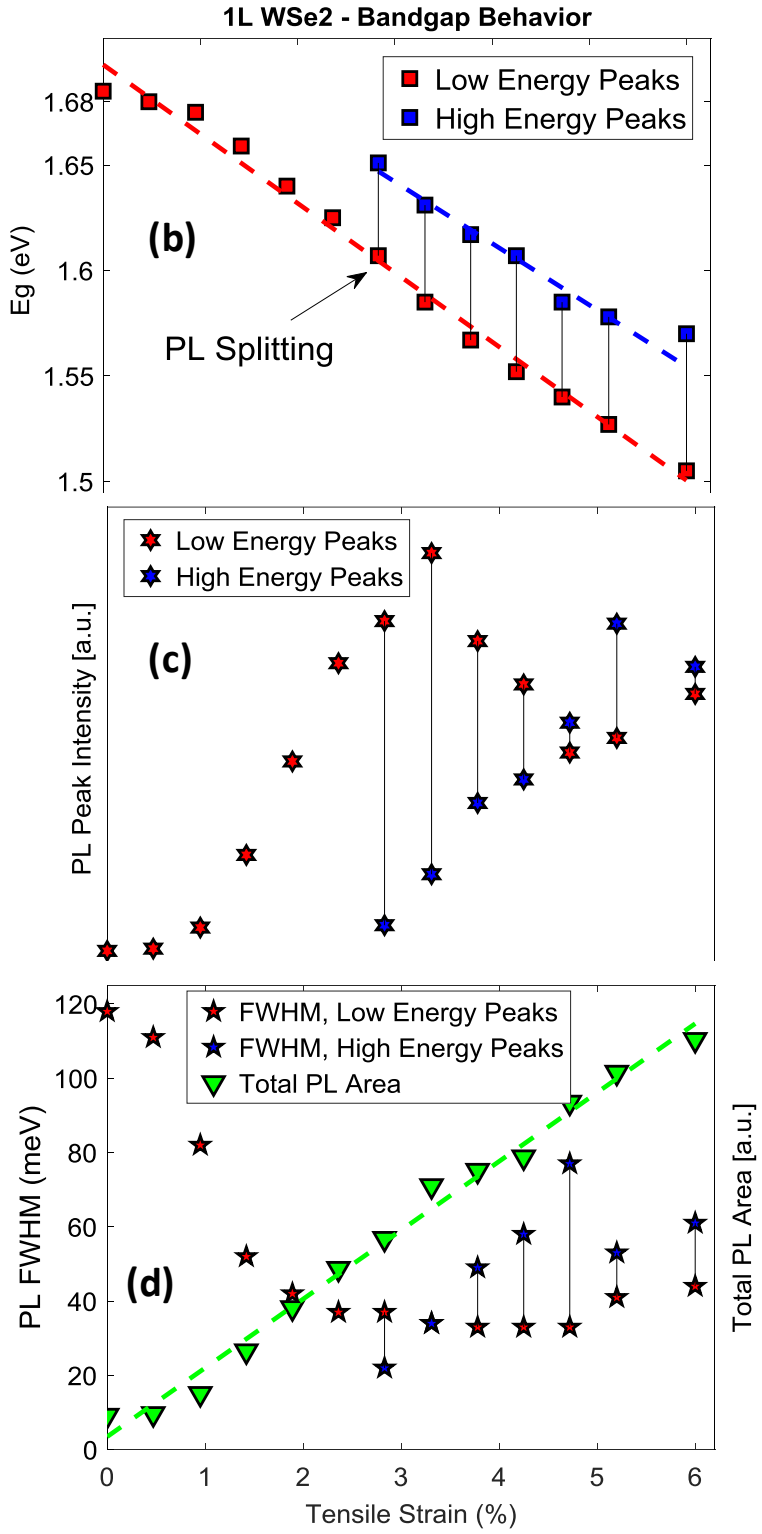

Figure 6.2-4 – PL signals processing of WSe2 monolayer under tensile strain in zigzag direction. Continuous and linear bandgap redshift until 2.85% in which the splitting is observed by showing up another peak which redshifts with the same slope with strain (top). (Middle): PL peak intensity increase by strain until the second peak (high energy peak) shows up at which the intensity of low energy peak decrease while the intensity of high energy peak increase. (Bottom): total PL area increase linearly by strain. Meanwhile, FWHM decrease until splitting happens in which the FWHM of the high energy peak grows by strain.

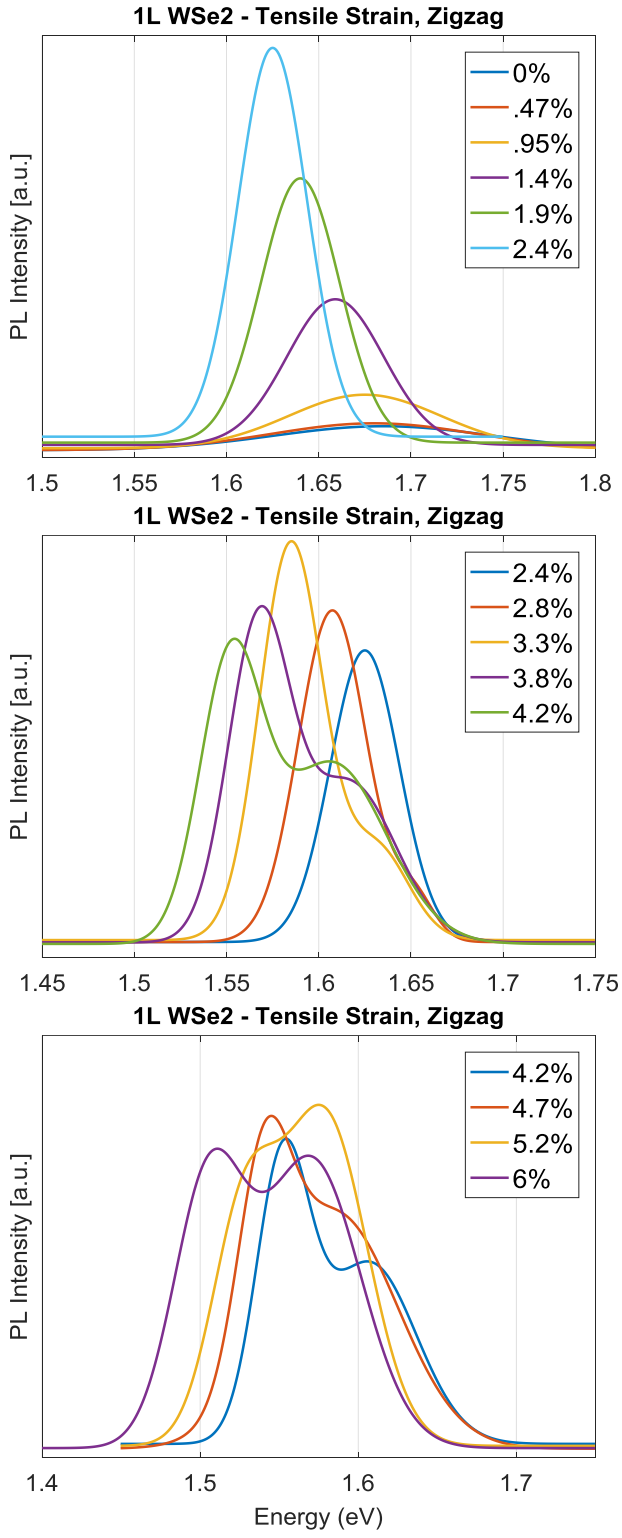

Figure 6.2-5 – PL studies of WSe2 monolayer under tensile strain in zigzag direction. PL signals are not normalized to better illustrate the splitting which happens at 2.85%. (Top): PL under strain 0-2.4%. (Middle): PL under strain 2.4%-4.2%. At 2.85% splitting is observed by showing up another high energy peak. (Bottom): PL under strain 4.2% - 6%.

6.2.2 – Monolayer WS2 Under Tensile Strain

Fig. 6.2-6 shows PL studies of monolayer WS2 under tensile strain in armchair direction. Intensity of PL signals increase by strain as it is shown in the inset. This is similar behavior comparing with WSe2 under armchair straining. PL peaks are normalized to better illustrate their shapes and locations. All peaks monotonically redshift by strain as it is shown in Fig. 6.2-7. Interestingly, intensity also continuously and monotonically increase by applied strain. Meanwhile, Full Width at Half Maximum (FWHM) of the PL signals drastically decrease by strain up to about 2.5% then, start to increase.

Interestingly – similar to WSe2 monolayers - shown in section 6.2.1, by applying strain in zigzag direction to WS2, we observe splitting of peaks after 2.85% strain that is shown in Fig. 6.2-8 and 6.2-9.

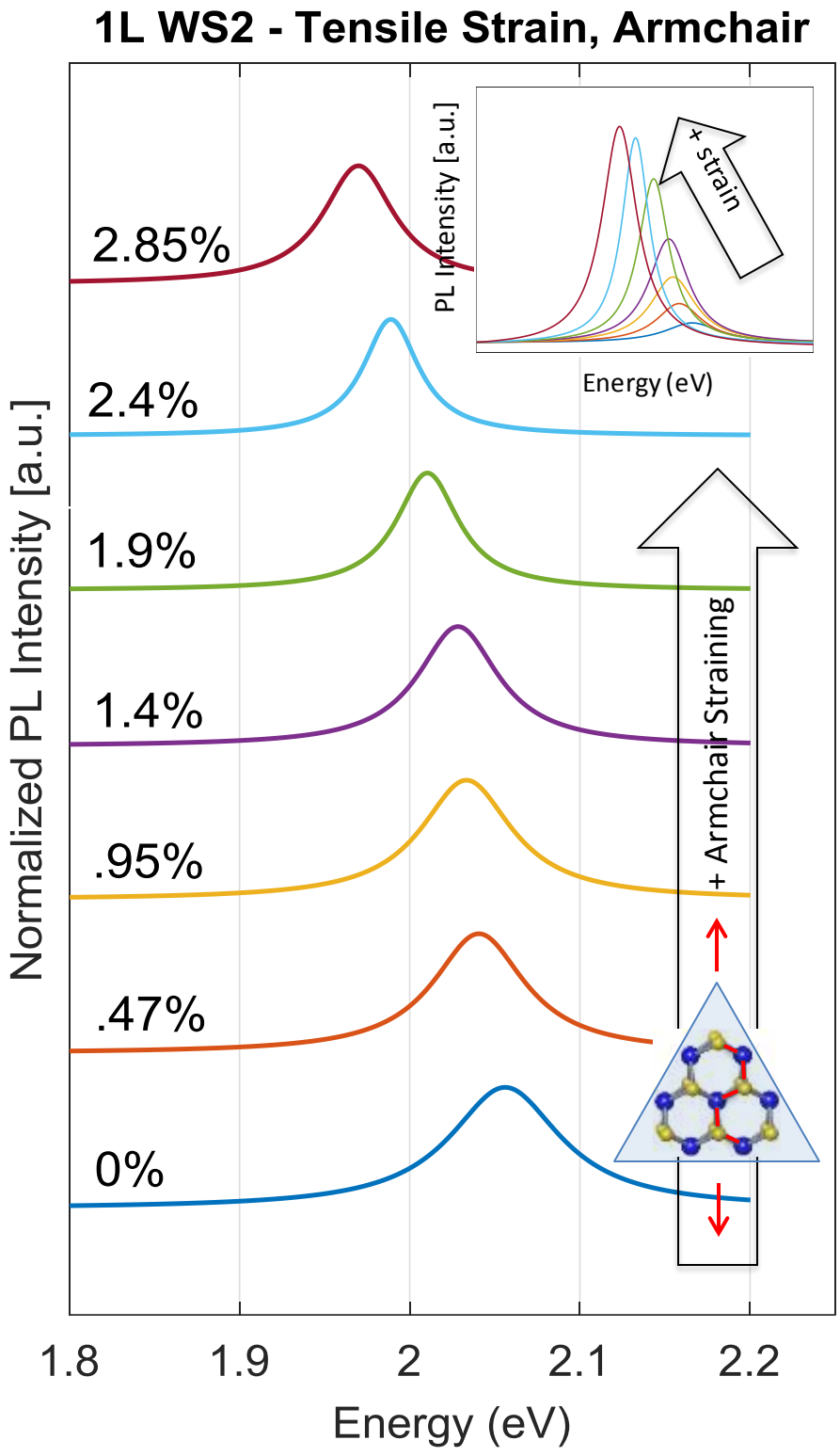

Figure 6.2-6 – PL studies of WS2 monolayer under tensile strain in armchair direction. PL signals are normalized to their maximum intensities and shifter in y-direction for better illustration. Inset: normal PL – not normalized to demonstrate the behavior of intensity change under strain.

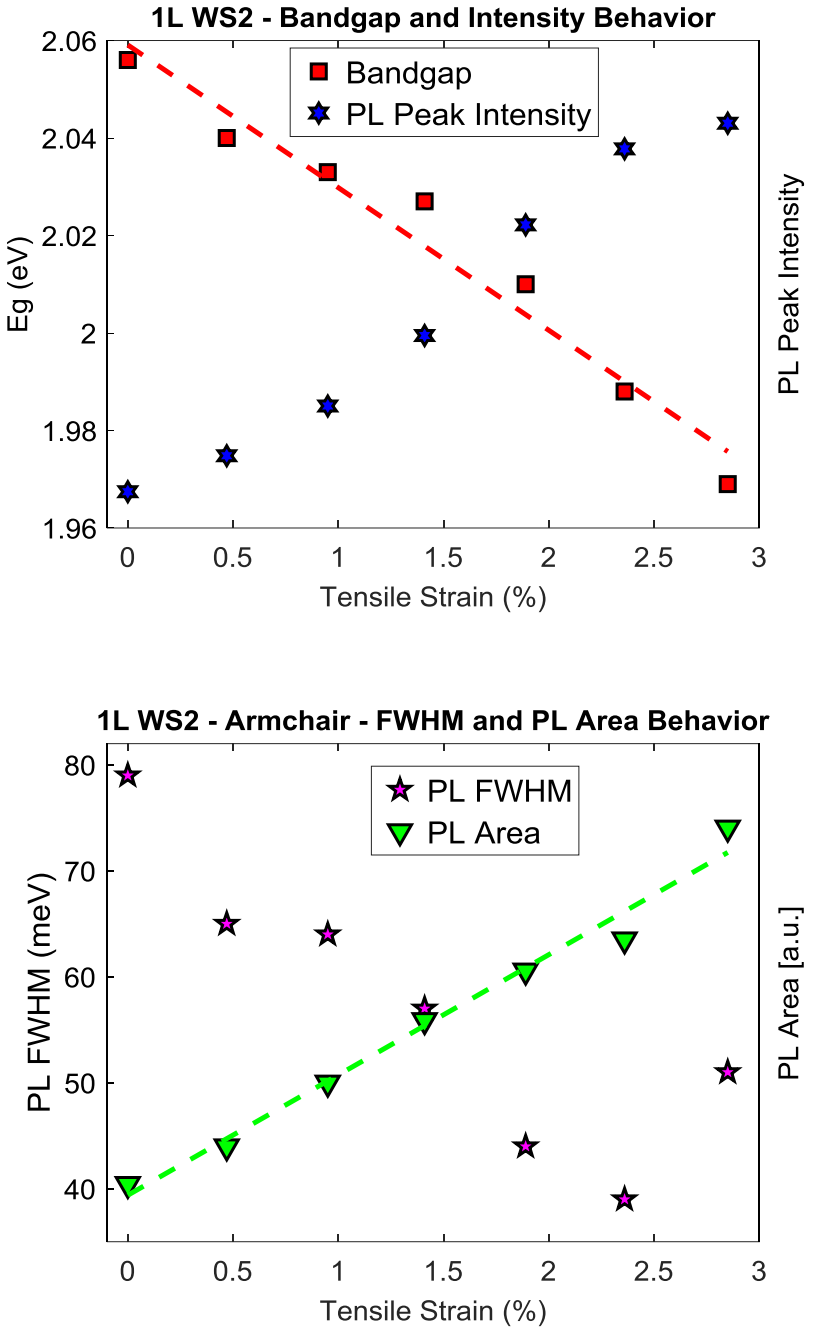

Figure 6.2-7 – PL signals processing of WS2 monolayer under tensile strain in armchair direction. Continuous and linear bandgap redshift and continuous monotonic intensity increase by tensile strain (top). Drastic decrease of FWHM until 2.5% then slow increase after, under tensile strain.

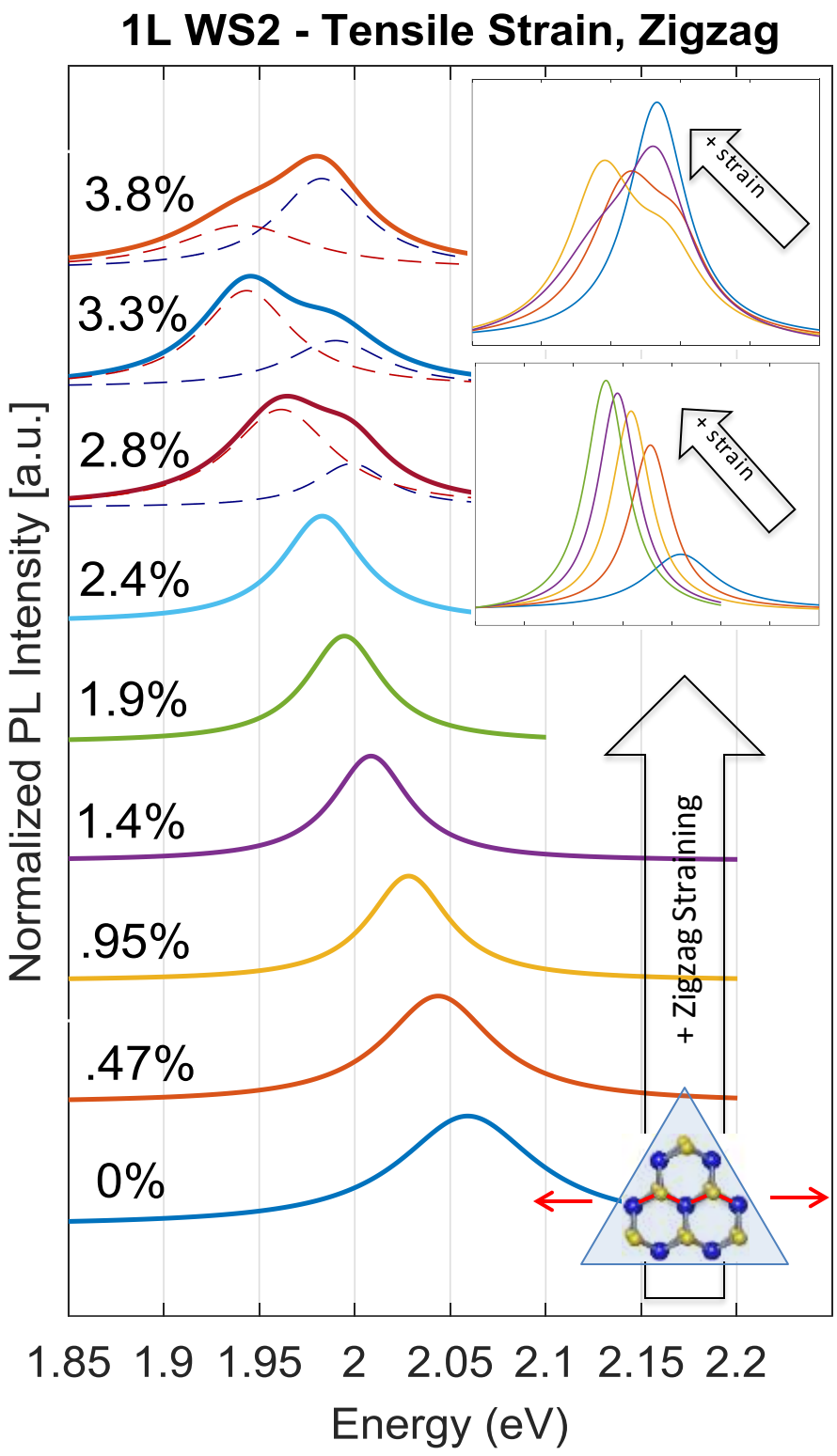

Figure 6.2-8 – PL studies of WS2 monolayer under tensile strain in zigzag direction. PL signals are normalized to their maximum intensities and shifter in y-direction for better illustration. We observe PL signals splitting at 2.85% strain when a second peak starts showing up – similar results as WSe2 under zigzag strain. Bottom inset: normal PL – not normalized before splitting, and top inset: after splitting - to demonstrate the intensity change.

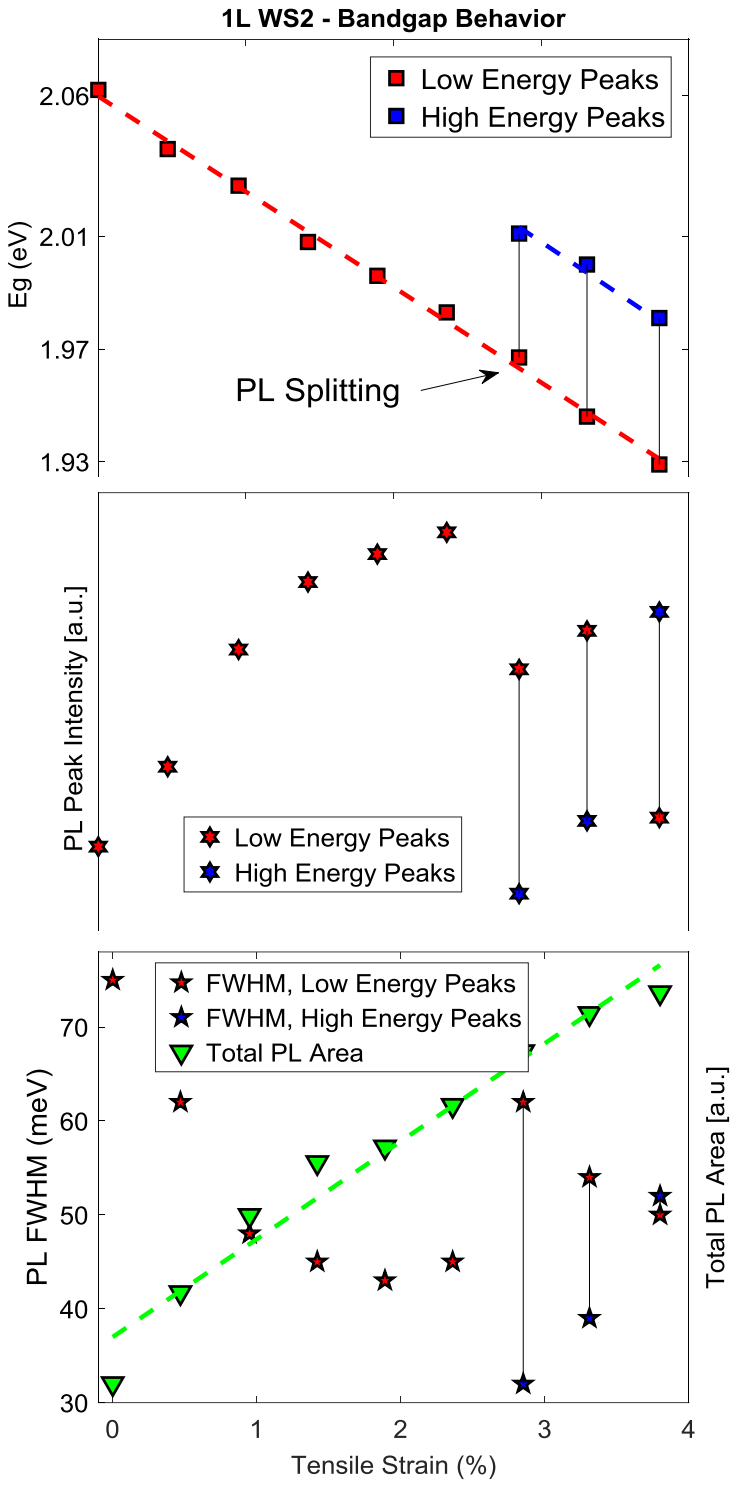

Figure 6.2-9 – PL signals processing of WS2 monolayer under tensile strain in zigzag direction. Continuous and linear bandgap redshift until 2.85% in which the splitting is observed by showing up another peak which redshifts with the same slope with strain (top). This is similar to WSe2 monolayers when they are strained in zigzag direction. (Middle): PL peak intensity increase by strain until the second peak (high energy peak) shows up at which the intensity of low energy peak decrease while the intensity of high energy peak increase. (Bottom): total PL area increase linearly by strain. Meanwhile, FWHM decrease until splitting happens in which the FWHM of the high energy peak grows by strain.

6.2.3 – Monolayer MoSe2 Under Tensile Strain

We are specifically interested in this material since it is a TMD with different metal (molybdenum) – instead of other two TMDs which are tungsten based. Fig. 6.2-10, 6.2-11, 6.2-12, 6.2-13 show PL studies of monolayer MoSe2 under tensile strain in armchair and zigzag directions.

Interestingly, this material shows identical properties for both directions. With that said, we observe PL splitting at both directions and at 2.85% - the same strain that we observe splitting at zigzag direction for WSe2 and WS2.

Another interesting difference between MoSe2 and WSe2, WS2 is the intensity behavior. As you see the intensity increase for WSe2 and WS2 by applying strain. In contrary, for MoSe2, intensity monotonically decrease by strain which is an opposite characteristic.

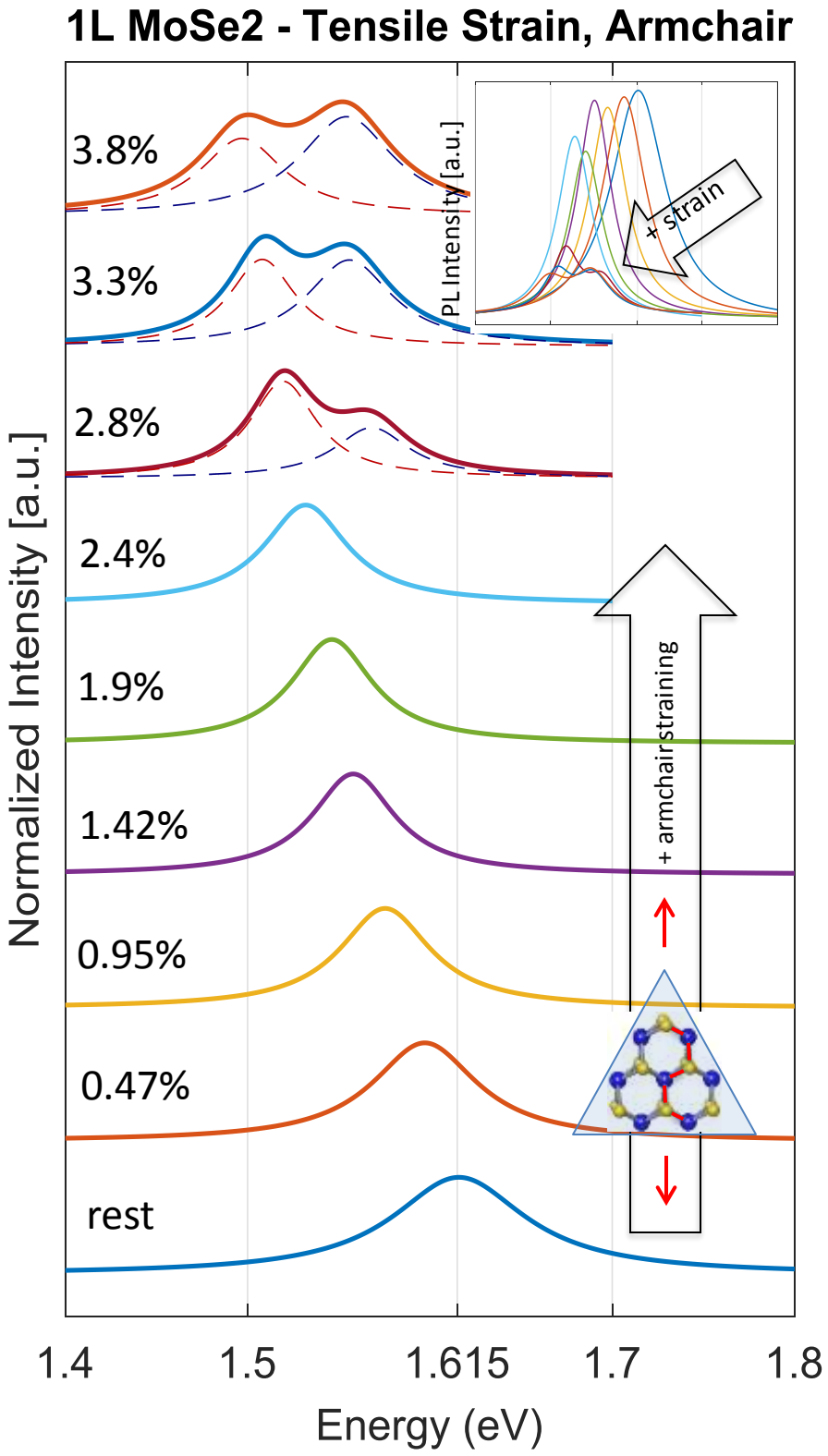

Figure 6.2-10 – PL studies of MoSe2 monolayer under tensile strain in armchair direction. PL signals are normalized to their maximum intensities and shifted in y-direction for better illustration. We observe PL signals splitting at 2.85% strain when a second peak starts showing up – similar results for straining in zigzag direction. Inset: normal PL – not normalized - to demonstrate the intensity change.

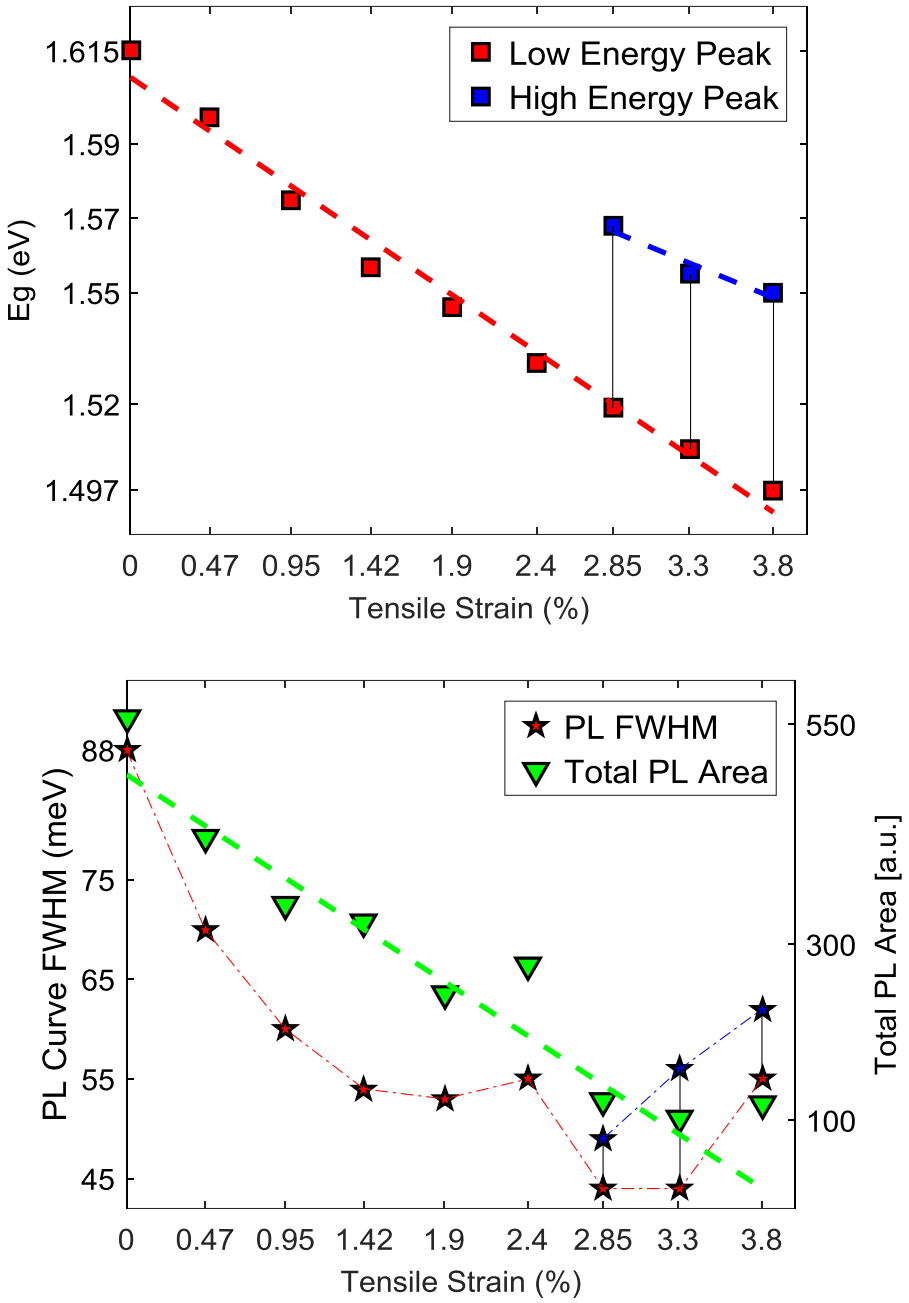

Figure 6.2-11 – PL signals processing of MoSe2 monolayer under tensile strain in armchair direction. (Top): Continuous and linear bandgap redshift until 2.85% in which the splitting is observed by showing up another peak with higher energy which redshifts with the same slope with strain. (Bottom): total PL area increase linearly by strain. Meanwhile, FWHM decrease until splitting happens in which the FWHM of the high energy peak grows by strain.

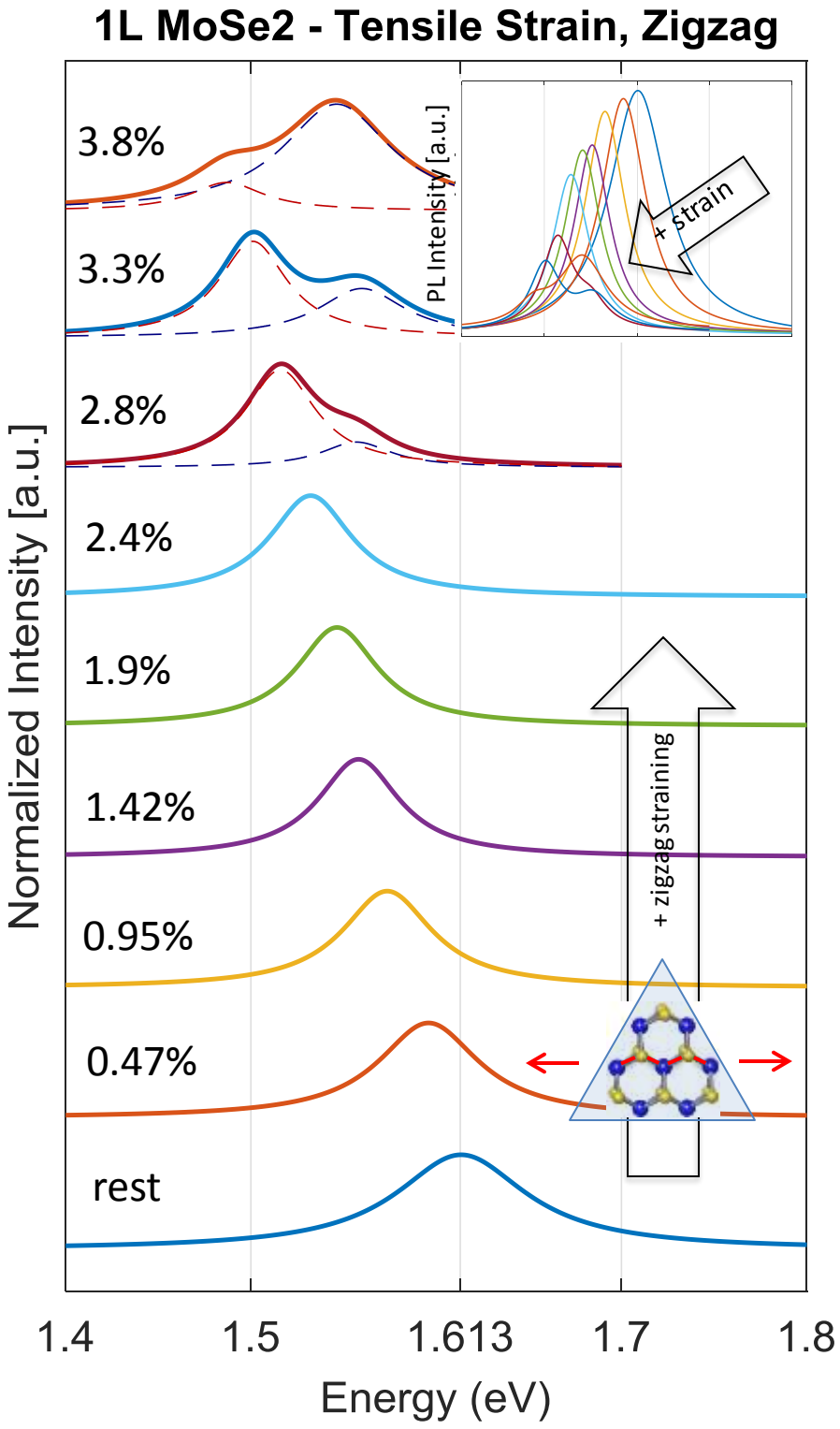

Figure 6.2-12 – PL studies of MoSe2 monolayer under tensile strain in zigzag direction. PL signals are normalized to their maximum intensities and shifted in y-direction for better illustration. We observe PL signals splitting at 2.85% strain when a second peak starts showing up – similar results for straining in armchair direction. Inset: normal PL – not normalized - to demonstrate the intensity change.

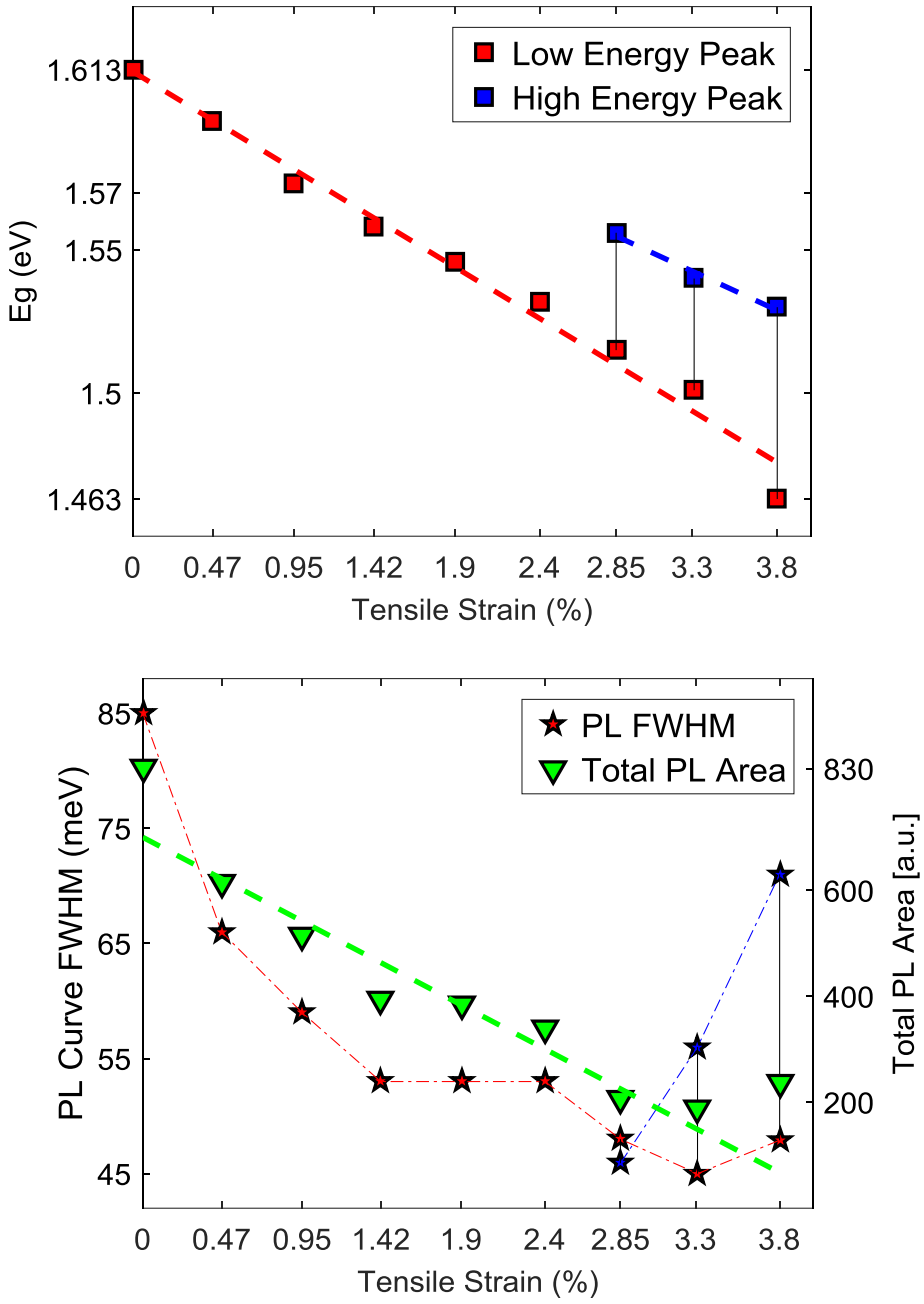

Figure 6.2-13 – PL signals processing of MoSe2 monolayer under tensile strain in zigzag direction. (Top): Continuous and linear bandgap redshift until 2.85% in which the splitting is observed by showing up another peak with higher energy which redshifts with the same slope with strain – similar result as observed in armchair direction. (Bottom): total PL area increase linearly by strain. Meanwhile, FWHM decrease until splitting happens in which the FWHM of the high energy peak grows by strain – identical results comparing to armchair direction.

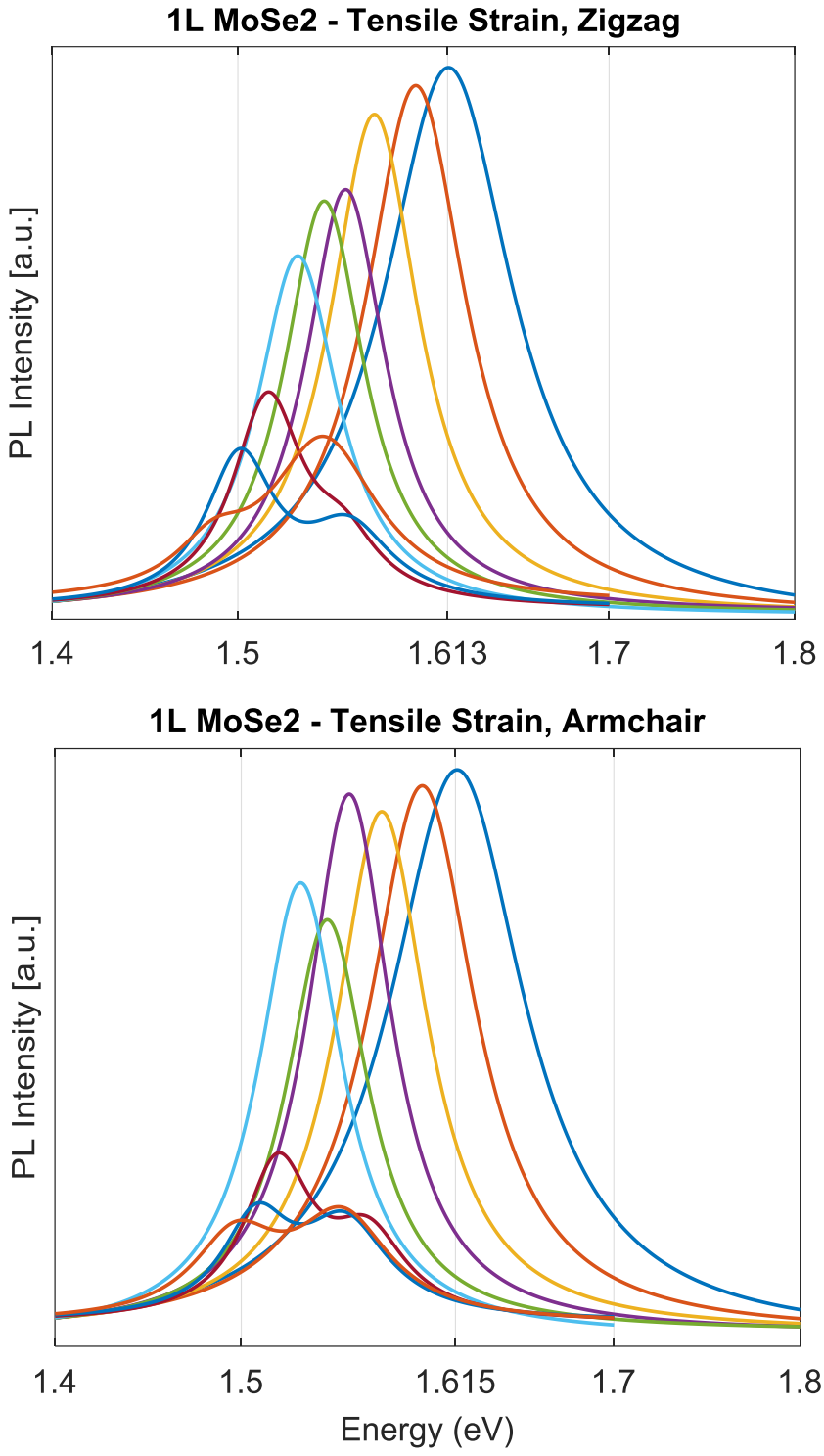

Figure 6.2-14– PL spectrums of monolayer MoSe2 under tensile strain, not-normalized. Graphs not normalized to better illustrate the intensity change before and after splitting. (Top): zigzag direction, (bottom): armchair direction

6.2.4 – Monolayer WSe2 Under Compressive Strain

In order to confirm the results we've got for tensile strain of WSe2, we can apply compressive strains as explained in chapter 4. By flipping over the polymer our polymer substrate, and bending in z-direction, we will be able to apply compressive strain since the device will be under neutral axis. For more information, please refer to chapter 4.

In order to focus laser spot and do experiments, we need to optically find the desired TMD flake inside polymer stack which is not trivial for flipped samples. Then we washed the tope polymer in order to minimize reflection from the substrate and then shined the laser from the back side while checking for the best focus. As a result, we could apply limited strain because of lack of top polymer. The limited strain for armchair direction was -1.65% maximum, while for the zigzag direction, it was -1.2%.

Fig. 6.2-15 and 6.2-16 show PL data for zigzag and armchair direction under compressive strains. PL signals blue-shifts with applied compressive strain. In addition, PL intensity decrease while FWHM of PL signals increase with compressive strains. These data are exactly in contrary with the data for WSe2 under tensile strains.

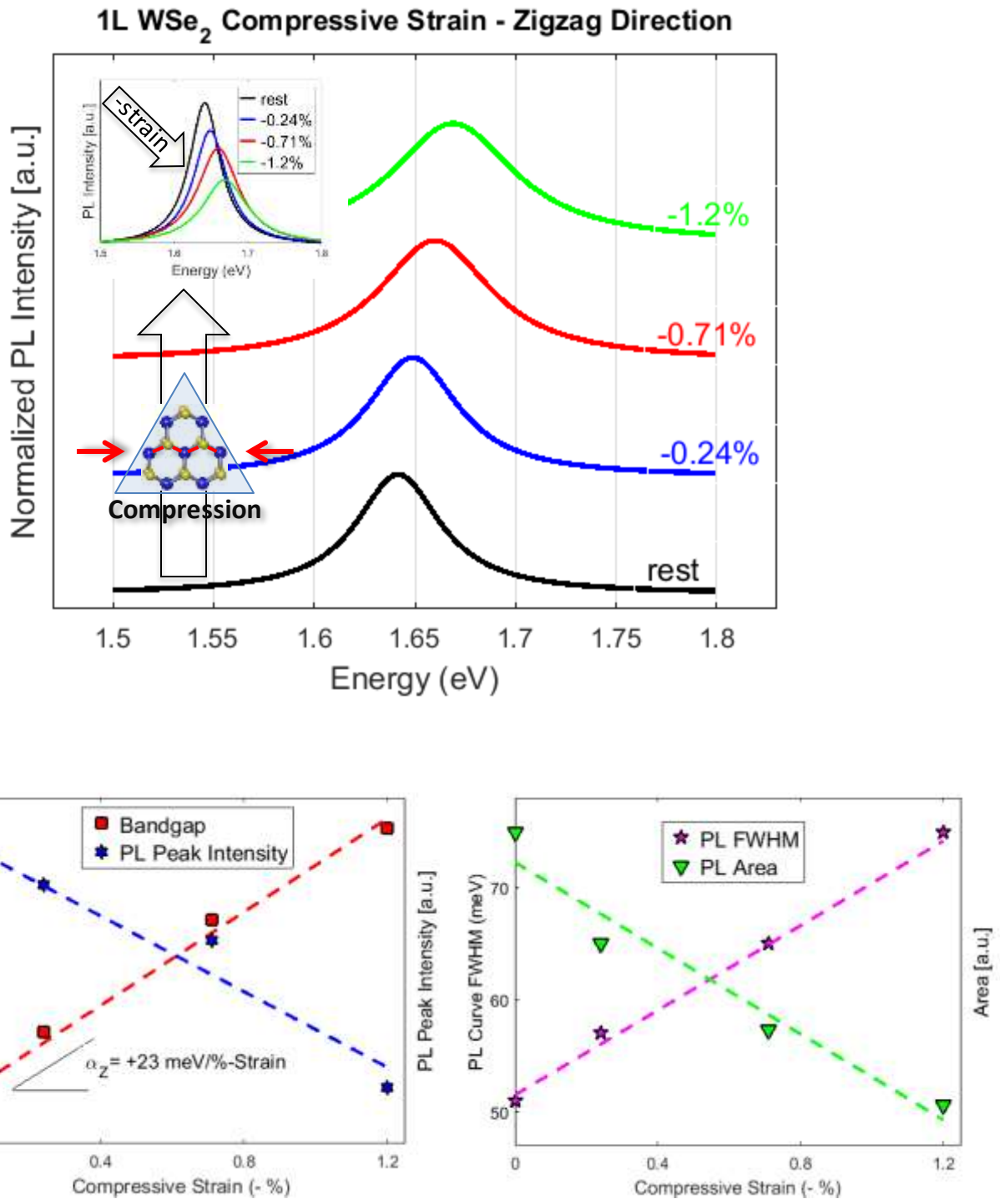

Figure 6.2-15 – PL signals processing of WSe2 monolayer under compressive strain in zigzag direction. Results show opposite behaviors with compare to tensile strains. These opposite behaviors include: bandgap blue shift, intensity decrease by compressive strain and FWHM increase.

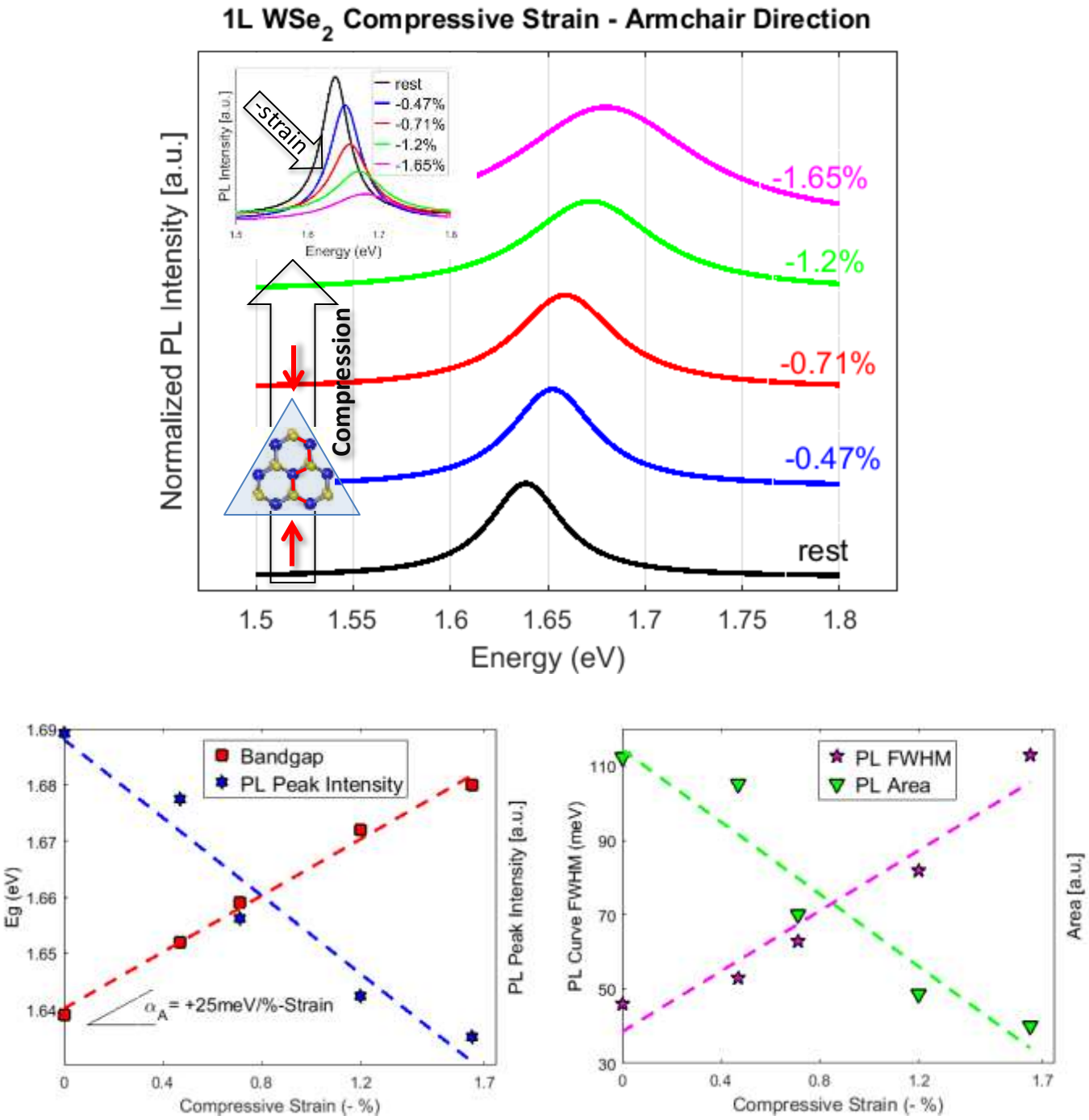

Figure 6.2-16 – PL signals processing of WSe2 monolayer under compressive strain in armchair direction. Results show opposite behaviors with compare to tensile strains. These opposite behaviors include: bandgap blue shift, intensity decrease by compressive strain and FWHM increase.

Conclusion:

The scientific reasons of splitting needs to be investigated more in details. We speculate trions are involved in splitting [76]. We used our CVD grown WSe2 monolayer samples and measured the photoluminescence at different doping levels to compare the results with the mentioned reference. Fig. 6.2-17 shows the photoluminescence data of WSe2 with different back gate doping drawn on the picture from that reference. Fig. 6.2-18 is from the mentioned reference in which shows the trions and excitons for WSe2 and MoSe2. As it is clear from the image, there is about 50 meV energy difference between trions and neutral excitons. In addition, it is shown in the reference that neutral excions are not observable when we have doping. Comparing our PL data measured at various cryogenic temperatures, those values are very closed to the PL we measured in our samples. Then we believe those peaks we observe in WSe2 – for instance, are trion peaks and when we apply strain, the samples become less-doped or p-doped in which the n-doping level decreases and paves the way to neutral excitons to show up that we see it at 2.8% strain.

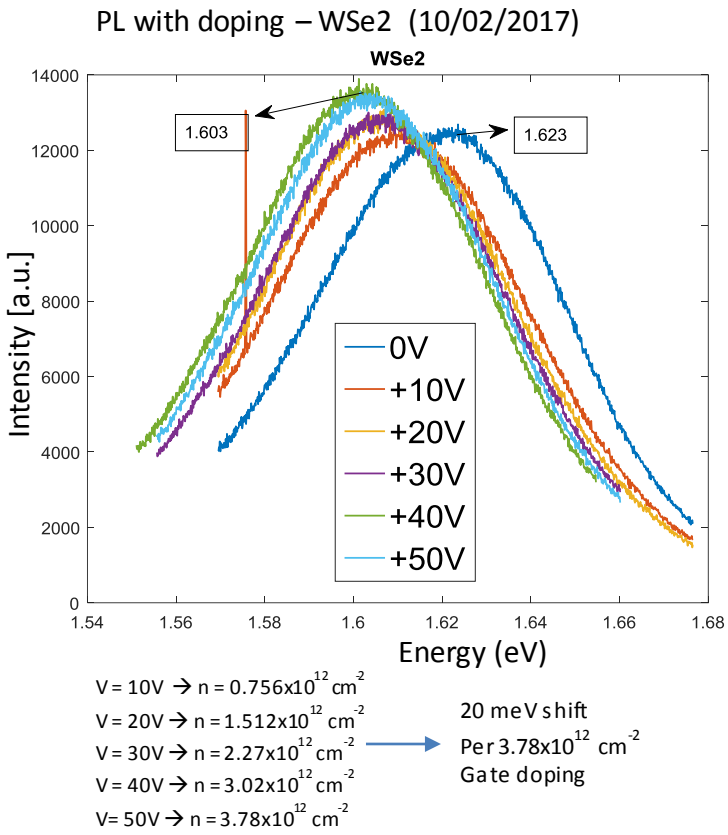

Figure 6.2-17 – Photoluminescence results of WSe2 samples at room temperature under various back gate doping. Data unveils 20 meV bandgap redshift for 50 V back gate doping which is about 3.78×10^{12} cm^{-2} electrons density.

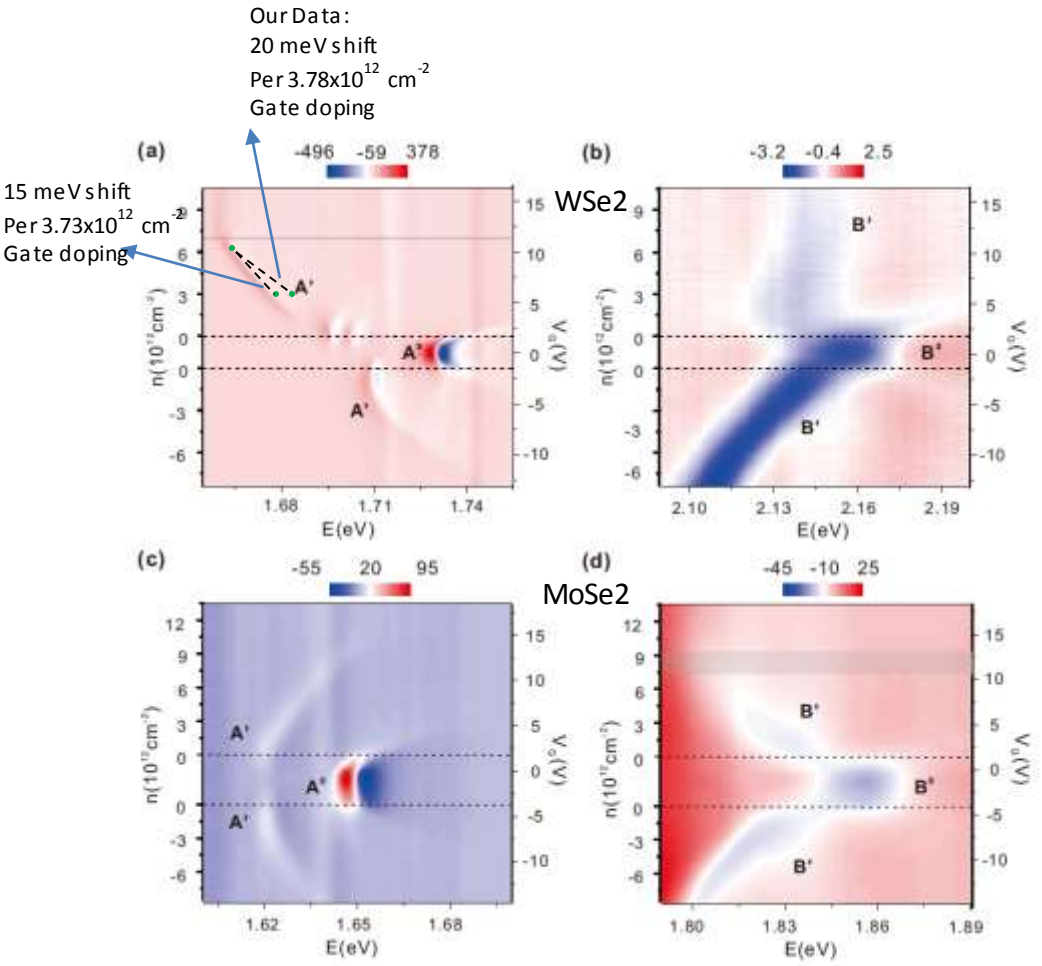

Figure 6.2-18 – main image from reference [76]. Our data matches with the trions data of the reference. We believe at zero strain; we observe only trions. Then doping effects diminish by strain until we observe neutral excitons.

6.2.5 – Bilayer WSe2 Under Tensile Strain

Bilayer TMDs have two peaks in their photoluminescence spectrums which correspond the direct bandgap at *K* point and indirect transition from Σ to *K* point. These are studies in the literature that is claimed that straining bilayer samples makes the sample exhibit direct bandgap [47]. A summary of these results are shown in Fig. 6.2-17.

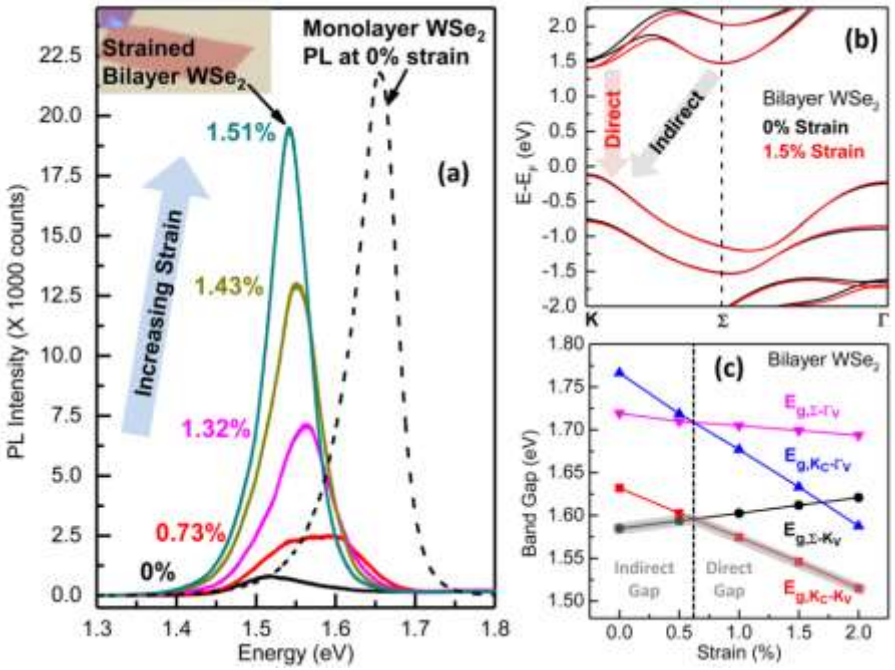

Figure 6.2-17 [47]– PL signals processing of WSe2 monolayer under compressive strain in armchair direction. Results show opposite behaviors with compare to tensile strains. These opposite behaviors include: bandgap blue shift, intensity decrease by compressive strain and FWHM increase.

In this literature it is claimed that after about 0.5% strain, the photoluminescence transits from indirect to direct bandgap.

In this section, we would like to apply higher strains to bilayer WSe2 to investigate the distinctions to this literature when apply higher strains. Fig. 6.2-18 shows the PL spectra under

armchair directions. Fig. 6.2-19 shows the peaks position and intensities analyses in armchair direction. Similar plots for zigzag directions are plotted in Fig. 6.2-20 and 6.2-21.

As it is understood from the plots, we are able to demonstrate indirect to direct bandgap transition as it was claimed in above mentioned article. In addition, because we are able to apply higher strains, we demonstrate entering to indirect region again. As it is clear from Fig. 6.2-19 and 6.2-21, it looks such that the low energy peak which is separated about 100 meV from the high energy peak, is "standing" that means the strain does not affect its energy (bandgap location). Instead, by applying tensile strain in either direction, the high energy peak starts red-shifting until overlaps the so-called standing peak which introduce direct bandgap. By applying more strain, the red-shifting peak separates from the standing low energy peak in which we could observe two peaks again.

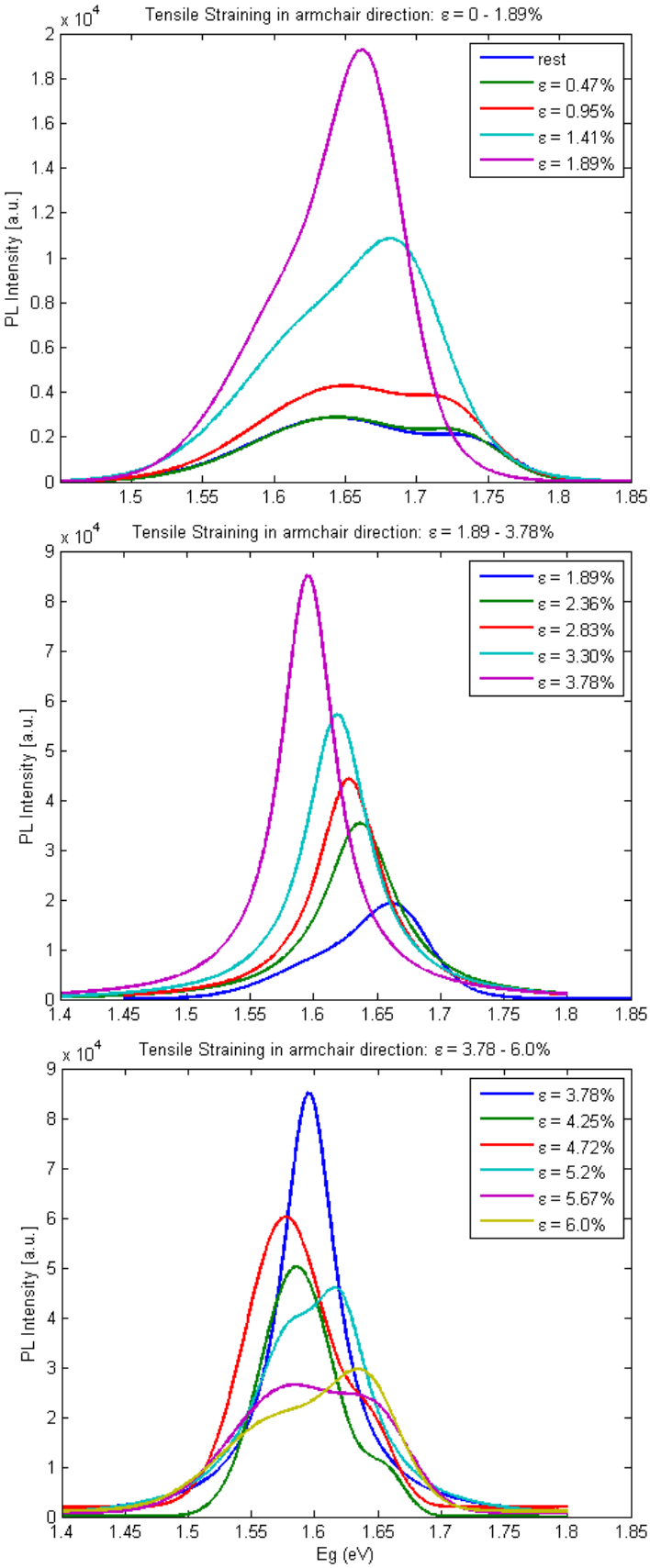

Figure 6.2-18– PL signals for bilayer WSe2 under tensile strain in armchair direction. Top: strain applied from 0 to 1.89%. Middle: strain range 1.89% to 3.78%. At about 2.8% strain peaks overlap. Bottom: strain range from 3.78% to 6.0%, splitting is observed again.

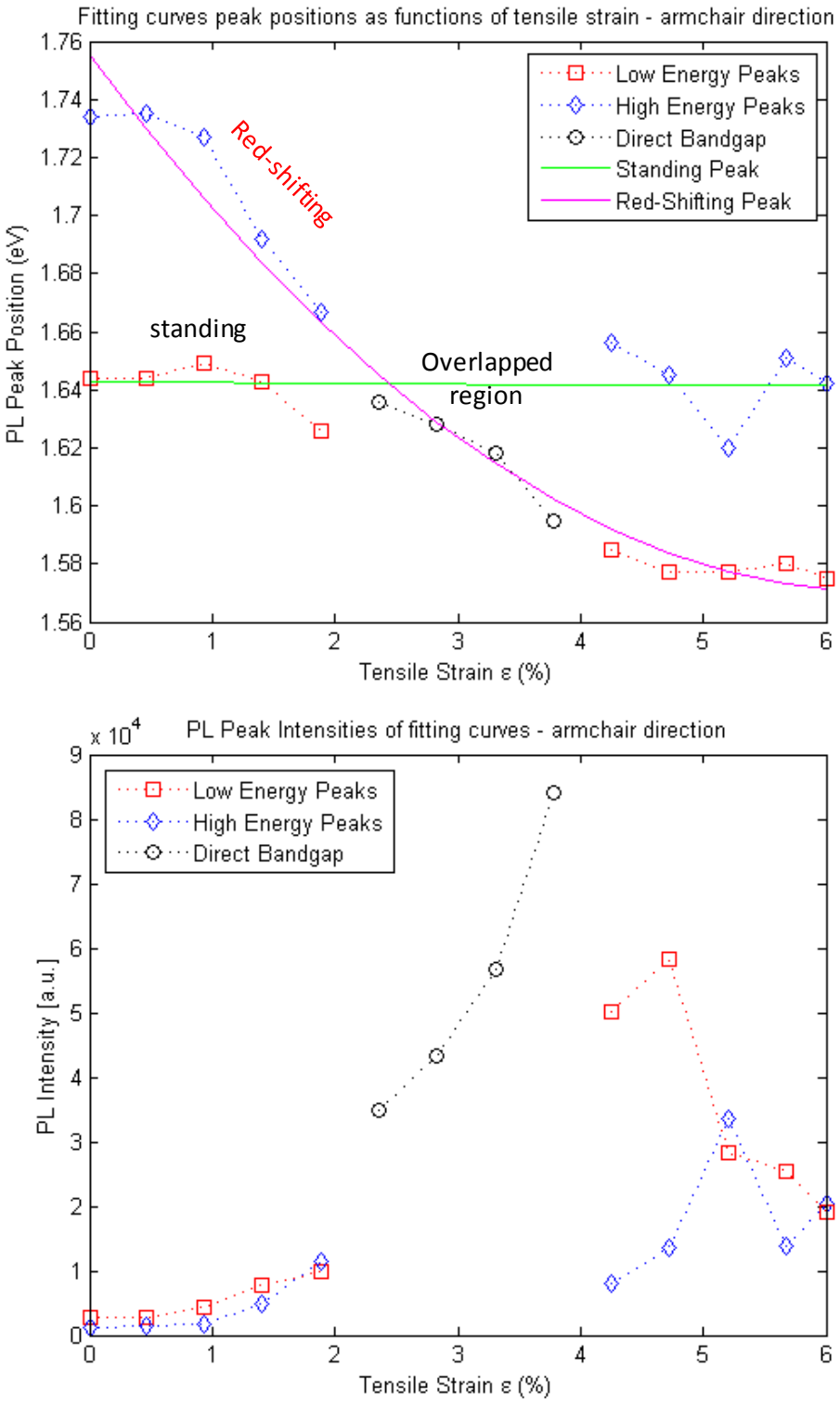

Figure 6.2-19– PL signals analyses for bilayer WSe_2 under tensile strain. Top: there are two peaks at rest which are separated about 100 meV. Applying strain, red-shifts high energy peak until it overlaps the low energy peak and the continues red-shifting with the increasing strain. Bottom: the PL peak intensities.

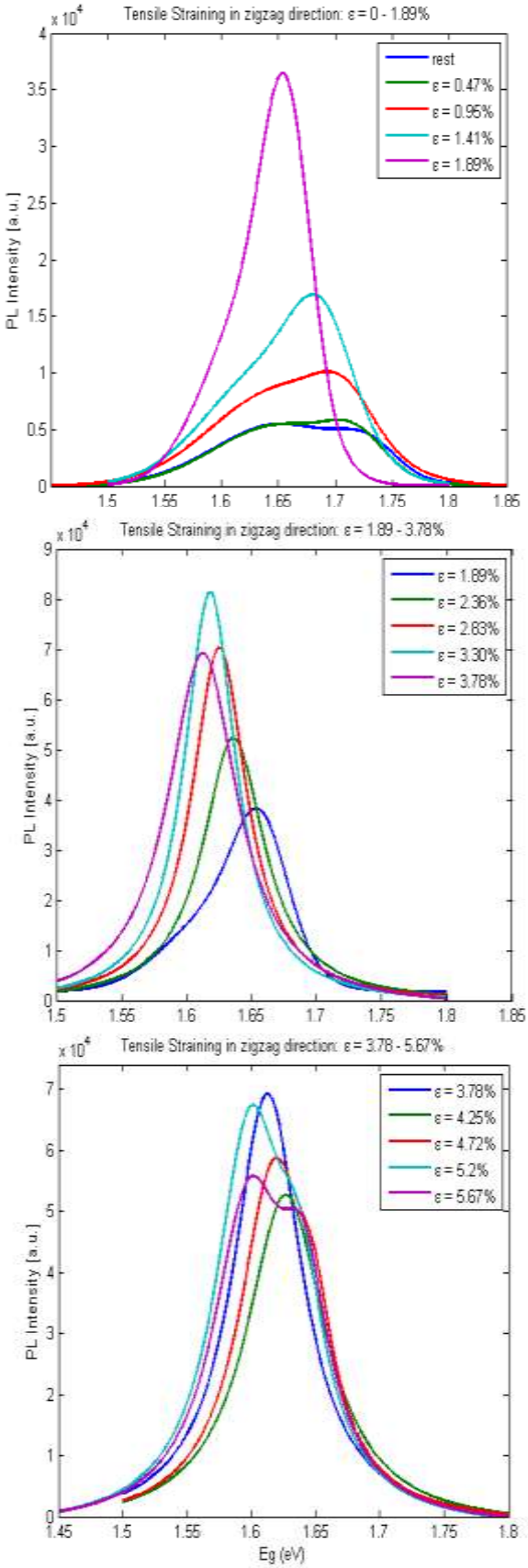

Figure 6.2-20– PL signals for bilayer WSe2 under tensile strain in zigzag direction. Top: strain applied from 0 to 1.89%. Middle: strain range 1.89% to 3.78%. At about 2.8% strain peaks overlap. Bottom: strain range from 3.78% to 6.0%, splitting is observed again.

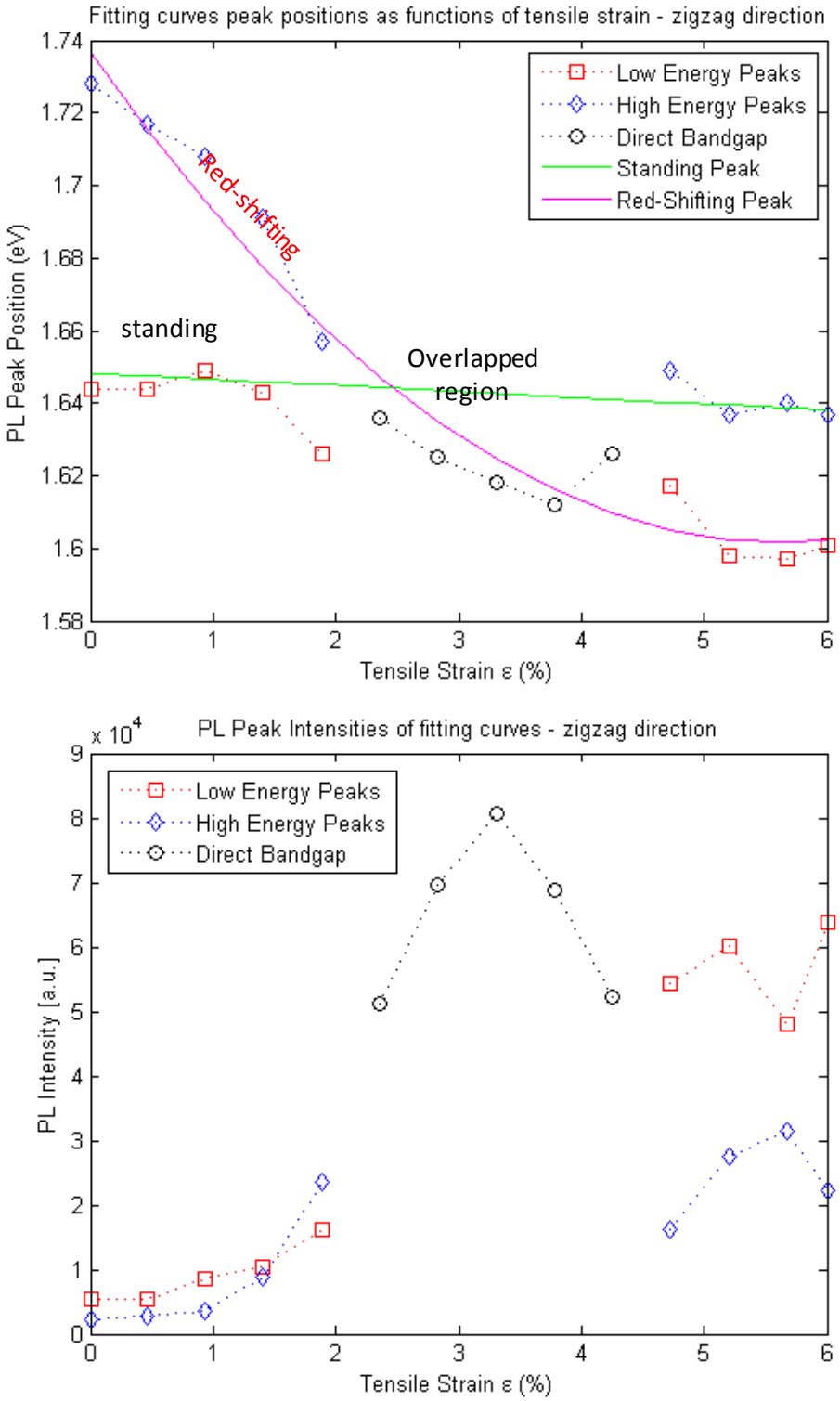

Figure 6.2-21– PL signals analyses for bilayer WSe_2 under tensile strain in zigzag direction. Top: there are two peaks at rest which are separated about 100 meV. Applying strain, red-shifts high energy peak until it overlaps the low energy peak and the continues red-shifting with the increasing strain. Bottom: the PL peak intensities.

PART C

TRANSPORT PROPERTIES OF PRISTINE AND CHEMICALLY DOPED GRAPHENE

CHAPTER 7

Quantum Transport of Pristine Graphene

We observed interesting results in transport measurements of nitrogen doped graphene and then repeated the experiments for pristine graphene in order to see if we observe the same physics or not. Although we started with nitrogen doped graphene, here we present our results of pristine graphene first since the nature of those devices are simpler and helps to present the basics. Methods of growing graphene both pristine and doping is explained in chapter 9. The detail of device fabrication is already discussed in chapter 5.

Fig. 7.1 is schematic diagram of pristine hall bar we made for these experiments. A controlled current flows through the graphene and the voltage between the shown contacts can measure the Vxx or Vxy in the case of across voltage. Meanwhile, an orthogonal magnetic field can be applied. All these measurements can be done in various temperatures as will be explained later.

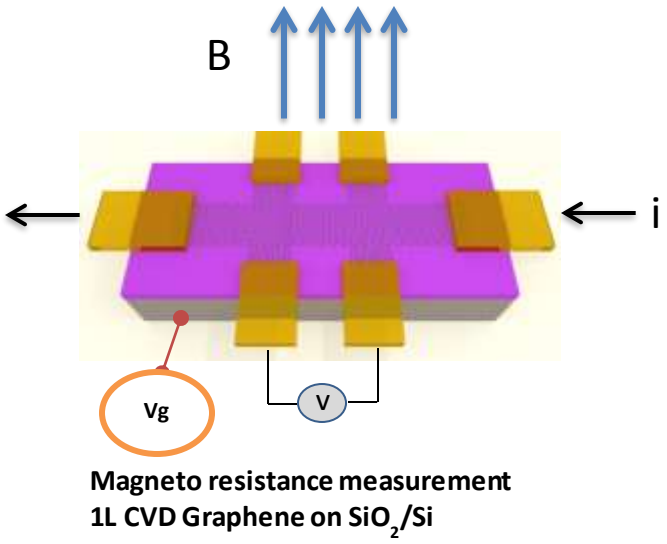

Figure 7.1 – Graphene Hall bar made on 285nm silicon dioxide dielectric substrate.

A voltage source is applied to the back of the device which is conductive silicon. By varying the amount of applied voltage, we can add different doping levels to the graphene layer to change the location of Dirac point. Dirac point is considered the point that gives the maximum resistivity or

the lowest conductivity. We name this voltage with the corresponding back gate voltage V_{NP} which tells the point where the holes and electrons are in balance. Normally for pristine graphene without any doping effect, this voltage should be $V_{NP} = 0$ meaning that the Dirac point is located at zero.

Mobility

Mobility is a measure to characterize how easily an electron moves through a material. In graphene it shows how clean the growth is. We will see in the next chapter that by doping graphene, we decrease the mobility of the devices. Mobility is defined as:

$$\mu = \frac{1}{\rho ne} = \frac{\sigma}{ne}$$

Where ρ is the resistivity in ohms, e is the electron's charge in coulombs, n is the carrier density and σ is the conductivity which is calculated from:

$$\sigma = \frac{AR}{R(0)}$$

In which the AR is the aspect ratio of the Hall bar – length divided by the width of the channel and $R(0)$ is the resistivity of the graphene at zero magnetic field. Then the mobility's relation would be simplified to:

$$\mu = \frac{AR}{neR(0)}$$

Calculating Carrier Density with Capacitance

Field Effective device are the nature of these devices we make and do our experiments. Thin silicon dioxide layer plays dielectric role to dope the electrons or wholes on the thin 2D materials.

$$C = \frac{q}{V} = \frac{neA}{V_g - V_{NP}}$$

$$n = \frac{C(V_g - V_{NP})}{Ae}$$

V_g is the back gate voltage, and V_{NP} is the corresponding Dirac point which is the gate voltage with maximum resistivity. The capacitance also can be calculated for thin silicon dioxide film as follow:

$$C = k\epsilon_0 \frac{A}{d}$$

d is the thickness of dielectric material – 285 nm in our devices, A is the area and k is the relative static permittivity which is $k = 3.9$ for silicon dioxide in vacuum and ϵ_0 is permittivity of vacuum. As a conclusion, the simplified and applied version of mobility is the following:

$$\mu = \frac{d}{k\epsilon_0} \frac{\sigma - \sigma_{res}}{V_g - V_{NP}}$$

For pristine graphene, we made two devices with the following measured mobilities:

$$Device\ P1: \mu = 3600\ cm^2V^{-1}s^{-1}$$

$$Device\ P2: \mu = 3000\ cm^2V^{-1}s^{-1}$$

Fig. 7.2 shows the resistivity and conductivity at various carrier densities. Device P2 results are identical with P1 then, we suffice to show only P1 as sample. The carrier densities are calculated with capacitance. As you notice from the pictures, the measurements were done in different temperatures and there is no drastic difference in conductance with respect to the temperature. Later in the next chapter we will see that this is totally different for nitrogen doped graphene.

Fig. 7.4 – top shows relative conductivity in holes and electrons side and the bottom images shows the how symmetric the conductivity change in electrons and holes side with respect to the Dirac point: $\Delta\sigma_h/\Delta\sigma_e$. As you notice, there are fundamental oscillations in both images at lower temperatures.

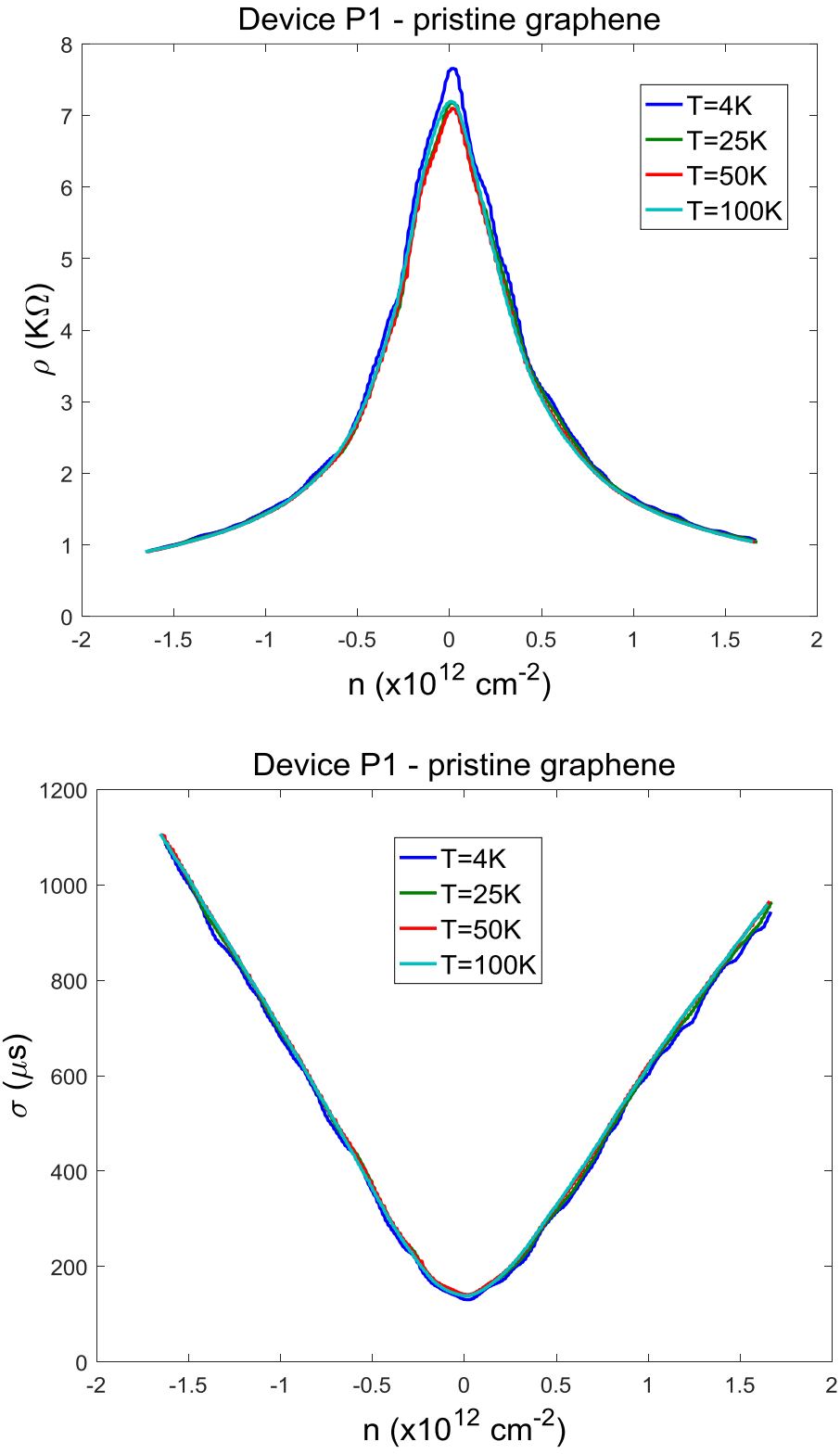

Figure 7.2 – Device P1 resistivity (top) and conductivity (bottom) versus various carrier densities.

These measurements are in perfect match with the other similar experiments reported in other articles [77]. According to Fig. 7.3, there are two main properties involved in pristine graphene that match with our pristine devices:

- symmetry in magneto conductivity
- the least (almost zero) temperature dependence

Later, we will compare these results with nitrogen doped graphene.

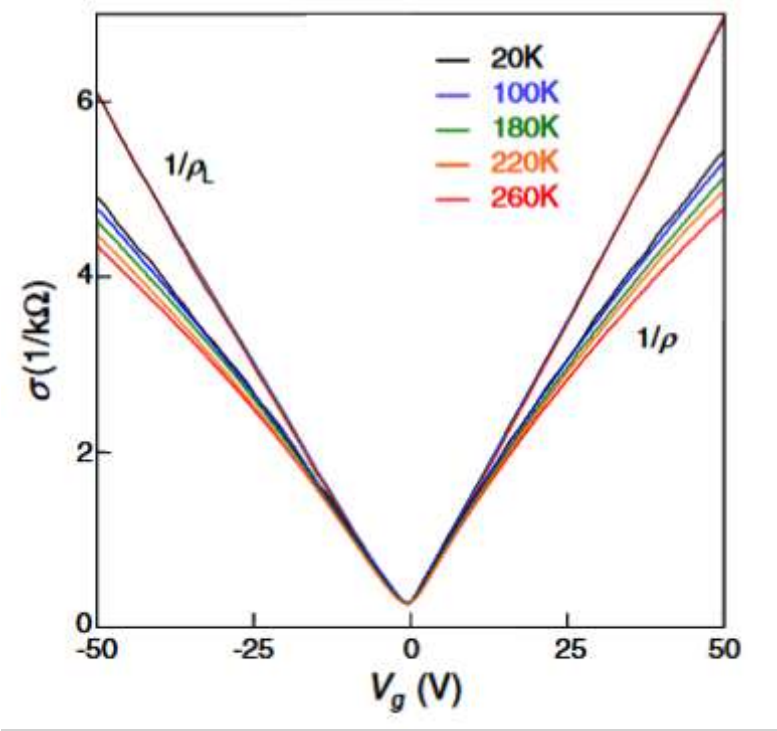

Figure 7.3 – Symmetry in magneto conductivity and very low temperature dependence in pristine graphene transport measurements [77]

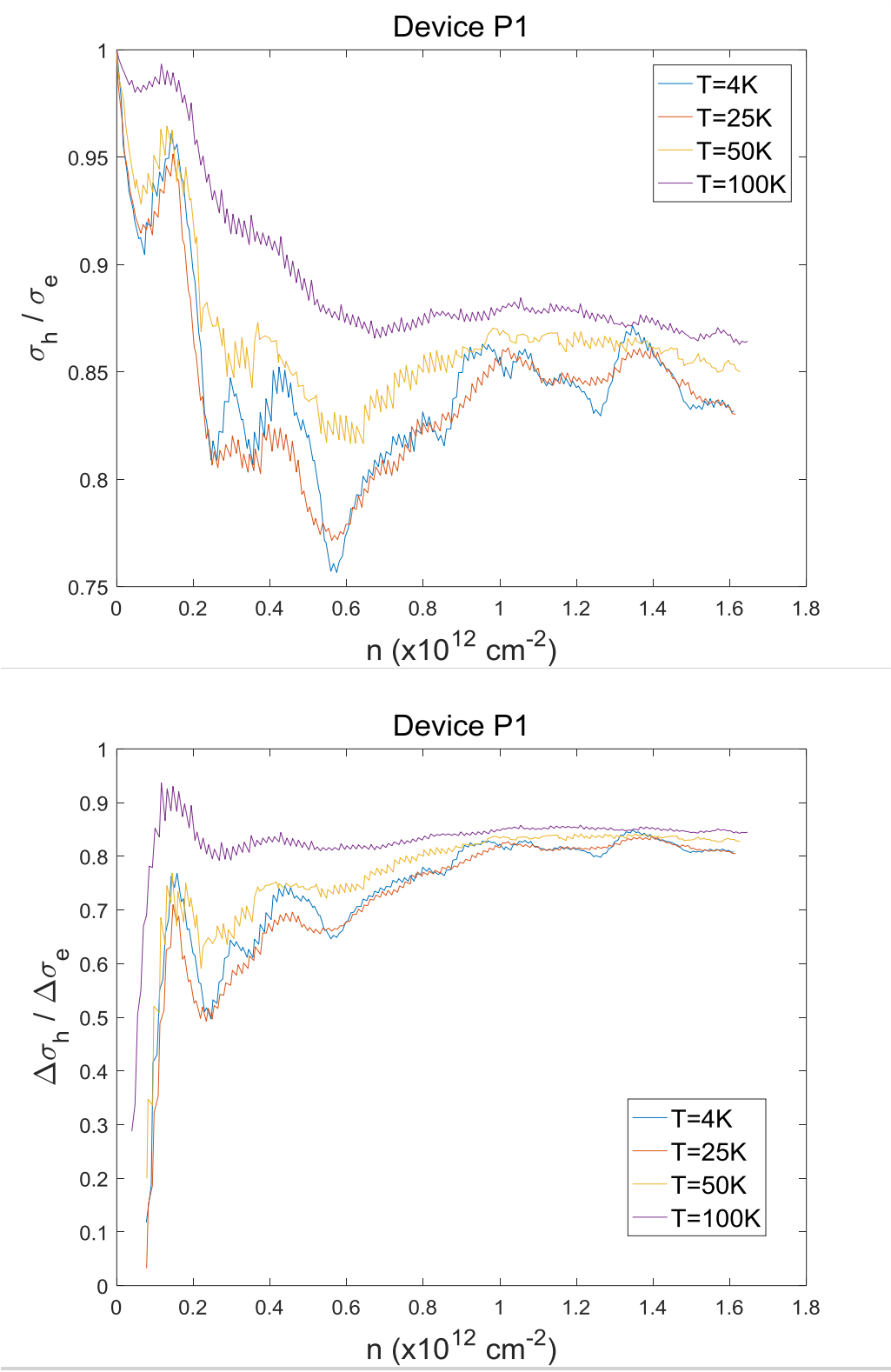

Figure 7.4– Device P1 – relative conductivity in holes and electrons region (top) and how symmetric these change away from the Dirac point (bottom)

Theory of Weak Localization [78]

Weak Localization is quantum correction of the conductivity. It explains electron dephasing due to the scattering caused by impurities. When a graphene device goes under vertical magnetic field, its conductivity obeys a complex mathematical relation as follows:

$$\frac{\pi h}{e^2}\Delta\sigma(B) = F\left(\frac{\frac{8\pi e}{h}B}{L_\emptyset^{-2}}\right) - F\left(\frac{\frac{8\pi e}{h}B}{L_\emptyset^{-2} + 2L_i^{-2}}\right) - 2F\left(\frac{\frac{8\pi e}{h}B}{L_\emptyset^{-2} + L_i^{-2} + L_*^{-2}}\right)$$

$$F(z) = Ln(z) + \psi(1/2 + 1/z)$$

$$L_*^{-2} = L_s^{-2} + L_w^{-2}$$

Where $L_\emptyset$ is inelastic scattering length, L_i is elastic scattering length or intervalley scattering, L_w is intra-valley scattering length and L_s is characteristics length for spin flip rate. The first term in the above equation is called Weak-Localization (WL) term in which represents the change of the conductivity with respect to the applied magnetic field. While, other two terms – the negative terms are called Weak-Anti Localization (WAL) which cause the conductivity decrease after a point.

There are two types of scatterings in graphene: inelastic and elastic. WL explains the sources of inelastic scattering which involves with phase change and is denoted by $L_\emptyset$ and $\tau_\emptyset^{-1}$ representing elastic scattering length and rate respectively.

- Inelastic scattering: $L_\emptyset$, $\tau_\emptyset^{-1}$
- Elastic scattering:
    - Spin-flip processes, breaking chirality, destroying interference between k' and k; reasons include: surface ripples, dislocations, atomically sharp defects: L_s, τ_s^{-1}
    - Intra-valley scattering, anisotropy of fermi surface, trigonal warping: L_w, τ_w^{-1}
    - Inter-valley scattering: restores suppressed interference; in narrow samples edges produce inter-valley scattering: L_i, τ_i^{-1}

Fig. 7.5 shows the WL and WAL graph with respect to magnetic field.

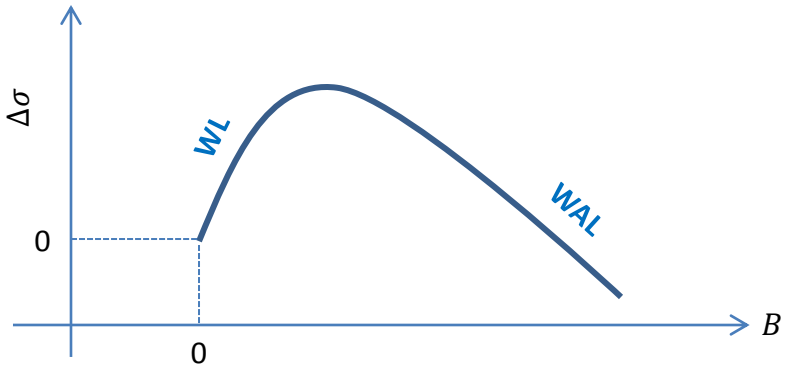

Figure 7.5– Graph of Weak Localization theory which shows the increase and decrease of conductivity labeled with Weak Localization (WL) and Weak Anti Localization (WAL)

If we measure $\Delta\sigma$ in different magnetic fields, after regression analysis, we can find the corresponding localization widths.

Now we measure the weak localization in different magnetic fields to produce the localization graph. For this purpose, we start measuring the magneto conductance at 5K and different carrier density or doping. Then we repeat these experiments at 25K and 50 to compare the results. These graphs are in Fig. 7.6, Fig. 7.7 and Fig. 7.8. As you see, there are fundamental oscillations at lower temperatures and Dirac region saturates much faster than holes and electrons regions. In general, holes regions have less sensitivity to the magnetic field.

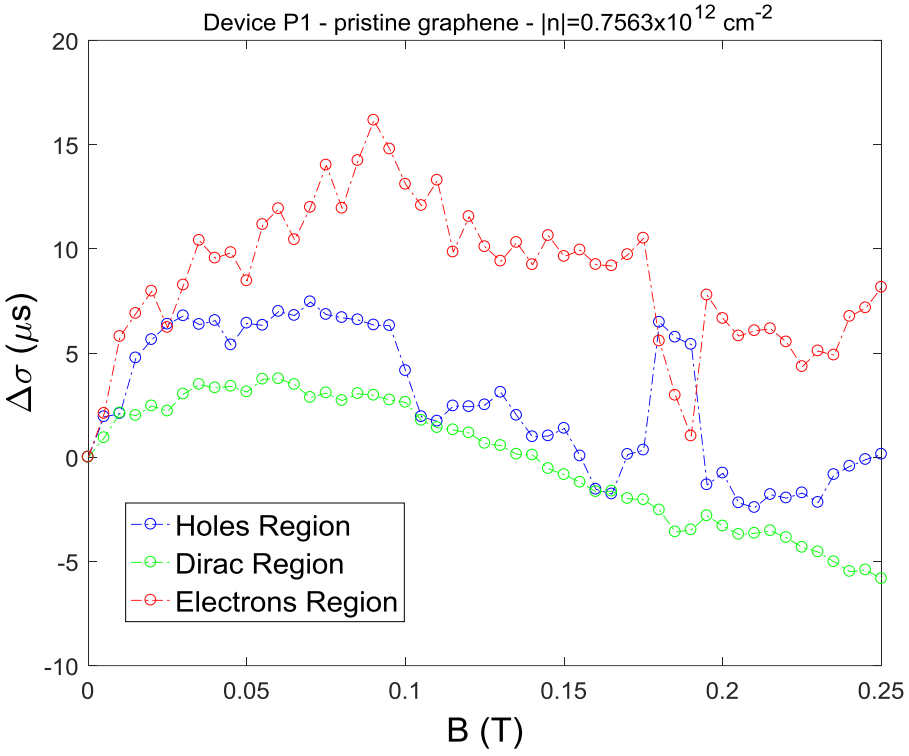
Device P1 - pristine graphene - |n|=0.7563x10^12 cm^-2
Δσ (μS)
B (T)
Holes Region
Dirac Region
Electrons Region
20
15
10
5
0
-5
-10
0
0.05
0.1
0.15
0.2
0.25

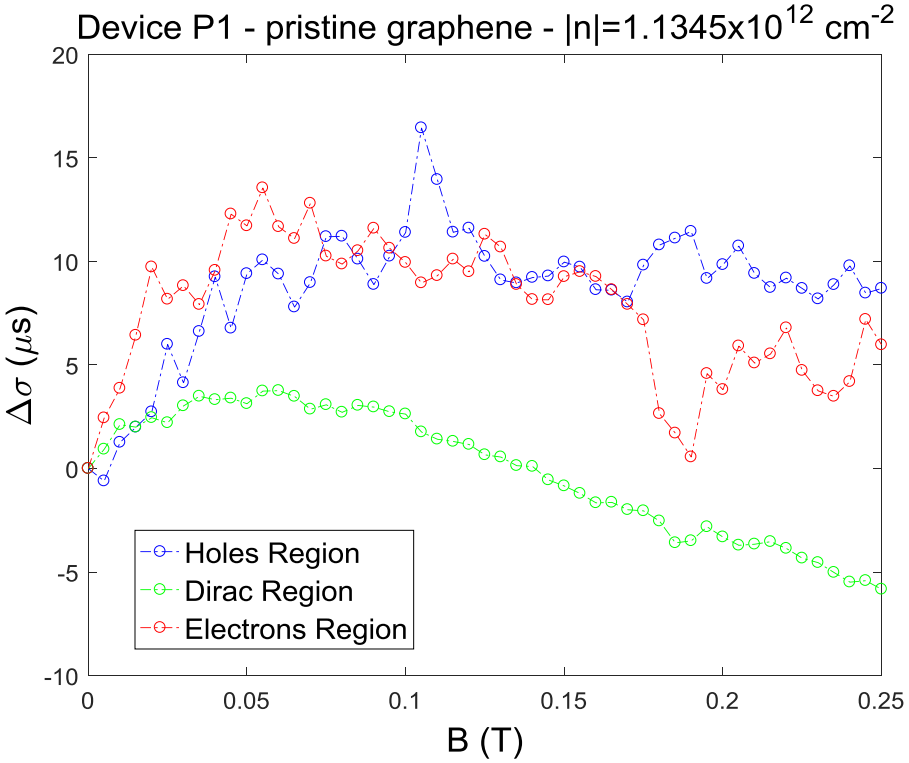
Device P1 - pristine graphene - |n|=1.1345x10^12 cm^-2
Δσ (μS)
B (T)
Holes Region
Dirac Region
Electrons Region
20
15
10
5
0
-5
-10
0
0.05
0.1
0.15
0.2
0.25

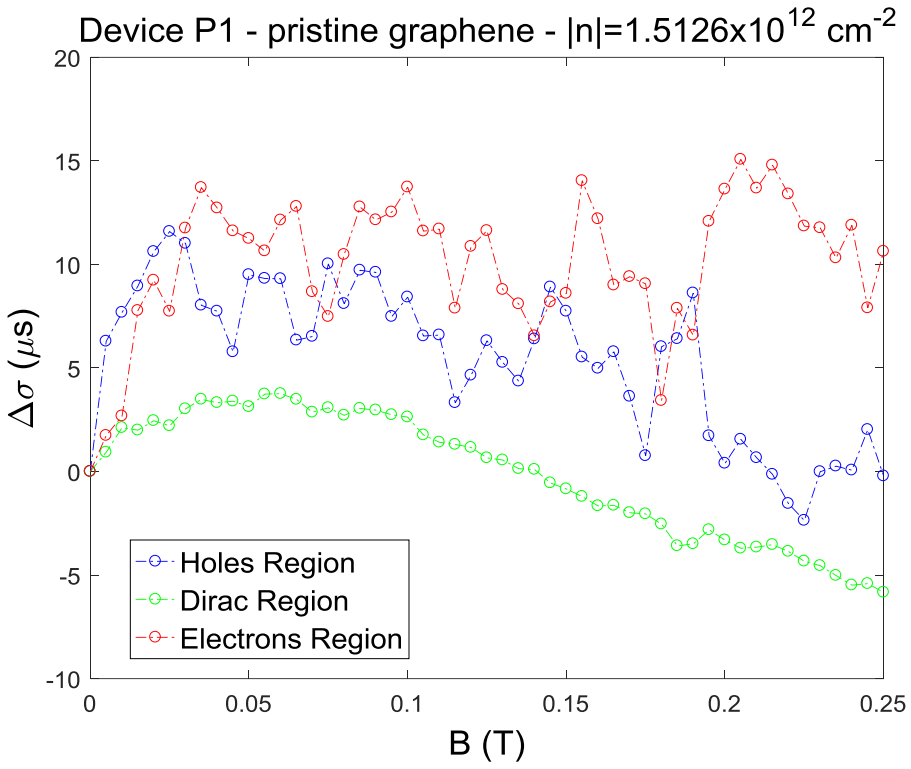

Figure 7.6– magneto conductance of pristine graphene – device P1 at 5K and at various magnetic fields showing the Weak Localization theory. Each graph is plotted in different electrons, holes and Dirac region with various carrier density levels.

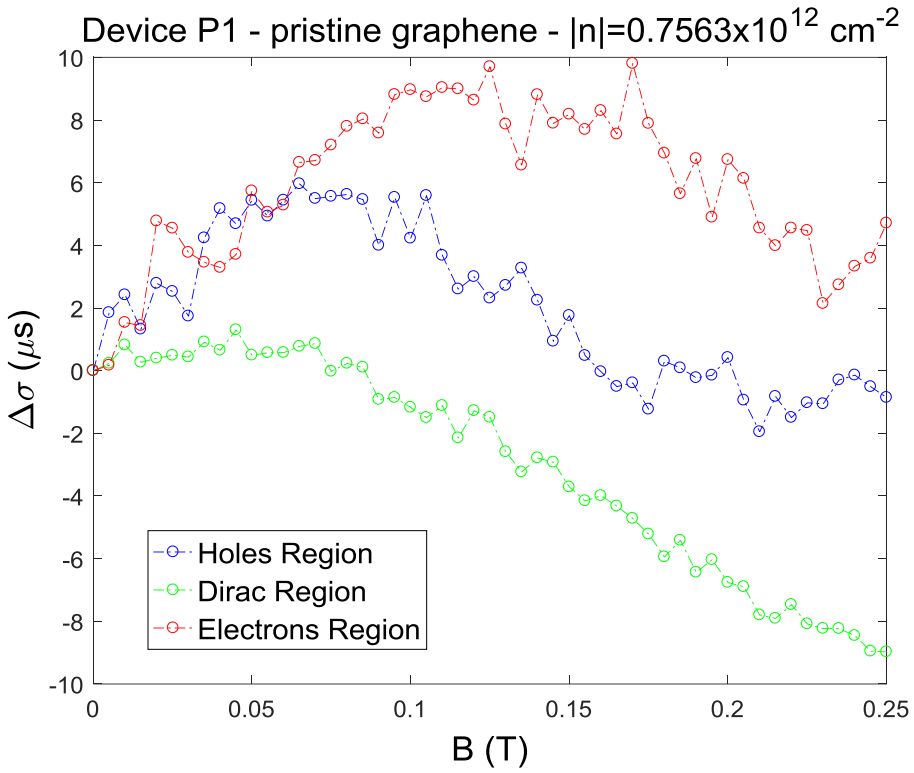
Device P1 - pristine graphene - |n|=0.7563x10^12 cm^-2
Δσ (μs)
B (T)
Holes Region
Dirac Region
Electrons Region

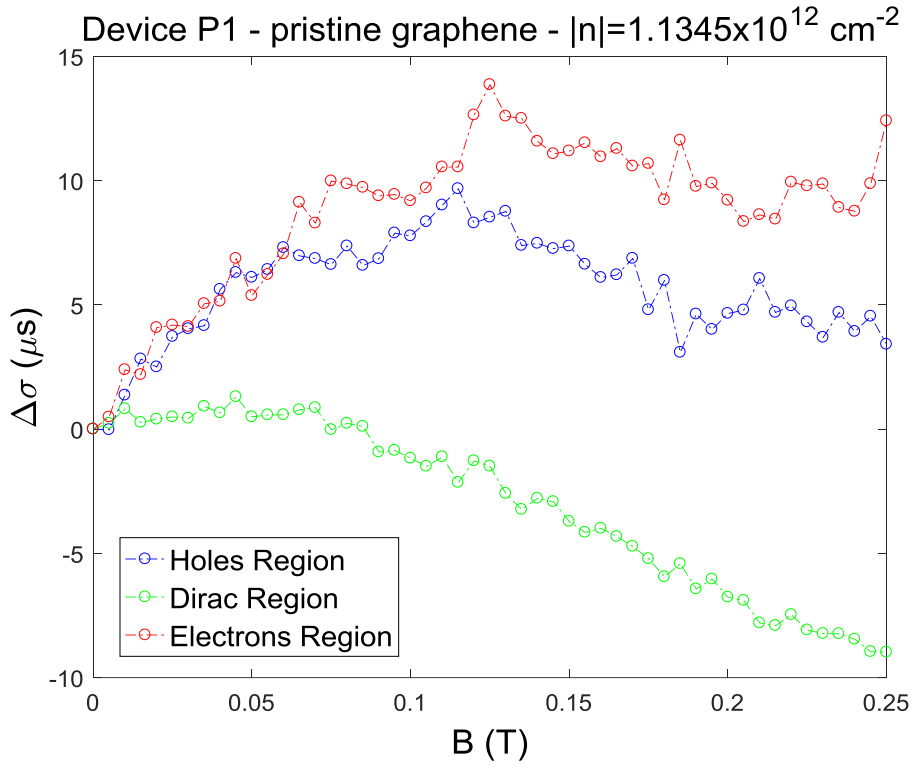
Device P1 - pristine graphene - |n|=1.1345x10^12 cm^-2
Δσ (μs)
B (T)
Holes Region
Dirac Region
Electrons Region

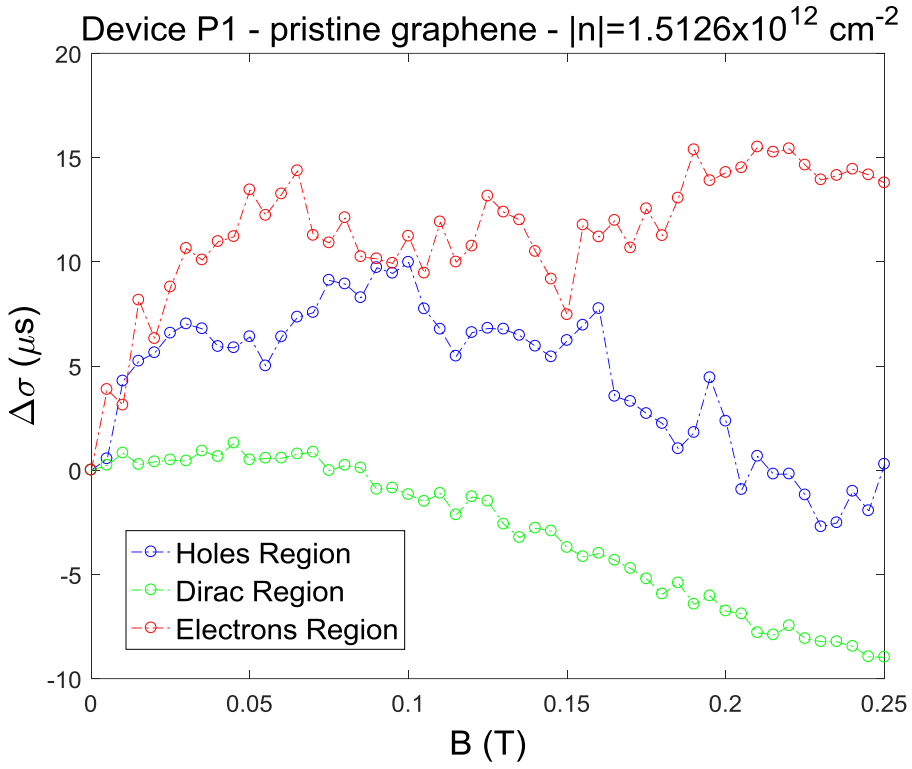

Figure 7.7– magneto conductance of pristine graphene – device P1 at 25K and at various magnetic fields showing the Weak Localization theory. Each graph is plotted in different electrons, holes and Dirac region with various carrier density levels.

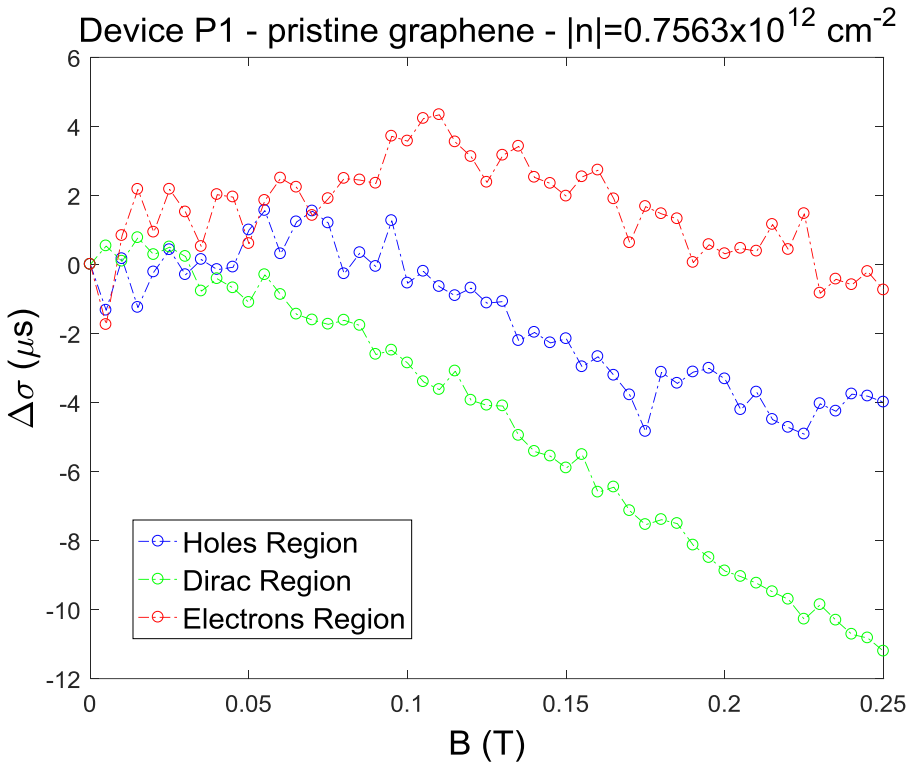
Device P1 - pristine graphene - |n|=0.7563x10^12 cm^-2
Δσ (μS)
B (T)
Holes Region
Dirac Region
Electrons Region

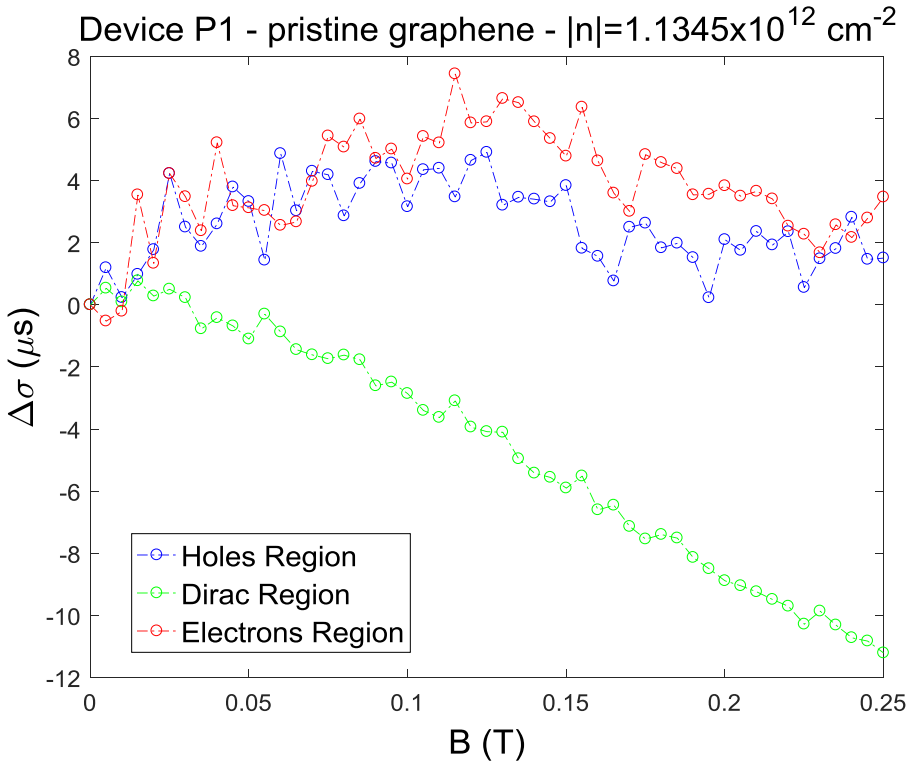
Device P1 - pristine graphene - |n|=1.1345x10^12 cm^-2
Δσ (μS)
B (T)
Holes Region
Dirac Region
Electrons Region

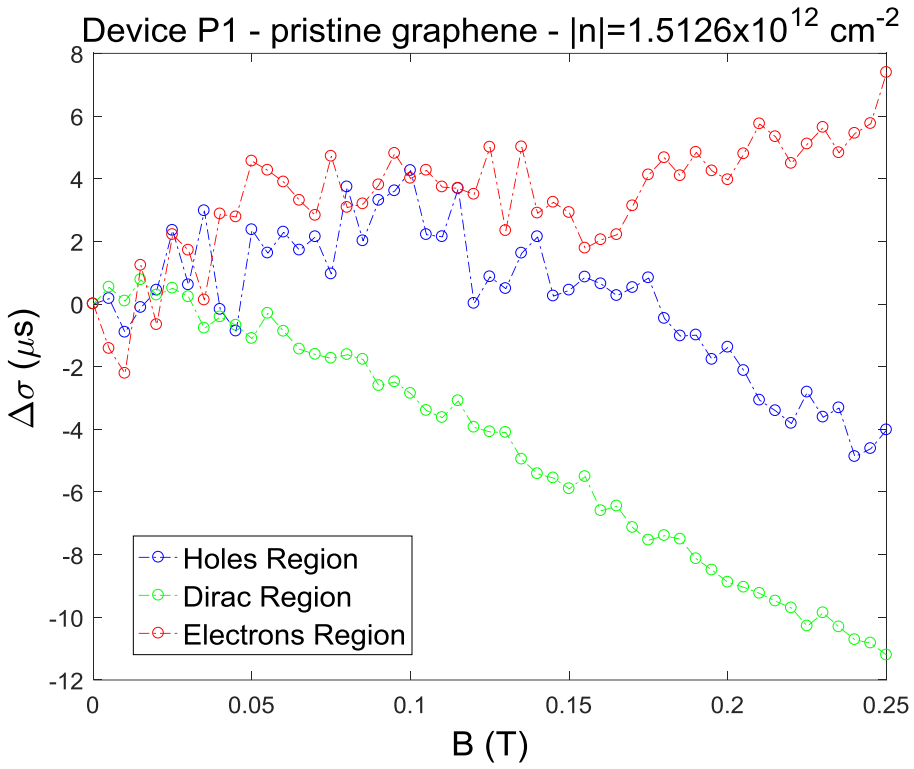

Figure 7.8– magneto conductance of pristine graphene – device P1 at 50K and at various magnetic fields showing the Weak Localization theory. Each graph is plotted in different electrons, holes and Dirac region with various carrier density levels.

CHAPTER 8

Quantum Transport of N-doped Graphene

We showed the transport properties of pristine graphene that match with the Weak Localization theory. These findings are also in perfect match with other articles that performed similar measurements that explained. Now we are going to show our results in nitrogen doped graphene (n-doped).

We made three Hall bar devices, one on hexagonal boron nitride and silicon dioxide and two others are just on silicon dioxide as shown in Fig. 8.1

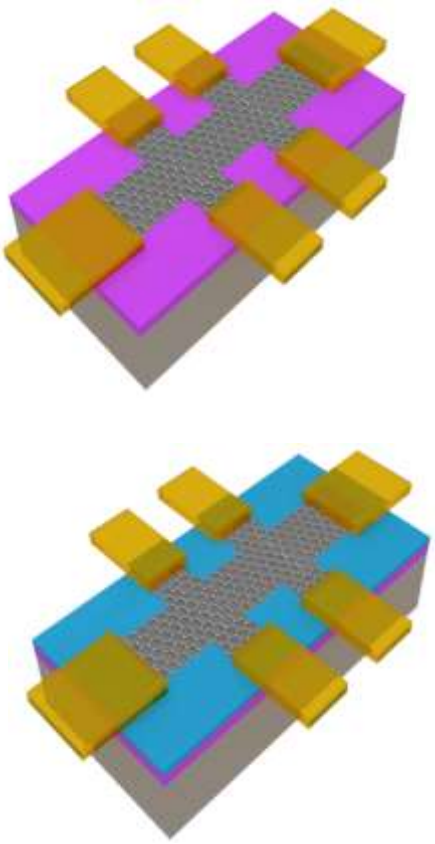

Figure 8.1– N-doped graphene Hall bar made on 285nm silicon dioxide dielectric substrate (top) and on hexagonal boron nitride stacked on silicon dioxide.

In order to clarify the distinction of these three devices, we first provide the mobilities:

$$Device\ 1 - Heavily\ Doped:\ \mu = 150\ cm^2V^{-1}s^{-1}$$

$$Device\ 2 - Lightly\ Doped:\ \mu = 750\ cm^2V^{-1}s^{-1}$$

$$Device\ 3 - Moderately\ Doped:\ \mu = 500\ cm^2V^{-1}s^{-1}$$

Device 1 and 2 are on silicone oxide only while Device 3 is equipped with interlayer boron nitride to investigate its effects. In order to see the effect of n-doping, we plot the resistance versus back gate voltage for a heavily doped device. This graph is represented in Fig. 8.2 which reveals the Dirac point at $V_{NP} = -34.7V$.

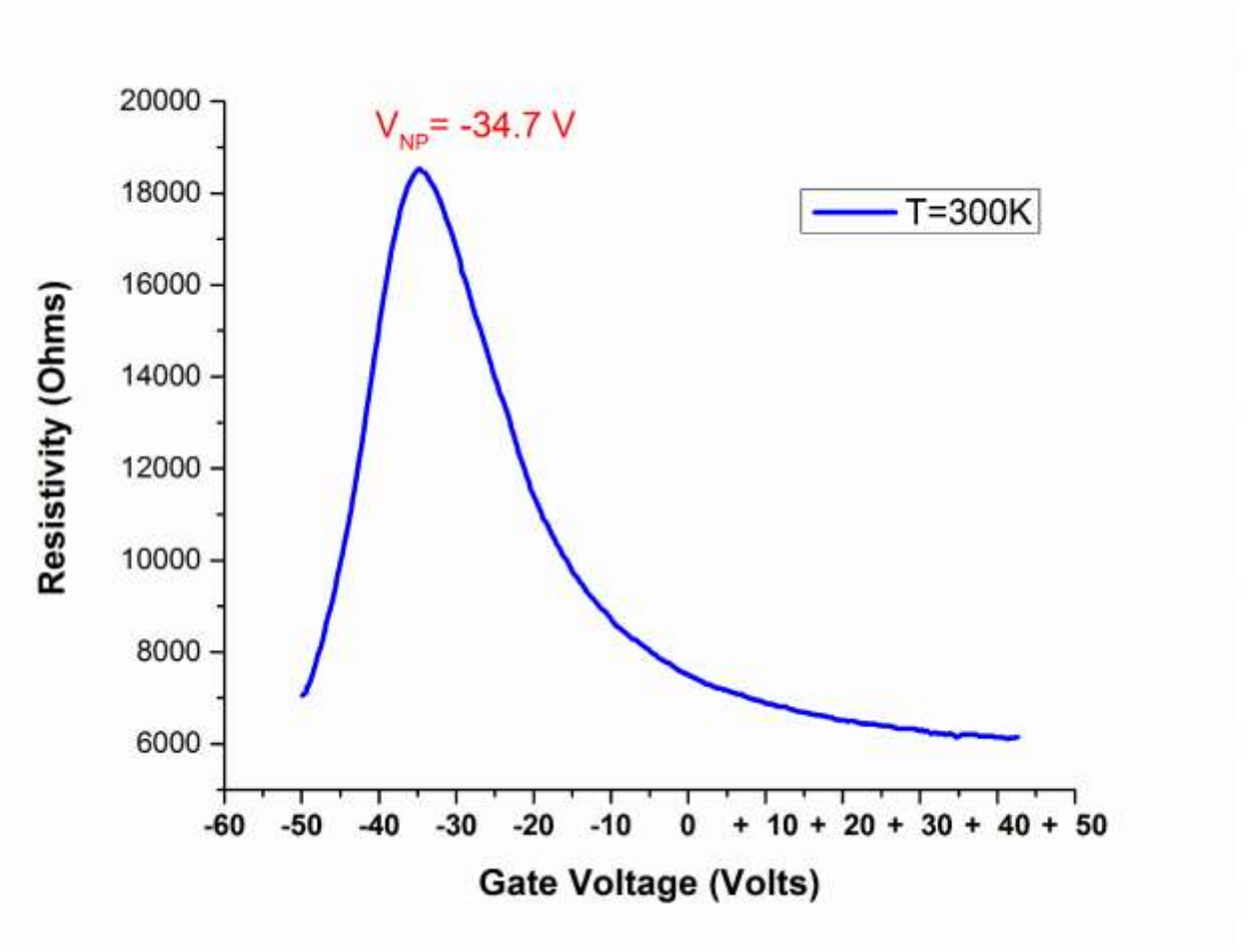

Figure 8.2– Measuring the Dirac point of heavily nitrogen doped graphene devices reveals the Dirac point at $V_{NP} = -34.7V$ at room temperature. For pristine graphene this should lie at 0 V without considering the substrate effects.

We observed that silicon oxide makes graphene p-doped. This shifts the Dirac point to the positive side. Then, in order to measure the real Dirac point, all substrate effects should be taken into account. Fig. 8.3 shows another Dirac point measurement of Device 3 – moderately doped graphene which is about $V_{NP} = -9\ V$.

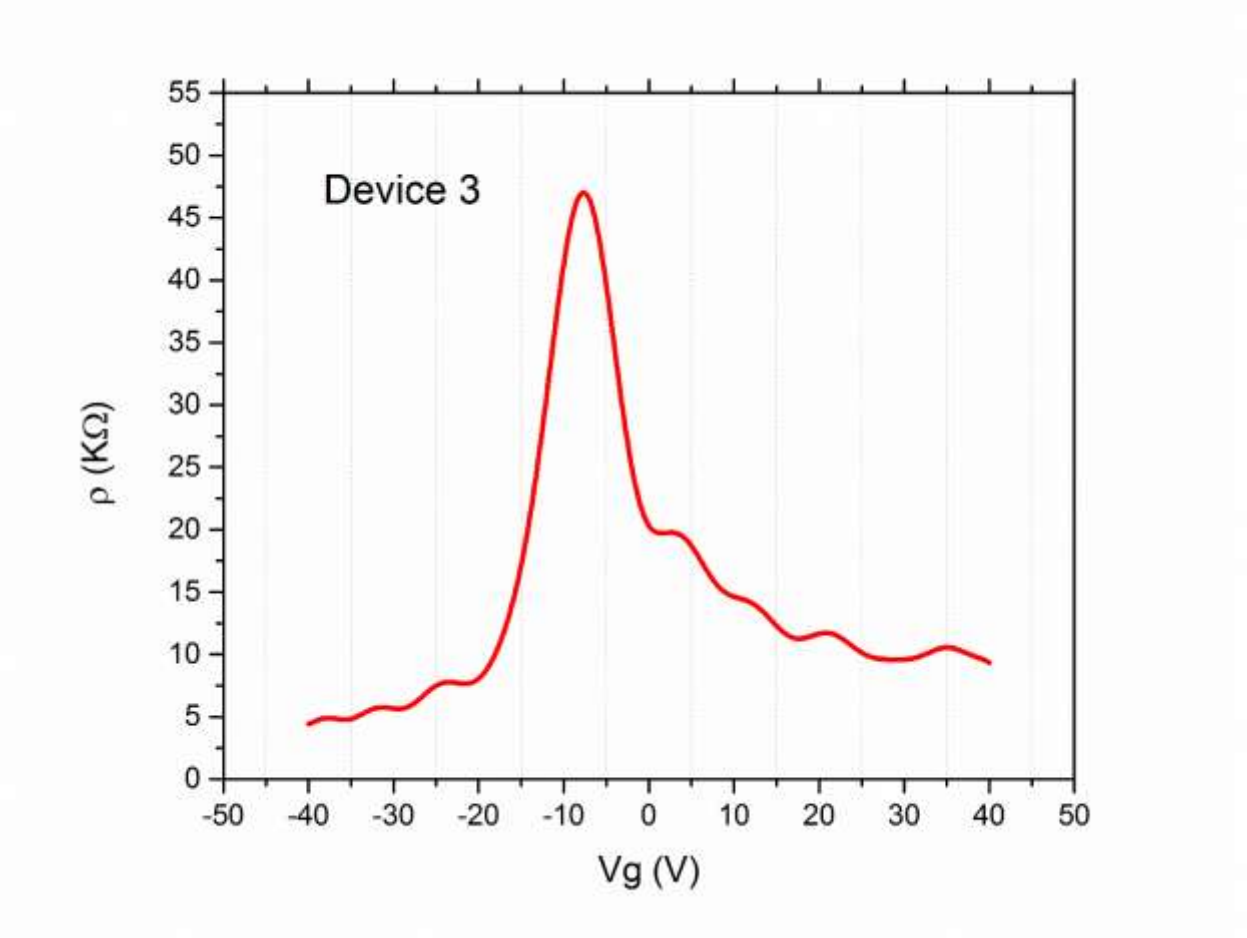

Figure 8.3– Measuring the Dirac point of moderately nitrogen doped graphene devices reveals the Dirac point at $V_{NP} = -9\ V$ at room temperature.

In order to compare the doping and substrate effects between doped and pristine devices we present our measurements on the Device P1 which is a pristine graphene. As you see, the Dirac point is at about $V_{NP} = +20\ V$ which claims stong substrate or positive doping effects. This is shown in Fig. 8.4.

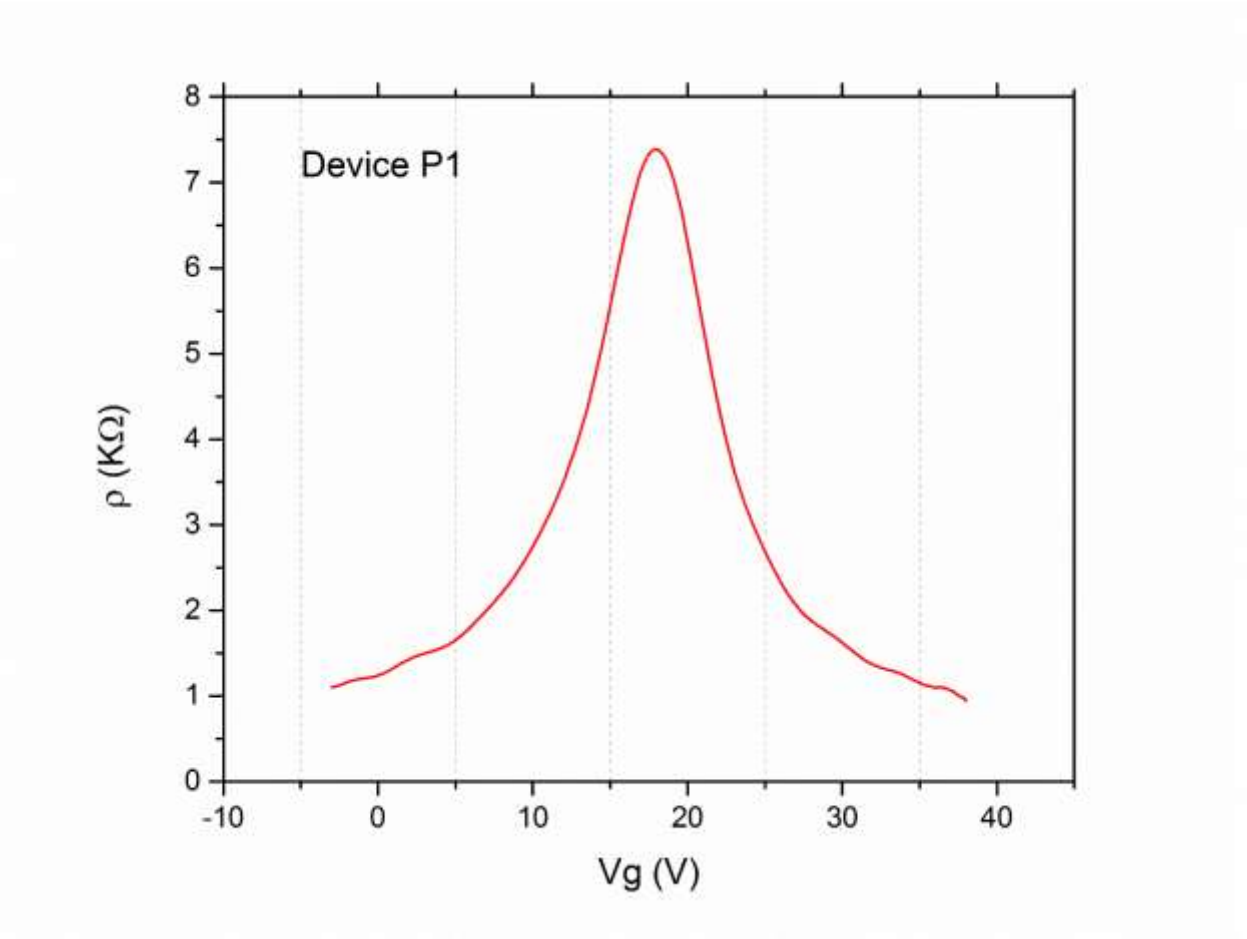

Figure 8.4– Measuring the Dirac point of pristine graphene device P1 reveals the Dirac point at $V_{NP} = +20\ V$ at room temperature.

One interesting observation before continuing our experiments was the strong electron and holes asymmetry existing in nitrogen doped graphene that never exist in pristine graphene devices.

Now, before starting measuring the effects of magnetic field to the conductivity, we first measure the conductivity and resistivity at various back gate (carrier doping) and also different temperatures. These results are shown in Fig. 8.5 and 8.6. Graphs are shifted to their associated Dirac point.

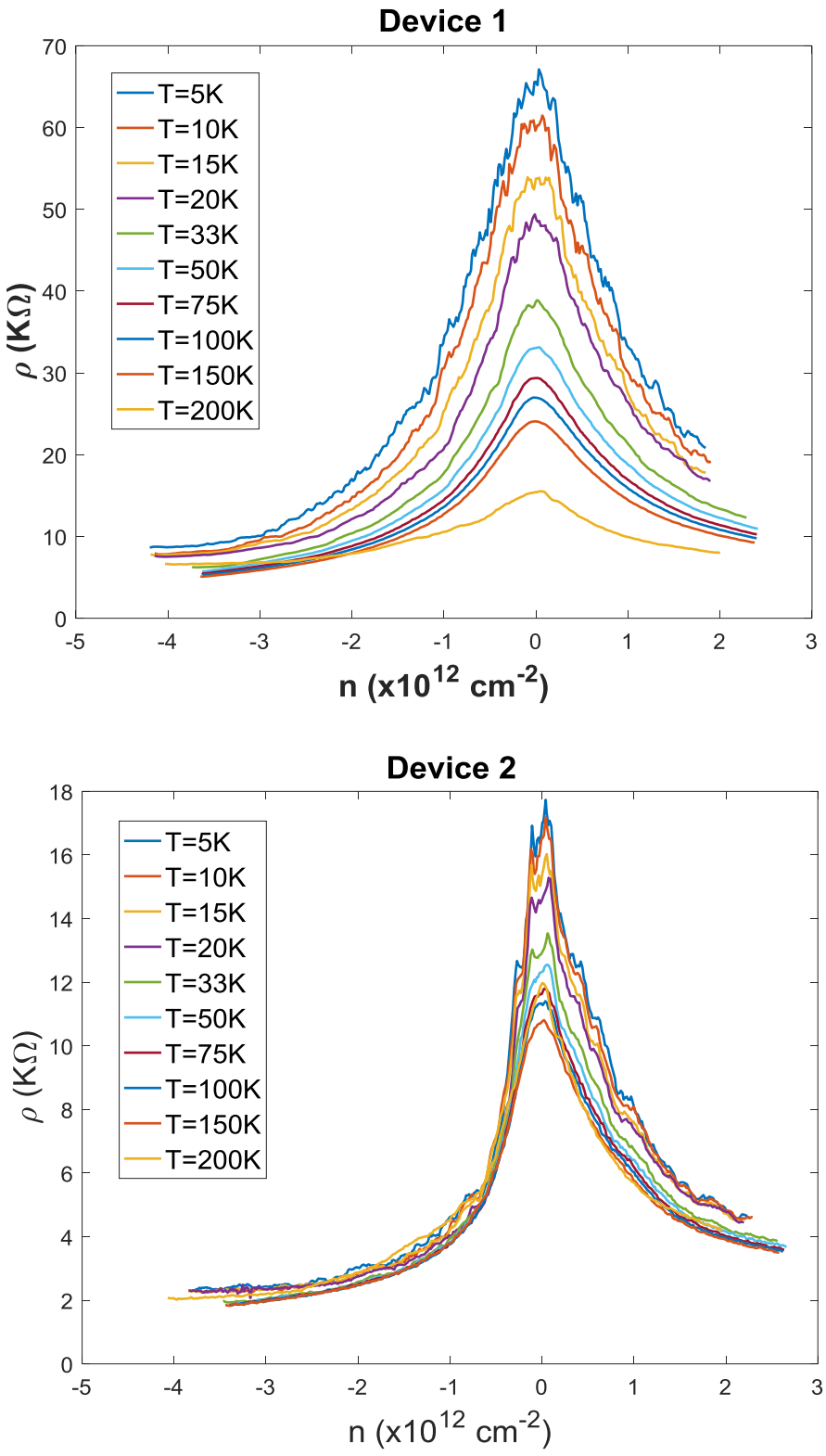

Figure 8.5– Resistivity of doped graphene Device 1 – heavily doped (top) and Device 2 – lightly doped (bottom). Curves shifted to their corresponding Dirac point.

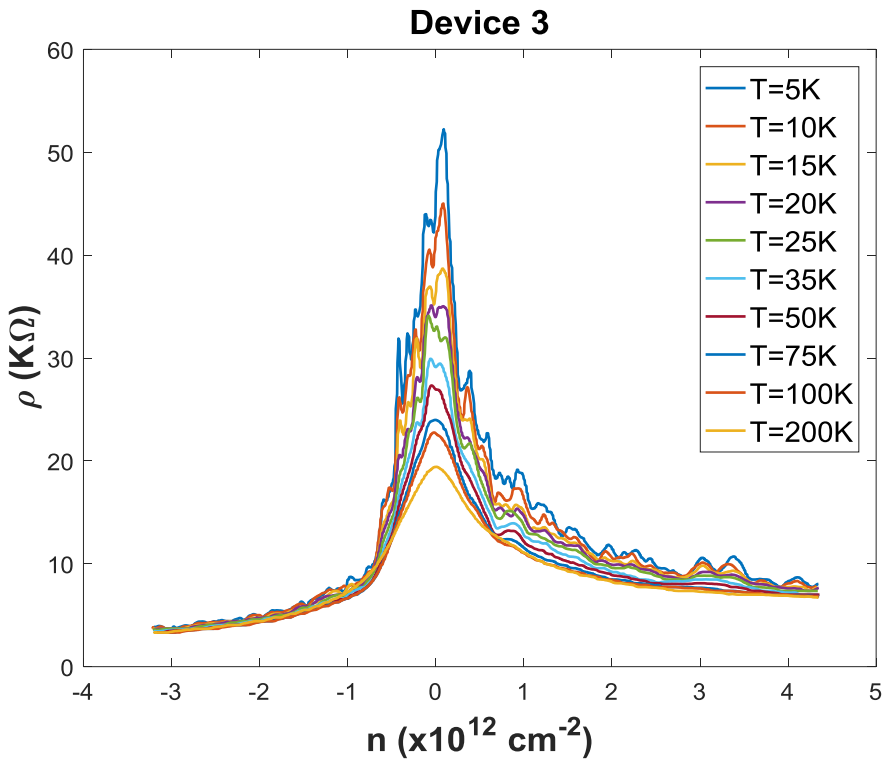

Figure 8.6– Resistivity of doped graphene Device 3 – moderately doped graphene on hexagonal boron nitride film. Curves shifted to their corresponding Dirac point.

Here are three important findings which are totally different comparing with pristine graphene:

- *Strong electron-holes asymmetry*
- *Strong temperature dependence*
- *Strong resistivity (also conductivity) oscillation at lower temperatures*

These effects are similar in all three devices with severe effects on heavily doped graphene.

Before proceeding to the analysis of these findings, we would complete our experiments under varying magnetic fields to see the correlated effects. We first analyze the Weak Localization effects on the lightly and moderately doped graphene devices. Fig. 8.7 shows the measured conductance for Device 2 – moderately doped graphene.

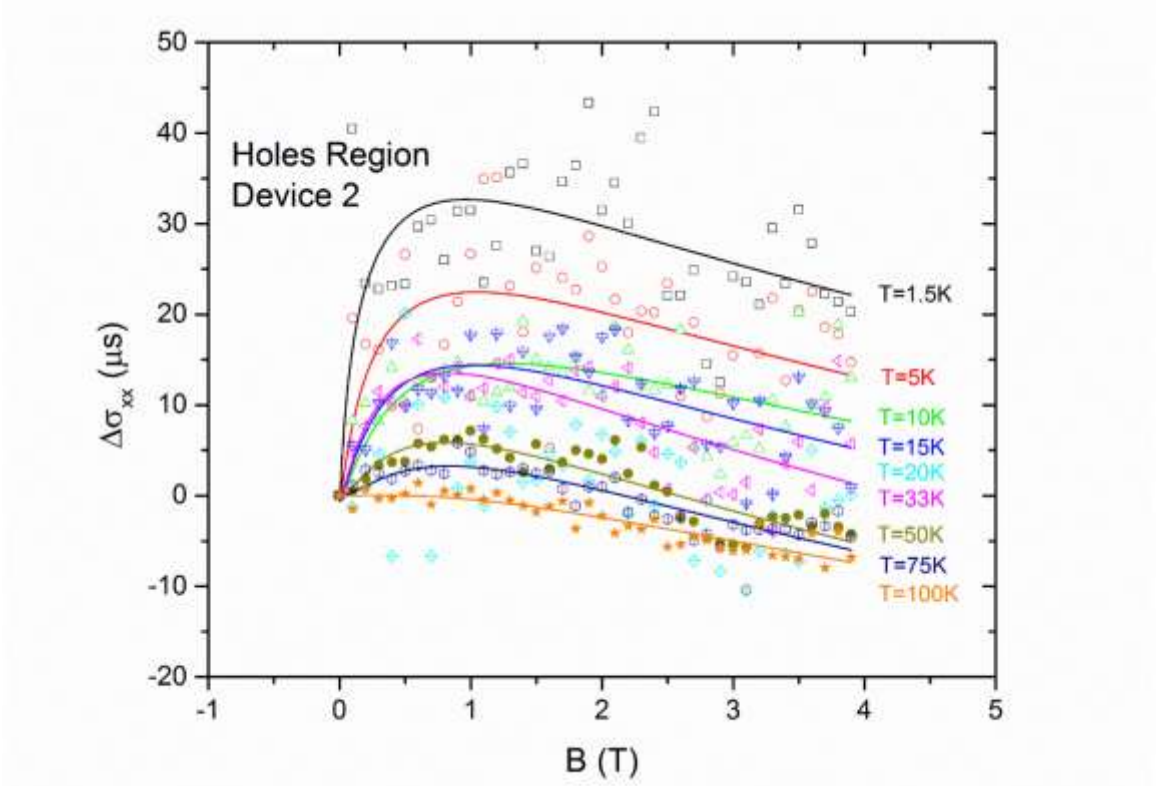
Holes Region
Device 2
T=1.5K
T=5K
T=10K
T=15K
T=20K
T=33K
T=50K
T=75K
T=100K
Δσxx (μs)
B (T)

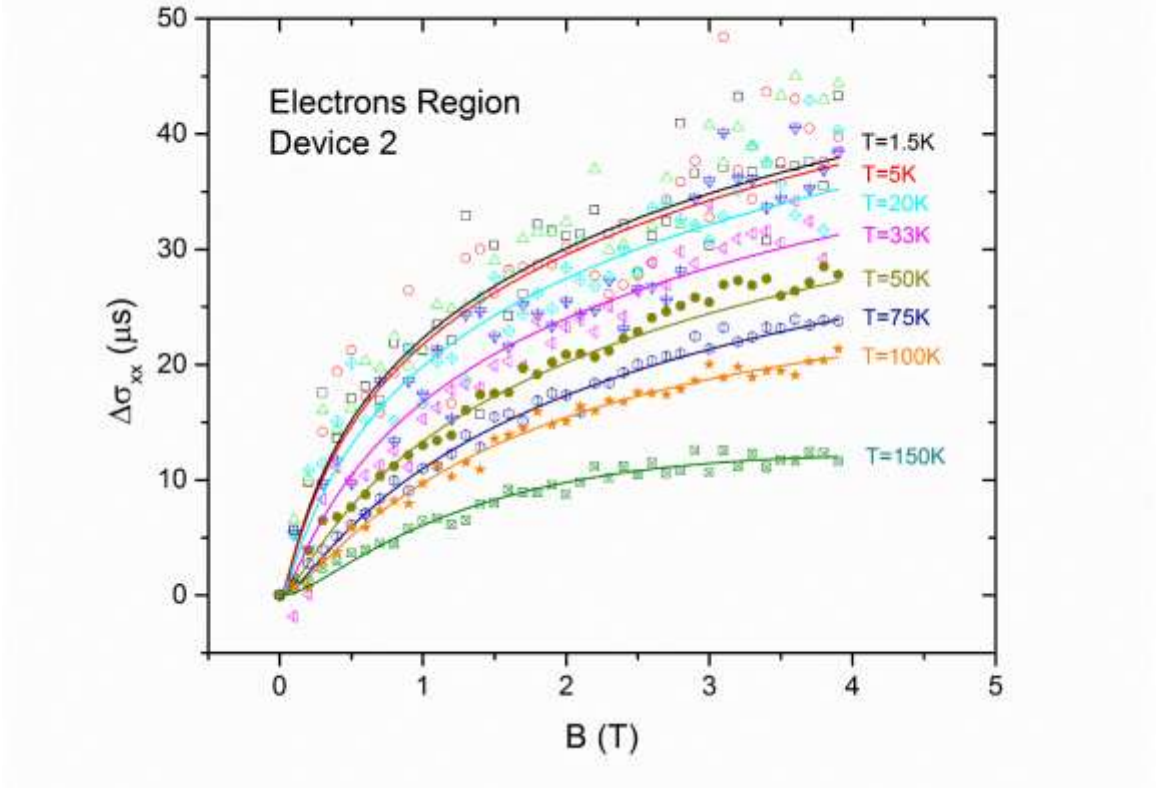
Electrons Region
Device 2
T=1.5K
T=5K
T=20K
T=33K
T=50K
T=75K
T=100K
T=150K
Δσxx (μs)
B (T)

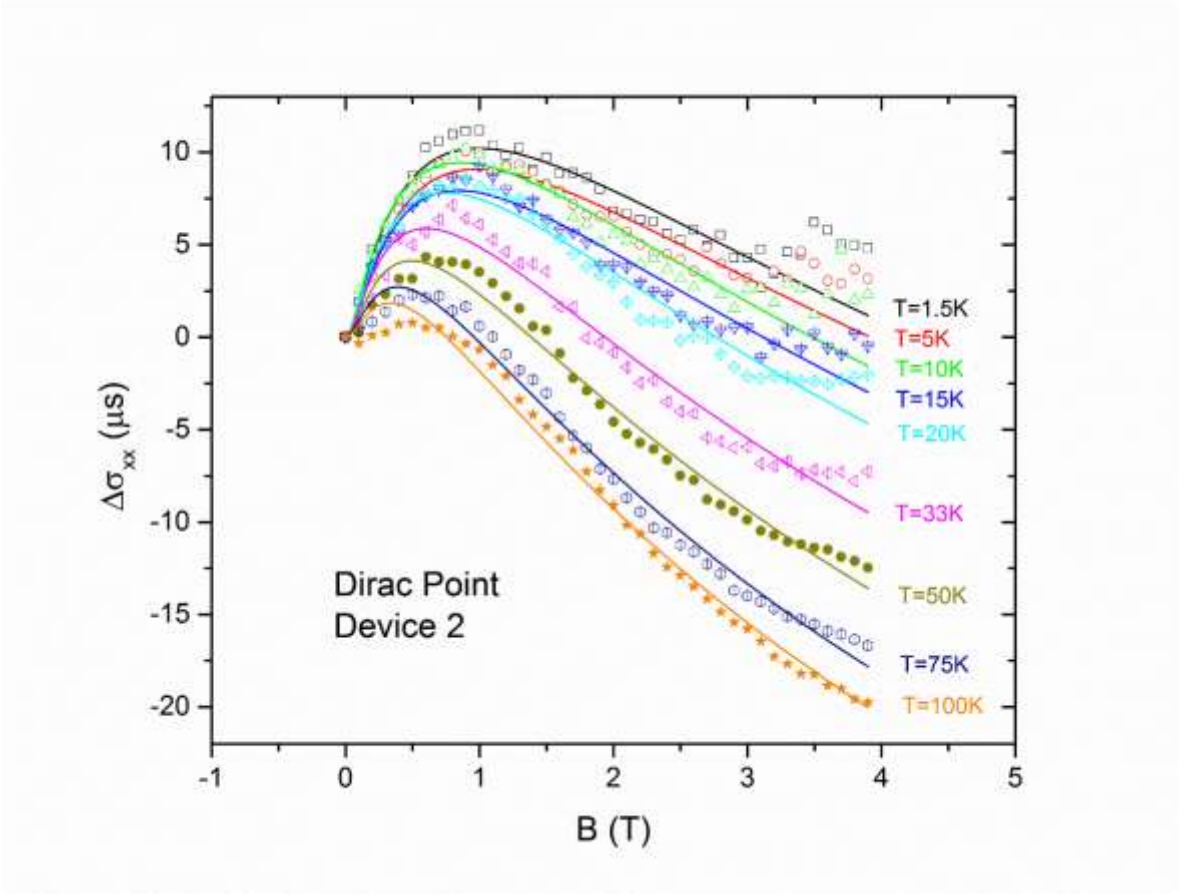

Figure 8.7– Conductivity vs magnetic field at different temperatures for Device 2 – moderately doped graphene. Points are measured points and solid lines are the fitted curves with the Weak Localization function. Measurements are done: far from Dirac point at in the hole's side (top), in the electrons side (middle) and at the Dirac point (bottom)

Fig. 8.8 and 8.9 shows these results for Device 3 (lightly doped) and Device 1 (heavily doped) respectively. As you notice, the more doping is, the high saturation field will be. That is, for lightly doped devices, we clearly see the Weak Localization (WL) and Weak Anti Localization (WAL) in holes and Dirac's region but not in electrons regions. These terminologies are described in chapter 7. In electrons regions device behaves like a metal, magnetic field doesn't saturate conductance which not in perfect agree with the localization theory. In Device 3 which contains higher dopants, even holes region also does not exhibit Weak Anti Localization. In Fig. 8.9 which

is the heavily doped device – Device 1, there is neither holes side nor electrons side not Dirac region show Weak Anti Localization.

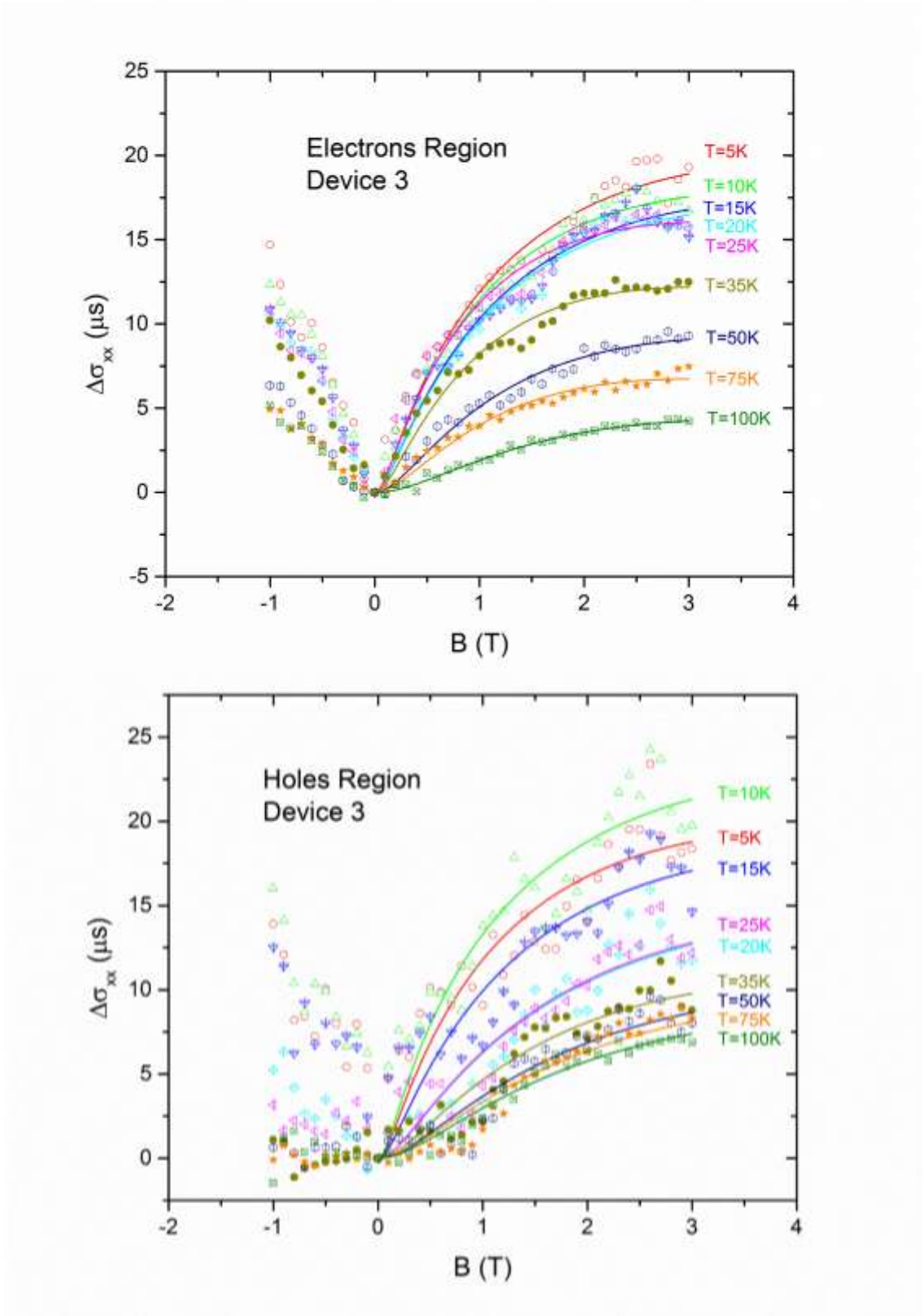

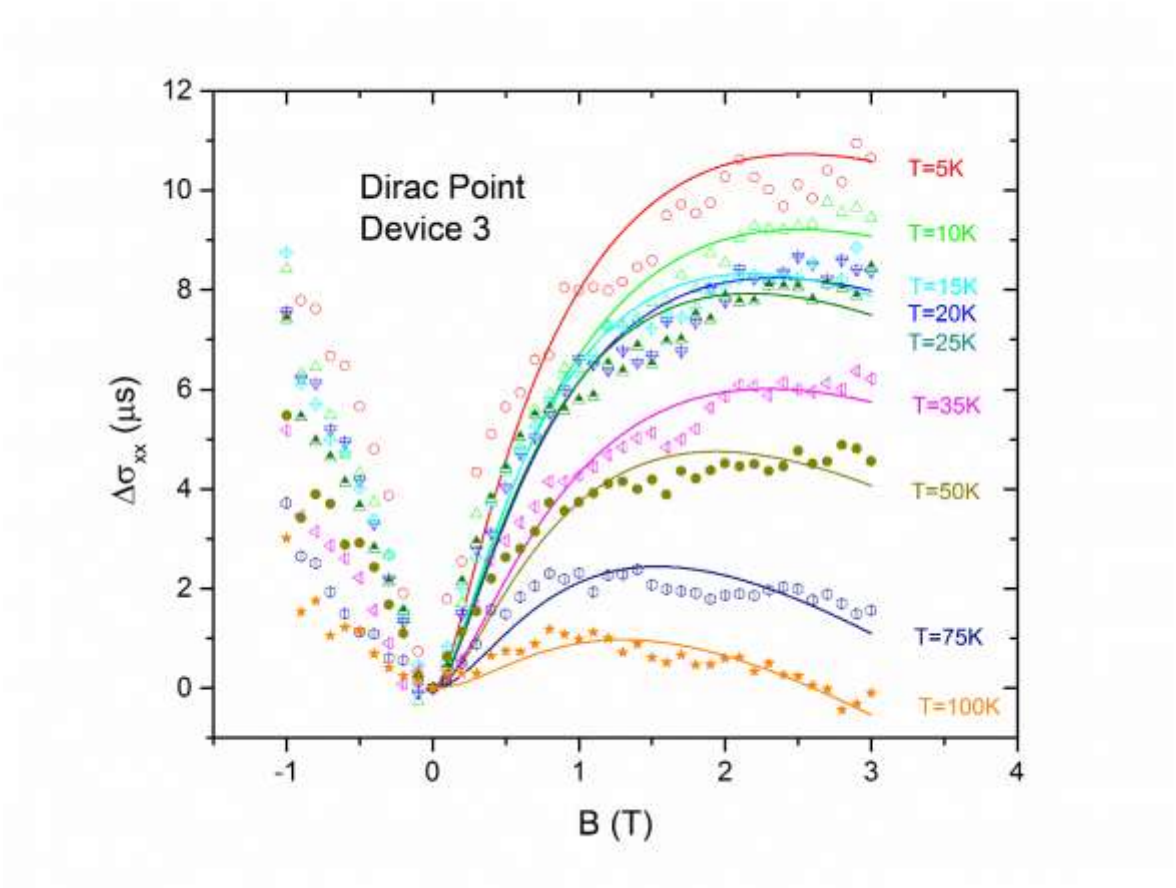

Figure 8.8– Conductivity vs magnetic field at different temperatures for Device 3 – lightly doped graphene. Points are measured points and solid lines are the fitted curves with the Weak Localization function. Measurements are done: far from Dirac point at in the hole's side (top), in the electrons side (middle) and at the Dirac point (bottom)

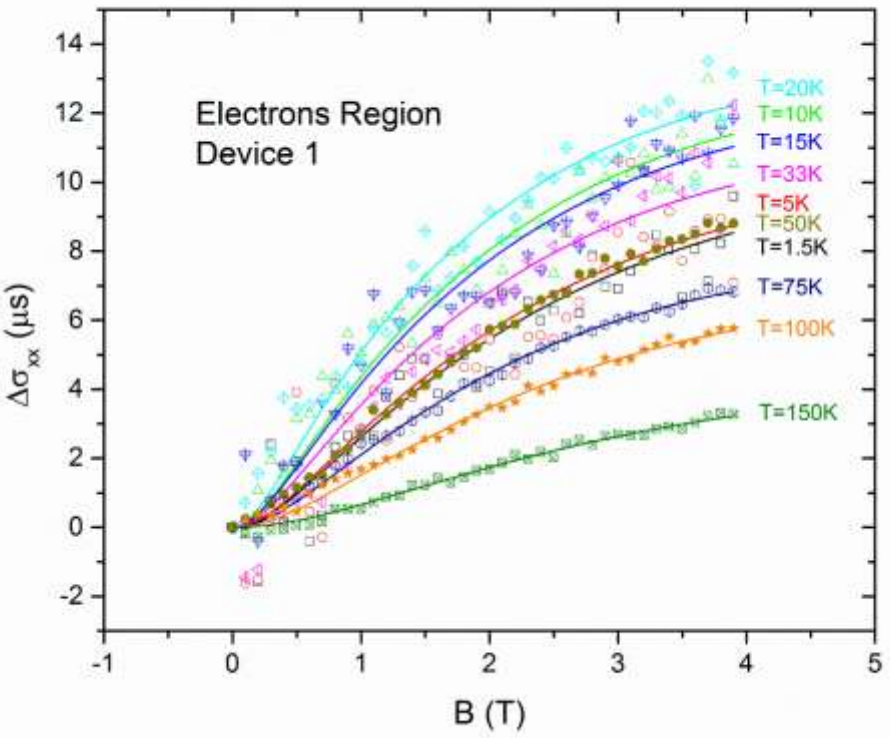
Electrons Region
Device 1
T=20K
T=10K
T=15K
T=33K
T=5K
T=50K
T=1.5K
T=75K
T=100K
T=150K
Δσxx (μS)
B (T)

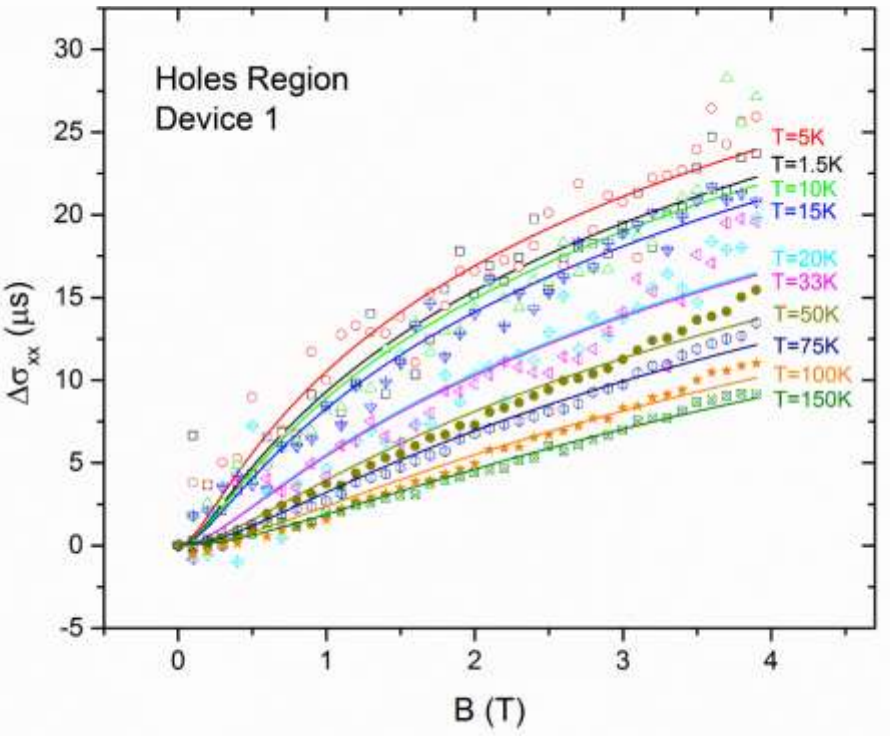
Holes Region
Device 1
T=5K
T=1.5K
T=10K
T=15K
T=20K
T=33K
T=50K
T=75K
T=100K
T=150K
Δσxx (μS)
B (T)

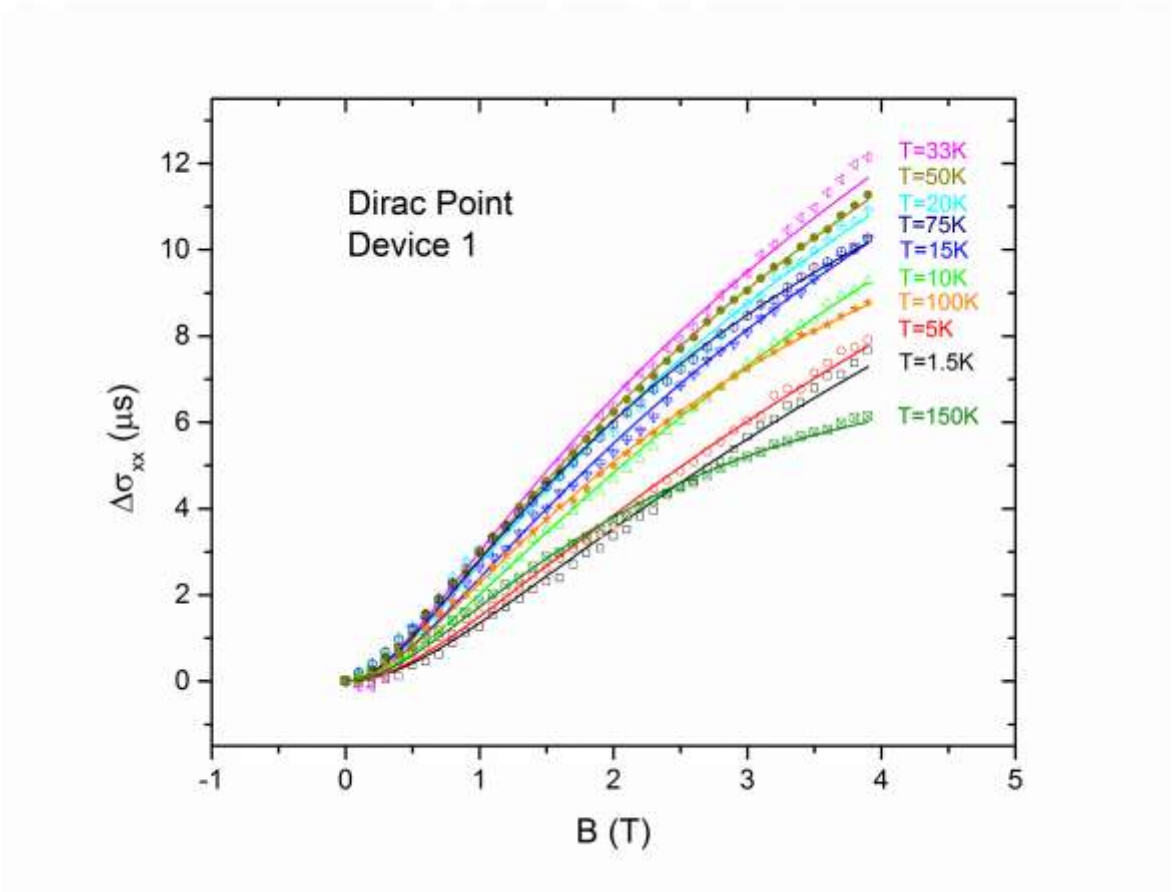

Figure 8.9– Conductivity vs magnetic field at different temperatures for Device 1 – heavily doped graphene. Points are measured points and solid lines are the fitted curves with the Weak Localization function. Measurements are done: far from Dirac point at in the hole's side (top), in the electrons side (middle) and at the Dirac point (bottom)

In the next step, we would like to compare the magneto conductivity in electrons, holes and Dirac region in one graph and at a specific temperature. To follow our order, we first present Device 2 – lightly doped, then Device 3 – moderately doped, followed by Device 3 – heavily doped. Fig. 8.10, 8.11, 8.12 show magneto conductivity graphs for Device 2, 3, 1 respectively at different temperatures. Graphs show strong asymmetry between electrons and holes region. They also depict how the localization and magneto conductivity change with the increasing temperature.

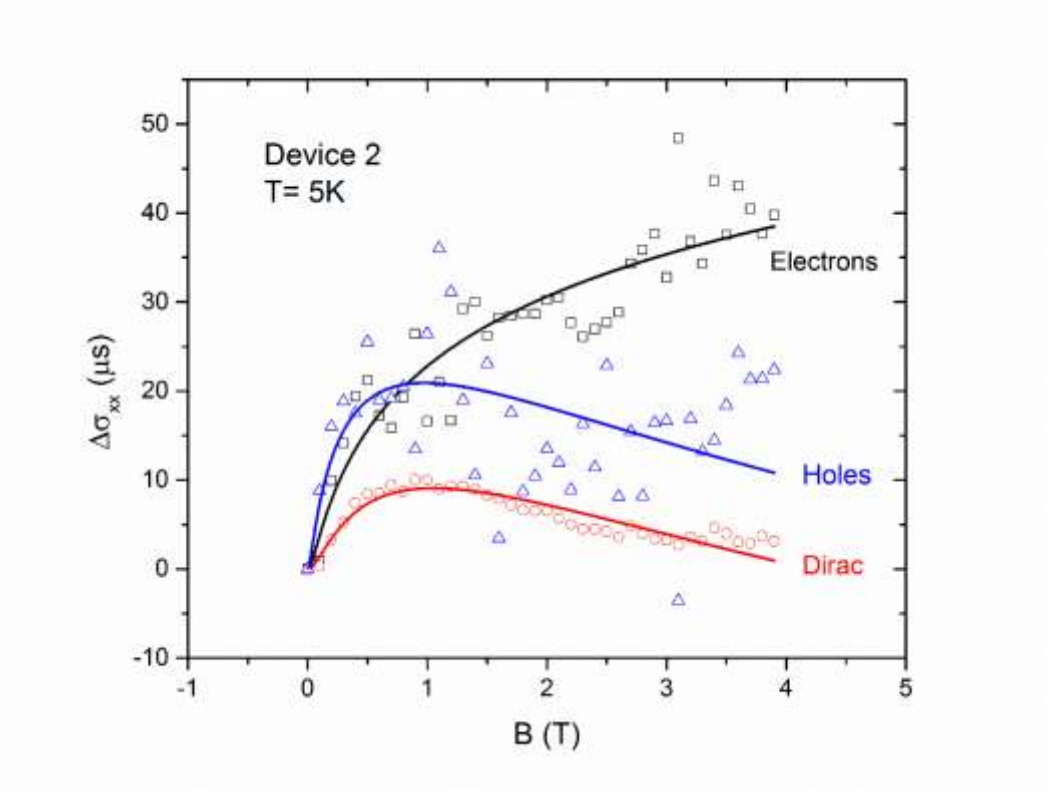
Device 2
T= 5K
Electrons
Holes
Dirac
Δσxx (μs)
B (T)

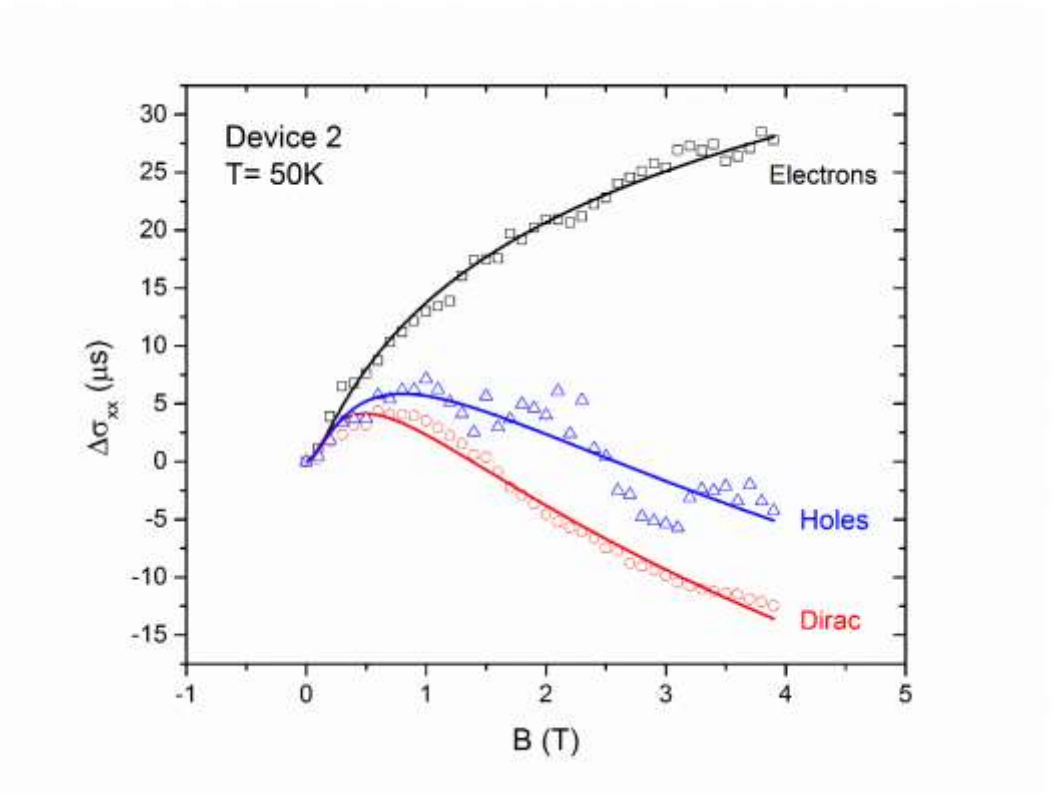
Device 2
T= 50K
Electrons
Holes
Dirac
Δσxx (μs)
B (T)

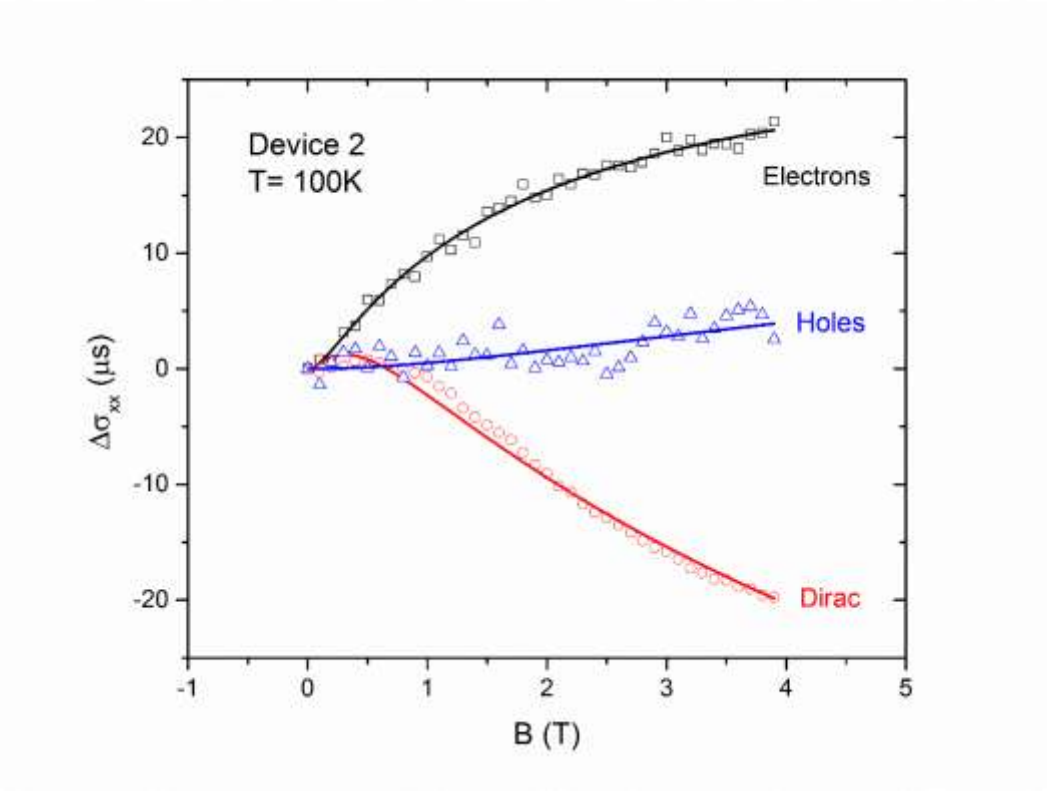

Figure 8.10– Magneto conductivity of Device 2 at 5K (top), 50K (middle) and 100K (bottom). Graphs show strong asymmetry in different regions and how the behavior changes with increasing temperature. Electrons region never show WAL effects.

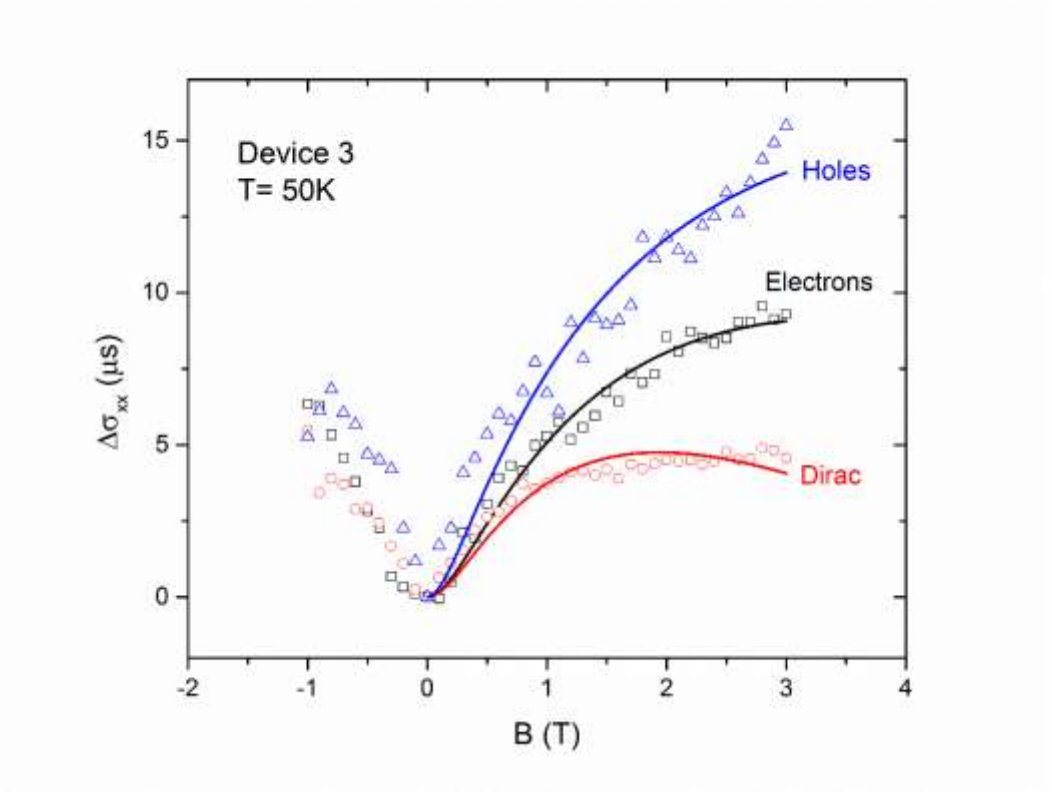
Device 3
T= 50K
Holes
Electrons
Dirac
Δσxx (μS)
B (T)

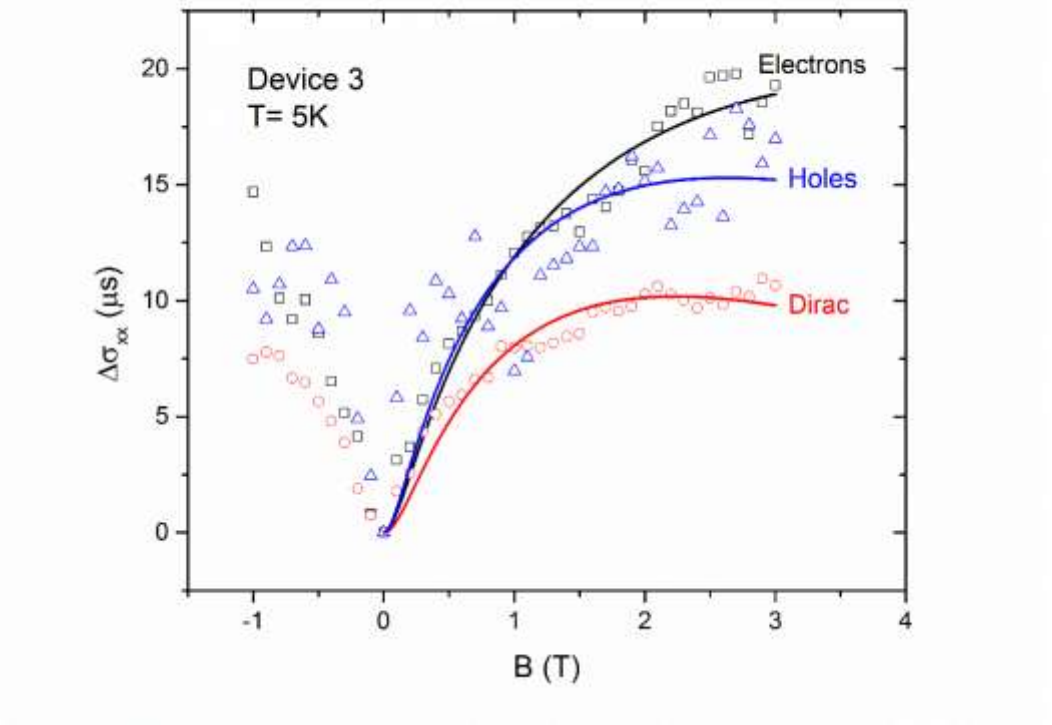
Device 3
T= 5K
Electrons
Holes
Dirac
Δσxx (μS)
B (T)

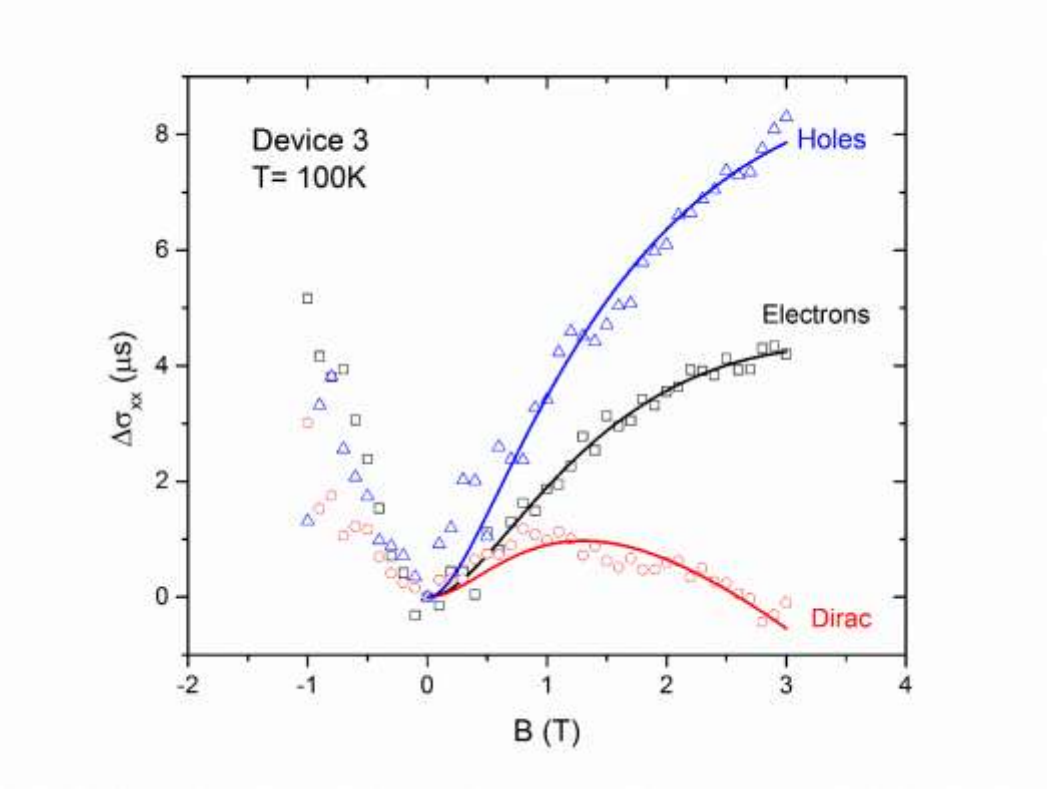

Figure 8.11– Magneto conductivity of Device 3 at 5K (top), 50K (middle) and 100K (bottom). Graphs show strong asymmetry in different regions and how the behavior changes with increasing temperature. Electrons region never show WAL effects.

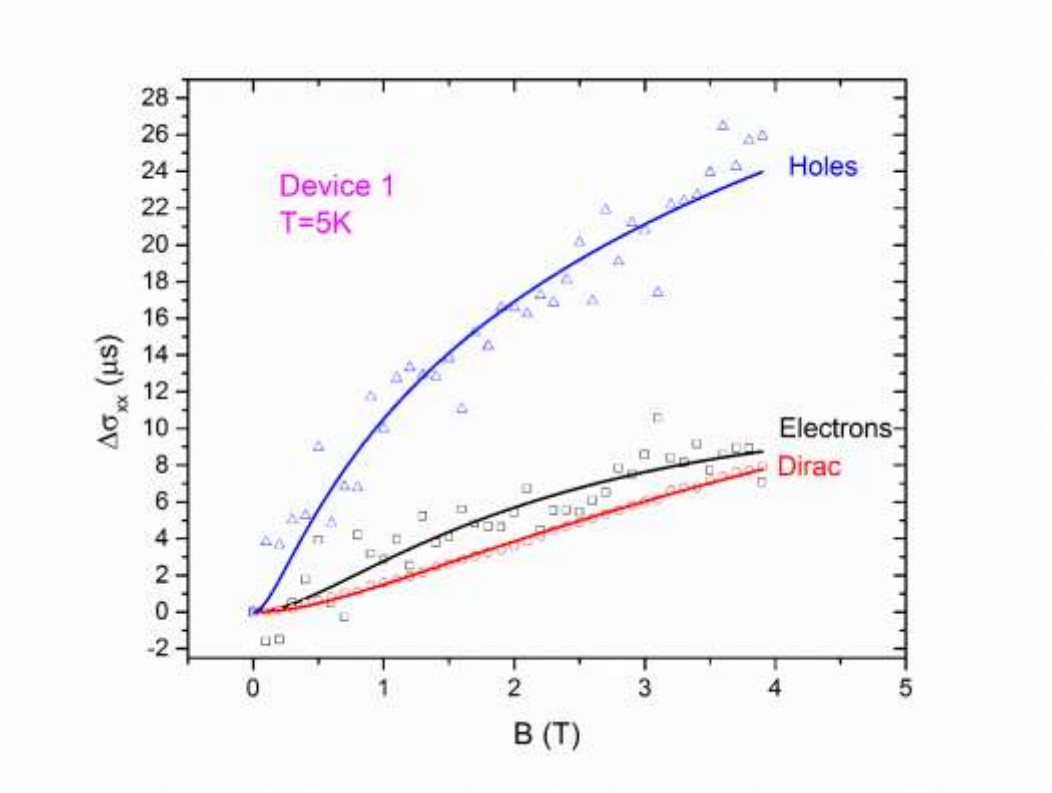
Device 1
T=5K
Holes
Electrons
Dirac
Δσxx (μS)
B (T)

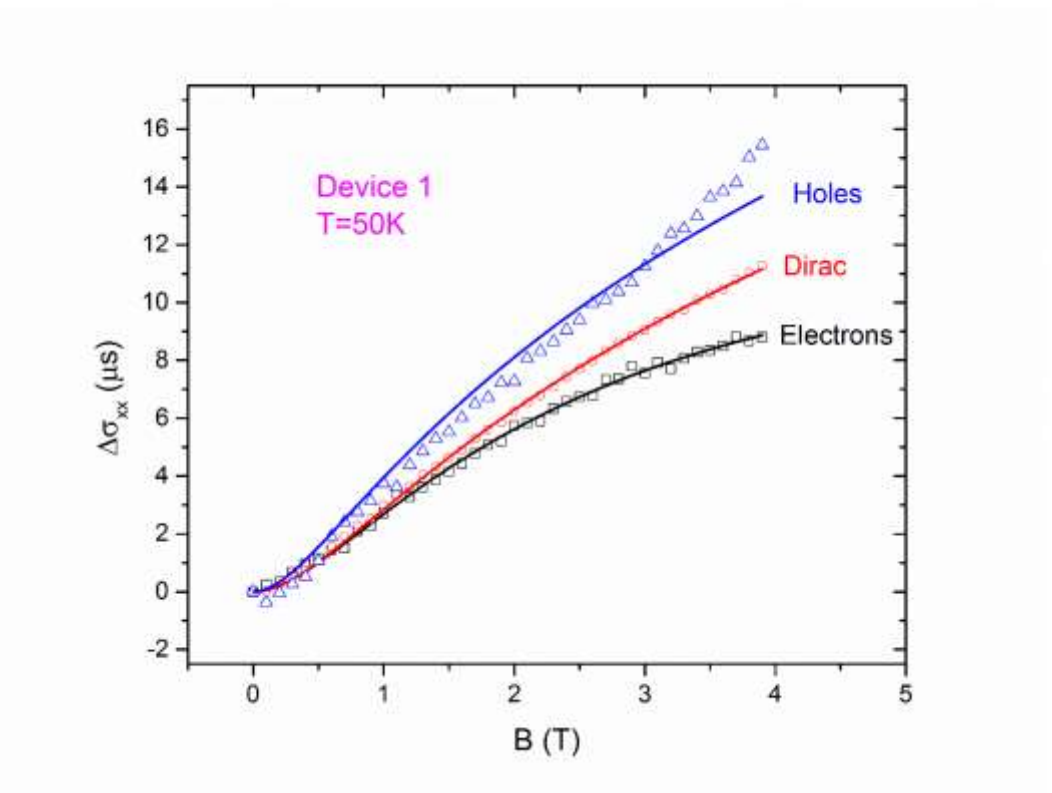
Device 1
T=50K
Holes
Dirac
Electrons
Δσxx (μS)
B (T)

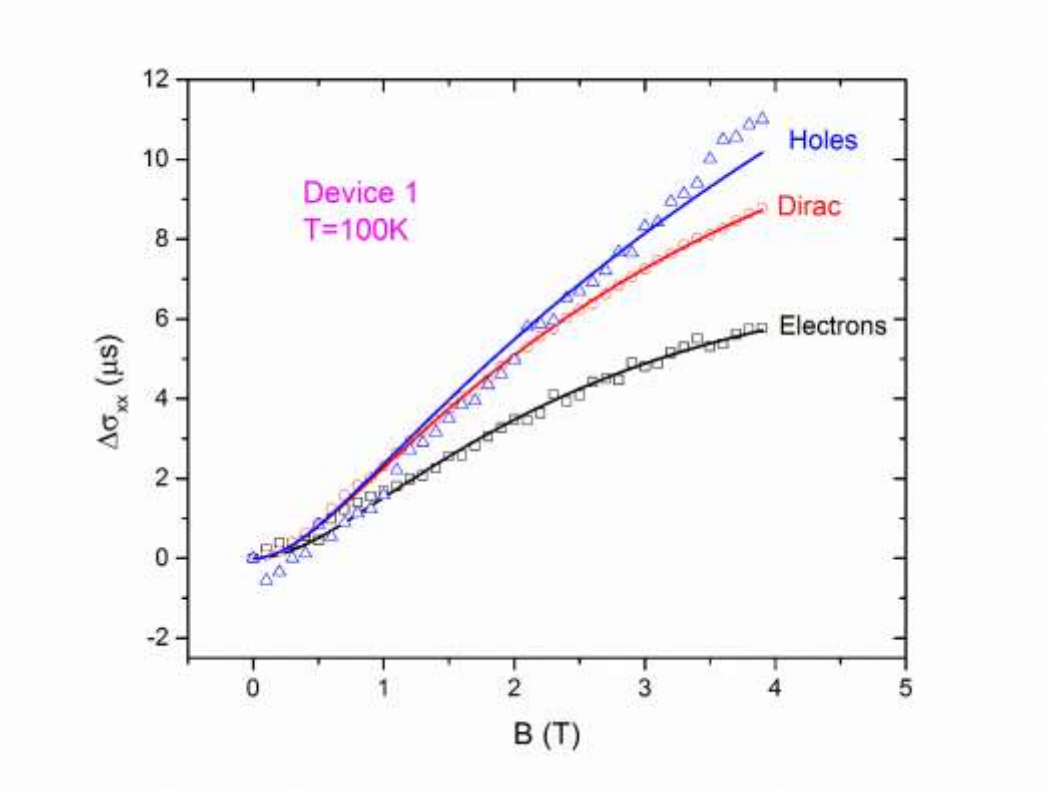

Figure 8.12– Magneto conductivity of Device 1 at 5K (top), 50K (middle) and 100K (bottom). Graphs show strong asymmetry in different regions and how the behavior changes with increasing temperature. None of the regions show WAL effects – magneto conductivity increases with magnetic field at all regions.

Concretely, more nitrogen dopant level which introduces higher amount of impurities to the system, changes localization properties of graphene and violates Weak Localization theory [78]. In order to dig more in detail of Weak Localization theory, we would extract characteristics parameters from that theory in the next section.

Now that we have fitted Weak Localization curves to the measured points, we can extract scattering lengths according to the Weak Localization theory explained in Chapter 7. The scattering lengths of interest according to the theory are:

$L_{\emptyset}$: inelastic scattering length,

L_i : elastic scattering length or intervalley scattering,

L_w : intra-valley scattering length,

L_s : characteristics lengths for spin-flip-rate

$L_*^{-2} = L_s^{-2} + L_w^{-2}$

we would like also calculate the rate of each scattering mechanisms. From Fick's Law:

$$\tau^{-1} = DL^{-2}$$

$$D = v_F\, l/2$$

$$l = \frac{\sigma h}{k_F 2e^2}$$

$$\sigma = \frac{AR}{R(0)}$$

$$k_F = \sqrt{\pi n}$$

Where D is *diffusion constant*, v_F is *Fermi velocity* in which for graphene: $v_F = 1.5 \times 10^6 m/s$, l is *mean free path*, h is Plank's constant, e is electron charge, k_F is Fermi wave vector and n is carrier density. Then, given scattering length, carrier density, measured resistivity, we can calculate the corresponding scattering rate.

Fig. 8.13 shows the analyzed scattering lengths for Device 2. As explained we used these numbers to calculate associated scattering rates which are presented in Fig. 8.14. Similar results for Device 3 and Device 2 are shown in Fig. 8.15, 8.16, 8.17, 8.18.

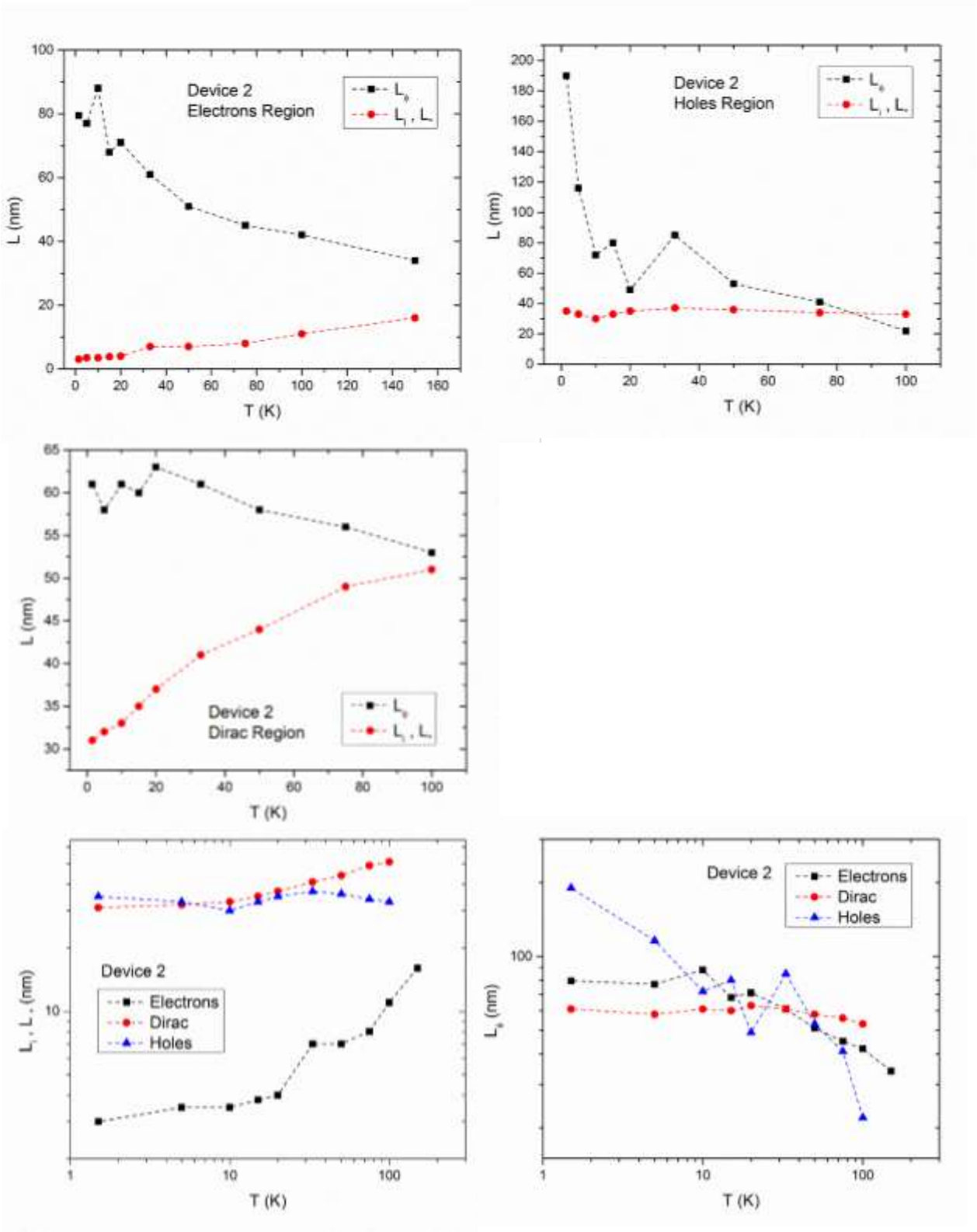

Figure 8.13– Various scattering lengths for Device 2 – lightly doped graphene at different regions.

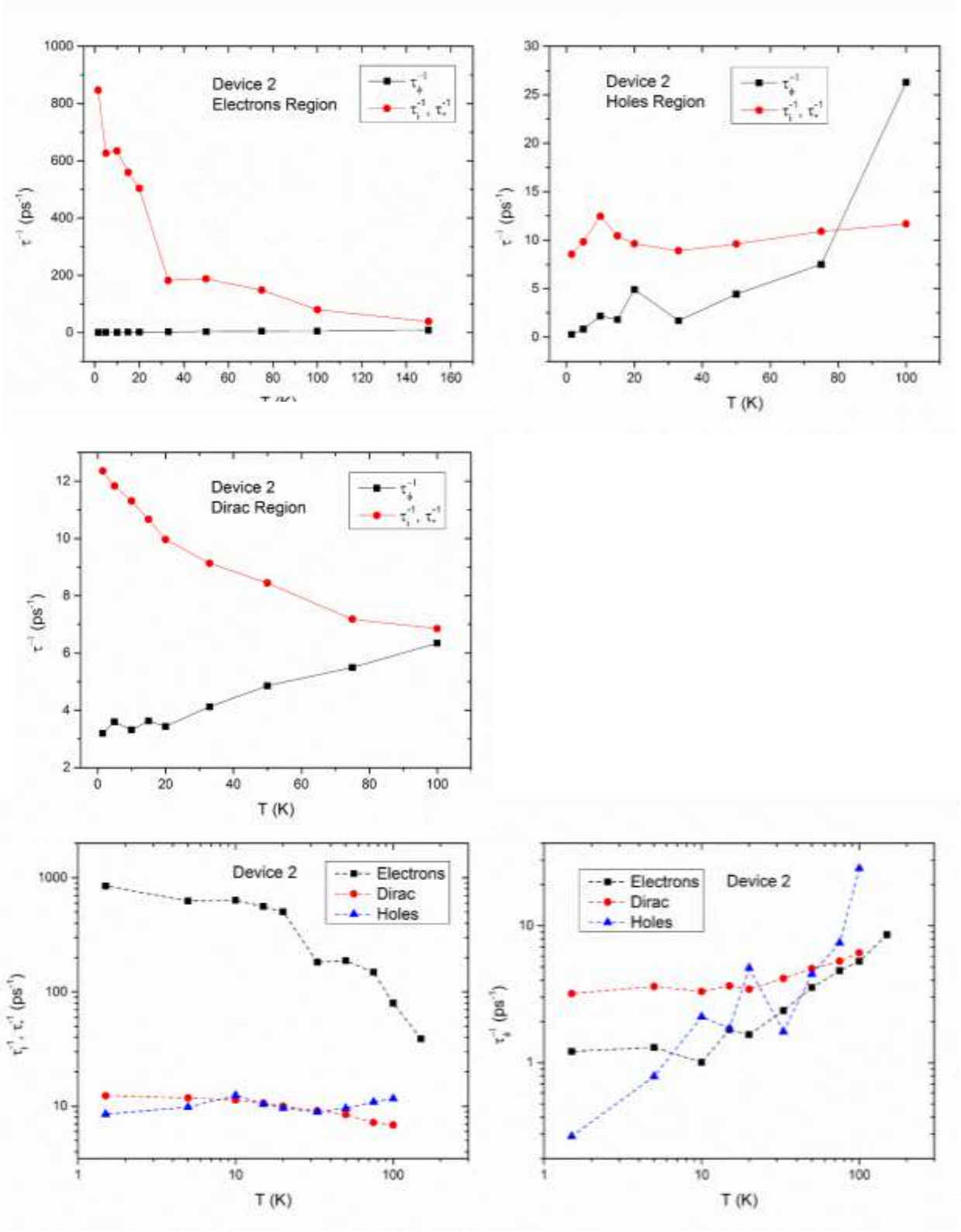

Figure 8.14– Various scattering rates for Device 2 – lightly doped graphene at different regions.

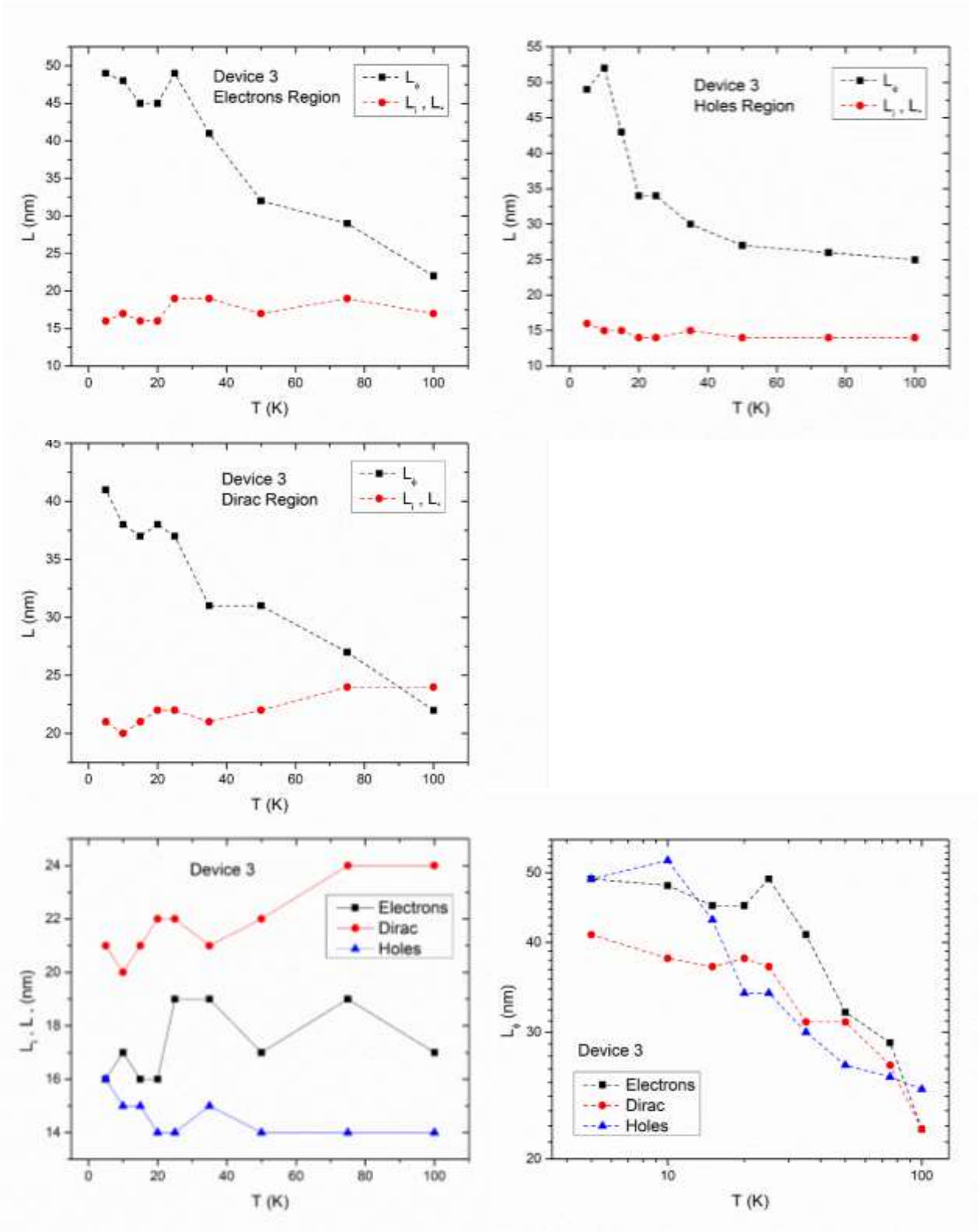

Figure 8.15– Various scattering lengths for Device 3 – moderately doped graphene at different regions.

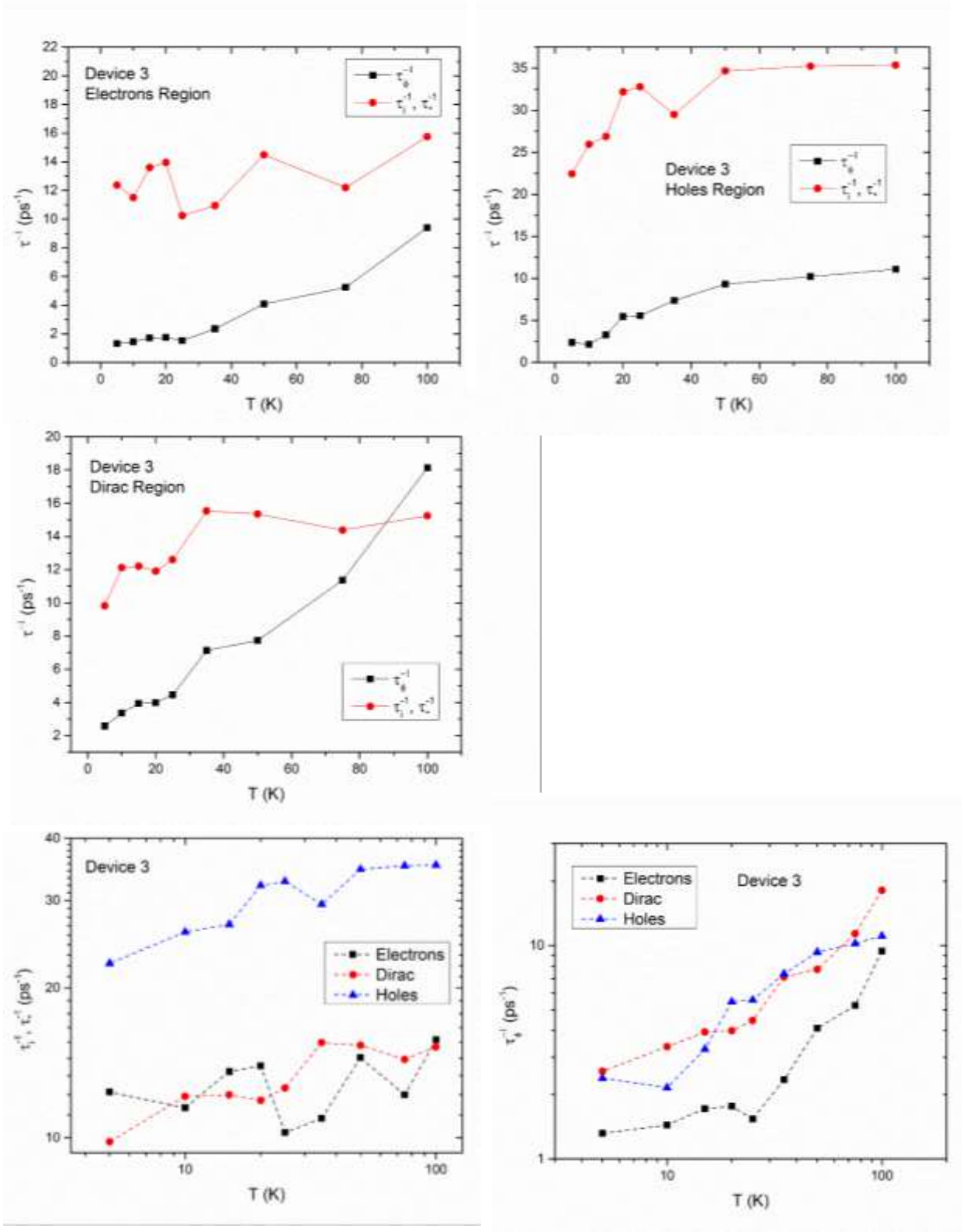

Figure 8.16– Various scattering rates for Device 3 – moderately doped graphene at different regions.

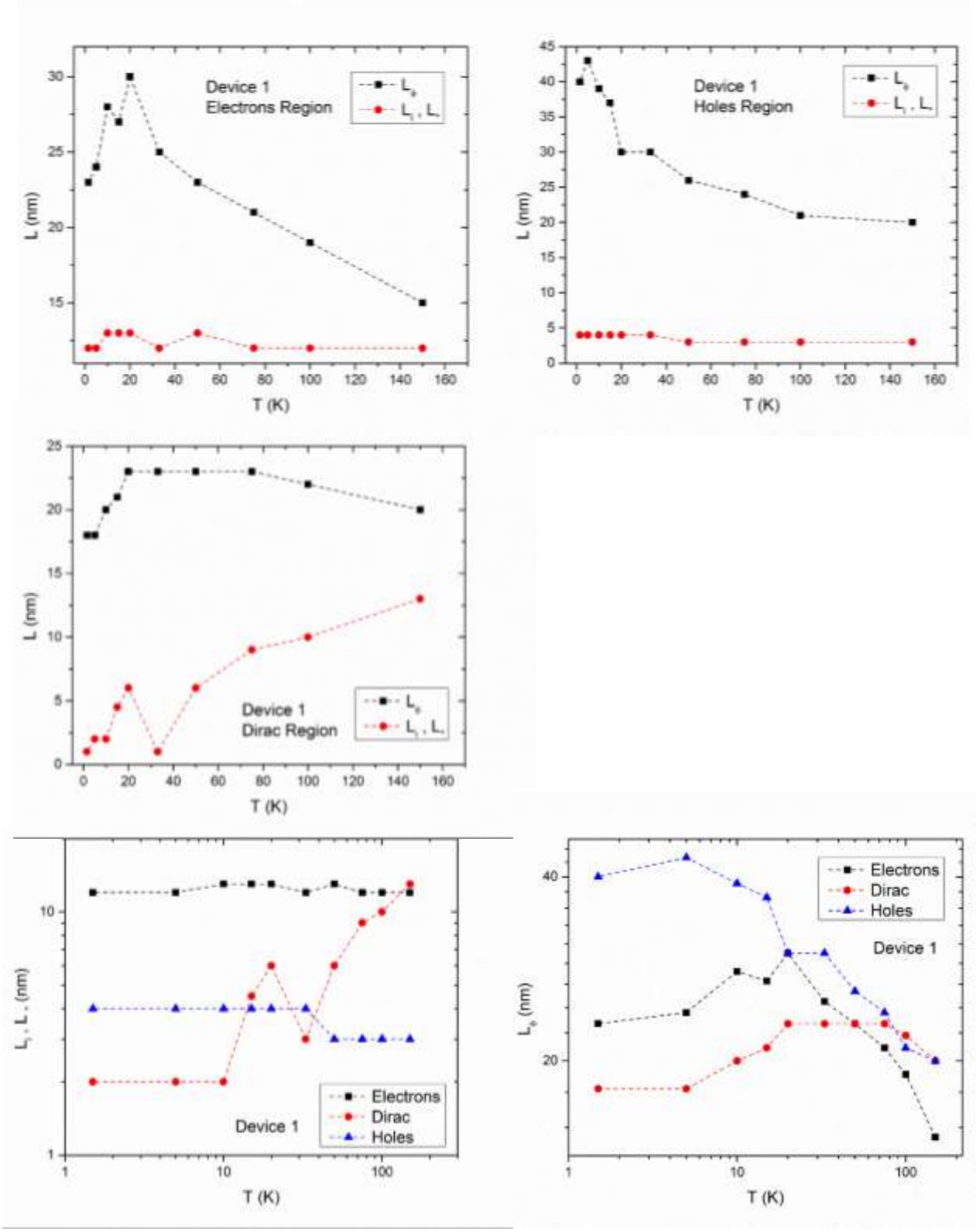

Figure 8.17– Various scattering lengths for Device 1 – heavily doped graphene at different regions.

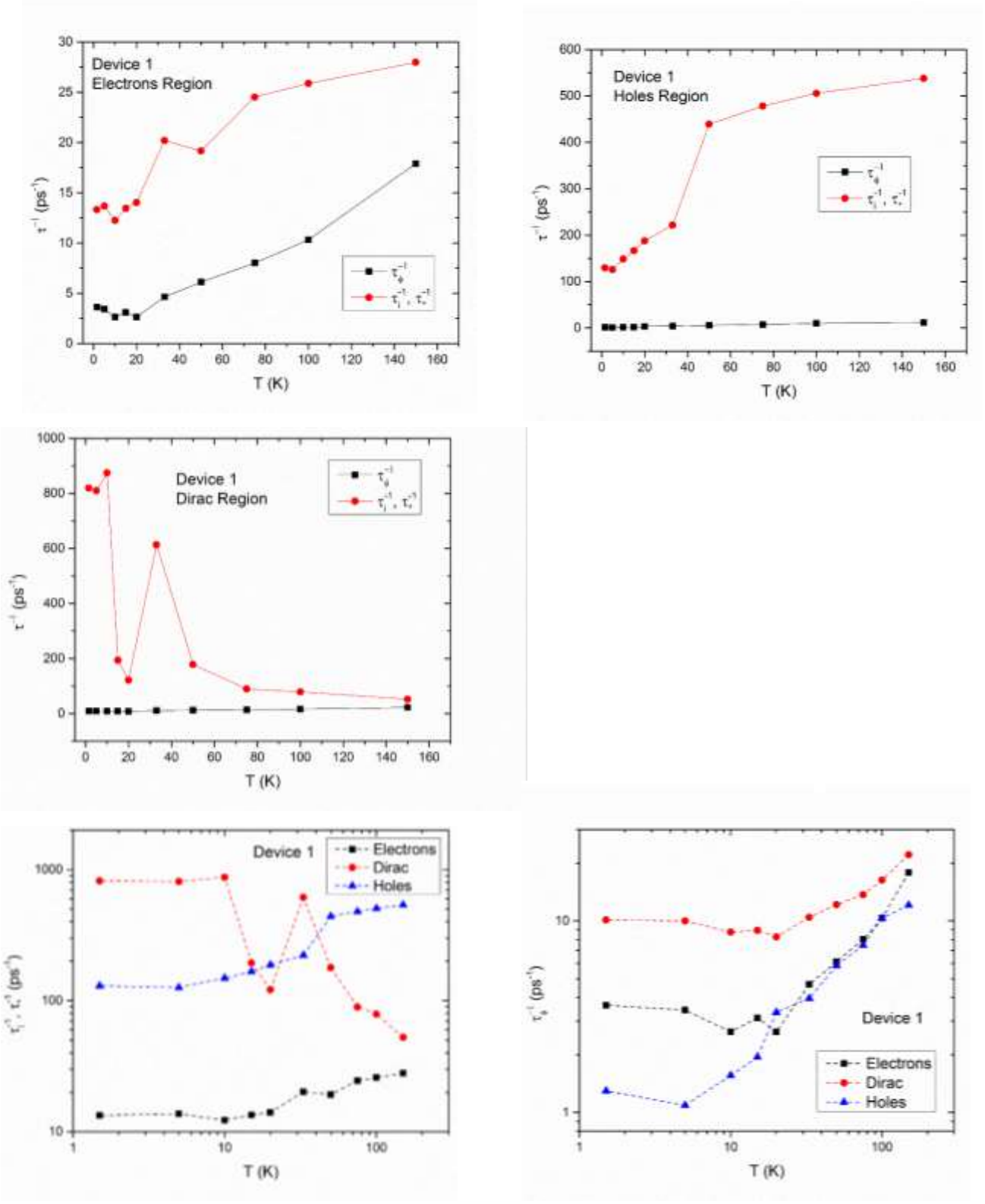

Figure 8.18– Various scattering rates for Device 1 – heavily doped graphene at different regions.

Contemplating what we've got so far reveals some unusual results about scattering lengths:

- For lightly doped device – Device 2, elastic scattering lengths remain unchanged for Dirac and Holes regions; meanwhile, it increases for Electrons region.
- For moderately doped device – Device 3, elastic scattering lengths in all regions remain unchanged with increasing temperature
- For lightly doped Device – Device 2, inelastic scattering length do not change with temperature for Dirac and Electrons region – only Holes regions show reasonable results (decrease with temperature)
- For heavily doped device – Device 1, inelastic scattering length increases for Electrons and Dirac region while it decreases for Holes region

Concretely, the sources of these calculation which is the Weak Localization theory, might not be a good fit for doped graphene with impurities.

Before investigating a theory that matches our results, we would like to check the oscillation behaviors of magneto conductivity at different carrier densities and various magnetic fields.

Oscillation of Conductivity

In order to study the conductivity oscillation, we focus on Device 2 and 3, lightly and moderately doped devices since the heavily doped device – Device 1 exhibits totally different behaviors as we noticed. For each of Device 2 and 3, we investigate oscillation of conductivity under the following conditions:

- Conductivity versus carrier densities at zero magnetic field – done at different temperatures.

$$\sigma(n)_{B=0}\big|_T$$

- Conductivity versus magnetic field at Electrons and Holes regions – done at different temperatures.

$$\sigma(B)_{n,p}\big|_T$$

In order to get these data, we first need to remove the background conductivity to generate pure oscillations. We used various mathematical filters. A combination of following functions worked the best for our set of data:

- Low-pass filter with various spans
- Local regression using weighted linear least squares and 2nd degree polynomial fit
- Savitsky-Golay filter

Once we remove the background conductivity at each of the above mentioned cases, we have to investigate if there is fundamental oscillation – or it is just a noise. For this we use autocorrelation function as follow to probe the period of oscillation – if there is any.

$$A(x) = \frac{\int f(x')f(x'+x)dx'}{\int |f(x')|^2 dx'}$$

After finding all oscillation behaviors we will compare all them together.

Conductivity versus Carrier Densities – zero field $\sigma(n)_{B=0}\big|_T$

Fig. 8.19, 8.20 and 8.21 show these results at 5K, 15K and 33K for Device 2 and consequently, Fig. 8.22, 8.23, 8.24 show the same results at the same temperatures for Device 3.

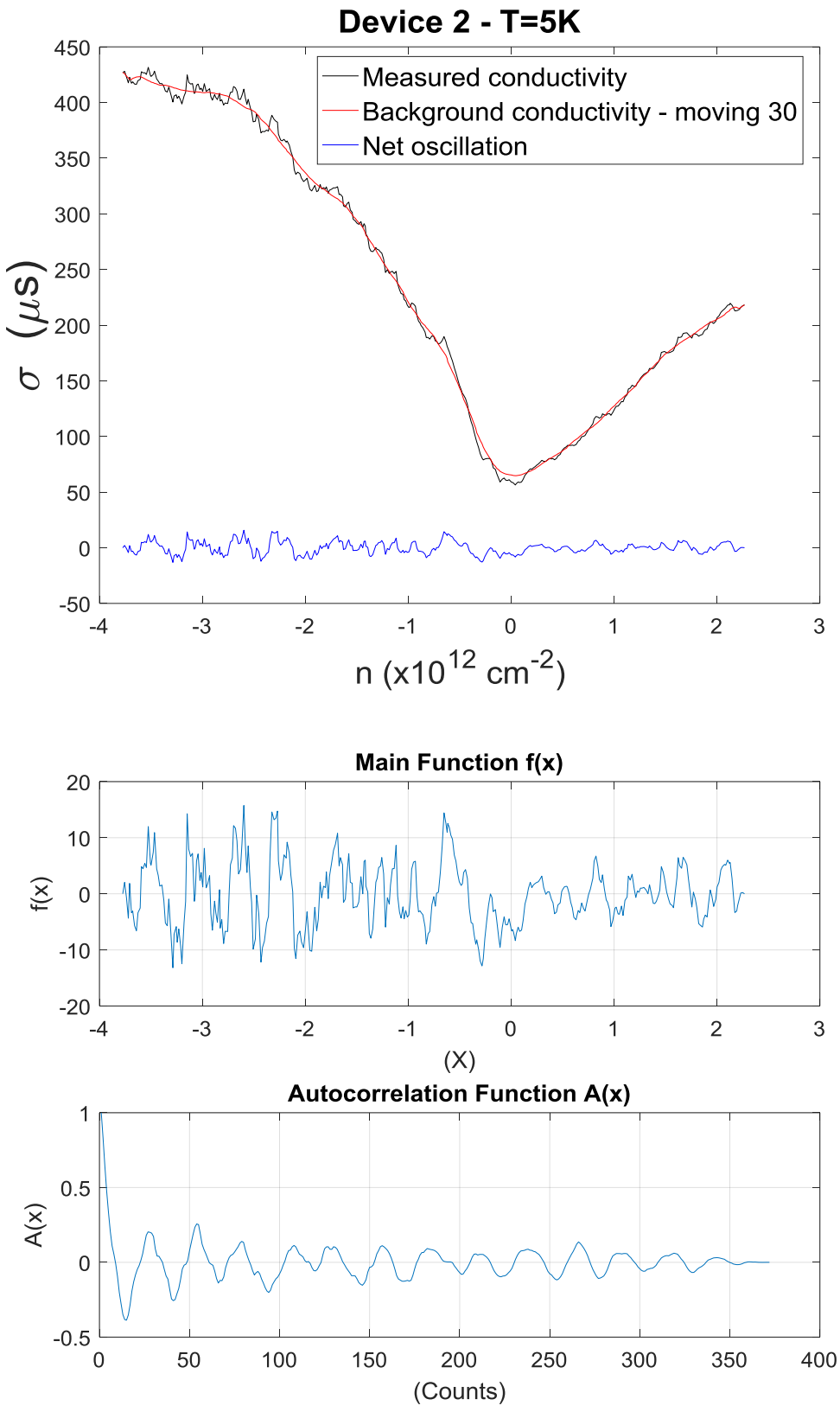

Figure 8.19– Device 2, constructing the conductivity oscillation versus carrier densities at 5K

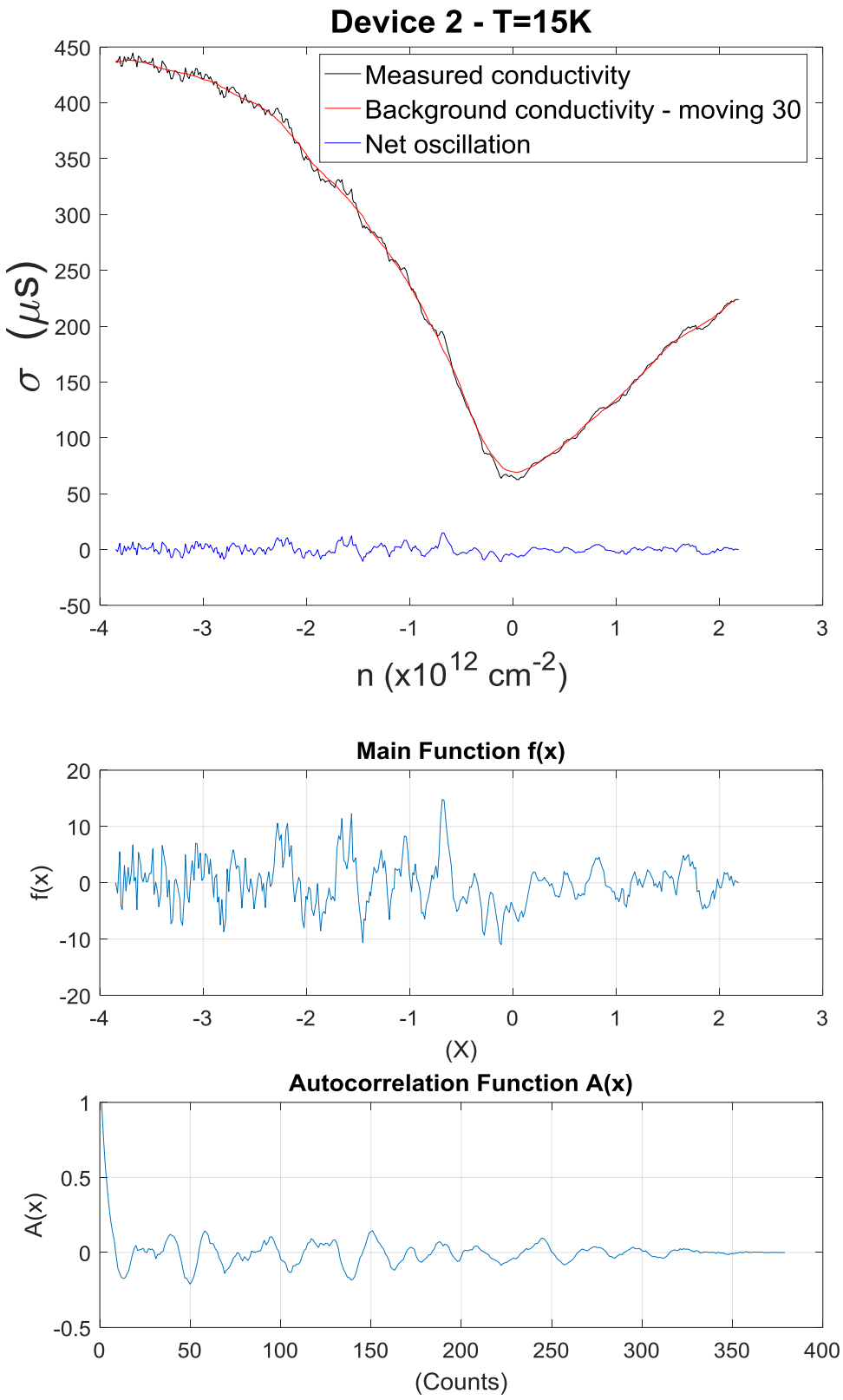

Figure 8.20– Device 2, constructing the conductivity oscillation versus carrier densities at 15K

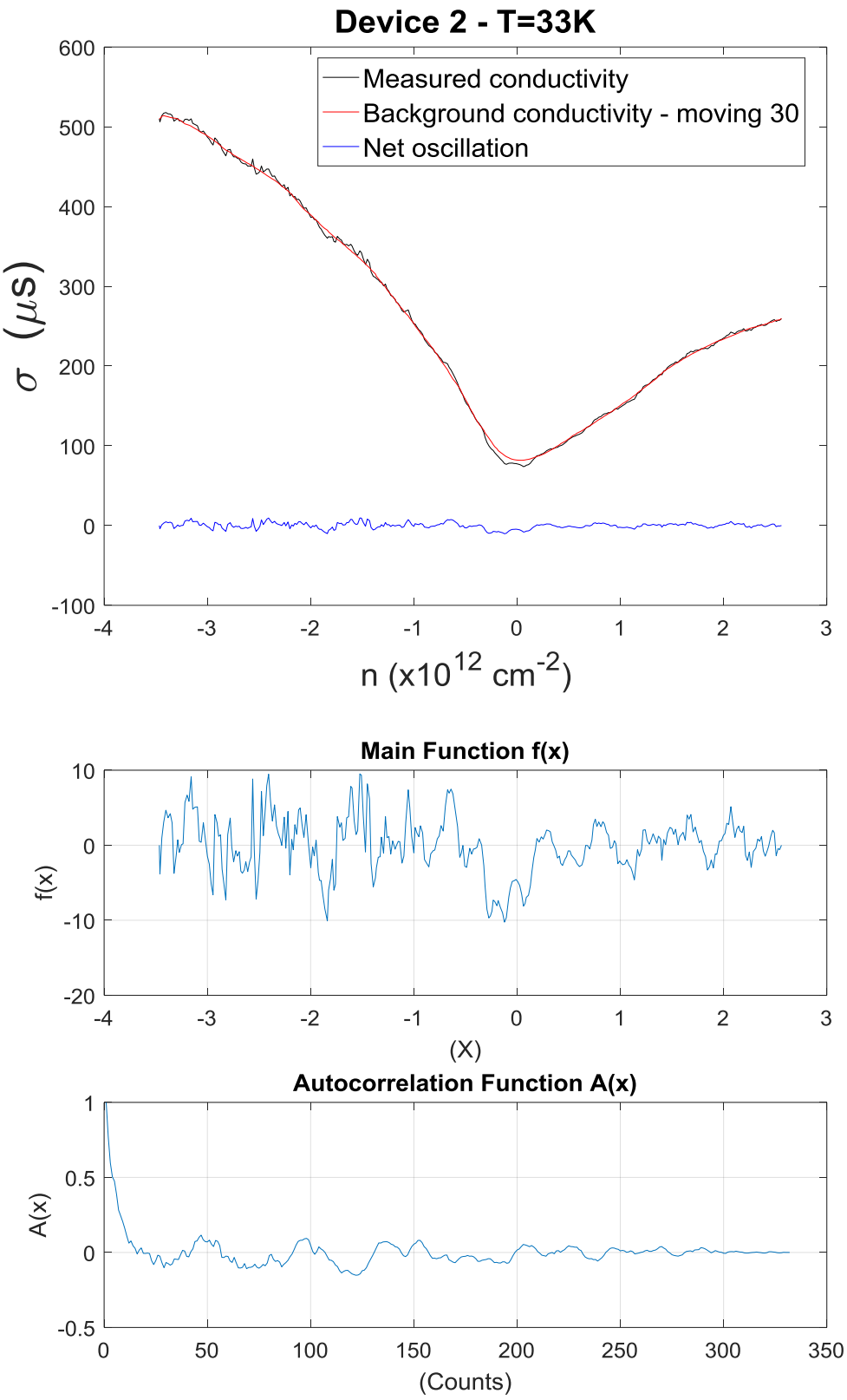

Figure 8.21– Device 2, constructing the conductivity oscillation versus carrier densities at 33K

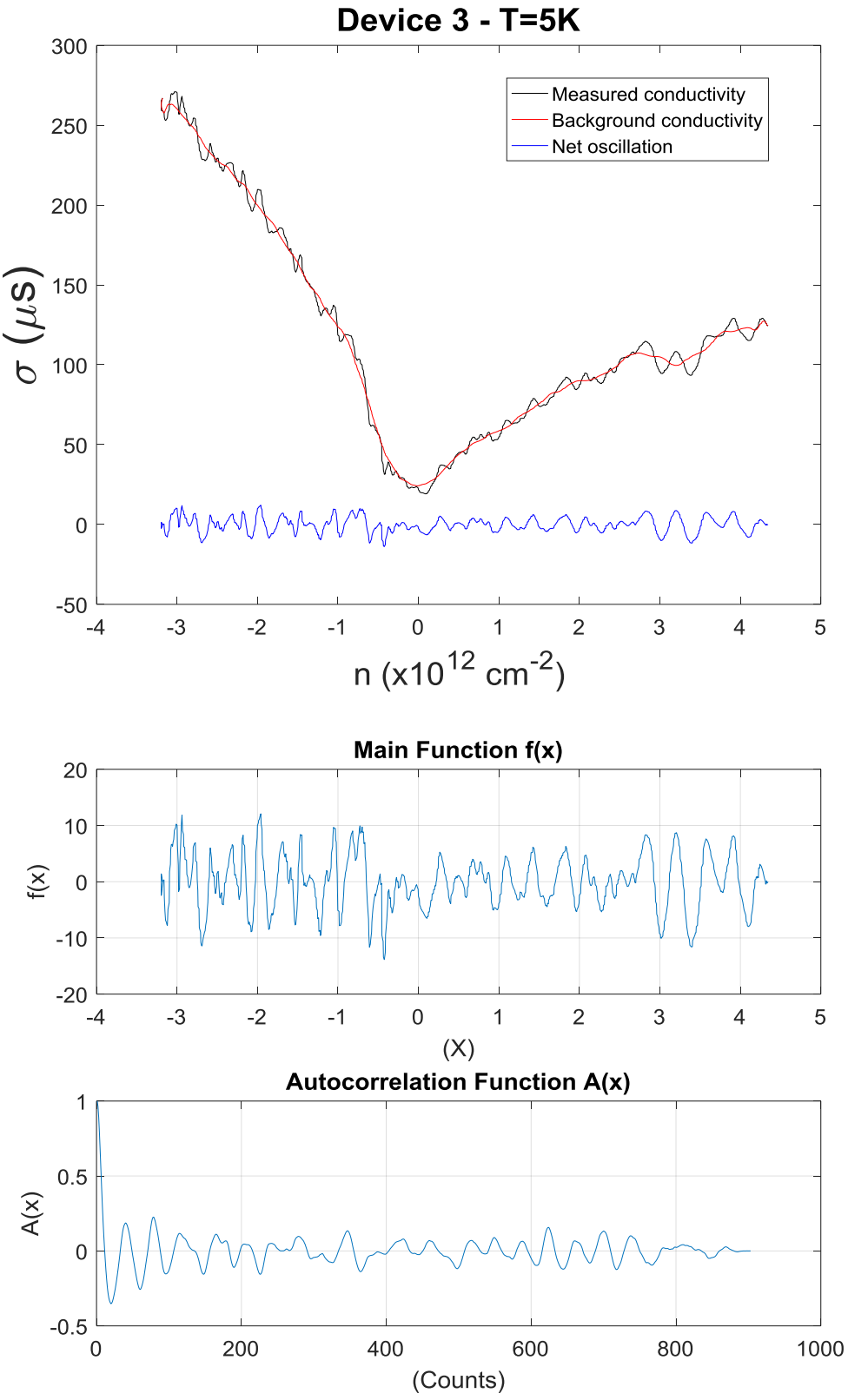

Figure 8.22– Device 3, constructing the conductivity oscillation versus carrier densities at 5K

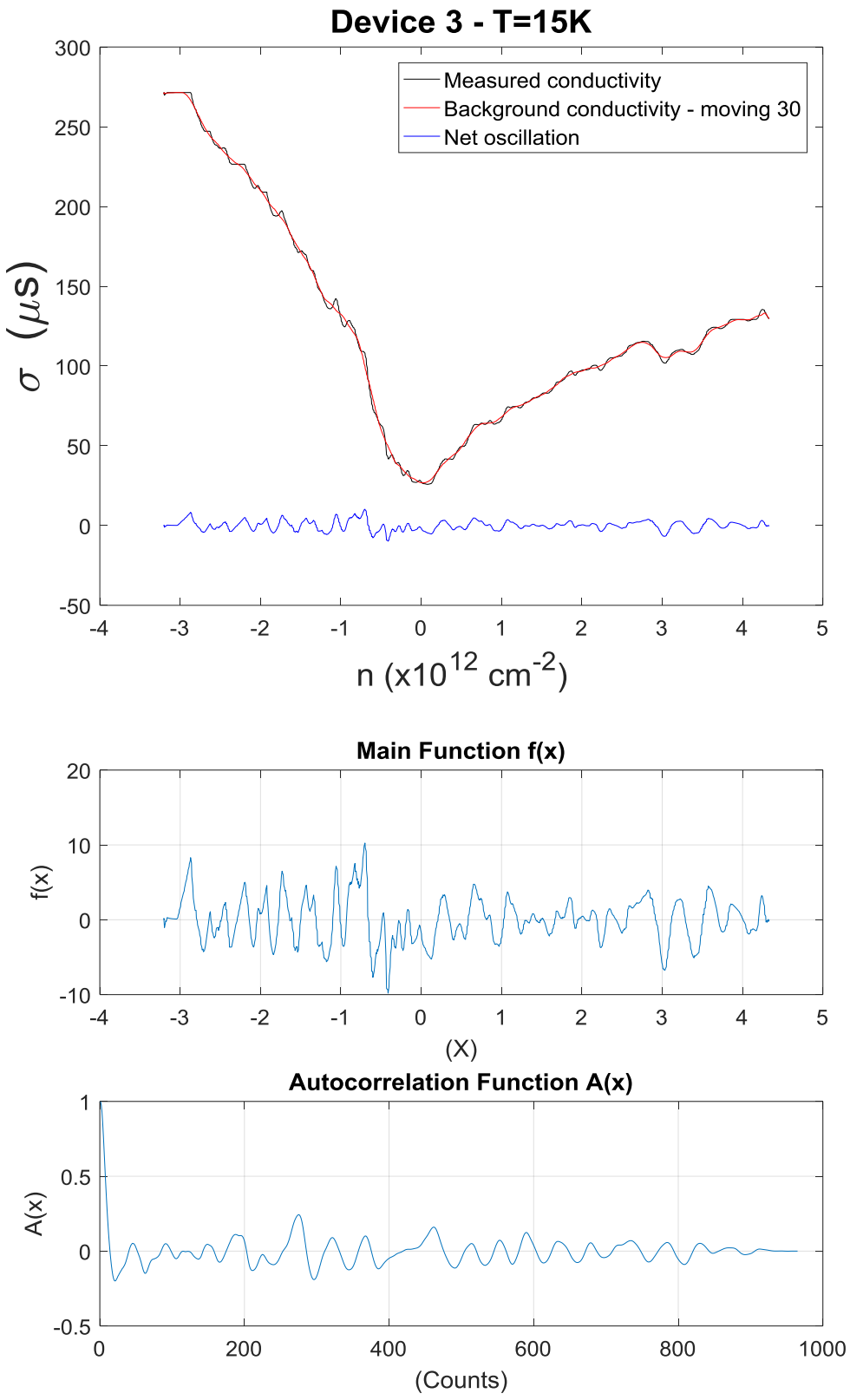

Figure 8.23– Device 3, constructing the conductivity oscillation versus carrier densities at 15K

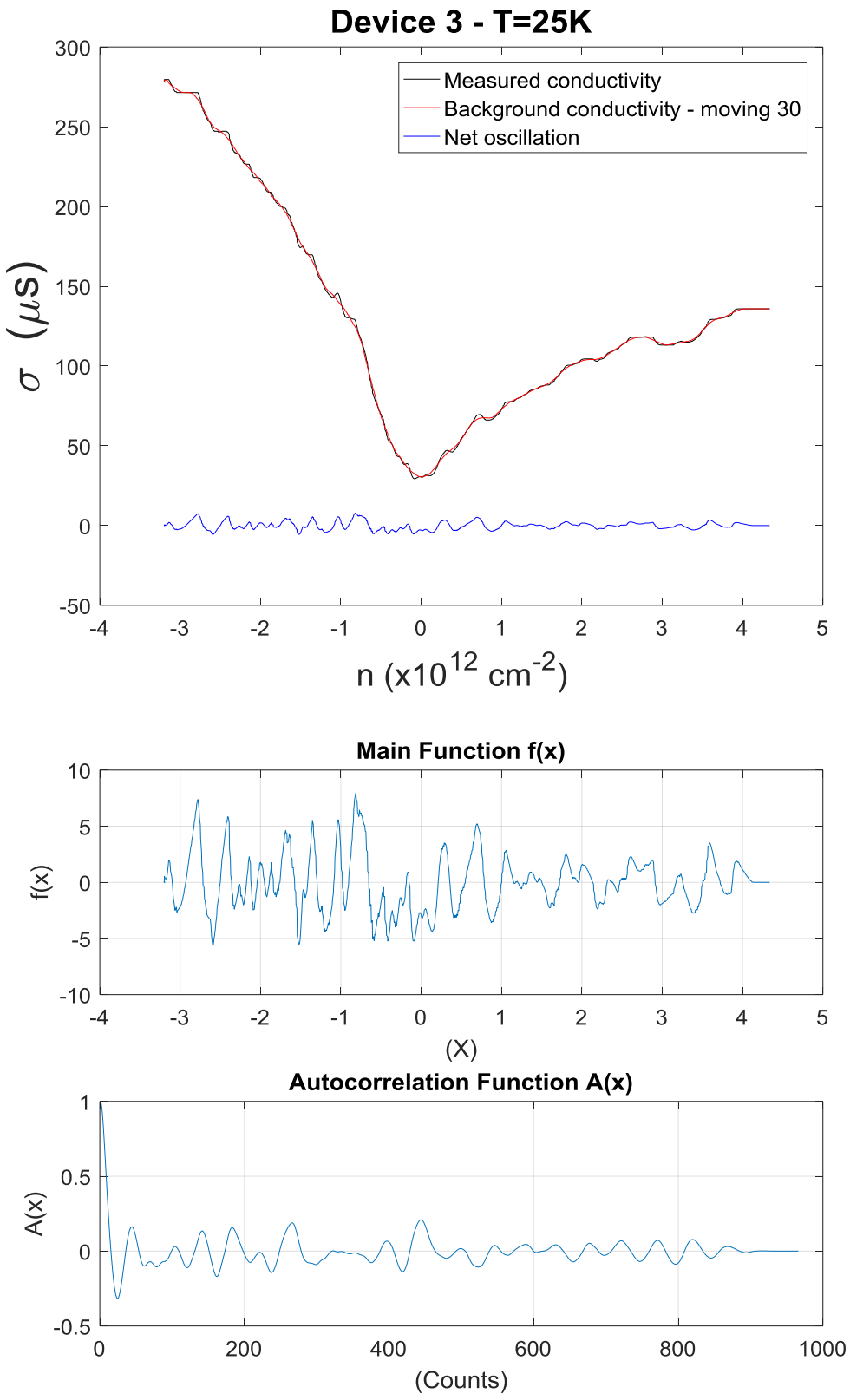

Figure 8.24– Device 3, constructing the conductivity oscillation versus carrier densities at 25K

Conductivity versus Magnetic Field – at different carrier regions $\sigma(B)_{n,p}\big|_T$

Now we do the same analysis for the magneto conductivity at different carrier regions: Electrons and Holes regions at three different temperatures.

Fig. 8.25-8.30 are the corresponding data for Device 2: Fig. 8.25, 8.26 show conductivity oscillation for Electrons, Holes regions at 5K respectively. 8.27, 8.28 show conductivity oscillation for Electrons, Holes regions at 15K respectively. Fig. 8.29, 8.30 show conductivity oscillation for Electrons, Holes regions at 33K respectively.

Similar data for Device 3 are shown in Fig. 8.31-8.36

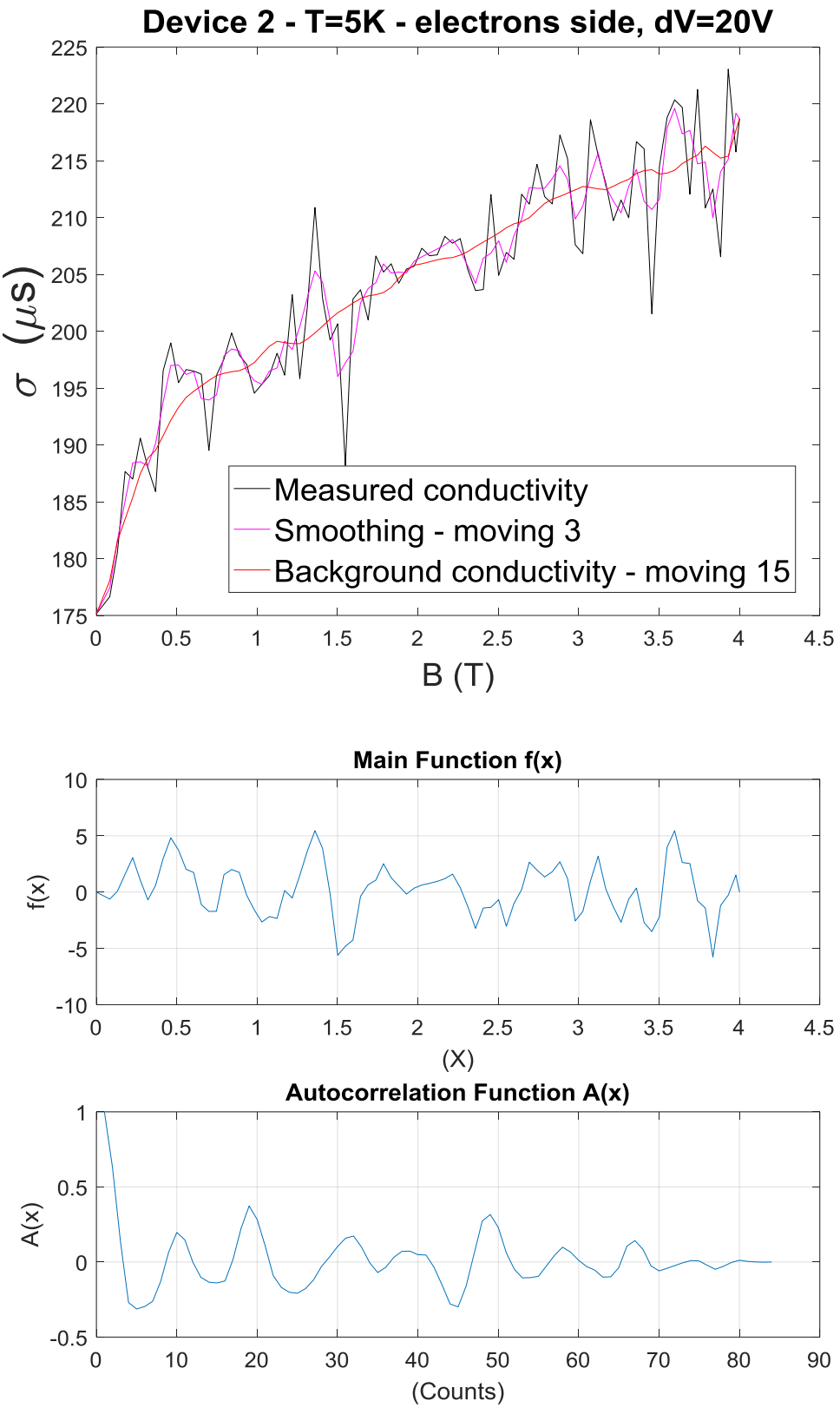

Figure 8.25– Device 2, Electrons region: constructing the conductivity oscillation versus magnetic field at 5K

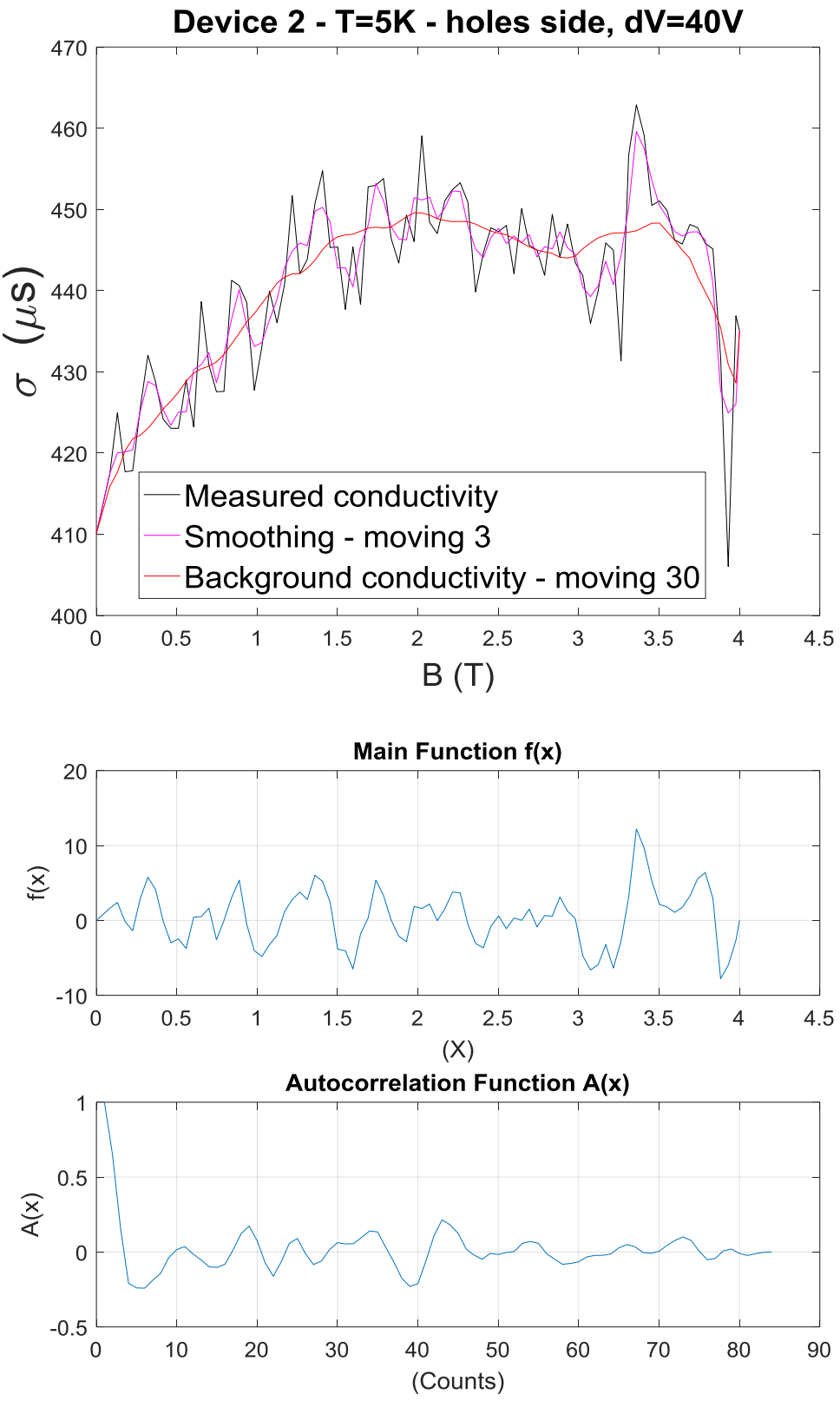

Figure 8.26– Device 2, Holes region: constructing the conductivity oscillation versus magnetic field at 5K

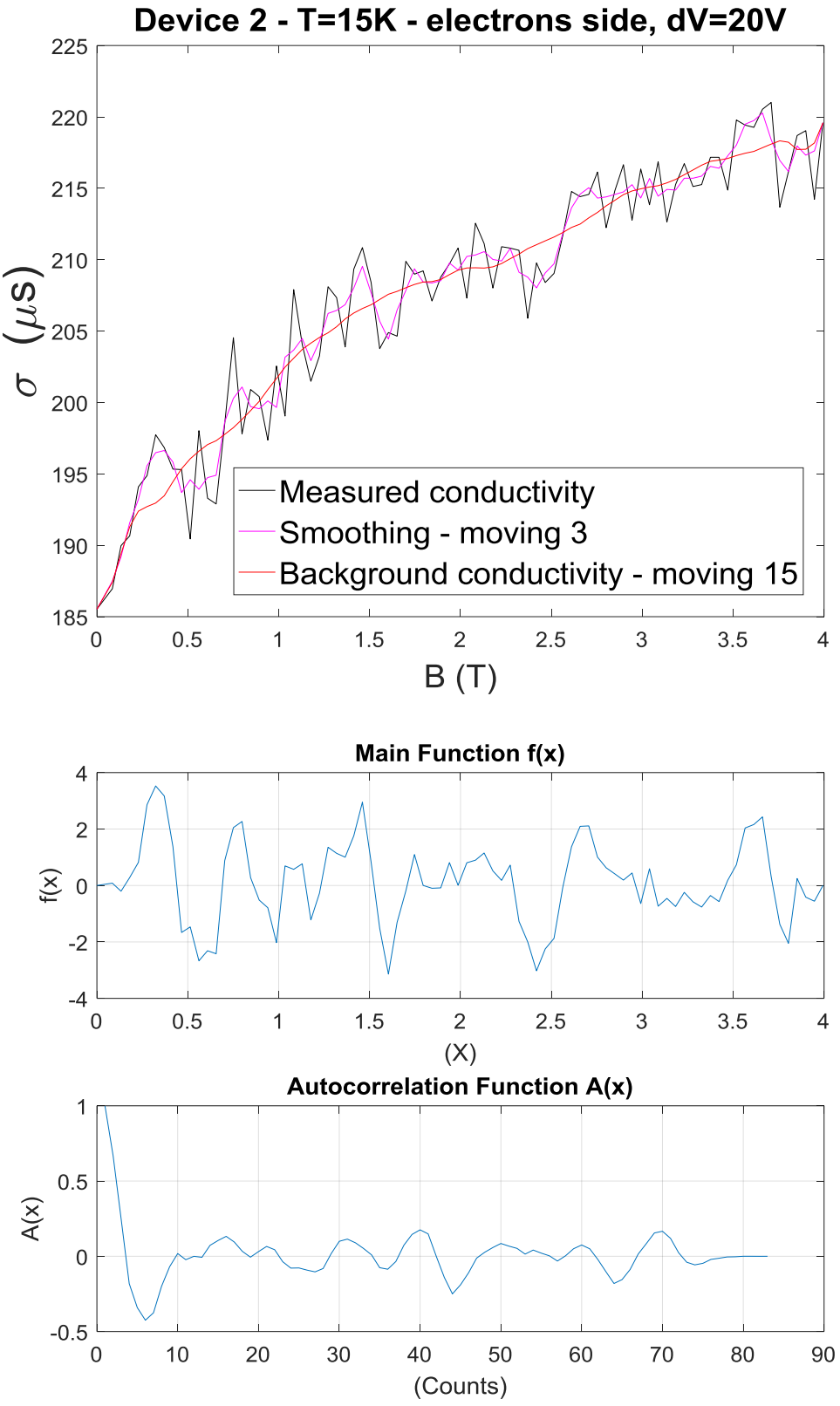

Figure 8.27– Device 2, Electrons region: constructing the conductivity oscillation versus magnetic field at 15K

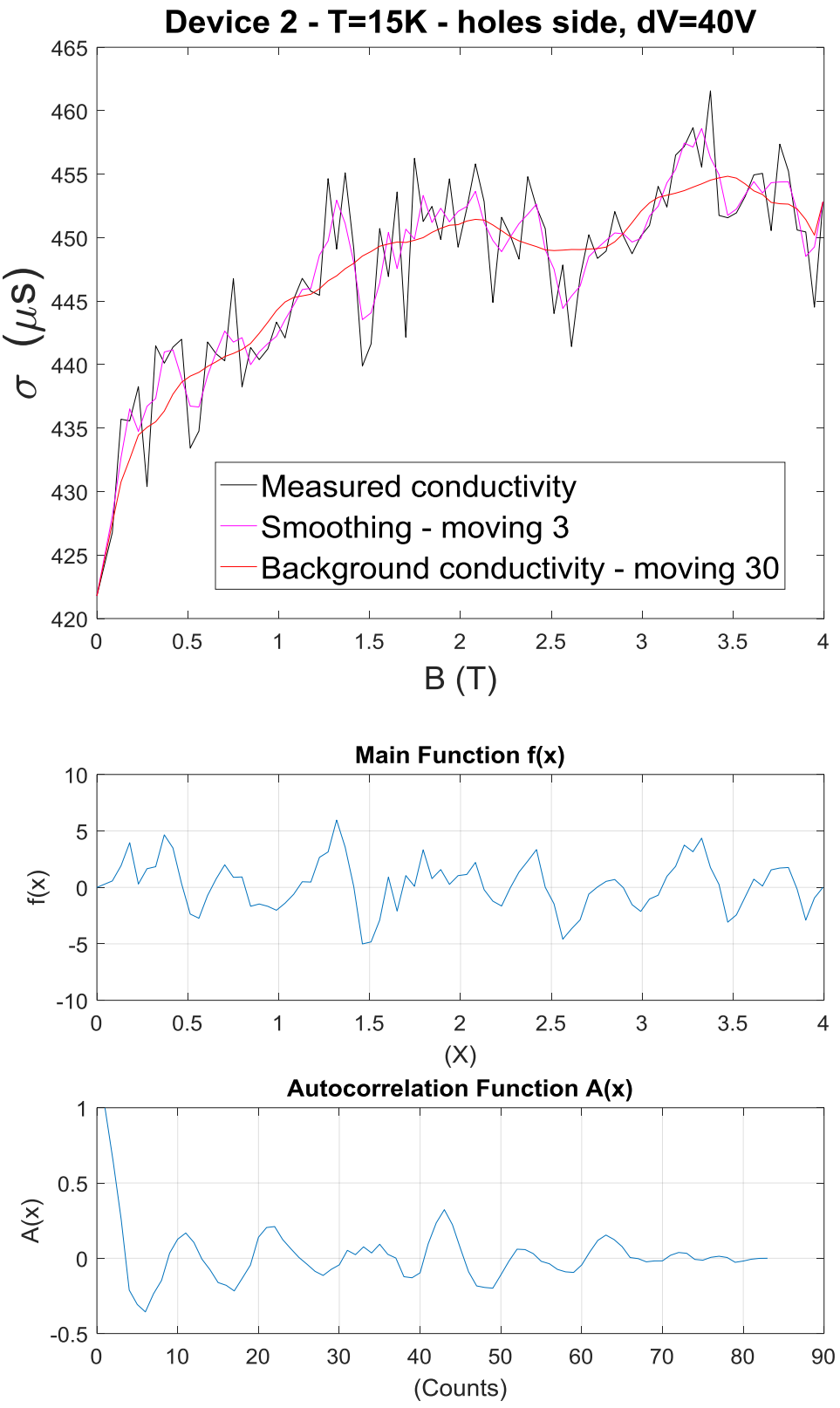

Figure 8.28– Device 2, Holes region: constructing the conductivity oscillation versus magnetic field at 15K

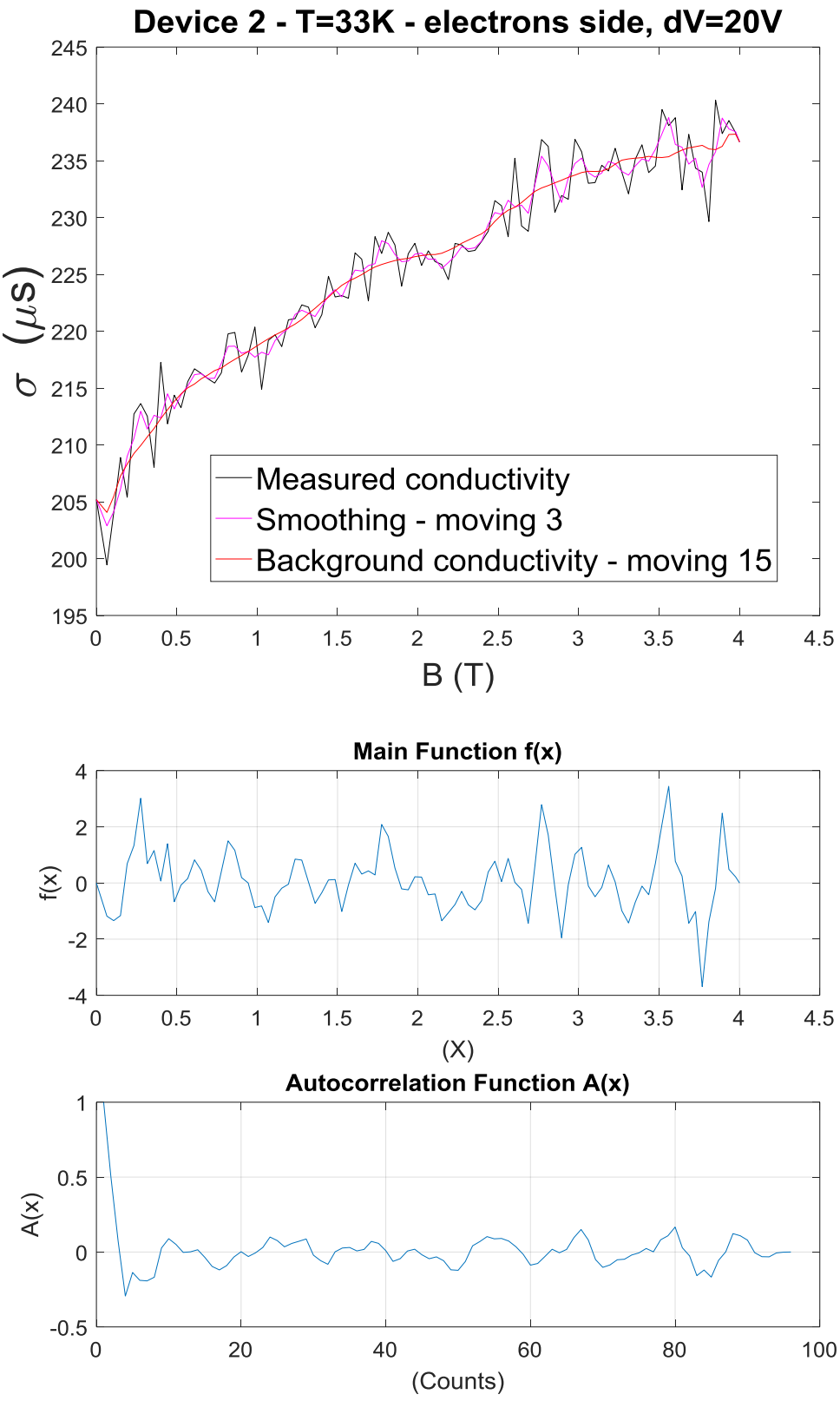

Figure 8.29– Device 2, Electrons region: constructing the conductivity oscillation versus magnetic field at 33K

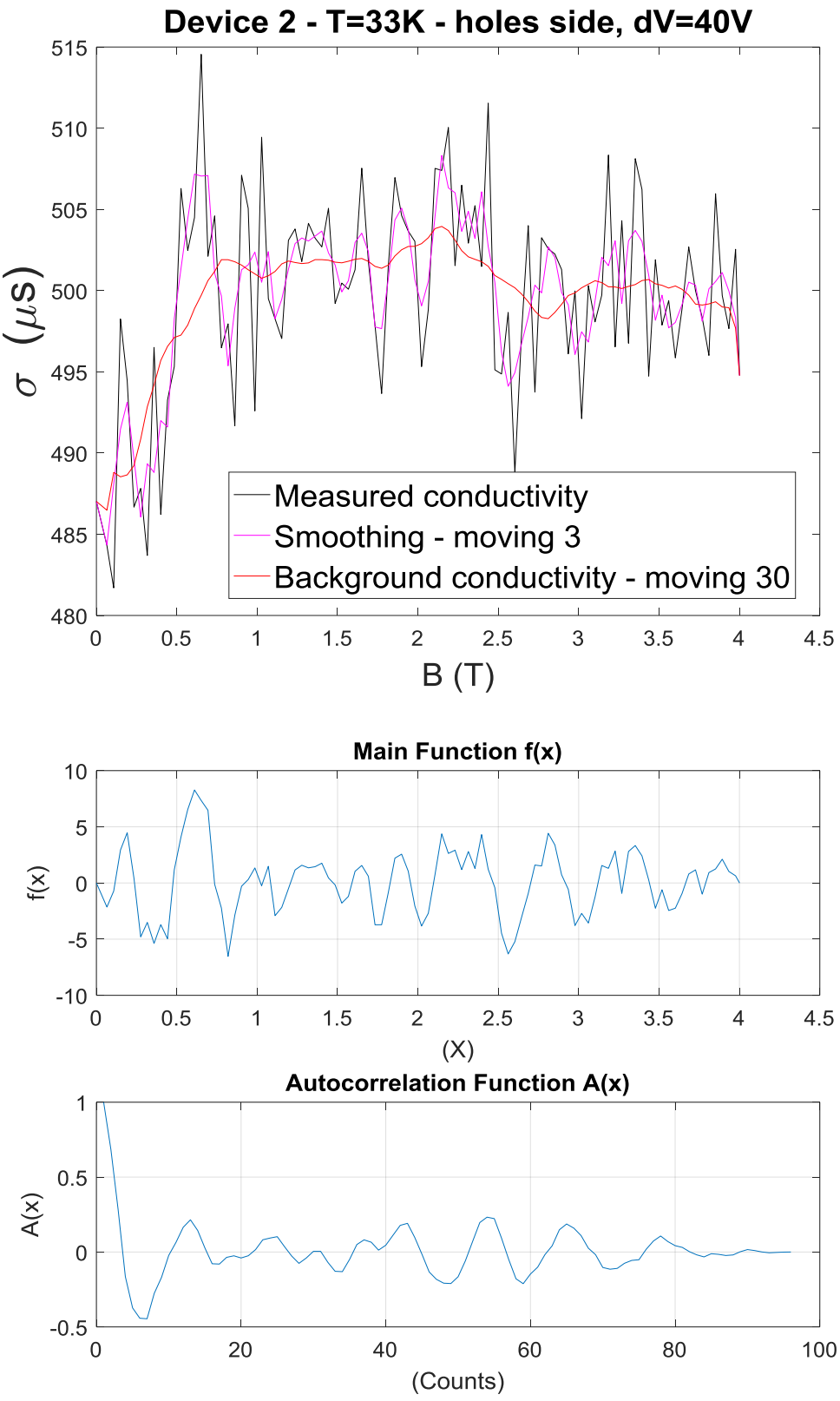

Figure 8.30– Device 2, Holes region: constructing the conductivity oscillation versus magnetic field at 33K

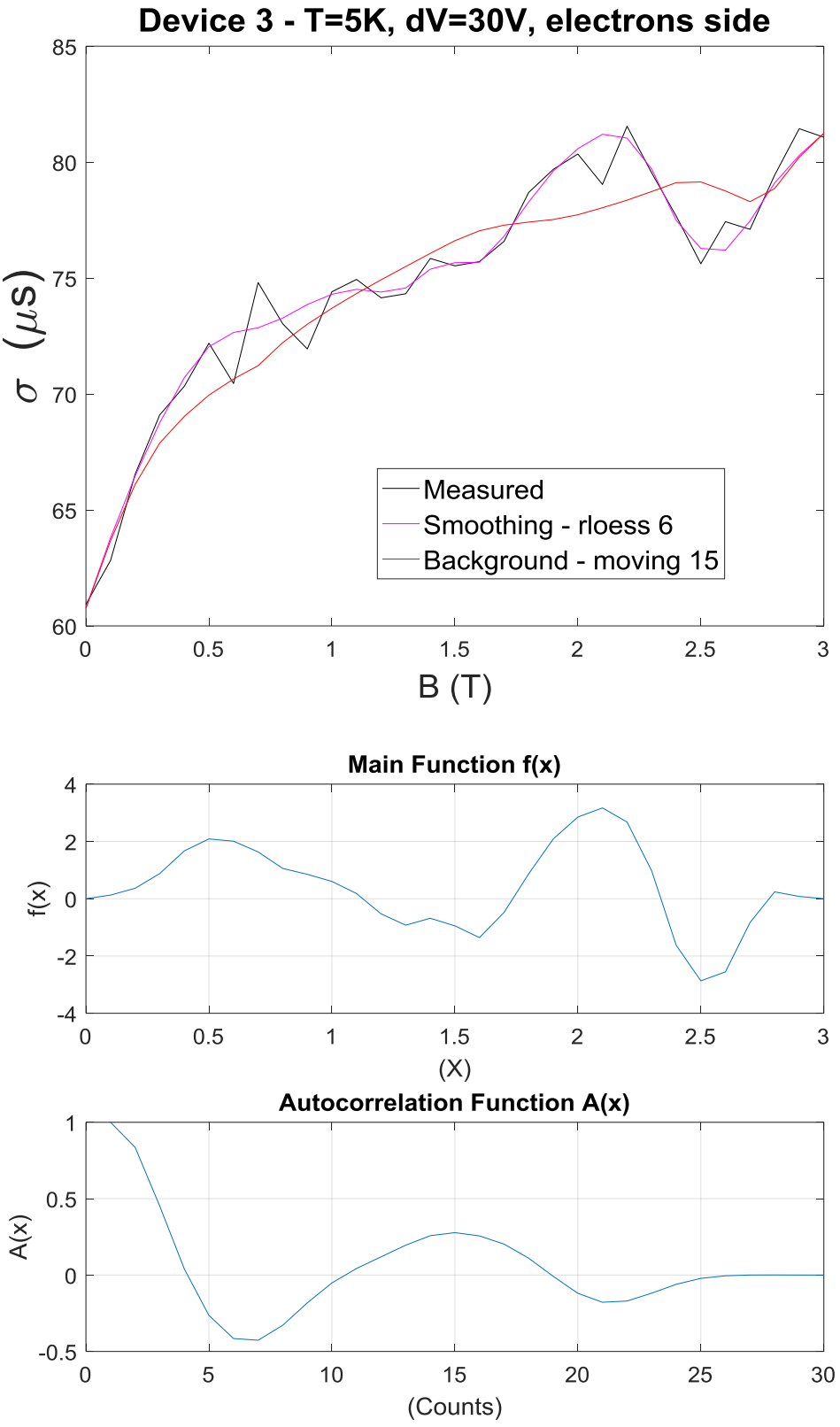

Figure 8.31– Device 3, Electrons region: constructing the conductivity oscillation versus magnetic field at 5K

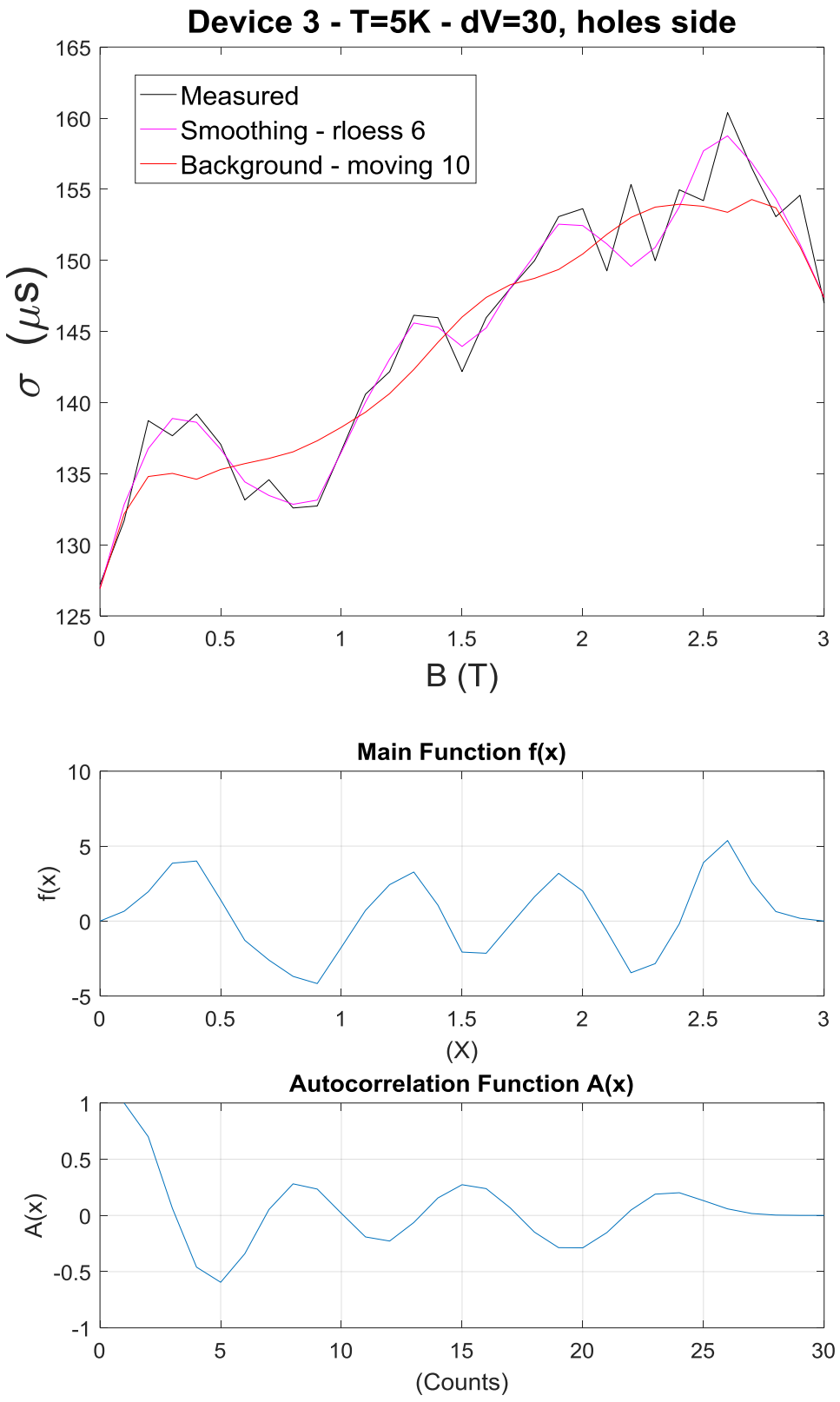

Figure 8.32– Device 3, Holes region: constructing the conductivity oscillation versus magnetic field at 5K

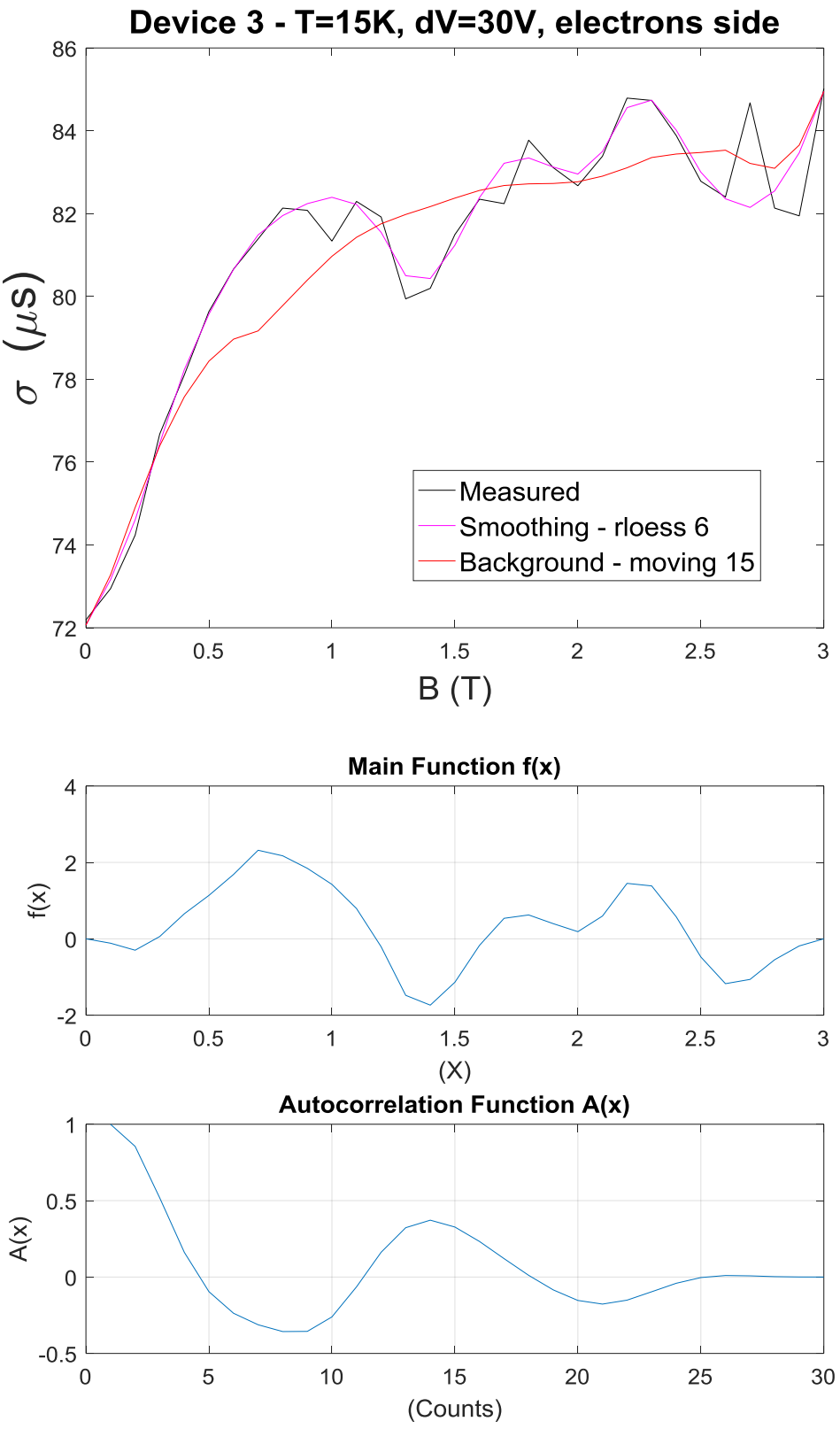

Figure 8.33– Device 3, Electrons region: constructing the conductivity oscillation versus magnetic field at 15K

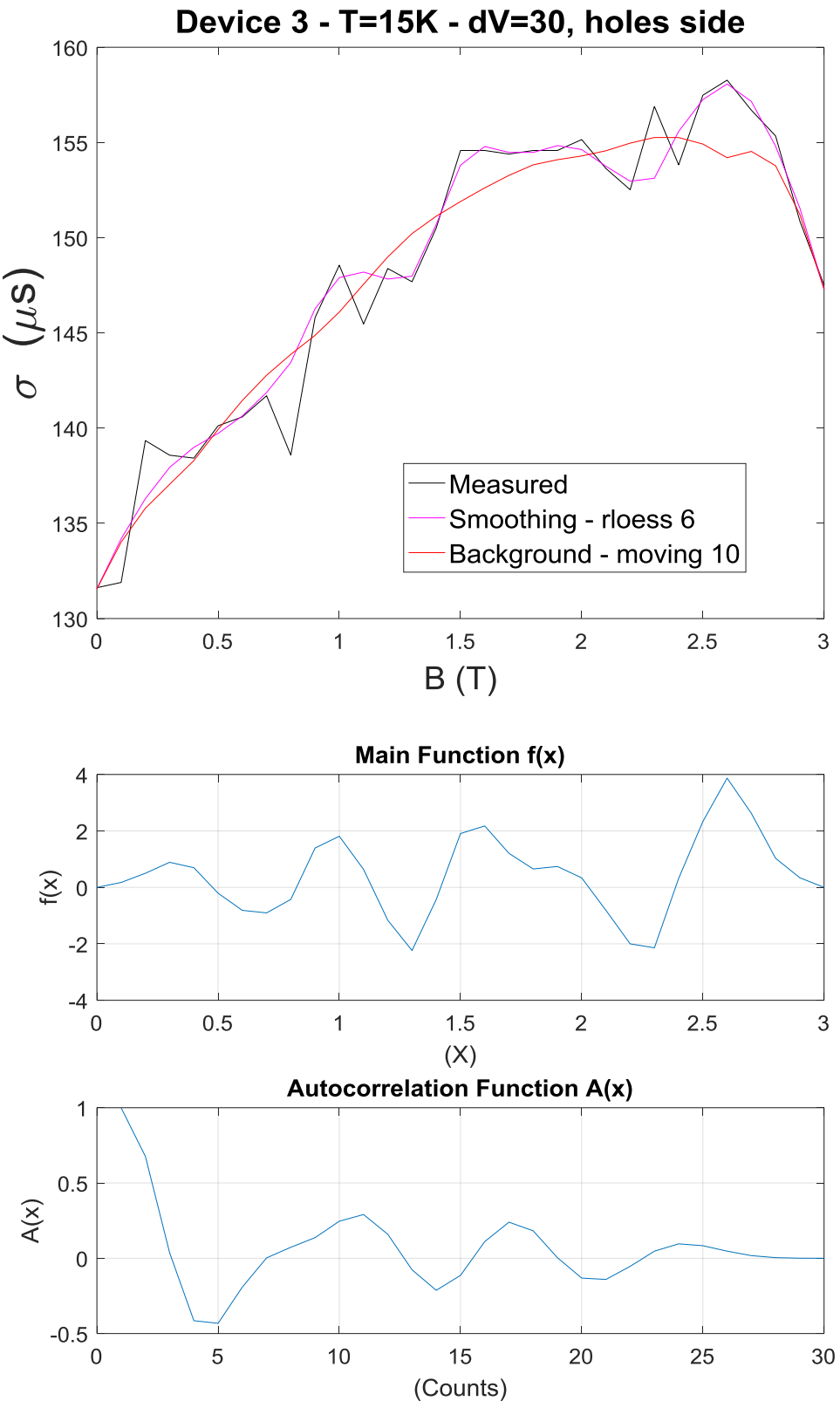

Figure 8.34– Device 3, Holes region: constructing the conductivity oscillation versus magnetic field at 15K

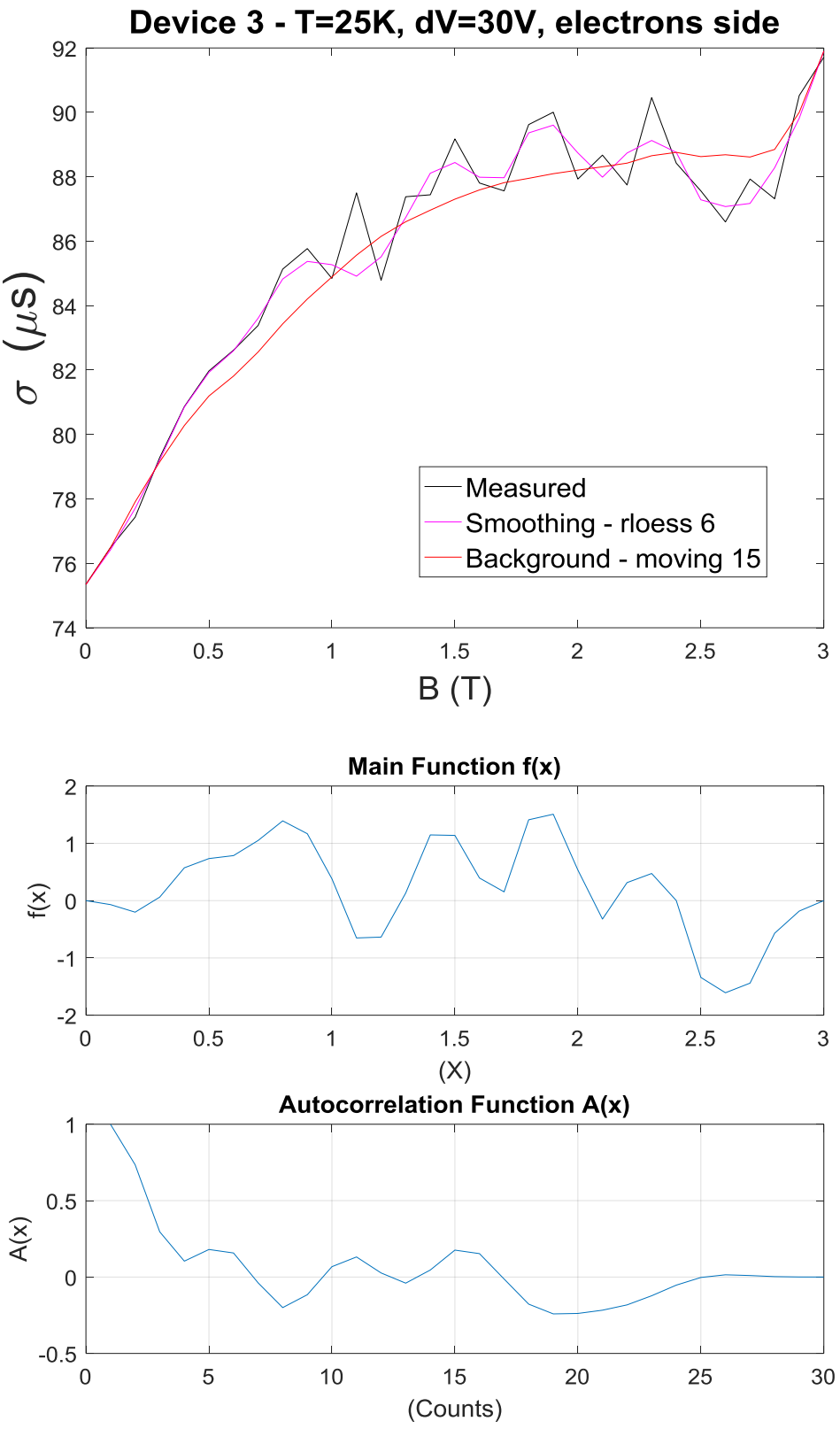

Figure 8.35– Device 3, Electrons region: constructing the conductivity oscillation versus magnetic field at 25K

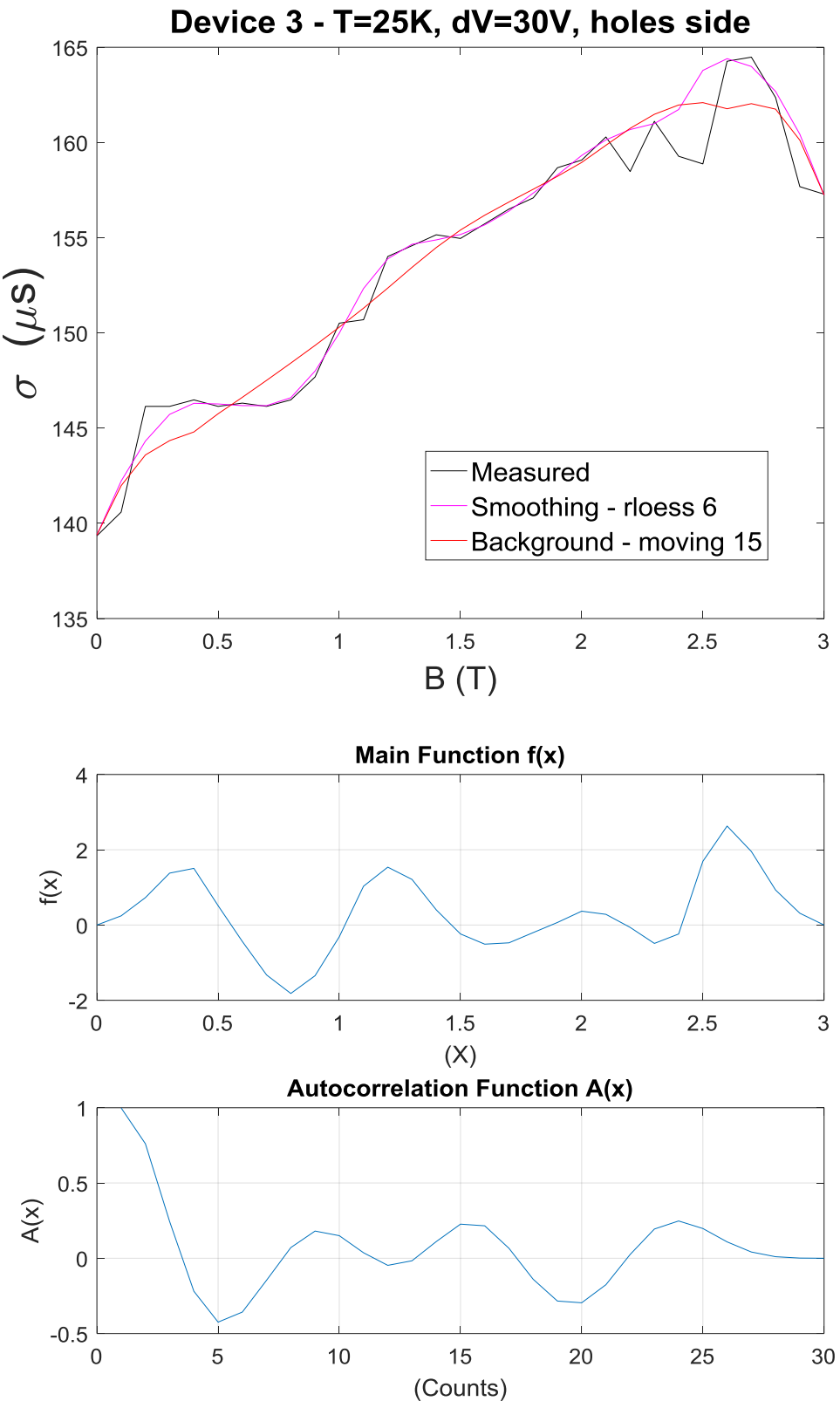

Figure 8.36– Device 3, Holes region: constructing the conductivity oscillation versus magnetic field at 25K

Now that we have constructed all oscillation characteristics, we come all together to compare to investigate if there are any common properties. It is also desirable if we can compare the oscillation properties at different carrier densities with the oscillation at varying magnetic fields.

Comparison of conductivity oscillations

Here we show the oscillation of conductivity at different temperatures with varying carrier densities for Device 2 and Device 3. Fig. 8.37 shows these results for both devices. As you notice, oscillations are not symmetric in Electrons and Holes side but the frequencies match. Fig. 8.38 shows the oscillation of conductivity versus magnetic field for Device 2 at Electrons side and Holes side. Fig. 8.39 shows the similar graphs for Device 3. As you notice, for Device 3, we have fewer data points which makes graphs roughly approximated.

Analyses of these plots and mathematical investigations leads us to the following findings:

- Oscillation of conductivity versus carrier densities in zero magnetic field, has a period of $0.38 \times 10^{12} cm^{-2}$ and is identical for both electrons and holes side
- Oscillation of conductivity versus carrier densities in zero magnetic field, has an amplitude of $10\mu s$ for holes side and it is almost half $(5\mu s)$ for electrons side
- Oscillation of conductivity versus magnetic field, has a period of $0.3T$ and is identical for both electrons and holes regions.
- Oscillation of conductivity versus magnetic field, has an amplitude of $6\mu s$ for holes side and it is almost half $(5\mu s)$ for electrons side.

Conclusion:

We demonstrated that there are interesting physics in nitrogen doped graphene which is totally different from pristine graphene. A summary of differences and findings are as below:

1- Conductivity (or resistivity) is strongly temperature dependent. More doping level is; more severe temperature dependency will be.
2- Nitrogen doping introduces metallic behavior to the system which causes the devices do not perfectly obey theory of Weak Localization.
3- There is strong electrons-holes asymmetry.
4- There are oscillation behaviors similarities as explained above.

Recommendations for future research:

Different device fabrication and measurements in this dissertation reveal that there are interesting physics that should be investigated more in depth. Since experimental data are solid and true, a more comprehensive theory needs to be developed to explain these exciting results.

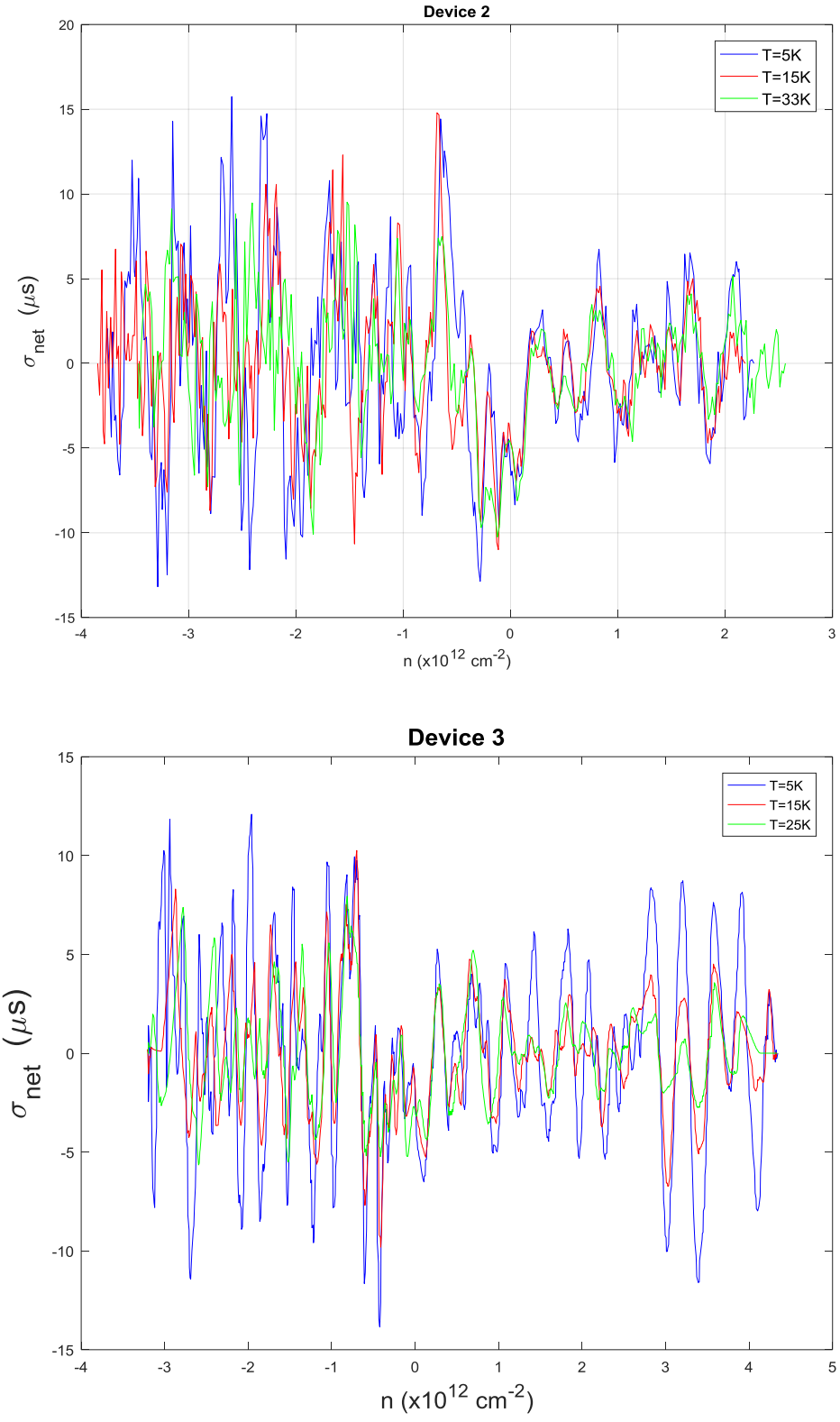

Figure 8.37– Oscillation of conductivity at varying carrier densities at different temperatures for Device 2 (top) and Device 3 (bottom)

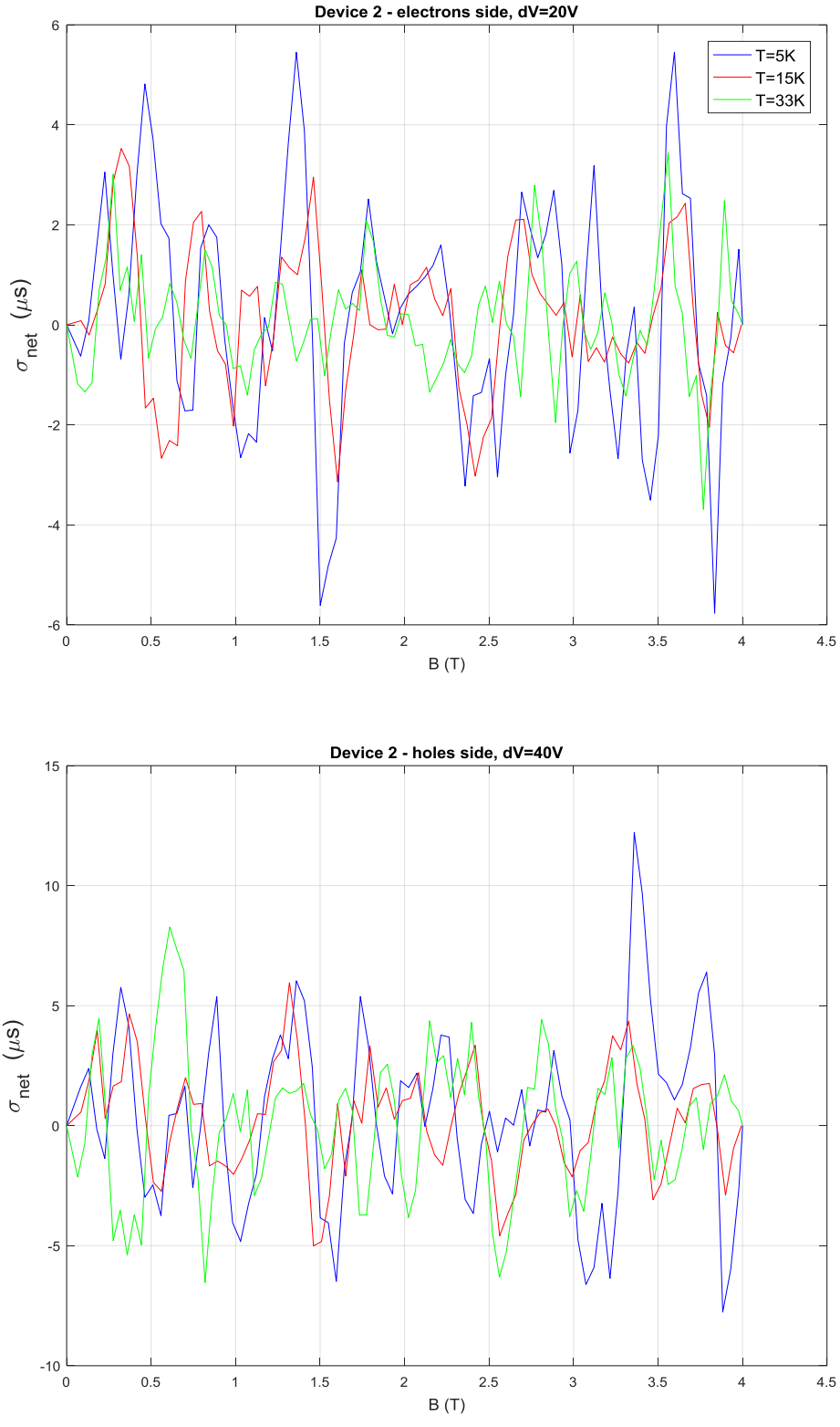

Figure 8.38– Oscillation of conductivity at varying magnetic field at different temperatures for Device 2 at Electrons side (top) and Holes side (bottom)

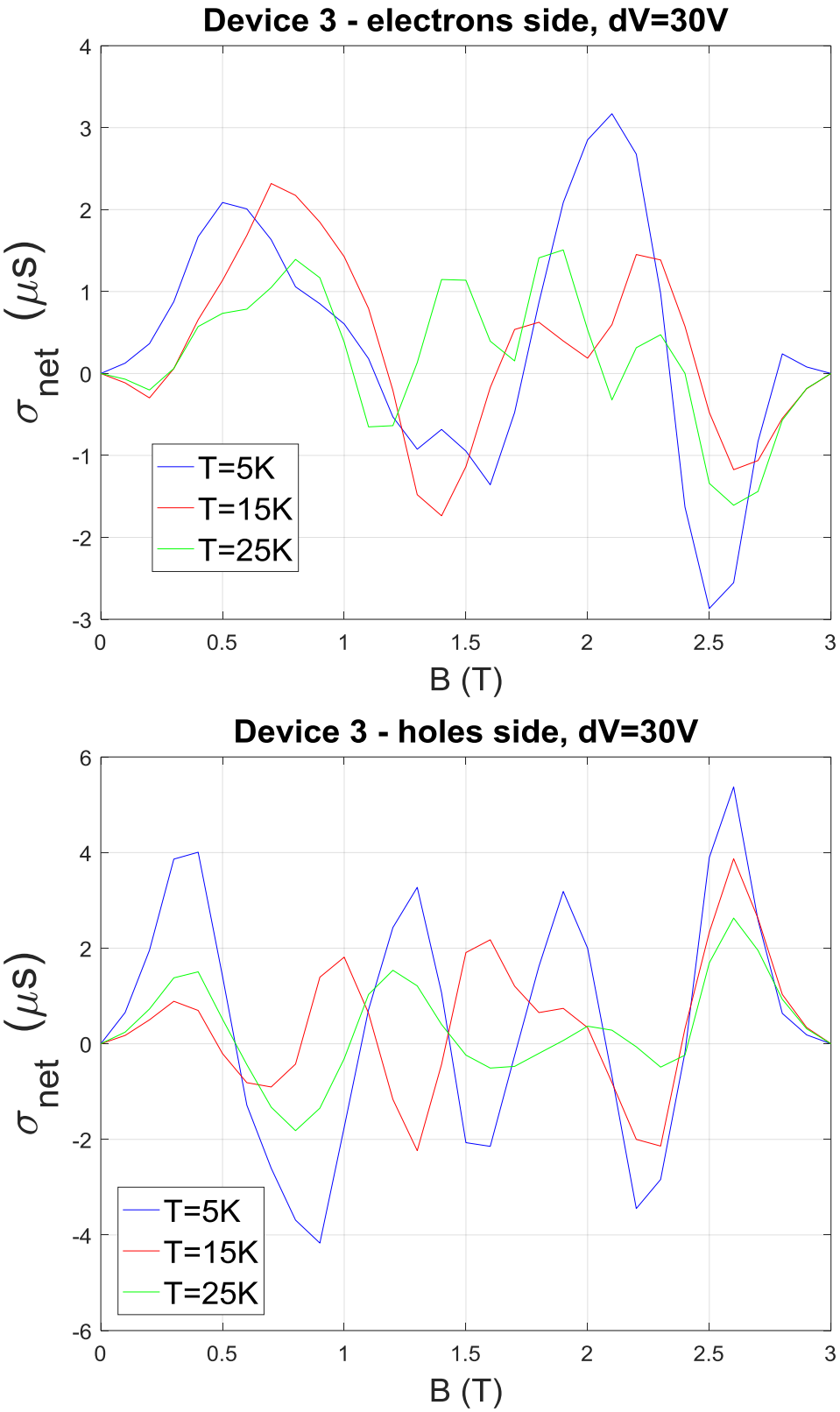

Figure 8.39– Oscillation of conductivity at varying magnetic field at different temperatures for Device 3 at Electrons side (top) and Holes side (bottom)

PART D

MANUFACTURING OF TWO-DIMENSIONAL MATERIALS

CHAPTER 9

Production of Pristine and N-doped Graphene

Graphene is a fundamental part for the new generation of 2D microdevices because of its outstanding physical properties. For this dissertation, we had to develop the optimum growth techniques in order to achieve the highest quality of graphene. Controlling the process and achieving the highest quality in not trivial especially when we want to add impurities (doping) to the graphene lattice. We noticed that doping destroys the quality of graphene. This made our research difficult especially when we tried to achieve high quality n-doped graphene. We first introduce the n-doped graphene growth technique followed by pristine graphene fabrication.

n-doped graphene technique:

preparation:

1- Install your tube on the furnace.

(put your coper foil inside)

(coper foils are the crucial parts, some of them do not give good growths - the one we used are from Nippon Mining Inc.)

2- Put vacuum head on the tube

- make sure valves are closed

3- Turn on the pump

- gently open the valve to prevent socking in

- pump for about 3 minutes

4- Cu folios usually have O- and OH- bounds on the surface which are not good for graphene growth. One effective way to clean is to dip in acetic acid overnight. And wash with DI water / N2 dry. Since surface becomes hydrophilic after acetic acid cleaning, N2 dry becomes little bit tricky and difficult,

5- Set all gas pressures to 6 psi. For calibrating ammonia line, refers to item 3 below.

Growth:

1- Clean. Set Ar=200 sccm for 5 min.

2- While pumping, close Ar, until pressure reaches the minimum pressure of the setup (0.00* -3 torr)

3- Calibrating ammonia line. Open the main valve. Slowly open the needle valve until the pressure goes to 0.03-0.15 torr.

(higher the pressure, the higher N-doping will be)

- Close the ammonia's needle valve

4- Clean. Do step 1 and 2 again until you reach the lowest pressure. (Ammonia is very sticky to tube's wall)

5- Set Ar=200, H2=10 sccm

6- Set temperature=1000 C

NOTE: higher the temperature, the better growth will be; should be close to the melting point of the copper. Some coppers have melting point of 1080C while the others 1050C. This is also highly dependent on the equipment and how the temperature is measured; if coppers evaporate at 1050C then 1000 is fair temperature to do growth

7- When the temperature=1000 C, move the furnace to the left on the copper foil.

Wait 10 min

8- Growth. Set Methane=170 sccm and Ammonia=desired pressure. Open simultaneously.

Wait 18 min.

(Growth gasses: ammonia, methane=170, H2=10)

9- Set temperature=20C

- wait to cool down to 550 C

10- When the temperature=550C

- set H2=0, Methane=0, Ammonia=0, Ar=200 sccm

- move the furnace to right

11- Wait until RT

pristine graphene technique:

preparation:

1- Install your tube on the furnace.

(Put your coper foil inside)

(Copper foils are the crucial parts, some of them do not give good growths – we used copper from Nippon Mining Inc.)

2- Put vacuum head on the tube

- make sure valves are closed

3- Turn on the pump

- Gently open the valve to prevent socking in

- Pump for about 3 minutes

Growth:

1- Clean. Set Ar=200 sccm for 5 min.

2- While pumping, close Ar, until pressure reaches the minimum pressure of the setup (0.00* -3 Torrs)

6- Set temperature=1000 C, Ar=200, H2=10 sccm

7- When the temperature=1000 C, move the furnace to the left on the copper foil.

Wait 10 min

Rev A (Ali): Ar=200, H2=10, Wait time=30 - 60 min

8- Growth. Set Ar=0, Methane=170, H2=10 sccm

Wait 18 min.

9- Set temperature=20C

- wait to cool down to 550 C

NOTE: You may follow the fast cooling recipe:

Put the nut set (spacer) 7cm in your left side with respect to the furnace center to open the lid 3cm then move furnace to right by 7cm

10- When the temperature=550C

- set H2=0, Methane=0, Ar=200 sccm

- move the furnace to right

11- Wait until RT

CHAPTER 10

Production of Transition Metal Dichalcogenides

As a part of fulfillment to the degree of Doctor of Philosophy, I started growing TMDs particulary MoSe2. We mainly focused on Chemical Vapor Deposition (CVD) technique to grow thin layer TMDs. Although our first attempts were not clean, we could grow mono layers in atmospheric pressure without using vacuum pumps. The schematic of furnace is shown in Fig.10.1. In the top, a simple schematic of precursors is shown. For MoSe2, we sued Sulphur and MoO3 solid precursors and heated at different temperatures during the process. Hydrogen as a reacting gas and Argon as a neutral carrier gas were also used. After investigating several process conditions, we established the optimum process conditions and then were able to grow monolayer MoSe2. The grown samples and photoluminescence studies are indicated in Fig. 10.2. Since the grown samples at atmospheric pressure, were not as clean as we expected – although normal when using solid precursors in atmosphere, we switched to vacuum – low pressure CVD growths. In this new setup, we used three solenoid valves for different gasses. The pressure is lowered by a dry, scroll vacuum pump (oil-free). The whole process was controlled by PC. Other than the amount of the material, and different temperature zones for each, we had also access to control the pressure with PC. We used LabView© to program the required control mechanisms.

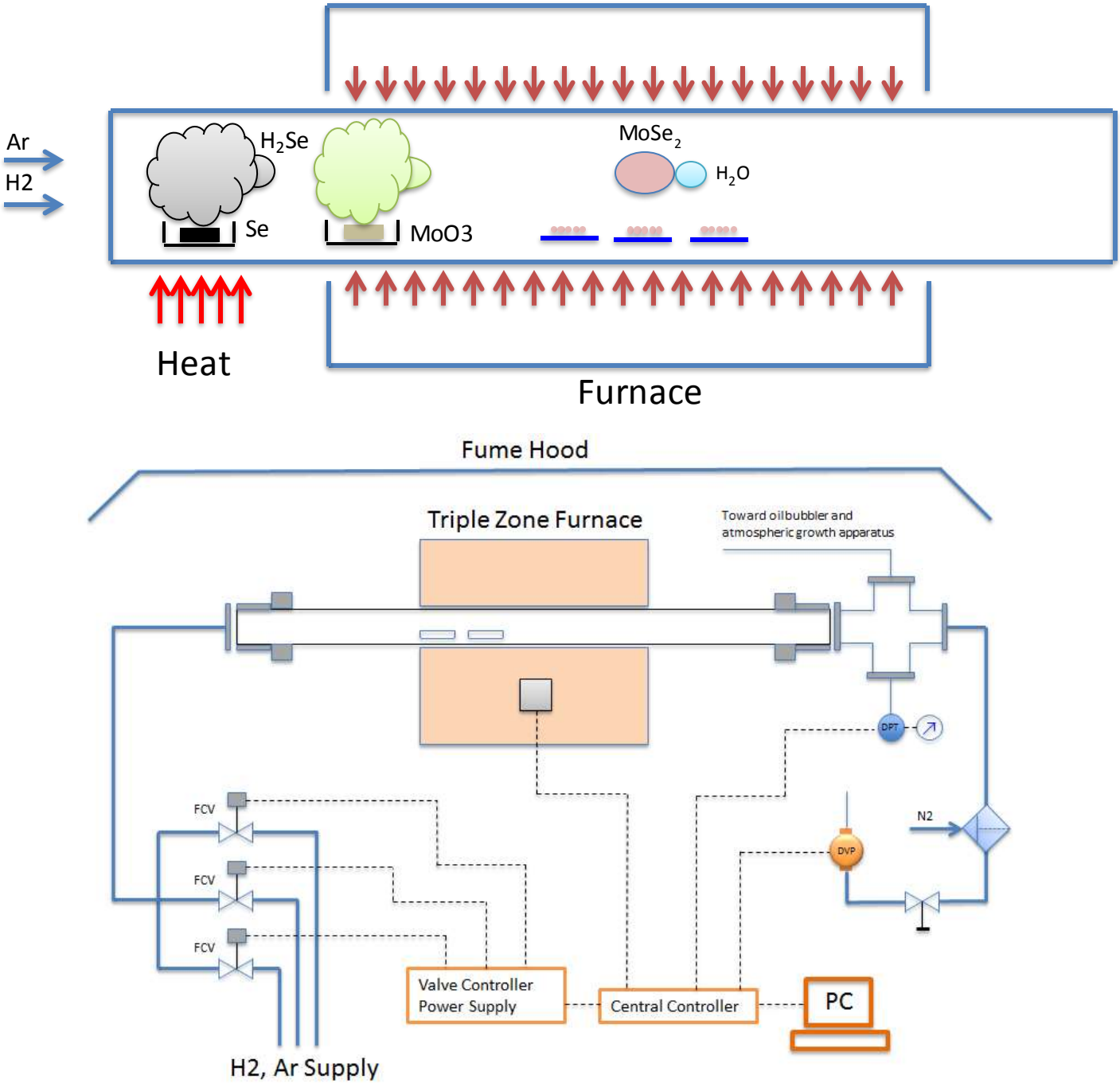

Figure 10.1. Furnace setup designed to produce TMDs, in atmospheric pressure (top) and in the vacuum using a dry vacuum pump solenoid valves all computer-controlled (bottom).

Fig. 10.2 shows the results of these growths. On the top, there are hexagons of single layers while in the bottom image, both single layer and double layer exist. These images are taken on August 2013, when there were no any report of CVD grown MoSe2.

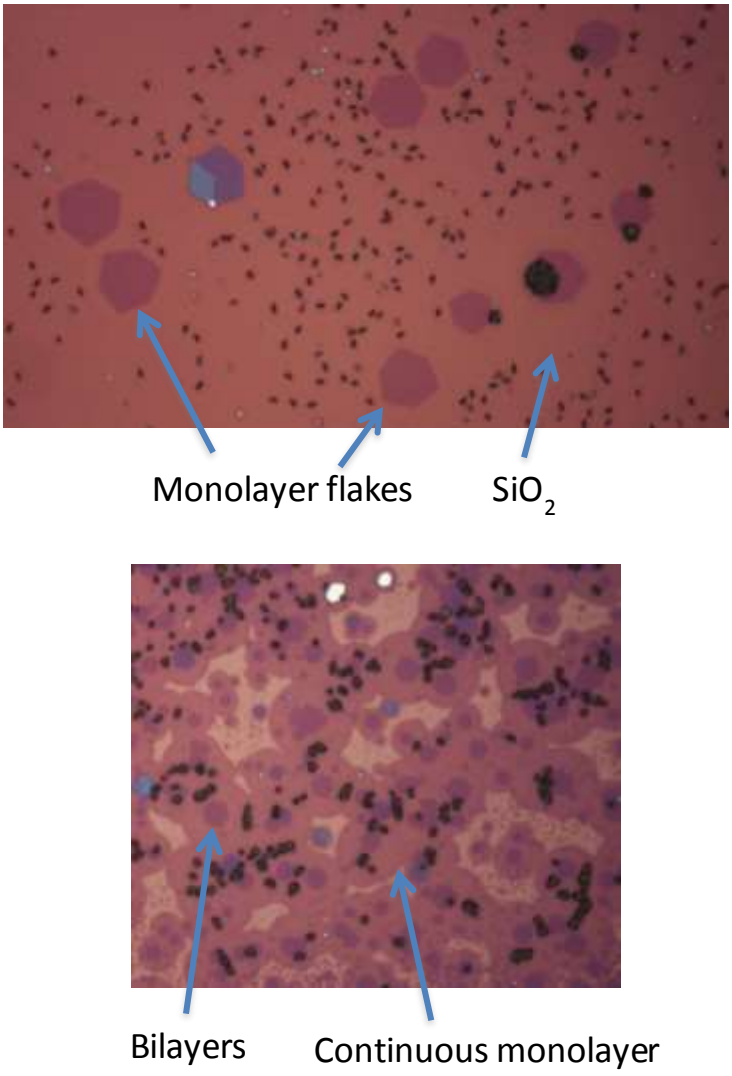

Figure 10.2. CVD grown MoSe2 containing both single layer (continuous and isolated) and double layers – August 2013, Physics Department, Columbia University, New York, United States.

Shown in Fig. 10.3 are the photoluminescence spectroscopy of these growths to verify if the grown samp

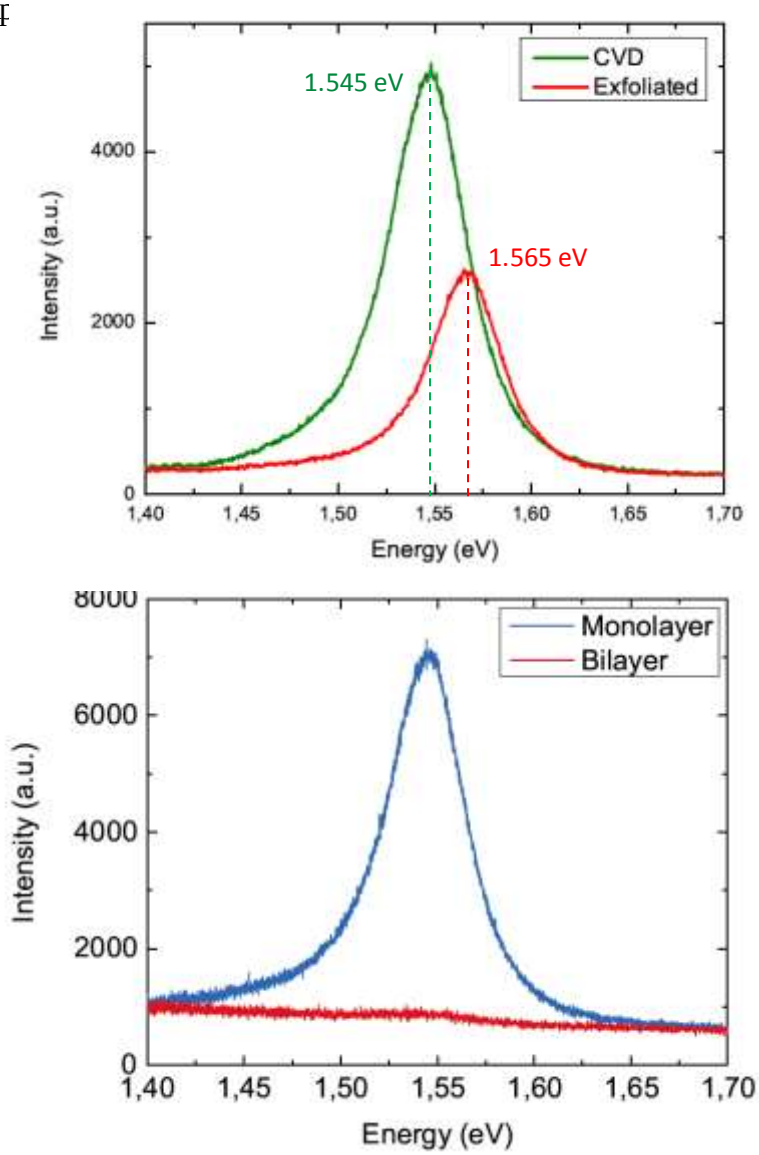

Figure 10.3. Photoluminescence studies of CVD grown MoSe2 with comparison to the exfoliated mono layers (top) and comparison of CVD grown mono layer to bilayer MoSe2 (bottom)

Interestingly, the single layer CVD samples has sharper peaks with higher intensities with respect to exfoliated samples. This might be the reason of doping effects or the chemical quality of the crystals used for exfoliation.

The comparison of photoluminescence spectra of single layer and double layer MoSe2 agrees with the publications [63]. Bilayer of ach TMD may exhibit different behavior when comparing to their corresponding single layer.

Growing samples for strain experiments

Our samples for strain experiments were grown in Mechanical Engineering Department of Stevens Institute of Technology. Here we explain the method were used to produce those samples.

Growth of Monolayer WS_2 on SiO_2 Substrates

The sample was comprised of a tungsten source carrier chip (5nm WO3 thin film on 90 nm SiO2) and bare SiO2/Si substrate (90 nm thick SiO2, WRS materials). Tungsten oxide (WO3, 99.99%, Kurt J. Lesker) was deposited on SiO2 via electron beam evaporation. The tungsten source chip was covered, in face-to-face contact, by a bare SiO2/Si substrate as the growth substrate. The sample was loaded into the center of a 3" diameter and 1 m long quartz tube (MTI Corp.), and a ceramic boat with 0.8 g of sulfur powder (99.98%, Sigma-Aldrich) was located upstream in the quartz tube. After loading, the ambient gas of the tube was purged out via mechanical pump to the base pressure of 400 mTorr. The furnace was heated to 700 ˚C at a 20 ˚C/min ramping rate and then to 900 ˚C at 5 ˚C/min. 60 sccm of Ar gas (5.0 UH purity, Praxair) was introduced at 150 ˚C (increasing temperature) to reduce moisture inside of the tube and closed at 600 ˚C (decreasing temperature). Hydrogen (40 sccm, 5.0 UH purity, Praxair) gas was supplied

to improve WO3 reduction from 700 ˚C (increasing temperature) to 600 ˚C (decreasing temperature). The growth pressure was 7 Torr. After 25 min at 900 ˚C, the furnace was cooled down to room temperature.

Growth of Monolayer WSe_2 on a SiO_2 Substrates

The sample was comprised of a tungsten source carrier chip (5nm WO3 thin film on 90 nm SiO2) and bare SiO2/Si substrate (90 nm thick SiO2, WRS materials). Tungsten oxide (WO3, 99.99%, Kurt J. Lesker) was deposited on SiO2 via electron beam evaporation. The tungsten source chip was covered, in face-to-face contact, by a bare SiO2/Si substrate as the growth substrate. The sample was loaded into the center of a 2" diameter and 24" long quartz tube (MTI Corp.), and a ceramic boat with 0.8 g of selenium powder (99.99%, Sigma-Aldrich) was located upstream in the quartz tube. After loading, the ambient gas of the tube was purged out via mechanical pump to the base pressure of 100 mTorr. The furnace was heated to 700 ˚C at a 20 ˚C/min ramping rate and then to 900 ˚C at 5 ˚C/min. 20 sccm of Ar gas (5.0 UH purity, Praxair) was introduced at 150 ˚C (increasing temperature) to reduce moisture inside of the tube and closed at 600 ˚C (decreasing temperature). Hydrogen (10 sccm, 5.0 UH purity, Praxair) gas was supplied to improve WO3 reduction from 700 ˚C (increasing temperature) to 600 ˚C (decreasing temperature). The growth pressure was 1 Torr. After 25 min at 900 ˚C, the furnace was cooled down to room temperature.

References

1. Das Sarma, S., et al., *Electronic transport in two-dimensional graphene.* Reviews of Modern Physics, 2011. **83**(2): p. 407-470.
2. Castro Neto, A.H., et al., *The electronic properties of graphene.* Reviews of Modern Physics, 2009. **81**(1): p. 109-162.
3. Wang, Q.H., et al., *Electronics and optoelectronics of two-dimensional transition metal dichalcogenides.* Nat Nano, 2012. **7**(11): p. 699-712.
4. Mattheiss, L.F., *Band Structures of Transition-Metal-Dichalcogenide Layer Compounds.* Physical Review B, 1973. **8**(8): p. 3719-3740.
5. Duerloo, K.-A.N., Y. Li, and E.J. Reed, *Structural phase transitions in two-dimensional Mo- and W-dichalcogenide monolayers.* Nat Commun, 2014. **5**.
6. Lieth, R.M.A. and J.C.J.M. Terhell, *Transition Metal Dichalcogenides*, in *Preparation and Crystal Growth of Materials with Layered Structures*, R.M.A. Lieth, Editor. 1977, Springer Netherlands: Dordrecht. p. 141-223.
7. Podberezskaya, N.V., et al., *Crystal Chemistry of Dichalcogenides MX2.* Journal of Structural Chemistry, 2001. **42**(4): p. 654-681.
8. Yun, W.S., et al., *Thickness and strain effects on electronic structures of transition metal dichalcogenides: 2H-MX2 semiconductors (M=Mo, W; X=S, Se, Te).* Physical Review B, 2012. **85**(3): p. 033305.
9. Y., G.G. and W.Y. Liang, *The electronic structures of platinum dichalcogenides: PtS2, PtSe2 and PtTe2.* Journal of Physics, 1986. **19**(7).
10. Huang, Z., W. Zhang, and W. Zhang, *Bang gap engineering of PtSe2.* 2016.
11. Qian, X., et al., *Quantum spin Hall effect in two-dimensional transition metal dichalcogenides.* Science, 2014. **346**(6215): p. 1344-1347.
12. Lin, Y.-C., et al., *Atomic mechanism of the semiconducting-to-metallic phase transition in single-layered MoS2.* Nat Nano, 2014. **9**(5): p. 391-396.
13. Huang, M., et al., *Phonon softening and crystallographic orientation of strained graphene studied by Raman spectroscopy.* Proceedings of the National Academy of Sciences, 2009. **106**(18): p. 7304-7308.
14. Loudon, R., *Raman effect in crystals.* Advances in Physics, 1964. **13**

(52): p. 423-482.
15. Conley, H.J., et al., *Bandgap Engineering of Strained Monolayer and Bilayer MoS2.* Nano Letters, 2013. **13**(8): p. 3626-3630.
16. Wang, Y., et al., *Raman spectroscopy study of lattice vibration and crystallographic orientation of monolayer MoS2 under uniaxial strain.* Small, 2013. **9**(17): p. 2857-61.
17. Zhang, X.-Q., et al., *Synthesis of Lateral Heterostructures of Semiconducting Atomic Layers.* Nano Letters, 2015. **15**(1): p. 410-415.
18. Chenet, D.A., et al., *In-Plane Anisotropy in Mono- and Few-Layer ReS2 Probed by Raman Spectroscopy and Scanning Transmission Electron Microscopy.* Nano Letters, 2015. **15**(9): p. 5667-5672.

19. Chhowalla, M., et al., *The chemistry of two-dimensional layered transition metal dichalcogenide nanosheets.* Nat Chem, 2013. **5**(4): p. 263-275.
20. Saito, R., et al., *Raman Spectroscopy of Transition Metal Dichalcogenides.* Journal of Physics: Condensed Matter, 2016. **25**(35).
21. Saleh, B.E.A. and M.C. Teich, *Fundamentals of Photonics.* 2007.
22. Lebègue, S. and O. Eriksson, *Electronic structure of two-dimensional crystals from \textit{ab initio} theory.* Physical Review B, 2009. **79**(11): p. 115409.
23. Xiao, D., et al., *Coupled Spin and Valley Physics in Monolayers of ${\mathrm{MoS}}_{2}$ and Other Group-VI Dichalcogenides.* Physical Review Letters, 2012. **108**(19): p. 196802.
24. Zeng, H., et al., *Valley polarization in MoS2 monolayers by optical pumping.* Nat Nano, 2012. **7**(8): p. 490-493.
25. Zhu, Z.Y., Y.C. Cheng, and U. Schwingenschlögl, *Giant spin-orbit-induced spin splitting in two-dimensional transition-metal dichalcogenide semiconductors.* Physical Review B, 2011. **84**(15): p. 153402.
26. Splendiani, A., et al., *Emerging Photoluminescence in Monolayer MoS2.* Nano Letters, 2010. **10**(4): p. 1271-1275.
27. Andor, K., et al., *$k \cdot p$ theory for two-dimensional transition metal dichalcogenide semiconductors.* 2D Materials, 2015. **2**(2): p. 022001.
28. Lee, C., et al., *Elastic and frictional properties of graphene.* physica status solidi (b), 2009. **246**(11-12): p. 2562-2567.
29. Guzman, D.M. and A. Strachan, *Role of strain on electronic and mechanical response of semiconducting transition-metal dichalcogenide monolayers: An ab-initio study.* Journal of Applied Physics, 2014. **115**(24): p. 243701.
30. Maniadaki, A.E., G. Kopidakis, and I.N. Remediakis, *Strain engineering of electronic properties of transition metal dichalcogenide monolayers.* Solid State Communications, 2016. **227**: p. 33-39.
31. Johari, P. and V.B. Shenoy, *Tuning the Electronic Properties of Semiconducting Transition Metal Dichalcogenides by Applying Mechanical Strains.* ACS Nano, 2012. **6**(6): p. 5449-5456.
32. Wang, Y., et al., *Strain-induced direct–indirect bandgap transition and phonon modulation in monolayer WS2.* Nano Research, 2015. **8**(8): p. 2562-2572.
33. Hosseini, M., et al., *Strain-Induced Modulation of Electron Mobility in Single-Layer Transition Metal Dichalcogenides.* IEEE Transactions on Electron Devices, 2015. **62**(10): p. 3192-3198.
34. Ghorbani-Asl, M., et al., *Strain-dependent modulation of conductivity in single-layer transition-metal dichalcogenides.* Physical Review B, 2013. **87**(23): p. 235434.
35. Duerloo, K.-A.N. and E.J. Reed, *Structural Phase Transitions by Design in Monolayer Alloys.* ACS Nano, 2016. **10**(1): p. 289-297.
36. Song, S., et al., *Room Temperature Semiconductor–Metal Transition of MoTe2 Thin Films Engineered by Strain.* Nano Letters, 2016. **16**(1): p. 188-193.
37. Li, Y., et al., *Structural semiconductor-to-semimetal phase transition in two-dimensional materials induced by electrostatic gating.* Nature Communications, 2016. **7**: p. 10671.
38. Akinwande, D., N. Petrone, and J. Hone, *Two-dimensional flexible nanoelectronics.* Nature Communications, 2014. **5**: p. 5678.
39. Duerloo, K.-A.N., M.T. Ong, and E.J. Reed, *Intrinsic Piezoelectricity in Two-Dimensional Materials.* The Journal of Physical Chemistry Letters, 2012. **3**(19): p. 2871-2876.
40. Senturia, S.D., *Microsystems Design.* 2001.
41. Mohiuddin, T.M.G., et al., *Uniaxial strain in graphene by Raman spectroscopy: G peak splitting, Gruneisen parameters, and sample orientation.* Physical Review B, 2009. **79**(20): p. 205433.
42. Fang, W., et al., *Strain-induced phonon shifts in tungsten disulfide nanoplatelets and nanotubes.* 2D Materials, 2017. **4**(1): p. 015007.

43. Zhang, X., et al., *Phonon and Raman scattering of two-dimensional transition metal dichalcogenides from monolayer, multilayer to bulk material.* Chemical Society Reviews, 2015. **44**(9): p. 2757-2785.
44. Peelaers, H. and C.G. Van de Walle, *Effects of strain on band structure and effective masses in MoS2.* Physical Review B, 2012. **86**(24): p. 241401.
45. Cazalilla, M.A., H. Ochoa, and F. Guinea, *Quantum Spin Hall Effect in Two-Dimensional Crystals of Transition-Metal Dichalcogenides.* Physical Review Letters, 2014. **113**(7): p. 077201.
46. Wu, W., et al., *Piezoelectricity of single-atomic-layer MoS2 for energy conversion and piezotronics.* Nature, 2014. **514**(7523): p. 470-474.
47. Desai, S.B., et al., *Strain-Induced Indirect to Direct Bandgap Transition in Multilayer WSe2.* Nano Letters, 2014. **14**(8): p. 4592-4597.
48. Rice, C., et al., *Raman-scattering measurements and first-principles calculations of strain-induced phonon shifts in monolayer MoS${}_{2}$.* Physical Review B, 2013. **87**(8): p. 081307.
49. Yang, L., et al., *Lattice strain effects on the optical properties of MoS2 nanosheets.* Scientific Reports, 2014. **4**: p. 5649.
50. Zhu, C.R., et al., *Strain tuning of optical emission energy and polarization in monolayer and bilayer MoS2.* Physical Review B, 2013. **88**(12): p. 121301.
51. Amorim, B., et al., *Novel effects of strains in graphene and other two dimensional materials.* Physics Reports, 2016. **617**: p. 1-54.
52. Castellanos-Gomez, A., et al., *Local Strain Engineering in Atomically Thin MoS2.* Nano Letters, 2013. **13**(11): p. 5361-5366.
53. Dou, X., et al., *Tuning and Identification of Interband Transitions in Monolayer and Bilayer Molybdenum Disulfide Using Hydrostatic Pressure.* ACS Nano, 2014. **8**(7): p. 7458-7464.
54. Sahin, H., et al., *Anomalous Raman spectra and thickness-dependent electronic properties of WSe${}_{2}$.* Physical Review B, 2013. **87**(16): p. 165409.
55. Tonndorf, P., et al., *Photoluminescence emission and Raman response of monolayer MoS2, MoSe2, and WSe2.* Optics Express, 2013. **21**(4): p. 4908-4916.
56. Zhang, M., et al., *Two-Dimensional Molybdenum Tungsten Diselenide Alloys: Photoluminescence, Raman Scattering, and Electrical Transport.* ACS Nano, 2014. **8**(7): p. 7130-7137.
57. O'Brien, M., et al., *Mapping of Low-Frequency Raman Modes in CVD-Grown Transition Metal Dichalcogenides: Layer Number, Stacking Orientation and Resonant Effects.* Scientific Reports, 2016. **6**: p. 19476.
58. Robert, S., et al., *Reversible uniaxial strain tuning in atomically thin WSe 2.* 2D Materials, 2016. **3**(2): p. 021011.
59. Cong, C., et al., *Synthesis and optical properties of large-scale single-crystalline two-dimensional semiconductor WS2 monolayer from chemical vapor deposition.* arXiv:1312.1418, 2013.
60. Carvalho, B.R., et al., *Intervalley scattering by acoustic phonons in two-dimensional MoS2 revealed by double-resonance Raman spectroscopy.* Nature Communications, 2017. **8**: p. 14670.
61. Berkdemir, A., et al., *Identification of individual and few layers of WS2 using Raman Spectroscopy.* Scientific Reports, 2013. **3**: p. 1755.
62. Molina-Sánchez, A. and L. Wirtz, *Phonons in single-layer and few-layer MoS${}_{2}$ and WS${}_{2}$.* Physical Review B, 2011. **84**(15): p. 155413.
63. Chang, C.-H., et al., *Orbital analysis of electronic structure and phonon dispersion in MoS${}_{2}$, MoSe${}_{2}$, WS${}_{2}$, and WSe${}_{2}$ monolayers under strain.* Physical Review B, 2013. **88**(19): p. 195420.
64. Terrones, H., et al., *New First Order Raman-active Modes in Few Layered Transition Metal Dichalcogenides.* Scientific Reports, 2014. **4**: p. 4215.

65. Amin, B., T.P. Kaloni, and U. Schwingenschlogl, *Strain engineering of WS2, WSe2, and WTe2.* RSC Advances, 2014. **4**(65): p. 34561-34565.
66. Zhan-Yu, W. and e. al, *Effects of in-plane Stiffness and Charge Transfer on Thermal Expansion of Monolayer Transition Metal Dichalcogenide.* Chinese Phys. B, 2015(24): p. 026501.
67. Peng, B., et al., *Thermal conductivity of monolayer MoS2, MoSe2, and WS2: interplay of mass effect, interatomic bonding and anharmonicity.* RSC Advances, 2016. **6**(7): p. 5767-5773.
68. Cai, Q., et al., *Raman signature and phonon dispersion of atomically thin boron nitride.* Nanoscale, 2017. **9**(9): p. 3059-3067.
69. Kresse, G. and J. Hafner, *Ab initio.* Physical Review B, 1993. **48**(17): p. 13115-13118.
70. Kresse, G. and J. Furthmüller, *Efficient iterative schemes for ab initio total-energy calculations using a plane-wave basis set.* Physical Review B, 1996. **54**(16): p. 11169-11186.
71. Parlinski, K., Z.Q. Li, and Y. Kawazoe, *First-Principles Determination of the Soft Mode in Cubic ${\mathrm{ZrO}}_{2}$.* Physical Review Letters, 1997. **78**(21): p. 4063-4066.
72. K., P., *Software PHONON.* Cracow, 2010.
73. Perdew, J.P., K. Burke, and M. Ernzerhof, *Generalized Gradient Approximation Made Simple.* Physical Review Letters, 1996. **77**(18): p. 3865-3868.
74. Blöchl, P.E., *Projector augmented-wave method.* Physical Review B, 1994. **50**(24): p. 17953-17979.
75. Kresse, G. and D. Joubert, *From ultrasoft pseudopotentials to the projector augmented-wave method.* Physical Review B, 1999. **59**(3): p. 1758-1775.
76. Wang, Z., et al., *Probing the Spin-Polarized Electronic Band Structure in Monolayer Transition Metal Dichalcogenides by Optical Spectroscopy.* Nano Letters, 2017. **17**(2): p. 740-746.
77. Morozov, S.V., et al., *Giant Intrinsic Carrier Mobilities in Graphene and Its Bilayer.* Physical Review Letters, 2008. **100**(1): p. 016602.
78. McCann, E., et al., *Weak-Localization Magnetoresistance and Valley Symmetry in Graphene.* Physical Review Letters, 2006. **97**(14): p. 146805.